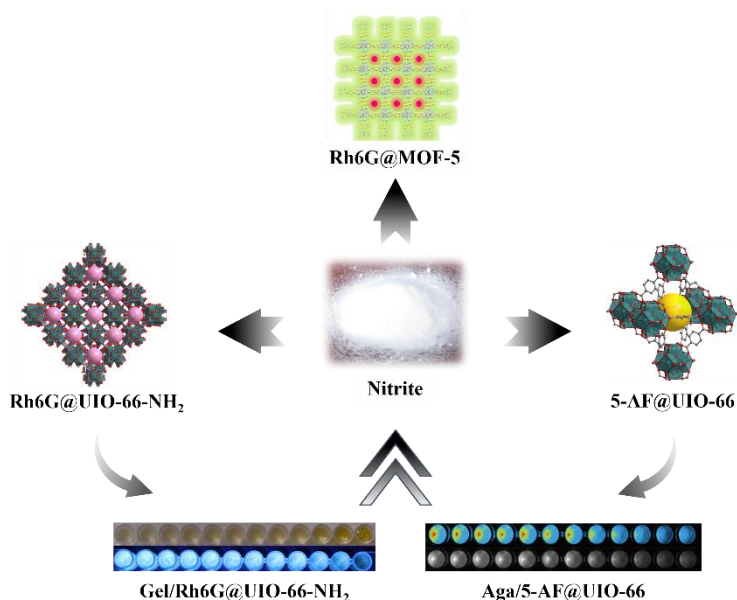


Study on Rapid Detection of Nitrite in Meat Products Based on Luminescent Metal-Organic Framework (LMOF) Nanocomposite



Author: Siyang DENG

Supervisor: Prof. Christophe BLECKER

Co-supervisor: Prof. Chunhui ZHANG

Year: 2024

COMMUNAUTÉ FRANÇAISE DE BELGIQUE

UNIVERSITÉ DE LIÈGE – GEMBLoux AGRO-BIO TECH

**Study on Rapid Detection of Nitrite in Meat
Products Based on Luminescent Metal-Organic
Framework (LMOF) Nanocomposite**

**Étude de la détection rapide des nitrites dans les produits carnés basée
sur un nanocomposite à structure métallo-organique luminescent
(LMOF)**

Siyang DENG

Supervisor: Prof. Christophe Blecker, Co-supervisor: Prof. Chunhui Zhang
Year: 2024

Copyright. Cette œuvre est sous licence Creative Commons. Vous êtes libre de reproduire, de modifier, de distribuer et de communiquer cette création au public selon les conditions suivantes:

- paternité (BY): vous devez citer le nom de l'auteur original de la manière indiquée par l'auteur de l'œuvre ou le titulaire des droits qui vous confère cette autorisation (mais pas d'une manière qui suggérerait qu'ils vous soutiennent ou approuvent votre utilisation de l'œuvre);

- pas d'utilisation commerciale (NC): vous n'avez pas le droit d'utiliser cette création à des fins commerciales;

- partage des conditions initiales à l'identique (SA): si vous modifiez, transformez ou adaptez cette création, vous n'avez le droit de distribuer la création qui en résulte que sous un contrat identique à celui-ci. À chaque réutilisation ou distribution de cette création, vous devez faire apparaître clairement au public les conditions contractuelles de sa mise à disposition. Chacune de ces conditions peut être levée si vous obtenez l'autorisation du titulaire des droits sur cette œuvre. Rien dans ce contrat ne diminue ou ne restreint le droit moral de l'auteur.

Siyang Deng (2023). “Study on rapid detection of nitrite in meat products based on luminescent metal-organic framework (LMOF) nanocomposite” (Ph.D. Dissertation in English).

Gembloux, Belgium, Gembloux Agro-Bio Tech, University of Liege.

162 Pages, 37 figures, 6 tables.

Summary:

Nitrite is a commonly used food additive in the meat industry that cannot be completely replaced. Its main functions include promoting color development, inhibiting microbial growth, providing antioxidant effects, and imparting a distinctive flavor to meat products. However, nitrite is also a highly toxic substance, and an excessive amount of nitrite in food can pose significant health risks. When interacting with proteins (such as primary and secondary amines), nitrite can produce carcinogenic nitrosamines. Additionally, food safety problems related to nitrite have occurred in recent years. Therefore, the rapid detection of trace concentrations of nitrite in food is extremely essential. Great efforts have been made to establish new methods to determine nitrite in food, however, the existing detection methods are not comprehensive enough. In comparison to other methods, fluorescence spectrometry has become an effective method for detecting nitrite ions due to its high sensitivity, good selectivity, low detection limit and simple detection conditions. The key to determining nitrite by the fluorescence method lies in designing and fabricating fluorescent nanoprobes with good selectivity and high sensitivity.

Metal-organic frameworks (MOFs), a novel class of multifunctional materials, have demonstrated excellent potential in various fields such as gas storage, adsorption and separation, catalysis, sensing, drug delivery and more in recent years. Due to their chemical design flexibility and tunable pore structures, MOFs exhibit inherent advantages in the field of fluorescence sensing. Therefore, it is both feasible and innovative to explore their application in nitrite detection and food safety protection. This study aims to design and synthesize several novel luminescent metal-organic framework (LMOF) based fluorescence nanoprobes. These probes are created by integration MOFs with different dyes and successfully applying them to detect nitrite in real meat samples. Moreover, to expand the application scope of powdered LMOF and develop the LMOFs-based sensing device, LMOFs were combined with natural hydrogel polymers to form a composite hydrogel test kit. This innovation approach opens a new avenue for the application of LMOF materials in the field of fluorescence sensing, particularly in the sensing and detecting of nitrite.

In the first part, a single-emission LMOF-based nanoprobe, denoted as Rh6G@MOF-5, was fabricated through a facile solvothermal synthesis method. The porous structure and chemical designability of MOF-5 material facilitate the good diffusion of the targeted analyte through the pre-gathering process, with rhodamine

6G as a recognition element for nitrite. This enables Rh6G@MOF-5 to serve as an ideal fluorescent sensing material with high selectivity and sensitivity during nitrite detection process. It exhibits a linear ranges of 0–200 $\mu\text{mol/L}$ and a low detection limit of 0.2 $\mu\text{mol/L}$. Moreover, the sensing platform can also be use for the nitrite detection in real meat samples. The results demonstrate that this material may be a promising candidate for nitrite detection in food.

In addition, to overcome limitations associated with single-emission sensing measurements, a ratiometric LMOF-based fluorescence sensor (Rh6G@UIO-66-NH₂) which coordinated by Zr metal ions, 2-amino-terephthalic acid ligands, and Rh6G dye molecular, was synthesized. Combining the sensing advantages of UIO-66-NH₂ with the chemical activity of Rh6G, the Rh6G@UIO-66-NH₂ composite exhibited excellent sensitivity for nitrite (LOD = 0.021 μM), a short response time, anti-interferece and stability. Although powder samples displayed certain properties, challenges persisted, including difficulties in recovery and utilization, high reagent consumption, and sensivity to environmental conditions. To address these issues, a portable dual-mode sensing test kit, which denoted as the Gel/Rh6G@UIO-66-NH₂ hydrogel kit, was further developed. This kit was prepared by immobilizing MOFs powders within gelatin hydrogel. Beyond the quantitative detection of nitrite by the Rh6G@UIO-66-NH₂ sensor using a ratiometric fluorescence method, the Gel/Rh6G@UIO-66-NH₂ hydrogel kit also qualitatively recognized nitrite with the naked eye through a colorimetric method. In the presence of nitrite, the visible colors of this dual-mode sensing test kit changed from pale yellow to golden yellow, and the corresponding fluorescence colors changed from bright to dark. This research could offer valuable prospect for well-designed LMOFs materials in the fluorescence sensing of nitrite ions in the food system.

Based on the above results, another facile ratiometric fluorescent sensor, named as 5-AF@UIO-66, was proposed by post-modifying 5-AF dye molecules within the framework. Under appropriately acidic conditions, nitrite was oxidized into nitrosyl cation (NO⁺), and it reacted with 5-AF to generate diazotized substances, leading to fluorescence quenching and the original resonance energy transfer from Zr-MOF to 5-AF. Due to its good water stability and the presence of amino groups on the framework, 5-AF@UIO-66 was successfully applied for nitrite turn-off fluorescence detection. The nanocomposite offers rapid response, low detection limit, good reproducibility, and naked-eye recognition of nitrite, making 5-AF@UIO-66 a promising material for practical applications. Based on that, a stimuli-responsive LMOF-based hydrogel test kit (Aga/5-AF@UIO-66) was fabricated for precisely quantifying nitrite content, combining it with a chemiluminescence imaging system. After exposure to nitrite for 10 min, the photo image of the Aga/5-AF@UIO-66 hydrogel test kit could be converted into digital data, creating a direct quantitative and visual method for nitrite identification. The Aga/5-AF@UIO-66 hydrogel test kit, as a colorimetric sensor, performed equally well for detecting nitrite in meat products with satisfactory recoveries.

In summary, this dissertation broadens the application scope of LMOFs, particularly in food science, offering a new approach for creating high-sensitivity LMOF-based sensing platforms. It introduces novel materials and technologies for reliable on-site nitrite detection, showcasing the promising application potential of stable LMOF nanoprobe and their hydrogel test kit in food safety monitoring. This research holds significant value in advancing the application of LMOFs in food research fields.

Keywords: metal-organic framework, hydrogel test kit, nitrite, fluorescence sensing, device

Résumé

Siyang Deng (2023). “Étude de la détection rapide des nitrites dans les produits carnés basée sur un nanocomposite à structure métallo-organique luminescent (LMOF)” (Thèse de doctorat en français)

Gembloux, Belgique, Gembloux Agro-Bio Tech, Université de Liège.

162 pages, 37 figures, 6 tableaux.

Résumé:

Le nitrite est un additif alimentaire couramment utilisé dans l'industrie de la viande, qui ne peut jusqu'à présent être complètement remplacé. Ses principales fonctions consistent notamment à favoriser le développement de la couleur, à inhiber la croissance microbienne, à fournir des effets antioxydants et à conférer une saveur distinctive aux produits carnés. Cependant, le nitrite est également une substance hautement toxique, et une quantité excessive de nitrite dans les aliments peut présenter des risques importants pour la santé. Lorsqu'ils interagissent avec des protéines (comme les amines primaires et secondaires), les nitrites peuvent produire des nitrosamines cancérigènes. De plus, des problèmes de sécurité des aliments liés aux nitrites sont survenus ces dernières années. Par conséquent, la détection rapide de traces de nitrites dans les aliments est extrêmement essentielle. De grands efforts ont été déployés pour établir de nouvelles méthodes permettant de déterminer les nitrites dans les aliments, mais les méthodes de détection existantes ne sont pas suffisamment complètes. Par rapport à d'autres méthodes, la spectrométrie de fluorescence est devenue une méthode efficace pour détecter les ions nitrites en raison de sa sensibilité élevée, de sa bonne sélectivité, de sa faible limite de détection et de ses conditions de détection simples. La clé pour déterminer les nitrites par la méthode de fluorescence réside dans la conception et la fabrication de nanosondes fluorescentes présentant une bonne sélectivité et une sensibilité élevée.

Les structures métallo-organiques (MOF), une nouvelle classe de matériaux multifonctionnels, ont démontré un excellent potentiel dans divers domaines tels que le stockage, l'adsorption et la séparation des gaz, la catalyse, la détection, l'administration de médicaments et bien plus encore ces dernières années. En raison de leur flexibilité de conception chimique et de leurs structures de pores réglables, les MOF présentent des avantages inhérents dans le domaine de la détection de fluorescence. Par conséquent, il est à la fois opportun et innovant d'explorer leur application dans la détection des nitrites et la protection de la sécurité alimentaire. Cette étude vise à concevoir et synthétiser plusieurs nouvelles nanosondes de fluorescence basées sur un cadre organométallique luminescent (LMOF). Ces sondes sont créées en intégrant des MOF avec différents colorants et en les appliquant avec succès pour détecter les nitrites dans de vrais échantillons de viande. De plus, pour élargir le champ d'application du LMOF en poudre et développer le dispositif de détection basé sur les LMOF, les LMOF ont été combinés avec des polymères

d'hydrogel naturels pour former un kit de test d'hydrogel composite. Cette approche innovante ouvre une nouvelle voie pour l'application des matériaux LMOF dans le domaine de la détection de fluorescence, en particulier dans la détection et la détection des nitrites.

Dans la première partie, une nanosonde basée sur LMOF à émission unique, notée Rh6G@MOF-5, a été fabriquée grâce à une méthode de synthèse solvothermique facile. La structure poreuse et la conception chimique du matériau MOF-5 facilitent la bonne diffusion de l'analyte ciblé tout au long du processus de pré-collecte, la rhodamine 6G étant un élément de reconnaissance du nitrite. Cela permet au Rh6G@MOF-5 de servir de matériau de détection fluorescent idéal avec une sélectivité et une sensibilité élevées pendant le processus de détection des nitrites. Il présente des plages linéaires de 0 à 200 $\mu\text{mol/L}$ et une faible limite de détection de 0,2 $\mu\text{mol/L}$. De plus, la plateforme de détection peut également être utilisée pour la détection des nitrites dans de vrais échantillons de viande. Les résultats démontrent que ce matériau pourrait être un candidat prometteur pour la détection du nitrite dans les aliments.

De plus, pour surmonter les limitations associées aux mesures de détection d'émission unique, un capteur de fluorescence ratiométrique basé sur LMOF (Rh6G@UIO-66-NH₂) coordonné par les ions métalliques Zr, les ligands de l'acide 2-amino-téréphthalique et le colorant moléculaire Rh6G, a été synthétisée. Combinant les avantages de détection de l'UIO-66-NH₂ avec l'activité chimique du Rh6G, le composite Rh6G@UIO-66-NH₂ présentait une excellente sensibilité au nitrite (LOD = 0,021 μM), un temps de réponse court, une anti-interférence et une stabilité. Bien que les échantillons de poudre présentaient certaines propriétés, des défis persistaient, notamment des difficultés de récupération et d'utilisation, une consommation élevée de réactifs et une sensibilité aux conditions environnementales. Pour résoudre ces problèmes, un kit de test de détection bimode portable, appelé kit d'hydrogel Gel/Rh6G@UIO-66-NH₂, a été développé. Ce kit a été préparé en immobilisant des poudres de MOF dans un hydrogel de gélatine. Au-delà de la détection quantitative des nitrites par le capteur Rh6G@UIO-66-NH₂ grâce à une méthode de fluorescence ratiométrique, le kit hydrogel Gel/Rh6G@UIO-66-NH₂ a également reconnu qualitativement les nitrites à l'œil nu grâce à une méthode colorimétrique. En présence de nitrite, les couleurs visibles de ce kit de test de détection bimode sont passées du jaune pâle au jaune doré, et les couleurs de fluorescence correspondantes sont passées du clair au foncé. Cette recherche pourrait offrir des perspectives précieuses pour les matériaux LMOF bien conçus dans la détection par fluorescence des ions nitrites dans le système alimentaire.

Sur la base des résultats ci-dessus, un autre capteur fluorescent ratiométrique facile, nommé 5-AF@UIO-66, a été proposé en post-modifiant les molécules de colorant 5-AF. Dans des conditions acides appropriées, le nitrite a été oxydé en cation nitrosyle (NO⁺) et a réagi avec le 5-AF pour générer des substances diazotées, conduisant à une extinction de la fluorescence et au transfert d'énergie de résonance d'origine du Zr-

MOF au 5-AF. En raison de sa bonne stabilité dans l'eau et de la présence de groupes aminés sur la structure, le 5-AF@UIO-66 a été appliqué avec succès pour la détection de la fluorescence par désactivation des nitrites. Le nanocomposite offre une réponse rapide, une faible limite de détection, une bonne reproductibilité et une reconnaissance à l'œil nu du nitrite, faisant du 5-AF@UIO-66 un matériau prometteur pour des applications pratiques. Sur cette base, un kit de test d'hydrogel basé sur LMOF (Aga/5-AF@UIO-66) sensible aux stimuli a été fabriqué pour quantifier avec précision la teneur en nitrite, en le combinant avec un système d'imagerie par chimiluminescence. Après une exposition au nitrite pendant 10 minutes, l'image photo du kit de test d'hydrogel Aga/5-AF@UIO-66 a pu être convertie en données numériques, créant ainsi une méthode quantitative et visuelle directe pour l'identification des nitrites. Le kit de test d'hydrogel Aga/5-AF@UIO-66, en tant que capteur colorimétrique, s'est également révélé efficace pour détecter les nitrites dans les produits carnés avec des récupérations satisfaisantes.

En résumé, cette thèse élargit le champ d'application des LMOF, en particulier dans la science alimentaire, offrant une nouvelle approche pour créer des plates-formes de détection basées sur les LMOF à haute sensibilité. Elle a introduit de nouveaux matériaux et technologies pour une détection fiable des nitrites sur site, démontrant le potentiel d'application prometteur des nanosondes LMOF stables et de leur kit de test d'hydrogel dans la surveillance de la sécurité alimentaire. Cette recherche revêt une valeur significative pour faire progresser l'application des LMOF dans les domaines de la recherche alimentaire.

Mots-clés: structure métallo-organique, kit de test d'hydrogel, nitrite, détection de fluorescence, dispositif

Acknowledgments

I would like to express my deepest appreciation and gratitude to all those who have contributed to the successful completion of my Ph.D. dissertation. Thanks for the project of Gembloux Agro-Bio Tech, the University of Liege, and the Chinese Academy of Agricultural Science. I am grateful for the financial support provided by the National Key R & D Program of China (2021YFD2100103), Beijing Science and Technology Planning Project (grant no. Z221100007122010), National Natural Science Foundation of China (32001775), and China Scholarship Council (CSC), which enabled the successful execution of the experiments and the acquisition of necessary resources.

First and foremost, I am sincerely thankful to my promoters, Prof. Christophe Blecker and Prof. Chunhui Zhang, for their unwavering guidance, invaluable insights, and continuous support throughout the entire research journey. Their mentorship has been instrumental in shaping the direction and quality of this work. It was kind of them to provide me with opportunities to attend various scientific conferences, meetings, and workshops. I am indebted to them for their professional, social, and moral support throughout my PhD.

I extend my appreciation to the members of my thesis committee, Prof. Karoui Romdhane, Prof. Purcaro Giorgia, for their constructive feedback, scholarly expertise, and time devoted to reviewing and improving this research. My heartfelt thanks go to my colleagues and fellow researchers at the Unit of Food Science and Formulation, Gembloux Agro-Bio Tech, especially for Jacquet Nicolas, Marjorie Servais, Sandrino Filocco, Eskin Harun, Mariem Boukraa, Alfred Kouassi, Xin Fan, Caiyan Huang, Fangzhou Wang, and Xiaoxian Liu, who provided a stimulating academic environment and collaborative spirit. The exchange of ideas and discussions greatly enriched the depth of this study. Thanks to Huan Liu from Beijing Academy of Agricultural and Forestry Science, and the members of Laboratory of Agro-Products Processing, Institute of Food Science and Technology (CAAS), especially for Xia Li, Feng Huang, Dong Han, Yunhe Liu, Junmei Liu, Hongru Zhang, Shuyi Qian, for helping with my work and life.

Finally, I want to express my deepest gratitude to my family and friends for their unwavering encouragement, understanding, and patience. Their emotional support has been my anchor throughout this challenging yet rewarding academic endeavor.

This dissertation is a testament to the collaborative efforts and encouragement of many, and I am sincerely thankful to each and every one of you.

Siyang Deng
15/11/2023 in Gembloux, Belgium

Tables of Contents

Abstract	I
Résumé	V
Acknowledgments	IX
Tables of Contents	XI
List of Figures	XV
List of Tables	XIX
List of Abbreviations	XXI
Chapter I. General Introduction	1
1.1. Context	3
1.2. Objectives	5
1.3. Research roadmap and outline	5
1.3.1. Research roadmap	5
1.3.2. Research Outline	6
Chapter II. Literature review on luminescence metal organic framework (LMOF) and LMOF-based hydrogels for detection of nitrite in food safety sensing	9
2.1. Introduction	11
2.2. Spectrofluorimetric method for nitrite detection	12
2.2.1. Nitrosation-based spectrofluorimetric methods	13
2.2.2. Diazotization-based spectrofluorimetric methods	14
2.2.3. Vicinal aryl diamines-based spectrofluorimetric methods	14
2.3. MOFs based fluorescent sensors in food industries	18
2.3.1. Sensing mechanism for food targets	19
2.3.2. Evaluation of food spoilage	20
2.3.2.1. Dipicolinic acid	20
2.3.2.2. Biogenic amines	20
2.3.3. Detection of food hazards	21
2.3.3.1. Mycotoxins	21
2.3.3.2. Harmful ions	22
2.3.3.3. Food additives	23
2.3.3.4. Pesticide	23
2.3.3.5. Veterinary medicines	24
2.4. Application of MOFs in food packaging	25
2.4.1. Anti-bacterial packaging	25
2.4.2. Gases measurement	25
2.4.3. Food security label	26
2.5. MOF-based hydrogels	27
2.5.1. The methods for fabricating MOF-based hydrogels	27
2.5.1.1. Direct mixing method	27
2.5.1.2. In situ MOF growth method	27
2.5.2. The categories of MOF-based hydrogels	28
2.5.2.1. Pure MOF hydrogels	28
2.5.2.2. MOF@biology derived organic macromolecules hydrogels	30

2.5.2.3. MOF@biocompatible hydrogels.....	33
2.5.2.4. MOF@graphene hydrogels.....	34
2.6. Conclusion	36
Chapter III. LMOF (Rh6G@MOF-5) serve as food preservative nanosensor for sensitive detection of nitrite in meat products.....	37
3.1. Introduction.....	40
3.2. Materials and Methods.....	41
3.2.1. Chemicals and Materials.....	42
3.2.2. Instrumentation	42
3.2.3. Synthesis of Rh6G@MOF-5.....	42
3.2.4. Quantitative detection of nitrite	42
3.2.5. Selectivity measurement of nitrite	43
3.2.6. Analysis of nitrite in meat products	43
3.2.7. Statistical analysis.....	43
3.3. Results and Discussion.....	43
3.3.1. Basic characterizations of Rh6G@MOF-5	43
3.3.2. Photoluminescence studies of Rh6G@MOF-5	45
3.3.3. Optimization of detection condition.....	48
3.3.4. Fluorescence detection for nitrite based on Rh6G@MOF-5 sensor.....	49
3.3.5. Anti-interference performance of Rh6G@MOF-5.....	50
3.3.6. Application in meat products	51
3.4. Conclusion	52
Chapter IV. Synchronous fluorescence detection of nitrite in meat products based on dual-emitting Rh6G@UiO-66-NH₂ and its portable hydrogel test kit53	
4.1. Introduction.....	56
4.2. Materials and Methods.....	58
4.2.1. Chemicals and Materials.....	58
4.2.2. Synthesis of UiO-66-NH ₂	59
4.2.3. Synthesis of Rh6G@UiO-66-NH ₂	59
4.2.4. General procedure of nitrite determination using Rh6G@UiO-66-NH ₂ sensor	59
4.2.5 Selectivity and anti-interference test using Rh6G@UiO-66-NH ₂ sensor	59
4.2.6 Analysis of real samples using Rh6G@UiO-66-NH ₂ sensor.....	60
4.2.7 Preparation of portable test kit using Rh6G@UiO-66-NH ₂ immobilized gelatin hydrogels.....	60
4.2.8 Nitrite determination using Gel/Rh6G@UiO-66-NH ₂ hydrogel test kit	61
4.2.9 Selectivity and anti-interference using Gel/Rh6G@UiO-66-NH ₂ hydrogel test kit.....	61
4.2.10 Apparatus	61
4.3. Results and Discussion.....	62
4.3.1 Characterizations of Rh6G@UiO-66-NH ₂	62
4.3.2 Photophysical properties of Rh6G@UiO-66-NH ₂	65
4.3.3 Optimization of detection condition.....	68

4.3.4 Establishment of Rh6G@UIO-66-NH ₂ -based sensor for nitrite.....	69
4.3.5. Selectivity and Anti-interference performance of Rh6G@UIO-66-NH ₂ toward nitrite	70
4.3.6. Application in real samples.....	71
4.3.7. Precise sensing of nitrite by a portable test kit.	72
4.4. Conclusion.....	75
Chapter V. Application ratio fluorescent nanoprobe 5-AF@UIO-66 and its hydrogel test kit for on-site and visual detection of nitrite in meat products	77
5.1. Introduction	80
5.2. Materials and Methods	83
5.2.1. Chemicals and Instruments.....	83
5.2.2. Synthesis of 5-AF@UiO-66	83
5.2.3. Preparation of a nitrite detection kit using 5-AF@UiO-66 immobilized agarose hydrogels	84
5.2.4. General procedure of nitrite determination.....	84
5.2.5. On-site detection of nitrite by hydrogel test kit	85
5.3. Results and Discussion	85
5.3.1. Chemical, structural, and morphological composition of 5-AF@UIO-66 nanoprobe	85
5.3.2. Photoluminescence behavior of 5-AF@UIO-66 nanoprobe.....	88
5.3.3. Optimization of detection condition	90
5.3.4. Ratiometric sensing measurement toward nitrite.....	91
5.3.5. Selectivity and anti-interference performance.....	93
5.3.6. Precise sensing of nitrite by agarose hydrogel test kit.....	94
5.3.7. Application in actual meat samples	96
5.3.8. Evaluation of the proposed fluorescence sensors	97
5.4. Conclusion.....	98
Chapter VI. General discussion, conclusion, and perspective.....	101
6.1. General discussion.....	102
6.1.1. Possible mechanism of Rh6G@MOF-5 nanoprobe to nitrite.....	102
6.1.2. Possible mechanism of Rh6G@UiO-66-NH ₂ nanoprobe to nitrite	103
6.1.3. Possible mechanism of 5-AF@UIO-66 nanoprobe to nitrite.....	104
6.2. Conclusions	106
6.3. Perspectives	107
References	109
Appendix-publications	137

List of Figures

Figure 1-1 Thesis research roadmap.	6
Figure 2-1 The advantages and disadvantages of various nitrite detection methods.	13
Figure 2-2 Different sensing mechanisms toward food targets.....	19
Figure 2-3 The fabrication process of MOF-based hydrogels using (A) direct mixing method and (B) In situ MOF growth method (Sun et al., 2023).....	28
Figure 2-4 (A) Photographs of (a) Tb-Dy MOF hydrogels, (b) Eu-Tb MOF hydrogel, (c) Eu-Dy MOF hydrogel, and (d) Eu-Tb-Dy MOF hydrogel with mixed-metal ratios of 1:1 or 1:1:1 under sunlight and excitation at 275 nm (Chen et al., 2019). (B) Digital images of the luminescent patterns were written with H ₃ BTC-Tb, H ₃ BTC-Tb _{0.9} Eu _{0.1} , and H ₃ BTC-Eu, respectively (Zhao et al., 2021)	29
Figure 3-1 Schematic illustration for the construction of Rh6G@MOF-5 (A) and the possible mechanism for detection of nitrite (B).	41
Figure 3-2 (A) PXRD patterns of simulated MOF-5, synthesized MOF-5, 10 ⁻⁴ Rh6G@MOF-5, 10 ⁻³ Rh6G@MOF-5, 10 ⁻² Rh6G@MOF-5 and Rh6G. (B) FT-IR spectra of MOF-5, 10 ⁻⁴ Rh6G@MOF-5, 10 ⁻³ Rh6G@MOF-5, 10 ⁻² Rh6G@MOF-5 and Rh6G.	44
Figure 3-3 SEM images of MOF-5 (A), 10 ⁻⁴ Rh6G@MOF-5 (B), 10 ⁻³ Rh6G@MOF-5 (C) and 10 ⁻² Rh6G@MOF-5 (D) under magnification 500 ×.	45
Figure 3-4 (A) Photographs of Rh6G, Rh6G+MOF-5, MOF-5, and Rh6G@MOF-5 with different Rh6G concentrations under visual light and 365 nm UV light. (B) CIE chromaticity coordinates for Rh6G@MOF-5 with different Rh6G concentrations. (C) Time-resolved fluorescence decay curves of Rh6G and Rh6G@MOF-5.....	46
Figure 3-5 The 3D-fluorescence spectra of Rh6G (A), Rh6G+MOF-5 (B) MOF-5 (C), 10 ⁻⁴ Rh6G@MOF-5 (D), 10 ⁻³ Rh6G@MOF-5 (E) and 10 ⁻² Rh6G@MOF-5 (F) solid powders.	47
Figure 3-6 (A) Excitation spectrum for MOF-5, 10 ⁻⁴ Rh6G@MOF-5, 10 ⁻³ Rh6G@MOF-5 and 10 ⁻² Rh6G@MOF-5 under EM=570nm. (B) Emission spectrum for MOF-5, 10 ⁻⁴ Rh6G@MOF-5, 10 ⁻³ Rh6G@MOF-5 and 10 ⁻² Rh6G@MOF-5 under EX=350nm.....	48
Figure 3-7 (A) Effect of HCl concentration on the Rh6G@MOF-5-based sensor for nitrite (10 μM). F ₀ means initial emission intensity without nitrite ion and F means emission intensity after adding nitrite ion. (B) Fluorescence intensity of Rh6G@MOF-5 suspension after reaction with nitrite (10 μM) for different times.....	49
Figure 3-8 (A) Evolvement of the fluorescence emission spectra of the Rh6G@MOF-5 suspension under various concentrations of nitrite (0-300 μM). Inset shows the corresponding photos of Rh6G@MOF-5 in the absence (left) and presence (right) of 1 mmol/L nitrite ion under 365 nm UV	

light. (B), (C) and (D) Standard curve for the determination of nitrite concentration.	50
Figure 3-9 Fluorescence quenching efficiency $((F_0-F)/F_0)$ of the Rh6G@MOF-5 system containing different potential interferences (NO_3^- , SO_4^{2-} , CO_3^{2-} , Cl^- , K^+ , Na^+ , Ca^{2+} , Mg^{2+} , Pb^{2+} , Zn^{2+} , Cu^{2+} , Mn^{2+} , Fe^{2+} , Fe^{3+} , Al^{3+} , H_2PO_4^- and HPO_4^{2-}). The concentration of NO_2^- is 10 μM . The concentration of all other interferences is 100 μM	51
Figure 4-1 (A) Schematic illustration of the synthetic procedure for LMOF Rh6G@UIO-66-NH ₂ nanoprobe and their sensing mechanism toward analytes of NO_2^- . (B) Reaction process of the Gel/ Rh6G@UIO-66-NH ₂ hydrogel test kit for NO_2^- assay.	58
Figure 4-2 (A) The PXRD patterns for the simulated UIO-66-NH ₂ (black curve), UIO-66-NH ₂ (red curve), Rh6G@UIO-66-NH ₂ (blue curve), and Rh6G (pink curve). (B) The PXRD patterns of Rh6G@UIO-66-NH ₂ nanoparticles with different Rh6G concentrations. (C) The FT-IR patterns of UIO-66-NH ₂ (red curve), Rh6G@UIO-66-NH ₂ (green curve), and Rh6G (blue curve). (D) The FT-IR patterns of Rh6G@UIO-66-NH ₂ nanoparticles with different Rh6G concentrations. SEM images of synthesized (E) UIO-66-NH ₂ and (F) Rh6G@UIO-66-NH ₂ . (G) Nitrogen (N_2) adsorption-desorption isotherms from UIO-66-NH ₂ and Rh6G@UIO-66-NH ₂	64
Figure 4-3 The 3D-fluorescence spectra of Rh6G@UiO-66-NH ₂ solid powders with (A) 0 mM Rh6G, (B) 0.5 mM Rh6G, (C) 1.0 mM Rh6G, (D) 1.5 mM Rh6G, and (E) 2.0 mM Rh6G in aqueous solution. Inset shows a photo of the corresponding UiO-66-NH ₂ and Rh6G@UiO-66-NH ₂ solid powders.	65
Figure 4-4 (A) The 3D-fluorescence spectra of Rh6G solid powder. (B) photographs of Rh6G solid powder under visual light and 365 nm UV light.	66
Figure 4-5 (A) The 3-D fluorescence spectra and (B) synchronous fluorescence spectroscopy of Rh6G@UiO-66-NH ₂ sample ($\Delta\lambda = 60$ nm).	67
Figure 4-6 UV-vis absorption spectra of Rh6G, UiO-66-NH ₂ , and Rh6G@UiO-66-NH ₂	68
Figure 4-7 (A) Effect of HCl concentration (H^+) on fluorescent intensity of Rh6G@UIO-66-NH ₂ -based sensor. (B) Fluorescence intensity of Rh6G@UIO-66-NH ₂ suspension after reaction with nitrite for different times.	69
Figure 4-8 (A) Synchronous fluorescence spectra of Rh6G@UIO-66-NH ₂ suspension toward different concentration of NO_2^- (0-1000 μM). Inset images shows the corresponding photos of Rh6G@UIO-66-NH ₂ in the absence (left) and presence (right) of NO_2^- ion under 365 nm UV light. (B) The trends of fluorescent intensity ratio $I_{264\text{nm}}/I_{440\text{nm}}$ with different concentration of nitrite.	70
Figure 4-9 (A) The selectivity and (B) specificity of proposed sensing platform.	

The concentration of NO_2^- is 100 μM and the concentration of all other interfering substances are ten times higher than NO_2^-71

Figure 4-10 (A) The photograph of kit with different concentrations of NO_2^- under sunlight (a) and UV light (b). (B) The normalized hue intensity of kit digitized by ImageJ software (under sunlight). (C) Corresponding relationship between the concentration of NO_2^- and hue intensity (under sunlight). (D) The normalized hue intensity of kit digitized by ImageJ software (under UV light). (E) Corresponding relationship between the concentration of NO_2^- and hue intensity (under UV light).....74

Figure 4-11 The photographs of kit in the presence of interfering ions, (A): selectivity; (B): anti-interfering. The corresponding normalized hue intensity of selectivity and interference effect in the kit under sunlight (C) and UV light (D).75

Figure 5-1 (A) Schematic diagram for the preparation of 5-AF@UIO-66 nanosensor; (B) Illustration of the bimodal ratiometric fluorometric detection of NO_2^- based on 5-AF@UIO-66 nanosensor; (C) Schematic illustration for Aga/5-AF@UIO-66 hydrogel kit preparation and the fluorescence response to NO_2^-82

Figure 5-2 (A) FT-IR spectra of UIO-66 and 5-AF@UIO-66; (B) PXRD patterns of simulated UIO-66, synthesized UIO-66 and 5-AF@UIO-66; SEM images of UIO-66 (C) and 5-AF@UIO-66 (D).....86

Figure 5-3 (A) The XPS spectra of UIO-66 and 5-AF@UIO-66; (B) The high-resolution XPS spectra of N 1s of UIO-66 and 5-AF@UIO-66. (C) Nitrogen (N_2) adsorption-desorption isotherms from UIO-66 and 5-AF@UIO-66. (D) The pore diameter distribution curve of UIO-66 and 5-AF@UIO-66.88

Figure 5-4 The 3D-fluorescence spectra of UiO-66 solid powder (A), and 5-AF@UiO-66 solid powders with (B) 0.1 mM 5-AF, (C) 0.5 mM 5-AF, (D) 1.0 mM 5-AF and (E) 5.0 mM 5-AF, respectively. (F) The photo of corresponding UiO-66 and 5-AF@UiO-66 solid powders under visual light and 365 nm UV light.....89

Figure 5-5 (A) The fluorescent intensity of residual 5-AF dye solution after UIO-66 absorbing. (B) CIE chromaticity coordinates for UIO-66 and 5-AF@UIO-66.....90

Figure 5-6 (A) Fluorescent intensities of 5-AF@UIO-66 in response to different concentrations of HCl with and without nitrite. (B) The Effect of HCl concentration on the 5-AF@UIO-66-based sensor with and without nitrite. (C) Time-dependent fluorescence intensity changes of 5-AF@UIO-66 in the presence of nitrite in HCl (0.3 M).....91

Figure 5-7 (A) Fluorescent intensity of 5-AF@UIO-66 suspension toward different concentration of NO_2^- . (B) The trends of fluorescent intensity ratio $I_{264\text{nm}}/I_{440\text{nm}}$ with different concentration of nitrite.....92

Figure 5-8 The selectivity and interference effect of proposed sensing platform.

The concentration of NO_2^- is 100 μM and the concentration of all other interfering substances are ten times higher than NO_2^-93

Figure 5-9 (A) The photograph of kit with different concentrations of NO_2^- . (B) The normalized hue intensity of kit digitized by ImageJ software. (C) Corresponding relationship between the concentration of NO_2^- and hue intensity.95

Figure 5-10 (A) Selectivity: the photographs of kit in the presence of NO_2^- or interfering ions. (B) Anti-interference: the photographs of kit in the presence of both NO_2^- and interfering ions. (C) The corresponding normalized hue intensity of selectivity and interference effect in the kit.....96

Figure 6-1 The mechanism of the Rh6G@MOF-5 sensing nanoprobe toward NO_2^- . UV-vis absorption of NO_2^- , fluorescence excitation and emission of Rh6G@MOF-5.....103

Figure 6-2 (A) Fluorescent and (B) absorbance intensity of reaction solution: 5-AF@UIO-66 (a), 5-AF@UIO-66 + NO_2^- (b), 5-AF@UIO-66 + H^+ (c), and 5-AF@UIO-66 + H^+ + NO_2^- (d).105

List of Tables

Table 2-1 Comparison of various spectrofluorimetric methods for nitrite detection	16
Table 2-2 The summary of MOF-based hydrogels	30
Table 3-1 Nitrite Determination in meat product samples by Rh6G@MOF-5 sensor system.....	52
Table 4-1 Nitrite determination in meat product samples by Rh6G@UIO-66-NH ₂ sensor system.....	72
Table 5-1 Nitrite Determination in meat product samples by Aga/5-AF@UIO-66 hydrogel test kit.	97
Table 5-2 Performance comparison of three novel sensor in this study compared with other reported nitrite detection methods.	99

List of Abbreviations

Rh6G	Rhodamine 6G
5-AF	5-aminofluorescein
Gel	Gelatin
Aga	Agarose
MOF-5	A type of Zn-based Metal organic frameworks
Rh6G@MOF-5	Rhodamine 6G@MOF-5
UIO-66-NH ₂	Zirconium aminobenzenedicarboxylate MOF
Rh6G@UIO-66-NH ₂	Rhodamine 6G@Zirconium aminobenzenedicarboxylate MOF
UIO-66	Zirconium 1,4-dicarboxybenzene MOF
5-AF@UIO-66	5-aminofluorescein@Zirconium 1,4-dicarboxybenzene MOF
Gel/Rh6G@UIO-66-NH ₂	Gelatin/Rh6G@Zirconium aminobenzenedicarboxylate MOF
Aga/5-AF@UIO-66	Agarose/5-AF@Zirconium 1,4-dicarboxybenzene MOF
MOFs	Metal organic frameworks
LMOF	Luminescent metal organic frameworks
λ_{ex}	Excitation wavelength
λ_{em}	Emission wavelength
$\Delta\lambda$	Wavelength offsets
Zn(NO ₃) ₂ ·6H ₂ O	Zinc nitrate hexahydrate
H ₂ BDC	1,4-benzenedicarboxylic acid
NO ₂ ⁻	Nitrite
NO ⁺	Nitrosyl cation
ZrCl ₄	Zirconium chloride
ATA	2-amino-terephthalic acid
DMF	N, N-dimethylformamide
AA	Acetic acid
HCl	Hydrochloric acid
PXRD	powder X-ray diffraction
FT-IR	Fourier transform infrared
SEM	Scanning electron microscopy
XPS	X-ray photoelectron spectroscopy
UV-Vis spectra	Ultraviolet-visible spectra
CE	Capillary electrophoresis
SFS	Synchronous fluorescence spectroscopy
CIE	Commission Internationale de L'Eclairage
IFE	Inner filter effect
FRET	Förster resonance energy transfer

ACQ
LOD
RSDs
3-D

Aggregation-caused quenching
Limit of detection
Relative standard deviations
Three-dimension

1

Chapter I. General Introduction

1.1. Context

Meat and meat products represent crucial sources of energy and nutrients for human consumption, underscored by their enduring historical significance, dating back approximately 3 million years (Specht, 2019; Zhang et al., 2023). Since the earliest stages of human existence, animal meat has constituted a primary dietary component, supporting the sustenance of primitive communities. However, the inherent instability of fresh meat renders it susceptible to deterioration within a few days. An age-old technique employed for food preservation is meat curing, a practice still prevalent today (Alvarado & McKee, 2007). This method involves the addition of nitrite/nitrate salt, common salt (NaCl), and spices to fresh meat at varying degrees of comminution and during diverse processing phases (Shakil et al., 2022). Predating the advent of refrigeration, meat preservation methods were crucial in effectively mitigating decay post-slaughter and extending the food supply during periods of scarcity.

Among the diverse additives employed in meat curing, nitrite salt holds considerable significance. Nitrite plays a crucial role as a major intermediary in the biological nitrogen cycle present in soil and water surfaces. It is a versatile chemical with a broad spectrum of applications, encompassing dye manufacturing and food preservation (Li et al., 2022). In the realm of food safety, nitrite serves as a pivotal indicator (Wang et al., 2018). Nitrites, found in various meat products such as cured meat, ham, and sausages, serve as significant preservatives, hindering the growth of numerous undesirable microorganisms (Yildiz et al., 2014). The primary rationales for employing nitrite as a preservative in meat are as follows: (1) nitrite is incorporated into cured meat at concentrations below 150 ppm to prevent the proliferation of microbiological organisms, such as *Clostridium botulinum*, a causative agent of food poisoning, thereby preventing food toxicity (Badea et al., 2004; Hospital et al., 2016). (2) Provision of the requisite bright red color in meat products like sausages, ham, salami, etc.. (3) Imparting characteristic texture and aroma to cured meats (Altunay & Elik, 2020). Furthermore, nitrite inhibits the oxidation of lipids in meat products, thereby preventing rancidity (off flavor) (Aminzare et al., 2019).

However, the excessive consumption of nitrite can react with amino compounds within the body or external environments, forming nitrosamine compounds that have been linked to various diseases, including methemoglobinemia in infants and central nervous system birth defects. Additionally, an excess of nitrite can react with secondary amines and amides present in food, leading to the production of carcinogenic nitrosamines (Almeida et al., 2020; Cross et al., 2010; Wolff & Wasserman, 1972). Consequently, recognizing the potential health risks associated with nitrite, the World Health Organization (WHO) has designated nitrite as a carcinogen and established a maximum permissible concentration of 3 mg/L (65 μ M) in drinking water. Furthermore, the Joint FAO/WHO Expert Committee on Food Additives (JECFA) has defined a maximum daily intake of 0.07 mg/kg body weight per day for nitrite in food (Gong et al., 2019; Wang et al., 2016). Consequently, the

precise and swift detection of nitrite holds paramount significance in safeguarding food quality and preserving environmental health.

As an emerging detection methodology, fluorescence probe technology holds considerable promise in the realm of nitrite detection. The fundamental principle involves the specific interaction of the fluorescence probe with nitrite, eliciting fluorescence signals that enable the detection of nitrite (Lu et al., 2015; Wu et al., 2019; Yu et al., 2021). In comparison to conventional methods, fluorescence probes offer notable advantages such as rapid detection, minimal need for specialized skills, stable fluorescence signals, heightened sensitivity, and robust selectivity, facilitating precise detection in intricate environments (Geng et al., 2023; Yang et al., 2023; X. Yang, et al., 2023; Zhao et al., 2023). Furthermore, dual-signal sensing through fluorescence and colorimetry has garnered significant attention due to its distinctive features, including dual-signal output, visual detection, straightforward operation, and on-site testing (Fraihat, 2017; Wu et al., 2019). Among the various fluorescent sensors employed for nitrite detection, diazotization-based fluorimetric methods, grounded in the diazotization of a suitable aromatic amine with acidified nitrite to produce diazonium salt, stand out for their elevated selectivity and sensitivity (Georgescu-State et al., 2018; Huang et al., 2019). Nevertheless, conventional organic fluorescent probes are often associated with intricate synthesis processes, limited Stokes shift, and low solubility in aqueous solutions (Wang et al., 2017). Hence, the imperative to develop nanosensors with facile preparation, high selectivity, ease of use, heightened sensitivity, and precise accuracy for the detection of trace nitrite in real samples remains pivotal.

Metal-organic frameworks (MOFs), formed by coordinating metal ions/clusters with organic ligands, exhibit distinctive characteristics including high porosity, a large surface area, ordered crystal structure, and exposed active sites (Wang et al., 2018). The remarkable porosity and easily tunable surface structure of MOFs render them particularly appealing for chemical sensors. Consequently, MOFs are employed in sensor design to create platforms with abundant target-response sites, rapid response dynamics, and modifiable response groups (H. Li et al., 2018). The nanometer size, extensive surface area, and porosity further enhance the diffusion of desired analytes, thereby augmenting the sensitivity of the sensing process (Rasheed & Rizwan, 2022). Notably, MOFs find utility in generating fluorescent or luminescent sensors as they can produce fluorescence arising from both metal ions and ligand units. Their properties can be finely tuned through interactions between building components (Della Rocca et al., 2011). MOFs thus present distinct advantages over other materials; for instance, organic ligands with aromatic or conjugated π moieties may emit fluorescence upon irradiation, while metal ions (e.g., lanthanides, inorganic clusters) can induce photoluminescence (Z. Hu et al., 2014). Luminescent MOFs (LMOFs), particularly as light-sensitive materials, have garnered significant attention owing to their adjustability and diversity in sensor applications (B. Wang et al., 2016). This unique feature positions LMOFs as suitable materials for developing fluorescent

sensors, especially in the detection of nitrite. Compared to alternative detection techniques, fluorescent sensor technology offers the advantages of low cost, simplicity, and heightened sensitivity, enabling the tracking of various analyses with a quick recovery within a low detection range (B. Wang et al., 2016; K. Zhu et al., 2019). In conclusion, ample opportunities exist for the development of novel MOFs-based fluorescence sensing strategies in the realms of food analysis and industrial applications.

1.2. Objectives

The general objectives of this study were to develop novel organic-inorganic hybrid MOF porous materials with the overarching goal of enhancing fluorescence sensing capabilities towards nitrite. Leveraging the physical and chemical properties of the analyte, we would like to construct a series of sensing materials based on LMOFs through post-synthetic modification using luminescent dyes. The approach yielded significant advancements, demonstrating high sensitivity and selectivity in fluorescence sensing for the target analyte nitrite. The specific objectives are outlined as follows:

(1) Seek simple, rapid, and cost-effective methods for preparing luminescent metal-organic framework (LMOF) fluorescent probes. Synthesize LMOFs with excellent fluorescence properties and biocompatibility for colorimetric fluorescence applications.

(2) Constructing a fluorescence sensor based on LMOF, target common meat additives, nitrites, to achieve fast, accurate, and specific detection of nitrites. Provide a theoretical foundation and practical basis for the application of fluorescent nanomaterials in the quality and safety testing of meat products.

(3) Develop a visual hydrogel assay kit for detecting nitrites in meat products. Establish various synchronized visual detection methods for nitrites, offering new approaches for real-time assessment of the quality and safety of meat products.

1.3. Research roadmap and outline

1.3.1. Research roadmap

The research roadmap is presented in **Figure 1-1**.

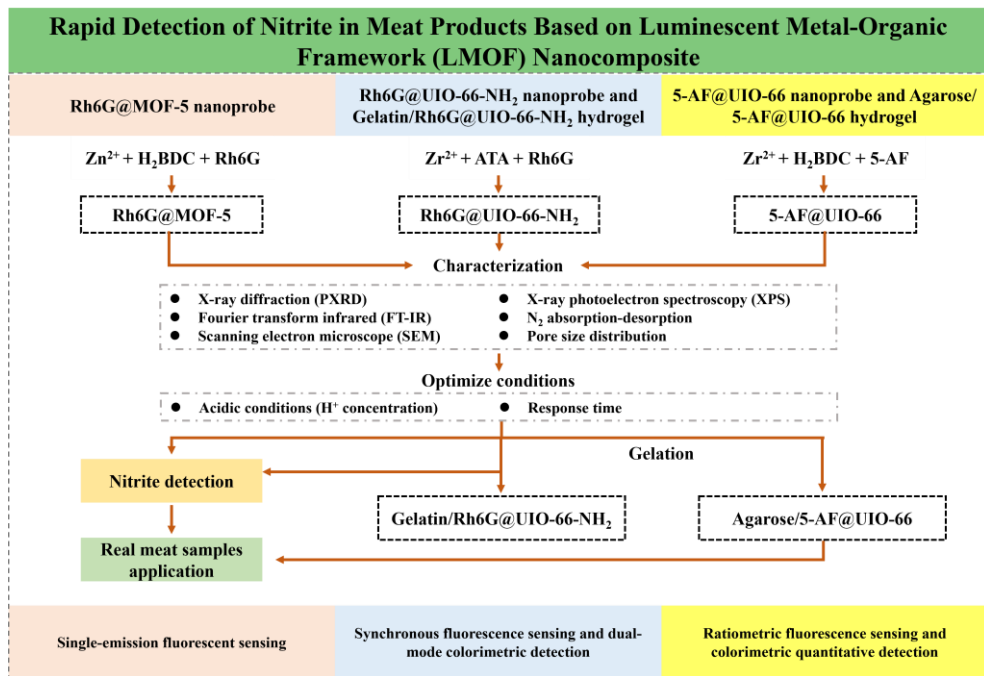


Figure 1-1 Thesis research roadmap.

1.3.2. Research Outline

The current research aims to develop several useful LMOF-based nanomaterials and their derivatives to assist in the fluorescence method for the rapid detection of nitrite in meat products.

In initial stage, as shown in Chapter III, a single-emission luminescent metal-organic framework (LMOF) was synthesized by incorporating rhodamine 6G (Rh6G) into the porous crystalline Zn-MOF (MOF-5) using a facile solvothermal synthesis approach. Powder X-ray diffraction (PXR), Fourier transform infrared (FT-IR), and scanning electron microscopy (SEM) etc. were employed to characterize the resulting Rh6G@MOF-5 composite, confirming the successful preparation of this LMOF nanosensor. The fluorescence spectra, Commission Internationale de L’Eclairage (CIE) chromaticity coordinates diagram, and fluorescence lifetimes was determined to optimize the concentration of the fluorogen Rh6G and demonstrate significant advantages for practical applications of Rh6G@MOF-5 in sensing. Subsequently, the solid powder of Rh6G@MOF-5 was utilized to detect nitrite in standard nitrite solutions under the optimized acidic conditions and best response time. Therefore, Rh6G@MOF-5 can serve as a nanoprobe and be applied in six real meat samples.

In Chapter IV, an innovative fluorescent sensing nanoprobe was developed through the in-situ encapsulation of Rh6G molecules into the Zr-MOF (UIO-66-NH₂)

architecture under solvothermal conditions. In addition to PXRD, FT-IR, SEM measurements, the nitrogen (N_2) adsorption-desorption isotherm was conducted to illustrate the porosity of Rh6G@UIO-66-NH₂. The synchronous fluorescence method was employed to obtain a self-calibration nanoprobe rather than a single-emission nanoprobe. Consequently, the ratio of fluorescence intensity (I_{Rh6G}/I_{MOF}), derived from the synchronous fluorescence spectrum, establishes a relationship curve with nitrite concentration. Gelatin, a commonly used hydrogel, served as a matrix to accommodate the Rh6G@UIO-66-NH₂ nanoprobe, facilitating the creation of a portable hydrogel test kit for on-site testing and promoting a broader practical application of the powder nanoprobe. Furthermore, following the reacting with nitrite solutions, the photographs of the Gel/Rh6G@UIO-66-NH₂ hydrogel test kit were captured by a smartphone camera, and the nitrite concentrations were analyzed using ImageJ software based on hydrogel color changes.

In chapter V, a facile LMOF nanocomposite, 5-AF@UIO-66, was proposed by post-modifying 5-AF dye molecules within the UIO-66 framework. Similar to chapter IV, fundamental characterization techniques, including PXRD, FT-IR, SEM, X-ray photoelectron spectroscopy (XPS), and nitrogen (N_2) adsorption-desorption isotherm, were employed on 5-AF@UIO-66 to illustrate the integrity of the sensor's structure. The fluorescence spectra, Commission Internationale de L'Eclairage (CIE) chromaticity coordinates diagram, optimized acidic conditions, and response time were measured to optimize the best detection parameters when the sensor is applied to nitrite. Based on that, Aga/5-AF@UIO-66 fluorescence platform was established through immobilizing 5-AF@UIO-66 into agarose. It was combined with a chemiluminescence imaging system and ImageJ software to quantify nitrite by colorimetry on the hydrogel test kit, allowing the proposed test kit to be used in real meat samples.

2

Chapter II. Literature review on luminescence metal organic framework (LMOF) and LMOF-based hydrogels for detection of nitrite in food safety sensing

Short overview

This study aims to develop a novel fluorescent probe/sensor for detecting nitrite by combining LMOF with spectrofluorimetry and expanding the application of solid-state nanoprobe powders. Therefore, at first, Chapter 2 focuses on a variety of spectrofluorimetric methods for nitrite detection. Among of them, as one of the novel spectrofluorimetric tools, MOF-based fluorescent sensors, which are applied in the food industry, have been reported. Finally, the present review summarizes different types of MOF-based hydrogel derivatives and their applications in the food system.

2.1. Introduction

Food safety constitutes a paramount concern for global consumers, presenting a ubiquitous challenge to public health worldwide. While developing countries often face a heightened risk of exposure, developed countries also necessitate stringent food safety regulations to mitigate the threat of food-borne pathogens (Griesche & Baeumner, 2020). The phenomenon of globalization has facilitated the cross-border distribution of food products, thereby augmenting the potential for the transmission of food-borne pathogens (Griffiths et al., 2017). According to the World Health Organization (WHO), an alarming array of over 200 diseases can be transmitted to humans through food consumption, often occurring without individuals' conscious awareness. These incidents bear significant consequences, exerting a substantial impact on both consumer well-being and national economies, thereby attracting substantial international attention. The issue of food contamination is pervasive, and concerted efforts are imperative to ensure food safety throughout the entire supply chain, culminating in the protection of consumers.

Protein-rich foods such as meat, fish, shrimp, milk, and eggs play a vital role in human nutrition, serving as significant sources of energy and essential nutrients (Zhang et al., 2023). Throughout human history, animal meat has constituted a fundamental component of our diet, sustaining early human populations. Nevertheless, the susceptibility of meat to spoilage during storage and transportation poses a challenge. During this deterioration process, proteins undergo microbial decarboxylation, resulting in the formation of biogenic amines (BAs). Excessive consumption of exogenous BAs can lead to food poisoning, manifesting as symptoms such as headaches, nausea, diarrhea, palpitations, fluctuations in blood pressure, respiratory distress, and other allergic reactions, some of which can be life-threatening (Benkerroum, 2016). Consequently, the meticulous inspection of food freshness is imperative. In pursuit of enhanced food preservation, humans experimented with cooking meat over fire, a practice that revealed roasted or smoked meat's improved stability during storage. Roasting and smoking emerged as among the earliest meat preservation methods (Zhang et al., 2023). The efficacy of smoking in preserving meat, coupled with the preference for the smoky flavor it imparts, has endured through time. As a result, roasted or smoked meat products remain popular and are widely consumed on a global scale.

The contemporary utilization of nitrate and nitrite salts in cured meat products traces its origins to ancient meat preservation techniques involving salting. Nitrite (NO_2^-), a naturally occurring form of nitrogen, holds multifaceted significance within the ecological and environmental contexts. It has found wide application within the food processing industry, serving as a conventional food additive and preservative agent over an extended period (Bedale et al., 2016; Guo et al., 2023; Wang et al., 2017a). The primary role of nitrite is to thwart the proliferation of foodborne pathogenic microorganisms, most notably *Clostridium botulinum*. It also contributes to stabilizing the characteristic color, enhancing the flavors of cured meat, and

retarding the onset of rancidity in meat products (Ferysiuk & Wójciak, 2020; Jia et al., 2020). The effectiveness of nitrite renders them indispensable additives, particularly in the context of cured meat products (Ferysiuk & Wójciak, 2020). However, it is crucial to exercise caution in the use of nitrite, as excessive intake can disrupt the body's oxygen transport system, resulting in tissue hypoxia. This occurs due to the irreversible conversion of hemoglobin to methemoglobin in the bloodstream, severely impairing hemoglobin's oxygen-carrying capacity. Such physiological changes can lead to various ailments, including methemoglobinemia, with pregnant women and infants being particularly vulnerable (Zhang et al., 2018; Zhang et al., 2023). Moreover, excess nitrite intake can elevate the risk of cancer, as nitrite can react with secondary amines and amides in the stomach, leading to the formation of carcinogenic N-nitrosamines (Honikel, 2008; Wu & Tong, 2020; Zhang et al., 2018). These health concerns pose a substantial threat to the global meat industry's overall well-being and development.

In light of these adverse health implications, numerous regulatory bodies and nations have implemented stringent constraints on their usage. The World Health Organization (WHO) has defined a maximum permissible nitrite concentration of 3 mg/L (equivalent to 65 μ M) in drinking water. Additionally, the Joint FAO/WHO Expert Committee on Food Additives (JECFA) has stipulated a maximum daily intake limit of 0.07 mg/kg body weight per day for dietary nitrite. Moreover, in China, the recommended upper limit for nitrite content in food products is set at 30 mg/kg (Deng et al., 2021; Guo et al., 2023; Zhang et al., 2023). As a result, the monitoring of nitrite levels and ensuring food safety have emerged as paramount concerns, underscoring the need for the development of innovative and highly sensitive detection methods.

2.2. Spectrofluorimetric method for nitrite detection

Fluorescence spectroscopy, or spectrofluorimetry, is an analytical technique that involves the examination of fluorescence emitted by a sample when exposed to a light beam, typically ultraviolet light. This excites the electrons in specific molecules, causing them to emit light, often within the visible spectrum, although not exclusively. This technique finds widespread application in the analysis of organic compounds across various scientific disciplines. Spectrofluorimetry, in particular, is extensively employed for nitrite detection due to its exceptional sensitivity, strong selectivity, impressive limits of detection, and straightforward assay protocols. In the majority of cases, spectrofluorimetric methods rely on monitoring changes in fluorescence intensity resulting from the interaction of fluorescent probes with nitrite. As shown in **Figure 2-1**, compared to conventional analytical methods, these fluorescent probes offer high sensitivity, excellent selectivity for their target analytes, portability, and rapid optical response. Fluorescence spectroscopic methods for nitrite determination can be categorized based on the underlying mechanisms, specifically nitrosation and diazotization. The advantages and disadvantages of each spectrofluorimetric method

have been evaluated and the detection principles and analytical parameters were tabulated in Table 2-1.

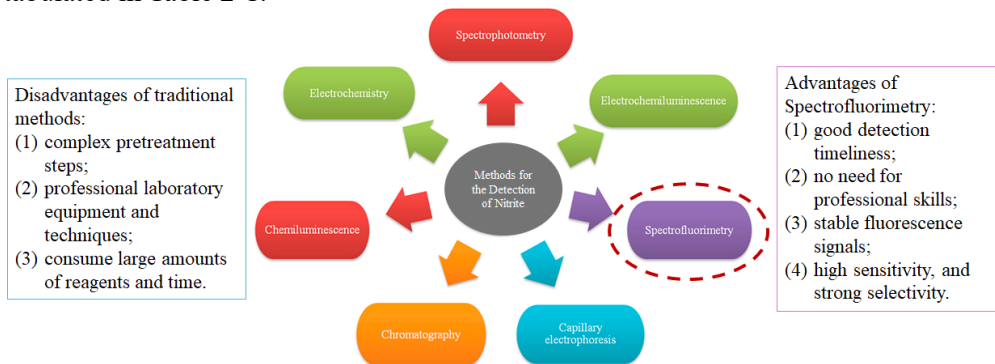


Figure 2-1 The advantages and disadvantages of various nitrite detection methods.

2.2.1. Nitrosation-based spectrofluorimetric methods

Several fluorescent probes have the capability to react with nitrite in an acidic environment, yielding nitroso derivatives as a result. For instance, Nakamura utilized resorcinol as a fluorimetric reagent to quantify nitrate, while Ohta et al. employed a similar approach for nitrite determination in saliva (Nakamura, 1980; Ohta et al., 1986). In their method, nitrosation of 4-hydroxycoumarin in an acidic medium was followed by reduction, leading to the formation of a fluorescent nitroso derivative known as 3-amino-4-hydroxy-coumarin. It's noteworthy that the fluorescence intensity of these probes may exhibit enhancement or quenching subsequent to the nitrosation reaction. Furthermore, the degree of fluorescence enhancement or quenching demonstrates a linear relationship within a defined range of nitrite concentrations.

Similarly, certain reagents containing secondary amine or amide groups have found utility in nitrite determination, as they are capable of reacting with nitrite to yield N-nitroso derivatives. For instance, Biswas et al. devised a spectrofluorimetric method for the analysis of ultra-trace levels of nitrite in various matrices such as air, water, soil, and forensic samples (Biswas et al., 2004). Their approach relies on the quenching effect exerted by nitrite on the intrinsic fluorescence of murexide (ammonium purpurate). It's worth noting that chloride ions can introduce interference in nitrite determination and, therefore, necessitate removal via precipitation with silver sulfate in this method. Liu et al. (2009), on the other hand, developed a fluorimetric method for the determination of trace nitrites using an unsymmetrical rhodamine derivative characterized by a high fluorescence quantum yield. However, the limited Stokes shift of the rhodamine compound can lead to self-quenching of fluorescence and potential detection errors attributable to Rayleigh scattering. For the analysis of trace nitrite levels, Zhang et al. (2003) and Gao et al. (2005) separately

devised sensitive nitrosation-based fluorescence quenching methods employing Rhodamine 110 and mono[6-*N*(2-carboxy-phenyl)]- β -cyclodextrin (OACCD), respectively. Notably, these proposed methods have been effectively employed for nitrite determination in diverse water, soil, and food samples, yielding satisfactory results.

2.2.2. Diazotization-based spectrofluorimetric methods

There are additional spectrofluorimetric techniques employed for nitrite determination, centering on the diazotization process of a suitable aromatic amine catalyzed by acidified nitrite to generate diazonium salts. These changes in fluorescence intensity serve as the basis for quantitative nitrite analysis.

One noteworthy diazotization-based fluorimetric method for nitrite determination was introduced by Axelrod and Engel (1975), where fluorescing products were produced in a single step using 5-aminofluorescein. Following this, aromatic compounds featuring primary amino groups, such as safranin O, neutral red, folic acid, 2-amino-4-chloro-1-hydroxybenzene-6-sulphonic acid, and indole, have been harnessed for nitrite determination based on the aforementioned mechanism (Huang et al., 2000; Jie et al., 1999; Lapat et al., 1997; Li et al., 2020; Lu et al., 2015).

In addition to the established reagents, researchers have been actively engaged in the development and design of innovative fluorescent probes. For example, Chen et al. (2007) introduced a novel fluorescent reagent, 2-amino-5,7-dimethyl-1,8-naphthyridine (ADMND), designed for the determination of trace nitrite. The reaction relies on the diazotization of naphthyridine amine with nitrite to form a diazonium salt, which undergoes hydrolysis upon boiling to yield hydroxyl group-substituted naphthyridine. The degree of fluorescence quenching exhibited by ADMND in response to nitrite ions shows linearity within the nitrite concentration range of 1×10^{-7} to 2.5×10^{-6} mol/L, with a detection limit of 4.06×10^{-8} mol/L. It is worth noting that this detection reaction necessitates boiling water bath conditions, and interference from nitrate in real samples can impact nitrite detection. Li et al. (2004) developed a new BODIPY reagent, 1,3,5,7-tetramethyl-8-(4'-aminophenyl)-4,4-difluoro-4-bora-3a, 4a-diaza-s-indacence (TMABODIPY), for the determination of trace nitrite. This method involves the reaction of nitrite with TMABODIPY initially in an acidic solution and subsequently in an alkaline solution to form diazonate, a stable and highly fluorescent product. Martínez-Tomé et al. (2009) employed immobilized aromatic diamino compound 2,3-diaminonaphthalene and cyclodextrin complexes in a sol-gel matrix to develop a novel fluorimetric sensor for nitrite detection without the need for nitrite pre-treatment. Huang et al. (2008) designed a novel probe, 1,3,5,7-tetramethyl-8-(3,4-diaminophenyl)-difluoroboradiaza-s-indacence (DAMBO), for the determination of ultra-trace levels of nitrite in human saliva. These proposed methods are characterized by their cost-effectiveness and ease of operation.

2.2.3. Vicinal aryl diamines-based spectrofluorimetric methods

Alternative methods for nitrite determination rely on the reaction of vicinal aryl diamines with nitrite, resulting in the formation of triazoles. In cases where a single compound contains two amino groups in the ortho-position, an intramolecular diazotization reaction can occur. This intramolecular diazotization reaction is specific to nitrite and strictly depends on the presence of an acid.

In recent years, several vicinal aryl diamines based on this mechanism have been reported. Notably, diamino fluoresceins like 4,5-aminofluorescein-2 (DAF-2) or its cell-permeable diacetate derivative (DAF-2 DA) have garnered attention. These compounds produce the highly fluorescent DAF-2-triazol (DAF-2T), similar to the diazotization reaction observed in DAN (Kojima et al., 1999). Additionally, a series of vicinal aryl diamines, including 5,6-diamino-1,3-naphthalene disulfonic acid (DANDS), 1,3,5,7-tetramethyl-8-(3',4'-diaminophenyl)-difluoroboradiaza-s-indacene (TMDABODIPY), and 1,3,5,7-tetramethyl-2,6-dicarbethoxy-8-(3',4'-diaminophenyl)-difluoroboradiaza-s-indacene (TMDCDABDIPY), have been developed for the indirect analysis of nitrite or NO (Huang et al., 2006; Li, 2003; Wang et al., 2000). TMDCDABDIPY, for instance, was designed for nitrite detection in meat and vegetables, utilizing O-phenylenediamine as the recognition site for nitrite. In the absence of nitrite, the probe experienced photoinduced electron transfer (PET), resulting in fluorescence quenching. However, the reaction between the O-phenylenediamine moiety and nitrite led to the formation of a triazole group, inhibiting PET and generating strong fluorescence. It's worth noting that some of these probes exhibit drawbacks such as poor water solubility, pH-dependence, susceptibility to self-oxidation and environmental oxidants, and a small Stokes shift. These limitations restrict their widespread application. Therefore, exploring alternative strategies and discovering new fluorescence modulating mechanisms that offer high sensitivity and specificity for nitrite detection is essential.

Over the past five years, significant developments have been made in the design of probes for nitrite detection. Another noteworthy development came from Wu et al. (2019), who designed a naphthalimide derivative for nitrite detection in sauerkraut and radish sticks. Upon reacting with nitrite, this probe inhibited photoinduced electron transfer (PET) and intramolecular charge transfer (ICT) processes, resulting in a bright green fluorescence. This probe exhibited rapid nitrite response (less than 4 minutes), exceptional selectivity, and a low limit of detection (84 nM). Ma et al. (2020a) synthesized a probe based on 2-(2-amino-4-carboxyphenyl) benzothiazole (ortho-BT) for nitrite detection. In acidic conditions, the probe's $-NH_2$ group reacted with nitrite to form a diazo group, which underwent an intramolecular coupling reaction, leading to the "turn-on" of fluorescence. Furthermore, this probe was encapsulated in a hydrogel for visual monitoring of nitrite. Besides, a 2-(1H-benzimidazol-2-yl)aniline-based probe was developed for nitrite detection, successfully applying it to sausages and radish sticks. The amino group in the probe underwent diazotization followed by intramolecular cyclization, resulting in the formation of a non-fluorescent benzotriazine derivative (Yang et al., 2021).

Table 2-1 Comparison of various spectrofluorimetric methods for nitrite detection

No.	Probe	Mechanism	Sample	Limit of detection ($\mu\text{mol/L}$)	Detection range ($\mu\text{mol/L}$)	RSD%	Ref.
1	4-hydroxycoumarin	Nitrosation	Saliva	–	$3.0\text{--}1.0\times 10^3$	0.5	Ohta et al. (1986)
2	Murexide (ammonium purpurate)	Nitrosation	Water/Soil	1.0×10^{-2}	$1.0\times 10^{-1}\text{--}2.17\times 10^{-1}$	0.4878	Biswas et al. (2004)
3	Unsymmetrical rhodamine	Nitrosation	Water	0.2×10^{-3}	$1.0\times 10^{-2}\text{--}3.5\times 10^{-1}$	2.36	Liu et al. (2009)
4	Rhodamine 110	Nitrosation	Water	7.0×10^{-4}	$1.0\times 10^{-2}\text{--}3.0\times 10^{-1}$	2.14	Zhang et al. (2003)
5	Monof[6-N(2-carboxy-phenyl)]- β -cyclodextrin (OACCD)	Nitrosation	Water/Soil/Food	0.2×10^{-3}	$2.0\times 10^{-2}\text{--}1.7$	1.38	Gao et al. (2005)
6	2-Amino-5, 7-dimethyl-1, 8-naphthyridine (ADMND)	Diazotization	Water	0.0406	0.1–2.5	0.23	Chen et al. (2007)
7	1,3,5,7-tetramethyl-8-(4'-aminophenyl)-4,4-difluoro-4-bora-3a,4a-diaza-s-indacence (TMABODIPY)	Diazotization	Water/Food	6.5×10^{-4}	$8.0\times 10^{-3}\text{--}0.3$	4.53	Li et al. (2004)
8	2,3-diaminonaphthalene (2,3-DAN)/Hydroxypropyl- β -cyclodextrin (HP- β -CD)	Diazotization	N/A	0.02	0–10	N/A	Martínez-Tomé et al. (2009)
9	DAMBO	Diazotization	Saliva	0.1×10^{-3}	0.006–0.5	1.12	Huang et al. (2008)
10	2-(2-amino-4-carboxyphenyl) benzothiazole (ortho-BT)	Vicinal diamines	N/A	0.04	1–100	N/A	Ma et al. (2020)

Chapter II. Literature review on luminescence metal organic framework (LMOF) and LMOF-based hydrogels for detection of nitrite in food safety sensing

11	2-(1H-Benzimidazol-2-yl)Aniline (BMA)	Vicinal diamines	arl	Food	0.06063	0–40	5.98	Yang et al. (2021)
12	Anthracene carboxyimide derivative (AC-NO ₂)	Vicinal diamines	arl	Food	0.084	0–75	8.22–17.81	Wu et al. (2019)

2.3. MOFs based fluorescent sensors in food industries

In recent years, nanomaterials have been increasingly incorporated into chemical sensing systems for the detection of target analytes in various sample matrices, particularly in the context of food analysis. This integration has resulted in enhanced sensitivity and reduced detection times. When utilized in sensor development, nanomaterials are often combined with selective recognition elements to achieve the desired specificity. Among the emerging technologies and functional materials, Metal-organic frameworks (MOFs) have emerged as a versatile and comprehensive platform with applications in areas such as agrochemical elimination and sensing (Wang et al., 2013). MOFs belong to the intriguing class of highly porous coordination polymers (PCPs) characterized by uniform structures formed through coordination bonding between metal ions or metal clusters and polyfunctional organic ligands, resulting in multidimensional periodic lattices (Chen et al., 2020; Rojas et al., 2022; Yan et al., 2022; Zhang et al., 2021).

MOFs offer numerous advantages that make them promising materials for designing and fabricating chemical sensors. These advantages include: (1) Versatile hybrid compositions, allowing for diverse tunability and customizable design; (2) Large specific surface areas and high porosity, enabling exceptional sorption capacities; (3) Straightforward and advanced functionalization capabilities, facilitating specific host-guest interactions; (4) Scalable synthesis (some MOFs are already commercially available); (5) Adequate thermostability and chemical stability profiles, ensuring their stability during function and preventing associated toxicity in animals and plants due to accumulation (Lian et al., 2017; Rojas et al., 2022; Velásquez-Hernández et al., 2021; Wang et al., 2019). Over the past few decades, MOFs have found applications in various fields, including sensing, luminescence, gas adsorption and separation, catalysis, drug delivery, and more (Pascanu et al., 2019; Raja Lakshmi et al., 2021; Rojas et al., 2019, 2022). Their unique properties have led to the rapid development of MOF composites as novel functional materials, offering tailored solutions that are particularly valuable in the realm of food safety.

Particularly, the luminescence-based MOFs (LMOFs) have been emerged in recent years and attracted extensive attentions thanks to their intriguing optical features. In the realm of chemical sensors, those predicated on LMOFs can be broadly classified into the following categories: (1) Integration of luminescent molecules as ligands within rigid and porous MOFs for the purpose of chemical sensing, (2) Utilization of lanthanide-functionalized MOFs for chemical sensing applications, and (3) Integration of diverse functional constituents into MOFs to enable chemical sensing functionalities (Wang et al., 2019). After the initial exploration of MOFs, significant strides have been made in the development and utilization of luminescent ligands for the creation of LMOFs. These LMOFs have found relevance in the realm of food safety, where they facilitate the detection of potentially hazardous substances. This comprehensive review centers its attention on the evolution of LMOF-based chemical

sensors with a specific emphasis on their application in the detection of diverse analyte species within samples relevant to the realm of food analysis. The overarching objective of this inquiry is to contribute to the enhancement of food quality and safety assurance through the deployment of LMOF-based sensing strategies.

2.3.1. Sensing mechanism for food targets

Prior to discussing the extensive applications of LMOFs in food safety, it is imperative to elucidate the fundamental sensing mechanisms. It is well-established that the diverse fluorometric sensing properties observed in food analysis primarily stem from the interactions between LMOF sensor materials and the specific target food constituents. Distinct sensing mechanisms are predominantly guided by the structure-signal relationship. Upon the introduction of food analytes, changes in the fluorescent signals of LMOFs, encompassing changes in both emission wavelength and intensity, are observed. These different fluorescent mechanisms yield a range of response types for the targets, as depicted in **Figure 2-2**, including emission wavelength shifts, fluorescence "turn-on," fluorescence "turn-off," and ratiometric responses. Notably, the structure-property correlations within LMOFs play a pivotal role in determining the sensing mechanisms directed towards the specific target analytes. Hence, by employing pre-designed fluorescence principles of LMOFs, tailored detection mechanisms can be harnessed to enhance their utility in diverse food targets, addressing the escalating demand for enhanced food safety and quality assurance.

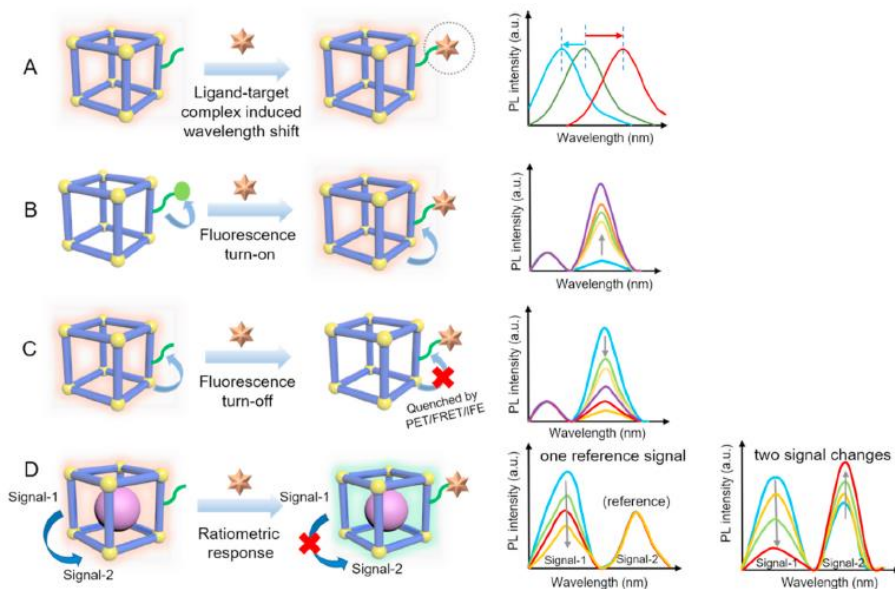


Figure 2-2 Different sensing mechanisms toward food targets.

2.3.2. Evaluation of food spoilage

A critical facet of food safety pertains to food spoilage. Bacterial contamination in food not only leads to food spoilage but can also give rise to numerous health-related incidents and long-term health concerns (Wang et al., 2019). Under such circumstances, certain chemical compounds generated during food spoilage serve as crucial indicators for monitoring and controlling food safety. Undoubtedly, rapid sensing techniques for the rapid monitoring of bacterial contamination represent a highly convenient approach for controlling bacterial exposure. Moreover, MOF-based sensors have found utility in the assessment and regulation of food quality.

2.3.2.1. Dipicolinic acid

Dipicolinate (DPA), recognized as a biomarker for *Bacillus anthracis* spores, can serve as a valuable indicator for assessing microbial contamination in food and evaluating the efficiency of several food sterilization procedures. The indirect detection of bacterial contamination in food through the analysis of bacterial spores has demonstrated its efficacy in this context.

For instance, Rieter et al. (2007) developed a ratiometric luminescent MOF sensor named $\text{Gd}(\text{BDC})_{1.5}(\text{H}_2\text{O})_2@\text{SiO}_2$ (where BDC = 1,4-benzenedicarboxylate) for the rapid detection of DPA. Additionally, Zhang et al. (2016) introduced Tb^{3+} and Eu^{3+} cations into the anionic framework of bio-MOF-1 via ion exchange, resulting in $\text{Tb}/\text{Eu}@$ bio-MOF-1, a compound exhibiting luminescent properties. The open sites of Tb^{3+} within $\text{Tb}/\text{Eu}@$ bio-MOF-1 could bind with DPA, leading to an efficient energy transfer from Tb^{3+} to Eu^{3+} and causing a fluorescence color change from orange-red to green. However, it is worth noting that the abovementioned sensors involve complex and laborious preparation procedures for the sensory material, including the application of high temperatures and the use of non-aqueous solvents for MOF dispersal. To address these limitations and develop a more practical sensor system, Bhardwaj et al. (2016) designed a water-dispersible Tb-MOF, $\text{Tb}(\text{BTC})(\text{H}_2\text{O})_6$ (where BTC = benzene-1,3,5-tricarboxylic acid), and presented a highly effective chemical sensor for the detection of DPA in aqueous media. This sensing method exhibited high sensitivity for DPA detection (with a limit of detection of 0.04 nM), demonstrating the potential of MOFs as promising candidates for efficient sensory materials in the recognition and quantification of spores across various samples.

2.3.2.2. Biogenic amines

Amines are prevalent in the organic sphere, yet they possess toxicity and harmfulness in nature. Notably, biogenic amines (BAs) can be generated during the storage and processing of protein-rich foods, rendering them valuable indicators of food spoilage. Therefore, the detection of BAs assumes significant importance in safeguarding food quality and safety. In this context, Xu et al. (2017) synthesized a MOF composite, methyl red@lanthanide MOFs (named $\text{MR}@$ EuMOFs), and

harnessed it for the development of fluorescent chemical sensors capable of detecting BAs associated with food spoilage. Utilizing the distinctive double-stimuli-responsive fluorescence properties of Eu^{3+} and MR within MR@EuMOFs, they established a portable chemical sensing system tailored for the detection of histamine (HI) as an evaluative measure for food spoilage.

2.3.3. Detection of food hazards

2.3.3.1. Mycotoxins

Mycotoxins, a group of natural toxins generated by molds, have obtained significant attention in recent years due to their unpredictable and inescapable presence in food. The contamination of feed and food with mycotoxins can lead to disease outbreaks in livestock and have detrimental health implications for humans (Bhat et al., 2010). Hence, the imperative task of establishing rapid and convenient sensing techniques for mycotoxin detection in both human food and animal feed has arisen to uphold food safety standards. In this regard, fluorescent MOFs techniques have been developed as effective tools for the detection of mycotoxins, contributing to the assurance of food safety.

For example, 3-nitropropionic acid (3-NPA), a highly toxic neurotoxin produced by moldy sugarcane, is associated with the development of various diseases. To counter these challenges, LMOFs have been developed. It's worth noting that mycotoxins in food systems often lead to significant changes in pH, which is why many sensors are designed to be sensitive to pH alterations, serving as an indicator of mycotoxin presence. Tian et al. (2018) synthesized an innovative Cd(II)-based fluorescent MOF for detecting 3-nitropropionic acid (3-NPA), a natural existing mycotoxin commonly found in moldy sugarcane. They harnessed the porosity of the Cd-MOF and the pH sensitivity of fluorescein isothiocyanate (FITC) dye molecules to create a solid-state luminescent composite material tailored for target-sensing (FITC@[Cd(L)]). This luminescent FITC@[Cd(L)] material demonstrated an effective fluorescence quenching response to the toxic 3-NPA, with a quenching efficiency of 85.6% for 3-NPA. Besides, Guo et al. (2020) engineered a nanoscale ratiometric LMOF (MPDB-PCN) featuring single-excitation ratiometric fluorescent pH sensing capabilities. The potential for 3-NPA detection in moldy sugarcane samples was assessed through real-time pH monitoring.

Furthermore, Hu et al. (2015) synthesized a novel luminescent sensor (LMOF-241) designed for the selective and rapid detection of aflatoxin B1 (AFB1) in corn. LMOF-241 exhibited high specificity and selectivity towards AFB1, achieving a low limit of detection (LOD) estimated at 46 ppb for AFB1 in corn. This case is considered a unique case of an LMOF exhibiting both fast response times and high sensitivity in the detection of mycotoxins. In another study, Li et al. (2019) utilized Zr-CAU-24, a distinct MOF, for the efficient detection of AFB1 in walnut and almond beverages. Their approach relied on fluorescence quenching and demonstrated improved sensitivity with an LOD of 19.6 ppb. Furthermore, Hu et al. (2017) offered a method

for crafting fluorescent sensors to detect ochratoxin A (OTA). In the presence of OTA, the recognition aptamer could bind to OTA, releasing the corresponding 5-carboxyfluorescein (FAM)-labeled aptamer from the $\text{Fe}_3\text{O}_4/\text{g-C}_3\text{N}_4/\text{HKUST-1}$ composite. This process resulted in gradual recovery of fluorescent intensity in the sensing system. The resulting fluorescent sensor exhibited high sensitivity, boasting an LOD of 2.57 ng/mL, and has since been employed for OTA detection in real corn samples.

2.3.3.2. Harmful ions

Water serves as a vital component for sustaining human life and is an essential resource in food production. However, drinking water may contain various potentially hazardous substances, including heavy metal ions, fluoride (F^-), and disinfectant (ClO^-), which can infiltrate food products during processing, resulting in serious food contamination. Among these contaminants, the presence of heavy metal ions in natural water resources, especially drinking water, poses a severe threat. Therefore, it is imperative to develop straightforward and highly efficient probes for detecting low concentrations of heavy metal ions in drinking water. To date, numerous LMOFs have proven to be excellent candidates as fluorescent probes for the detection of various heavy metal ions.

Mercury (II) ions, as typical hazardous pollutants, necessitate the development of both qualitative and quantitative detection methods. In response to address this challenge, Samanta et al. (2018) have created an alkyne-functionalized MOF-based chemodosimeter (UiO-66@Butyne) tailored for Hg^{2+} ion detection. Their research has demonstrated that the MOF's remarkable quenching capability arises from the interaction between Hg^{2+} ions and alkyne groups. In a similar study, Wu et al. (2016) devised a novel fluorescent sensor for Hg^{2+} detection in aqueous solutions. This innovative approach incorporated Hg^{2+} -specific single-stranded DNA (ssDNA) alongside a fluorescent FAM dye label as recognition elements, utilizing UiO-66-NH_2 as the quenching agent for Hg^{2+} sensing. Moreover, in efforts to improve the selectivity of chemical sensors for detecting various other metal ions, such as Cu^{2+} , Pb^{2+} , Al^{3+} , Fe^{3+} , Cr^{3+} , and Ba^{2+} , numerous strategies employing MOF-based materials have been proposed (Chen et al., 2017; Ji et al., 2017; Li et al., 2012; Lin et al., 2014; Lv et al., 2016; Wang et al., 2016).

Fluoride (F^-) represents one of the most prevalent anions in groundwater, thus posing a major challenge to drinking water safety. A recent development by Ebrahim et al. (2019), they proposed a novel lanthanide-based fluorescent MOF, denoted as SION-105. This MOF utilized the B-functionalized ligand (tctb^{3-}) equipped with the Lewis acid active site for F^- ion binding. Their work established a turn-off transduction mechanism, demonstrating that the quenching of red fluorescence from Eu^{3+} was predominantly controlled by F^- ions. Furthermore, a portable miniaturized fluorimeter device was fabricated for water sampling using SION-105, facilitating its practical applicability. In a parallel study, Ke et al. (2018) developed a MOF

composite consisting of MOF-801 and calcium fumarate (CaFu) as an adsorbent for the removal of F^- from brick tea infusion. The findings revealed that MOF-801 facilitated the removal of over 80% of the existing fluoride in brick tea infusion within the initial 5 minutes.

Similarly, ClO^- is widely employed as a household bleaching agent and a disinfectant in tap water. Nevertheless, an excess of ClO^- can pose severe health risks to humans and give rise to the production of harmful organic substances. In 2018, Li et al. (2018) developed an innovative fluorescence system, where they incorporated luminescent Eu^{3+} doped Fe_3O_4 nanoparticles into ZIF-8. The resulting MOF serves as a fluorescent probe for the detection of free ClO^- in tap water.

2.3.3.3. Food additives

In addition to contaminants introduced during food processing, illegal additives represent significant hazards in the food industry, posing serious health risks to consumers. Nitrite ions (NO_2^-), commonly used as additives in meat processing, can lead to tissue hypoxia symptoms if consumed in excess. Moreover, nitrite can form during the preservation of certain vegetables. Until now, LMOFs have been developed to detect nitrite in food products.

For instance, Zhu et al. (2020a) reported a UiO-66- NH_2 composite functionalized with citric acid (Cit) that exhibited favorable fluorescence performance and stability. As the concentration of NO_2^- increased (ranging from 0 to 800 μM), the emission intensity of UiO-66- NH_2 -Cit decreased correspondingly. The authors attributed this fluorescence quenching to the interaction between NO_2^- and linker of the MOFs frameworks. Vanillin, a widely used food additive in beverages, can lead to various diseases and harm liver and kidney functions when ingested in excess. To address this issue, Wang and Ni (2020) synthesized a fluorescent $[Co_2(Bpy)(Oba)_2]$ MOFs material that emitted violet light centered at 440 nm when excited by 297 nm UV light. This material exhibited high sensitivity to vanillin and could be selectively quenched without interference from common substances. The fluorescent probe demonstrated several advantages, including a rapid response time of 20 s, suitability for a wide pH range, excellent fluorescence stability, and cycle stability. However, there is currently a limited number of studies exploring the utilization of MOF as fluorescent sensors for the detection of nitrite, particularly in the context of identifying the food additive nitrite within food products. It is crucial to advance the development of more sensitive and efficient LMOF-based nanoprobe technologies and their applications. This objective constitutes the focus of our research endeavor.

2.3.3.4. Pesticide

In recent years, pesticides have assumed a crucial role in global agriculture. However, their abuse has heightened the risk of excessive pesticide residues in food, which poses a serious threat to ecological safety and leads to potentially harmful effects on human health through the food chain. Therefore, precise detection of these

chemicals is of paramount importance for ensuring food safety. Hence, various fluorescent MOFs have been employed for the detection of pesticide residues in food products.

He et al. (2019) devised a fluorescent Zr-LMOF characterized by its high water stability, making it suitable for in-situ detection of organophosphorous pesticides (OPPs). The Zr-LMOF exhibits a high surface area and intense fluorescence, rendering it highly responsive to the target compounds. The researchers identified the fluorescence quenching mechanisms as resulting from the electron-withdrawing capability of the $-\text{NO}_2$ group in parathion-methyl, which causes the transfer of photoexcited electrons from Zr-LMOF to parathion-methyl. Additionally, the Zr-LMOF was successfully employed in the analysis of spiked water and vegetable samples, enabling the rapid detection of pesticide residues, and thereby demonstrating its potential for detecting OPPs in food samples. Similarly, Singha et al. (2018) developed a novel cadmium-based MOF denoted as $[\text{Cd}_3(\text{PDA})_1(\text{tz})_3\text{Cl}(\text{H}_2\text{O})_4]\cdot 3\text{H}_2\text{O}$, which exhibits strong fluorescence emission at 290 nm upon excitation at 225 nm. This fluorescence property was utilized for the detection of pesticides in aqueous media. Furthermore, the sensitivity demonstrated in the detection of azinphos-methyl in apple and tomato juice extract proved its potential as a pesticide detector in practical applications.

2.3.3.5. *Veterinary medicines*

Veterinary medicines play a crucial role in food production. Nevertheless, the extensive utilization of veterinary drugs in animals and the resulting presence of veterinary residues in food and water constitute a risk to food safety and human health. Consequently, the development of rapid-response sensing methods for detecting these residues is of crucial importance in ensuring food safety. Currently, several noteworthy instances of LMOFs that can offer sensitive detection of pesticide residues in food.

Tetracycline (TC) residues are among the most prevalent antibiotic residues found in dairy products. Consequently, a lot of MOFs-based sensitive probes have been extensively explored for the rapid detection of tetracycline residues. For instance, Li et al. (2019) established a fluorescent MOF-based sensor, $\text{NH}_2\text{-MIL-53(Al)}$, designed for the detection of various TCs in milk. The abundant functional groups, such as $-\text{NH}_2$, $-\text{COOH}$, and $-\text{OH}$, on $\text{NH}_2\text{-MIL-53(Al)}$ contribute to the sensor with high water stability, acting as binding sites for TCs. The results demonstrated the involvement of inner-filter effects and electron transfer, which resulted in high quenching efficiency. This led to the quantitative detection of TCs in raw milk by $\text{NH}_2\text{-MIL-53(Al)}$, with low limits of detection (LODs) and satisfactory recoveries, highlighting its potential advantages, even in comparison to high-performance liquid chromatography (HPLC) method. Furthermore, Han et al. (2017) developed a highly stable luminescent heterometallic MOF, CTGU-7, composed of $[\text{NaEu}_2(\text{TATAB})_2(\text{DMF})_3]\cdot(\text{OH})$ to serve as a chemical sensor for the selective detection of oridazole antibiotics. Zhang et al.

(2017) reported a series of sensors based on Ln-MOFs, exploiting their anti-interference capabilities with nitrofurantoin antibiotics (NFA). The sensing mechanisms of Ln-MOFs composites offer portable chemical sensors for NFA, enabling applications in monitoring NFA-contaminated water and food, as well as detecting the misuse of antibiotics in livestock breeding.

2.4. Application of MOFs in food packaging

Food packaging occupies a pivotal role in the food industry, improving the preservation, transport, and shelf life of food products. Moreover, it serves to reduce the impact of physical, chemical, and biological factors that can compromise food safety. Consequently, extensive efforts have been invested in the exploration of innovative food packaging technologies and materials. The emergence of new materials offers a promising avenue for addressing the challenges confronted by current food packaging (Brockgreitens & Abbas, 2016; Mihindukulasuriya & Lim, 2014). While reports on the application of MOFs in food packaging remain limited, it is noteworthy that MOFs, particularly flexible MOF materials, exhibit unique physical and chemical properties, rendering them highly promising for the development of advanced and environmentally friendly materials tailored for food packaging purposes (Chang et al., 2015).

2.4.1. Anti-bacterial packaging

Kohsari et al. (2016) undertook the development of a range of nanofiber mats constructed from chitosan-poly(ethylene oxide) (CS-PEO) with varying loadings of ZIF-8 nanoparticles (3%, 5%, and 10%) using the electrospinning method. The CS-PEO-3% ZIF-8 mat exhibited satisfactory hydrophobic properties, as confirmed by a water contact angle measurement, and showed appropriate mechanical characteristics. Of particular significance, the CS-PEO-3% ZIF-8 mat demonstrated a remarkable antibacterial efficacy of 100% against both *Staphylococcus aureus* and *Escherichia coli* bacteria. As a result, it is regarded as a highly promising functional material with potential applications in the realm of food coating and packaging.

2.4.2. Gases measurement

Due to their distinctive porosity, MOF materials hold the potential for selective adsorption and desorption of chemicals, offering a means to control the ripening of fresh fruit within packaging. For example, conducted by Chopra et al. (2017), the effectiveness of Basolite C300 and Basolite A520 was assessed for their capacity to adsorb and release ethylene, as well as the ethylene inhibitor, 1-methylcyclopropene (1-MCP). The findings revealed that Basolite C300, serving as an ethylene-releasing agent, exhibited exceptional performance in the ripening of produce with high water content in the headspace of the packaging. The encapsulated ethylene within Basolite C300 facilitated the regulation of fruit and vegetable ripening within active packaging

systems, while concurrently minimizing interference from 1-MCP through the removal of this compound from the packaging headspace.

The measurement of gases, including CO₂, NH₃, and SO₂, holds significant importance in the assessment of food packaging integrity and the degree of food spoilage (Zhang et al., 2014). A sensor for the detection of CO₂ has been engineered by applying MOF (HKUST-1) coatings on optical fibers (Hromadka et al., 2018). The layer-by-layer techniques employed in the fabrication of thin HKUST-1 films proved to be highly efficient. Notably, films comprising a minimum of 40 layers demonstrated satisfactory sensing capabilities for CO₂, achieving low detection limits (LODs) as 401 ppm.

In addition, addressing the challenge of water and oxygen removal in food packaging design has always been of significance. The removal of water and oxygen plays a pivotal role in extending the shelf life of diverse food products, as it mitigates oxidation reactions that lead to food spoilage. MOFs exhibited their capacity to effectively scavenge residual water and oxygen, holding great potential for use in this application. Zhang et al. (2016) reported a strategy to enhance oxygen removal at room temperature by encapsulating ferrocene within MIL-101(Cr). The nanocrystals of the highly efficient water-scavenging MOF-801 [Zr₆O₄(OH)₄(fumarate)₆] have demonstrated the ability to harvest moisture even in environments with a relative humidity as low as 20%. On the basis, Bae et al. (2016) achieved the successful development of exceptionally effective water barrier films by utilizing MOF-801 and a hydrophobic cyclic olefin copolymer. The introduction of MOF-801 not only improved the film's resistance to water permeation but also laid the foundation for further exploration of MOF-based membranes in diverse industrial applications, including food packaging.

2.4.3. Food security label

The misrepresentation of food products through deceptive labeling poses a significant concern within the domain of food packaging. Accurate identification of these products is indispensable for upholding food authenticity and guaranteeing food safety. Consequently, the development of intelligent and standardized methods for the detection of mislabeled food products has become imperative in response to the growing demand for transparency within the food production industry, driven by both producers and consumers. In recent years, luminescent MOFs with diversely unique spectral properties have garnered increasing interest as promising materials for invisible security labeling or encoding (da Luz et al., 2015).

Wang et al. (2018) conducted an interesting study in which they successfully synthesized red, green, and blue (RGB) light-emitting nanoscale MOFs materials (nMOFs) utilizing Eu³⁺, Tb³⁺, Dy³⁺, phthalic acid, and UIO-66-NH₂. These RGB light-emitting nMOFs were subsequently utilized as inks to create colorful light-emitting boxes for the purpose of information encryption. Additionally, three black vertex boxes were used for precise positioning. This innovative approach ensured that

information pertaining to food authentication could only be deciphered under specific excitation conditions using 275 nm light, while it was invisible to the naked eye. These studies offer a diverse array of potential strategies to combat food counterfeiting and hold significant promise in upholding elevated standards of food safety.

2.5. MOF-based hydrogels

2.5.1. *The methods for fabricating MOF-based hydrogels*

The synthesized strategy for MOF-based hydrogel formation can be conceptualized as the integration of MOFs within the sol-gel transition process. In this context, MOFs act as the dispersed phase, while the hydrogel matrices represent the continuous phase, thereby forming composite structures to perform multiple functions. The methodologies employed in the fabrication of MOF-based hydrogels can be broadly categorized into two distinct classes: (1) Direct mixing method and (2) In situ MOF growth method (Gao et al., 2022; Sun et al., 2023; Wang et al., 2019; Zhang et al., 2021).

2.5.1.1. *Direct mixing method*

The direct mixing method can be described as the following preparation procedure, illustrated in **Figure 2-3A**. Firstly, the desired MOFs are synthesized through the interaction between a metal salt solution and organic ligands. Subsequently, MOF crystals are introduced into the sol-state matrix or the liquid precursor solution prior to the gelation process. Ultimately, under the influence of gelation induction, MOF-encapsulated hydrogel composites are formed. It is noteworthy that the MOF-based hydrogels generated through this direct mixing method typically necessitate subsequent post-processing steps to enhance the dispersion of MOFs within the composites.

2.5.1.2. *In situ MOF growth method*

An alternative approach to fabricating MOF-based hydrogels entails the *in situ* synthesis of MOFs within the porous structure of the hydrogel (**Figure 2-3B**). In this analogy, the pores of the hydrogel serve as bottles, while the MOF crystals represent ships. This technique involves a sequential introduction of metal precursors and organic linkers into the hydrogel matrix, subsequently anchoring them within the mesh of the hydrogels through physical or chemical interactions. This process facilitates the incorporation of MOF precursors into the hydrogel matrix, thereby yielding MOF-based hydrogels. This in situ MOF growth method ensures a relatively uniform dispersion of MOFs within the hydrogel network.

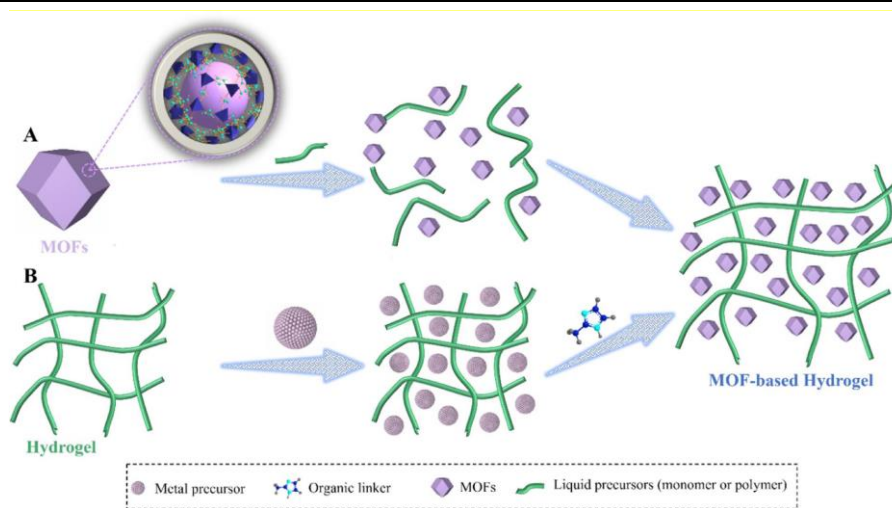


Figure 2-3 The fabrication process of MOF-based hydrogels using (A) direct mixing method and (B) In situ MOF growth method (Sun et al., 2023).

2.5.2. The categories of MOF-based hydrogels

Being novel materials with considerable application potential, a majority of MOFs primarily exist in a powdered crystalline state. This prevalent state imposes substantial limitations on the material's intrinsic advantages and its potential for industrial utility. The constraints associated with handling and mass transfer issues in powdered form hinder their practical applicability. Hydrogels, formed through a sol-gel transition, through combining MOFs to obtain MOF-based hydrogels to effectively mitigating the drawbacks of MOFs while significantly augmenting the performance attributes of hydrogels (Liu et al., 2019). In light of these considerations, excellent MOF-based hydrogel composites were designed to address the imperatives of industrial demand and application requirement. It is noteworthy that MOFs and hydrogels encompass diverse variations, and thus, the combination of different MOFs and hydrogels holds the potential to cater to specific target applications.

2.5.2.1. Pure MOF hydrogels

Lanthanide-MOF based hydrogels represent a distinct class of pure MOF hydrogels. These hydrogels are characterized by the coordinated combination of lanthanide (Ln) metal precursors and organic ligands, and they rely on specific mechanisms involving either swelling or layered growth processes to achieve gel formation. Ln-MOFs, notable for their intriguing luminescent characteristics, including high quantum yield, large stokes shift, long decay lifetimes, and undisturbed emission energy, stand out as one of the most auspicious classes of fluorescent materials (Hasegawa & Kitagawa, 2022; Yan, 2021).

Chen et al. (2019) have reported the fabrication of Ln-MOF hydrogels, characterized by their intrinsic and tunable emission colors. These hydrogels were synthesized using 5-boronoisophthalic acid and various ratios of Ln-ions (Tb^{3+} , Eu^{3+} , or Dy^{3+}), employing methodologies similar to conventional MOF synthesis. The Ln-ions and 5-boronoisophthalic acid components initially formed distinct layers, followed by anisotropic growth, forming nanoribbons that further intertwine to yield the hydrogels. **Figure 2-4A** illustrated the capacity to shape Eu-Tb-Dy MOF hydrogels into various forms, highlighting their tunable shape. While all these hydrogels exhibited the same coloration under sunlight, their perceptible color variations are obvious under single-wavelength excitation at 275 nm. This phenomenon is attributed to the generation of full-color emissions achieved by manipulating the type or proportion of Ln-ions used. In a similar vein, Zhao et al. (2021) harnessed Ln-ions, utilizing 1,3,5-benzenetricarboxylic acid (H_3BTC) as a sensitizer, to interact with Tb^{3+} and/or Eu^{3+} within an aqueous environment at room temperature. This strategy culminated in the development of luminescent hydrogels manifesting diverse emission colors, including red, green, and yellow (**Figure 2-4B**). Lanthanide ions not only instigate the coordinated self-assembly of H_3BTC into a three-dimensional porous structure but also confer the resultant hydrogels with promising luminescent attributes. Concurrently, H_3BTC -Ln hydrogels find utility as luminescent inks for anti-counterfeiting purposes, benefiting from their robust luminescence spectra, long luminescence lifetimes, invisibility under natural lighting conditions, and exceptional stability.

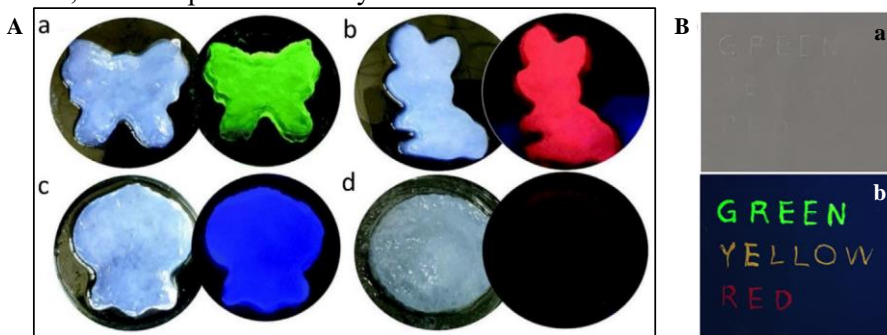


Figure 2-4 (A) Photographs of (a) Tb-Dy MOF hydrogels, (b) Eu-Tb MOF hydrogel, (c) Eu-Dy MOF hydrogel, and (d) Eu-Tb-Dy MOF hydrogel with mixed-metal ratios of 1:1 or 1:1:1 under sunlight and excitation at 275 nm (Chen et al., 2019). (B) Digital images of the luminescent patterns were written with H_3BTC -Tb, H_3BTC - $Tb_{0.9}Eu_{0.1}$, and H_3BTC -Eu, respectively (Zhao et al., 2021)

Table 2-2 The summary of MOF-based hydrogels

MOF	Matrix materials	Application	Ref.
UiO-66-NH ₂	agarose hydrogel	sensing	Gao et al. (2018)
ZIF-8	gelatin hydrogel	–	Garai et al. (2013)
HKUST-1	gelatin hydrogel	–	Garai et al. (2013)
CA@ZIF-8	chitosan	CO ₂ Capture	Ren et al. (2019)
Lanthanide coordination polymer (CP)	chitosan	sensing	Zhou et al. (2022)
HKUST-1	alginate hydrogel	water	Zhu et al. (2016)
ZIF-8	alginate hydrogel	water	Zhu et al. (2016)
MIL-100(Fe)	alginate hydrogel	water	Zhu et al. (2016)
ZIF-67	alginate hydrogel	water	Zhu et al. (2016)
Phosphonate MOF	alginate hydrogel	adsorption	Park et al. (2019)
EuNDC	alginate hydrogel	sensing	Zhao et al. (2019)
5-FU@MOF-5	carboxymethyl cellulose (CMC) hydrogel	drug release	Javanbakht et al. (2020)
UiO-66	carboxymethyl cellulose (CMC) hydrogel	wound dressing	Javanbakht et al. (2021)
MOF-UIO-66	Arabic gum	dye absorption	Ribeiro et al. (2019)

2.5.2.2. MOF@biology derived organic macromolecules hydrogels

Biology-derived organic macromolecules present an indisputably attractive material due to their innate origin in nature. These organic macromolecules, derived from biological sources, offer a unique amalgamation of advantages encompassing cost-efficiency, sustainability in production, and environmental friendliness. However, their potential application as matrices for the growth of MOFs remains a relatively underexplored field. In this part, the different types of MOF@biology derived organic macromolecules hydrogels have been summarized in **Table 2-2**.

Agarose, a widely recognized natural polysaccharide polymer, is readily sourced from seaweed, specifically *Rhodophyceae*. Its distinguished attributes, including exceptional biocompatibility, degradability, and the capacity for thermally reversible gelation, render it for the synthesis of innovative and functionalized hybrid materials through integration with MOF materials (Bergamaschi et al., 2022; Wang et al., 2019). Gao et al. (2018) successfully synthesized a noteworthy dye@MOF composite (RhB@Zr-MOF) and subsequently dissolved abovementioned composite into hot ultrapure water alongside dispersed agarose powder. The resulting solution was subsequently transferred into a 96-well plate and allowed to cool to yield MOF-based agarose hydrogel. Capitalizing on its portability, robustness, and ease of synthesis, this MOF-based agarose hydrogel is poised to exhibit considerable potential within the domain of clinical diagnostics. Furthermore, this synthetic approach holds promise for creating more composites between stable MOFs and agarose hydrogels.

Gelatin is recognized as a classical heterogeneous mixture of high-water solubility and high-molecular-weight proteins. It is derived from the partial hydrolyzation of collagen in the skin, tendons, hooves, and bones of various animals such as pigs, cattle, fish, and others (Hoque et al., 2011). Garai et al. (2013) employed a biomineral-inspired technique to cultivate two classical MOFs, namely ZIF-8 and HKUST-1, within an economically viable and non-toxic gelatin hydrogel matrix. This method involved the introduction of metal salts during the gelatin formation process to create cation-embedded hydrogels. By introducing metal salt solutions containing 1-hexyl-3-methylimidazolium or trimesic acid, ZIF-8 or HKUST-1 crystals could be synthesized respectively. Moreover, the gelatin hydrogel used as a modifier in the growth of macromolecular crystals was found to impact the degree of growth of the two MOFs, which is similar to the natural biomineralization process.

Chitosan is a cationic polymer derived from the deacetylation of natural polysaccharide chitin, widely present in the shell of crustaceans, possesses distinctive attributes including biocompatibility, biodegradability, antibacterial, anticancer, and immune-enhancing properties (Li et al., 2022; Peers et al., 2022). Ren et al. (2019) conducted a study wherein they incorporated carbonic anhydrase molecules into ZIF-8 (CA@ZIF-8). Subsequently, this composite was enveloped within poly(vinyl alcohol)-chitosan hydrogels to fabricate a composite hydrogel. The results indicated an immobilization efficiency of over 70% for the carbonic anhydrase molecules, attesting to the efficacy of the immobilization process. Comparative analysis with free carbonic anhydrase and the CA@ZIF-8 composite revealed that the proposed composite hydrogel displayed superior mechanical strength, stability, and reusability. In another report, Zhou et al. (2022) executed the self-assembly of europium (Eu^{3+}) and terbium (Tb^{3+}) ions in conjunction with guanylate and ciprofloxacin to synthesize lanthanide coordination polymers (CPs). These Ln-CPs were subsequently complexed with chitosan (CS) and dextran aldehyde (DEX) to fabricate a multicolor pH-responsive Ln-based hydrogel denoted as CS/DEX/CP. This hydrogel exhibited a polychromatic responsiveness to fluctuations in proton concentration arising from metabolism and bacterial growth, resulting in a transition in color from red to green or white, while simultaneously releasing ciprofloxacin (CIP) and CS.

Alginate acid, a natural polyuronic acid, has earned considerable attention and found application in various industries such as paper, food, and cosmetics, mainly owing to its remarkable attributes, including water solubility, film-forming capabilities, biodegradability, and biocompatibility (Guo et al., 2020; Yumin et al., 2022). As a biopolymer sourced from seaweed, the divalent cation ions cross-linking alginate hydrogels can be readily synthesized under mild conditions (Zhuang et al., 2016). These hydrogels serve as promising candidates for preparing MOFs-based composites for diverse applications, such as lithium (Li^+) adsorption, water purification, and the diagnosis of penicillin allergies (Zhu et al., 2016). Park et al. (2019) achieved successful synthesis of alginate hydrogels incorporating phosphonate MOFs upon the chemical and morphological characteristics of brown algae. Because the essential

functional groups involved in Li^+ adsorption were attributed to the phosphonate group of the plasma lipid membrane and the carboxylic acid group in alginates (Davis et al., 2003). It was observed that the growth of phosphonate MOFs in Alg(Al) exhibited homogeneity, while the growth in Alg(Cu) was heterogeneous, forming MOF particles on the surface of pMOF@Alg(Cu), accompanied by a modest augmentation in Li^+ adsorption. Zhao et al. (2019) developed an innovative fluorescence detection system utilizing biocompatible alginate in conjunction with poly(ethylene glycol) diacrylate (PEGDA). This approach circumvents the demanding preparation conditions associated with MOF films and addresses issues related to weak bonding between substrates and films, among other limitations. This work demonstrates the potential of biocompatible hydrogel fibers combined with MOFs as a portable platform for selective, real-time, and on-site quantitative monitoring, thereby contributing to the advancement of bioengineering and healthcare.

Cellulose, a macromolecular polysaccharide comprising of glucose, stands as one of the oldest and most prevalent natural macromolecules globally. Derived from a diverse array of sources, cellulose is extracted from biological materials such as trees, plants, fruits, vegetables, and various bioproducts. Its notable attributes, including biocompatibility, biodegradability, renewability, good mechanical strength, and environmental friendliness, make it widely applicable in environmental and energy fields (Zainal et al., 2021). Carboxymethyl cellulose (CMC), recognized as cellulose gum, represents a carboxymethylated derivative of cellulose distinguished by its exceptional attributes, such as water solubility, biocompatibility, and bacteriostatic properties (Chang & Zhang, 2011; Kanikireddy et al., 2020). In a prior investigation, a nanocomposite hydrogel bead named CMC/5-FU@MOF-5, composed of CMC and 5-fluorouracil-loaded MOF-5, was successfully developed (Javanbakht et al., 2020). This nanocomposite demonstrated sustained drug release behavior characterized by high dosing stability, attributed to the pH-sensitive properties of CMC, moreover, CMC afforded enhanced protection against acidic environments. This work provides a potential reference for the formulation of novel controlled release strategies. Javanbakht et al. (2021) achieved the successful formation of flexible hydrogel films by introducing UiO-66 nanoparticles into a carboxymethyl cellulose (CMC) hydrogel, thereby improving both antibiotic release profiles and mechanical performance. The incorporation of UiO-66 MOFs within the polymeric CMC network effectively modulated crystallinity and release characteristics. Furthermore, the introduction of TC@UiO-66 served to reinforce the polymeric network by acting as a crosslinking complex.

Arabic gum (AG), derived from the exudate of the acacia tree, scientifically known as *Acacia senegal*, consists primarily of components such as gum aldose, galactose, glucuronic acid, and others. AG have garnered considerable attention for their economical, non-toxic, biodegradable, and biocompatible properties (Ahmad et al., 2019; Wu et al., 2018). In a study by Ribeiro et al. (2019), a superabsorbent hybrid material was developed, incorporating AG and a cross-linkable inorganic substance,

to enhance its mechanical properties and increase aqueous dye absorption. On the basis of this research, the same group synthesized MOF hydrogel materials using a modified UiO-66 MOF via a solvent-assisted ligand incorporation method, known as UiO-66AA (de Lima et al., 2021). The resultant MOF-based hydrogels exhibited superior water absorption capacity and enhanced mechanical attributes, dependent on the quantity and crystal size of the UiO-66AA MOF integrated. This research provides a novel approach to the design of organic–inorganic hybrid hydrogels.

2.5.2.3. MOF@biocompatible hydrogels

Biocompatible hydrogels play an important role in several fields such as drug delivery and wound healing, however, they are often limited by their instability. To address this issue, the addition of MOFs in biocompatible hydrogels might be a good strategy to improve the mechanical properties of biocompatible hydrogels.

Polyvinyl alcohol (PVA) is a synthetic polymer renowned for its biocompatibility, biodegradability, hydrophilicity, non-toxicity. Its exceptional attributes, such as high tensile strength, flexibility, elevated viscosity, film-forming capabilities, and resistance to solvents, make PVA a promising material for hydrogel preparation (Rivera-Hernández et al., 2021). Wang et al. (2022) developed an innovative approach involving the in-situ synthesis of MOF nanoparticles within freeze-thawed PVA@alginate double-network (DN) hydrogels. Subsequently, these hydrogels were employed in the fabrication of stretchable hydrogel tubes. This research supplies a novel perspective for advancing the realm of soft MOF hydrogel composites.

Zhao et al. (2022) successfully engineered a nanoplatform exhibiting both antibacterial and photocatalytic properties by amalgamating gold nanoclusters (AuNCs), PCN-224, and a hydrogel, for application in treating infected wounds in diabetic rats. This endeavor entailed the encapsulation of AuNCs@PCN within hydrogels, specifically, a polyvinyl alcohol and alginate sodium matrix, yielding AuNCs@PCN@H. Importantly, this composite demonstrated the ability to impart a moisturizing effect on the wound, ensuring even distribution within the wound site. Furthermore, the inclusion of AuNCs rendered the composite exceptionally active in photothermal therapy (PTT).

Copper ions hold prospects in the treatment of chronic non-healing wounds. However, the excessive application of copper salts or copper oxides can potentially exacerbate wound conditions. To address this issue, Xiao et al. (2017) introduced a strategy wherein copper MOF nanoparticles, referred to as HKUST-1 NPs, were incorporated into an antioxidant thermosresponsive citrate-based hydrogel known as poly-(polyethyleneglycol citrate-co-N-isopropylacrylamide), denoted as PPCN. This approach not only accelerates wound healing but also mitigates the toxicity associated with copper ions. This study additionally affirms that the utilization of biologically incompatible MOF materials enveloped within biocompatible hydrogels can serve specific roles within the realm of biomedicine.

Gelatin methacrylate (GelMA), as a photopolymerizable hydrogel, frequently

utilized as a carrier for nanoparticles (Parani et al., 2018; Salahuddin et al., 2021). Hezari et al. (2022) innovatively devised a nanocomposite hydrogel loading with *Camellia sinensis*, achieved through a modification of gelatin in combination with an iron-MOF (MIL-53(Fe)). The process involved the conversion of gelatin into methacrylic acid gelatin by employing methacrylic anhydride. The incorporation of MIL-53(Fe) into the hydrogels yielded improvements in mechanical strength, porosity, drug-carrying capacity, and a reduction in their potential toxicity. The composite hydrogels exhibited a diverse range of attributes, encompassing a porous structure, inorganic-organic properties, and antibacterial characteristics. Consequently, these hydrogel dressings were harnessed to enhance drug loading capacity, antibacterial efficacy, and controlled drug release.

Furthermore, Ananthoji et al. (2011) devised a zeolite-like MOF to enhance the characteristics of the N-vinyl-2-pyrrolidinone hydrogel. The resultant composites featured a network structure enveloping the pores, and they exhibited superior mechanical stability in aqueous environments compared to the N-vinyl-2-pyrrolidinone hydrogel without the zeolite-like MOF. Chen et al. (2018) utilized MOF nanoparticles as a support for the anticancer drug doxorubicin, which was subsequently incorporated into a stimulus-responsive polyacrylamide/DNA hydrogel. The cross-linking of this hydrogel was achieved within a cage-like structure formed by double-stranded nucleic acids containing anti-adenosine triphosphate aptamers.

2.5.2.4. MOF@graphene hydrogels

Graphene, a classical two-dimensional material, assumes a pivotal role in the advancement of materials science and technology, owing to its high crystallinity, exceptional electronic properties, and versatile surface chemical structure (Huang et al., 2011). Moreover, the diversification of its application scope can be substantially broadened through the effective derivation of graphene (Ma et al., 2020). In the domains of chemical science and material science, the exploration of graphene materials, encompassing graphene, graphene oxide (GO), and reduced graphene oxide (rGO), is currently a hot topic. These materials are characterized by their three-dimensional (3D) graphene network, superior conductivity, and rich functional group structures (Huang et al., 2011).

The utilization of MOFs as sacrificial templates in conjunction with polymer hydrogels, possessing a profusion of functional groups, presents a promising methodology for the fabrication of compositionally functionalized, intricately structured micro/nano-hybrid materials (Liu et al., 2022; Yu et al., 2021). Yin et al. (2021) employed a carbon material derived from UiO-66, referred to as porous carbon-ZrO₂, to incorporate poly(4,4'-diphenylether-5,5'-bibenzimidazole) (OPBI) and to obtain self-assembled polyacrylamide (PAM) hydrogel membranes (denoted as BHC). The branched structure of OPBI was anticipated to enhance the dimensional stability of the self-assembled PAM hydrogel films. Additionally, UiO-66 served as both the precursor and template, simplifying the fabrication of porous carbon-ZrO₂

composites through thermal carbonization. This porous material, characterized by uniform pore size and a substantial surface area, exhibited an enhanced capacity to absorb phosphoric acid (PA), thereby augmenting proton conductivity. Furthermore, ZrO₂ within the porous carbon-ZrO₂ composite functioned as a critical component, leading to improved water and PA retention and enhanced mechanical properties of the membrane.

In the pursuit of augmenting the conductivity of a graphene hydrogel (GH) while preserving its oxygen functional groups, Li et al. (2020) achieved the successful fabrication of an all-carbon GH-based electrode material adorned with N-doped graphene quantum dots (N-GQD) and MOF-derived carbon (cZIF-8). Within the N-GQD@cZIF-8/GH composite, the GH established a robust cross-linked network structure that facilitated rapid ion and electron transport. The introduction of cZIF-8 imparted a considerable surface area and effectively mitigated charge transfer resistance and series resistance within the GH. This architectural ultimately led to an enhancement in capacitive performance and N-GQDs contributing to enhanced wettability.

Xu et al. (2021) proposed an eco-friendly and sustainable approach with low consumption to create a distinctive self-assembling material, namely reduced graphene oxide/N-doped porous carbon hydrogel (rGO/NPC). This material was developed through the in-situ growth of nanoparticles on sodium CMC, followed by carbonization and subsequent self-assembly with rGO, achieved via a straightforward hydrothermal process. The formation of a hierarchical porous structure was achieved by the 3D porous network of CMC and the uniform dispersion of ZIF-67 nanoparticles on the CMC surface. The introduction of rGO facilitated the encapsulation of ZIF-67/CMC, thereby enhancing the electrochemical properties of the resulting nanocomposite and allowing for the fabrication of an electrochemical capacitor electrode without the need for a binder.

Lee et al. (2012) effectively synthesized a GO derivative, denoted as A-GO, using a two-step reaction method. A-GO was subsequently employed to fabricate a MOF-GO composite hydrogel, named MOF-A-GO, achieved by mixing it with organic ligands in the presence of Zn²⁺ ions. MOF-A-GO exhibits a strong fluorescence enhancement upon gel formation, thereby demonstrating potential for selective recognition of trinitrotoluene. In addition, there exist other categories of MOF-based hydrogels, including ZIF-8/laponite clay hydrogel nanocomposites and HKUST-1@PVA-co-PE/PVA hybrid hydrogels (Chakraborty et al., 2018; Zhu et al., 2018).

In general, the types of MOF-based hydrogels remain relatively limited. Furthermore, given the increasing emphasis on environmental preservation, recycling, and related fields, the demand for stimulus-responsive and self-repairing hydrogels is steadily on the rise. Consequently, there is a compelling need for further research and exploration in this particular direction.

2.6. Conclusion

In summary, a range of innovative and refined synthesis and modification techniques for Metal-Organic Frameworks (MOFs) have been devised. However, there is a pressing need to focus on achieving high-quality MOFs tailored specifically for applications in food safety. Furthermore, the utilization of MOF-based materials has exhibited significant advantages in the realm of food analysis, encompassing advancements in sample preparation, the creation of sensing devices, and the amplification of detection signals. Both MOFs and MOF-based hydrogels have displayed promising potential in enhancing food safety measures, showcasing versatility in their applicability across various stages of the analytical process. While considerable strides have been made, it is anticipated that with the ongoing development of new MOFs and their derivatives, these materials will transition into a new era, playing a pivotal role in ensuring food safety. Therefore, given that nitrite is a common representative of food additives concerning food safety, this study draws inspiration from the aforementioned context to offer straightforward approaches for designing LMOFs nanosensors capable of more efficient and durable nitrite sensing, while also developing its hydrogel test kits for broadened exploration.

3

Chapter III. LMOF (Rh6G@MOF-5) serve as food preservative nanosensor for sensitive detection of nitrite in meat products

Short overview

Chapter 3 aimed to establish a single-emission “turn-off” type fluorescent nanoprobe (Rh6G@MOF-5) based on the benefits of metal-organic framework MOF-5 and luminescent rhodamine 6G (Rh6G). After optimizing the suitable nitrite sensing conditions (hydrochloric acid concentration and response time), the Rh6G@MOF-5 nanoprobe was utilized to detect nitrite, resulting in a significant quenching of its characteristic yellow-green fluorescence color.

The work from the present chapter was published on *LWT-Food Science and Technology*, as can be retrieved by:

Siyang Deng, Huan Liu, Chunhui Zhang, Xinting Yang, Christophe Blecker. (2022) LMOF serve as food preservative nanosensor for sensitive detection of nitrite in meat products. *LWT-Food Science and Technology*, 169, 114030. <https://doi.org/10.1016/j.lwt.2022.114030>.

Abstract: Nitrite (NO_2^-) is widely present in meat products as a vital food preservative, while excessive nitrite is a serious carcinogen to human beings, developing a sensitive and selective nitrite detection method is of great significance for food safety. Herein, a novel luminescent metal organic framework (LMOF) (Rh6G@MOF-5) is prepared through a facile one-pot synthesis as a fluorescent turn-off sensor for NO_2^- determination. Upon exposure to NO_2^- , significant fluorescence intensity decreases linearly along with NO_2^- concentration in the range of 0-200 $\mu\text{mol/L}$ and the detection limit is estimated to be 0.2 $\mu\text{mol/L}$. The developed nanocomposite has been shown to be an ultrasensitive and selective nanoprobe for detecting NO_2^- in meat products, with recoveries ranging from 96.1 % to 103.2 % with the RSDs less than 4%. Rh6G@MOF-5 nanoprobe offers insight into the fabrication of MOF-based sensors with low cost and convenient operation in analyte detection field.

Keywords: nitrite; rhodamine 6G; luminescent metal organic framework; meat products

3.1. Introduction

Nitrite (NO^{2-}) has been used as an essential food additive (such as chromogenic agents, flavoring agents and preservatives) in the food industry that can improve color, texture, and storage stability (Nam et al., 2018; Wang et al., 2016). Nevertheless, their application is controversial since excessive intake of nitrite in food would cause a serious health threat to the public. Nitrite can be converted to *N*-nitrosamines when reacted with secondary amines and amides, which have been identified as potential carcinogens and mutagens (Canbay et al., 2015; Kilfoy et al., 2011; Santarelli et al., 2010). Therefore, excessive consumption of nitrites in the human body will lead to numerous diseases such as esophageal cancer, infant methemoglobinemia and central nervous system deficiencies, etc (Brender et al., 2004; Greer et al., 2005; Maia & Moura, 2014; Zhou et al., 2014). Due to these toxic effects, the establishment of an efficient, facile, and sensitive method to detect nitrite is of great significance in food products, especially for meat products.

Conventional and reliable detection methods have been reported for nitrite determination, including capillary electrophoresis (CE) (Lee et al., 2008; Merusi et al., 2010), chromatography (Li et al., 2000; Pérez-López et al., 2016), electrochemical methods (Liu et al., 2017; Wan et al., 2017) and so on. Although these techniques have been widely used in the past, most of them have several drawbacks, including expensive instrumentation, laborious and time-consuming procedures, which have limited their wide utilization. In comparison, spectrofluorimetric analysis is a preferred selection for nitrite detection due to its high sensitivity, convenience, easy operation, low-cost, and ability to be used for on-line or visual on-site analysis (Hu et al., 2019; Zheng et al., 2016). Therefore, it is of significance to fabricate effective probes for nitrite recognition based on the fluorescent technique to work in an aqueous system.

Metal organic frameworks (MOFs), rising as a new class in microporous hybrid crystalline materials, are constructed by the coordination of metal centers and organic ligands via a self-assembly approach (Sahiner et al., 2017), and can be applied in various fields for their superior structures and physicochemical properties (such as high porosity, uniform nanoscale cavities, adjustable compositions, and functional surfaces) (Furukawa et al., 2013). As a novel class of exciting MOF materials, LMOF-based sensors are gaining interest as their nanoscale cavities and three-dimensional (3D) network architectures, which act as micro-reactors, provide adequate space for the identification and selective recognition of objective targets through signal amplification (Guo et al., 2019a). Acting as host matrices, MOFs can be viewed as unique platforms for stabilizing and confining functional groups, resulting in specific behavior inside the defined pore environments. Aggregation-caused quenching (ACQ) can also be limited through immobilizing organic dyes into the pores of MOFs (Guo et al., 2019a). Thus, LMOF composites introduce the organic dyes into MOFs through a “ship in a bottle” way and combine the advantages of MOFs’ crystalline benefit with the high luminous efficiency of luminescent genes, which have attracted extensive

attention due to their unique ability to recognize specific analytes (Ye et al., 2019). Accordingly, this prompted us to synthesis a superior LMOF that can be used to impede large-sized interferents and thus improve their specificity toward nitrite sensing, while also reducing the ACQ effect of the fluorescent dye itself. In the last few years, LMOFs have been probed for important applications such as temperature sensing, toxic or less environmentally friendly molecular (antibiotics, pesticides, metal ions, explosive, and so on) detecting (Let et al., 2020; Liu et al., 2019; Wang & Yan, 2019). However, to the best of our knowledge, such kind of LMOF based sensor for detection of nitrite in meat products have rarely been reported so far.

In this work, we prepared a high-quality LMOF based on organic dye and MOF hybrid materials via a facilely solvothermal synthesis approach, in which rhodamine 6G (Rh6G) was incorporated into the porous crystalline Zn-MOF (MOF-5) serving as a nitrite ion detecting sensor (**Figure 3-1A**). The optimized Rh6G@MOF-5 composite exerts a uniformly nanosized distribution and excellent MOF-5 porosity, and its suspension emits a distinctive yellow-green emission at 545 nm. Moreover, compared with free Rh6G dye, the LMOF in this study not only kept Rh6G molecules away from the ACQ effect but also exhibited higher photostability and longer fluorescence lifetime. These results showed that the Rh6G@MOF-5 could enhance the sensing ability towards nitrite ion through a “turn-off” fluorescence response in view of the inner filter effect (IFE) and electron-withdrawing effect. Moreover, the fascinating LMOF was successfully used to detect nitrite ions with satisfactory results in meat products’ system.

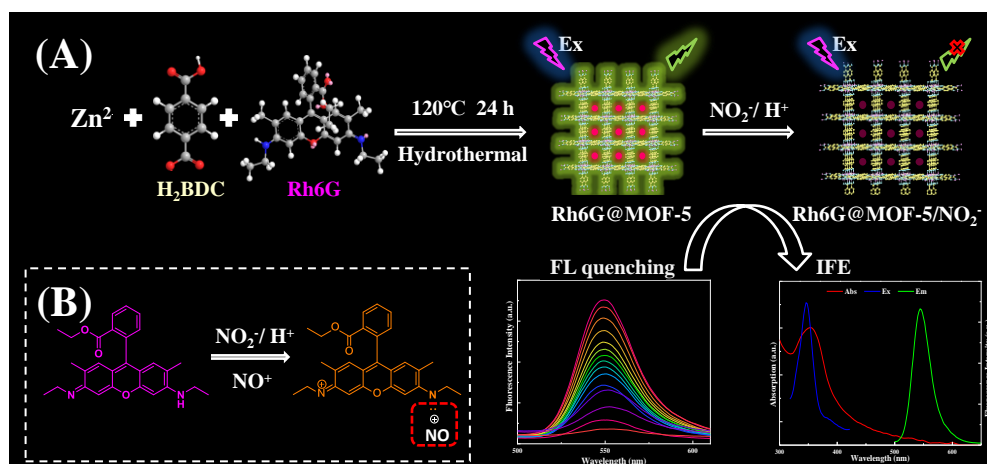


Figure 3-1 Schematic illustration for the construction of Rh6G@MOF-5 (A) and the possible mechanism for detection of nitrite (B).

3.2. Materials and Methods

3.2.1. Chemicals and Materials

Zinc nitrate hexahydrate ($\text{Zn}(\text{NO}_3)_2 \cdot 6\text{H}_2\text{O}$), 1,4-benzenedicarboxylic acid (H_2BDC), *N,N*-Dimethylformamide (DMF) and rhodamine 6G (Rh6G) were purchased from Aladdin reagent company (Shanghai, China). Nitrite (NO_2^-) and aqueous solutions of interference ions (NO_3^- , SO_4^{2-} , CO_3^{2-} , Cl^- , K^+ , Na^+ , Ca^{2+} , Mg^{2+} , Pb^{2+} , Zn^{2+} , Cu^{2+} , Mn^{2+} , Fe^{2+} , Fe^{3+} , Al^{3+} , H_2PO_4^- and HPO_4^{2-}) were supplied by Macklin Biochemical Co., Ltd. (Shanghai, China). And all chemicals and solvents were of analytical grade and used without further purification.

3.2.2. Instrumentation

The fluorescence spectra of the sensors were recorded with a fluorescence spectrometer (Hitachi F-7000, Tokyo, Japan), the integration time was set at 0.05 s and the emission and excitation slit widths were all 5 nm. The ultraviolet–visible (UV–Vis) spectra were scanned by a UV–Vis spectrophotometer (Hach DR6000, Loveland, USA) in the wavelength range of 300 nm–600 nm with a step size of 2 nm. Powder X-ray diffraction (PXRD) patterns were performed using the Panalytical X-ray Diffractometer Smartlab-9kW (Tokyo, Japan) employing Cu $K\alpha$ radiation ($\lambda = 1.5406 \text{ \AA}$, 40kV, 250mA) in the 2θ range of $2 - 50^\circ$. Fourier transform infrared (FT-IR) spectra were obtained using a FT-IR spectrophotometer (Thermo Scientific Nicolet IS5, USA) within the $4000\text{--}400 \text{ cm}^{-1}$ region. Scanning electron microscopy (SEM) images were obtained by a field-emission scanning electron microscope (FEI Inspect F50, USA). The fluorescence lifetimes were collected using the FLS1000 series of fluorescence spectrometers (Edinburgh FS5, Livingston, UK).

3.2.3. Synthesis of Rh6G@MOF-5

The synthesis of Rh6G@MOF-5 porous material was based on previous reports using a solvothermal method with some slight modification (Guo et al., 2019b). In brief, $\text{Zn}(\text{NO}_3)_2 \cdot 6\text{H}_2\text{O}$ (2 mmol) and H_2BDC (1 mmol) were dissolved in 40 mL of DMF and the mixture was treated with ultrasound for about 30 min. Then, various amounts of Rh6G were added into the above solution, with 30 min of sonication for each addition. Then, the mixture was placed in a 200 mL polytetrafluoroethylene stainless steel reactor and heated in an oven at $120 \text{ }^\circ\text{C}$ for 24 h. After the reaction was completed and the polytetrafluoroethylene stainless steel reactor cooled to room temperature, solid products were collected through centrifugation (8000 rpm/min, 5 min) and washed more than three times with DMF and methanol to remove unreacted ligand. Finally, the dye-encapsulated MOF composites (Rh6G@MOF-5) were dried at $120 \text{ }^\circ\text{C}$ in a vacuum oven for 12 h to obtain some solid powders. The control MOF-5 synthesis step was the same as above, except that no Rh6G molecules were added.

3.2.4. Quantitative detection of nitrite

To detect the nitrite response of the system, a series of different concentrations of nitrite aqueous solutions ($0\text{--}300 \text{ }\mu\text{mol/L}$) were prepared and the detection of nitrite

was performed in an acidic environment at room temperature. Firstly, 10.0 mg Rh6G@MOF-5 powder was dispersed in 25 mL deionized water and magnetically stirred for 20 min to form standard stock solution of Rh6G@MOF-5. Subsequently, 100 μL of Rh6G@MOF-5 stock solution was mixed with 800 μL of HCl solution (0.4 mol/L), then incrementally added 100 μL different concentrations of freshly prepared nitrite aqueous solution to the above mixture. The resulting suspension was mixed thoroughly before recording the fluorescence emission spectra with excitation at 350 nm. Furthermore, all the following peaks were recorded more than three times in order to guarantee the experimental reliability.

3.2.5. Selectivity measurement of nitrite

The selectivity of Rh6G@MOF-5 probe to nitrite was examined via adding some other interferences or common ions which coexist with nitrite in meat products, including NO_2^- , NO_3^- , SO_4^{2-} , CO_3^{2-} , Cl^- , K^+ , Na^+ , Ca^{2+} , Mg^{2+} , Pb^{2+} , Zn^{2+} , Cu^{2+} , Mn^{2+} , Fe^{2+} , Fe^{3+} , Al^{3+} , H_2PO_4^- , and HPO_4^{2-} , respectively, in a manner similar to that of nitrite.

3.2.6. Analysis of nitrite in meat products

Meat products (including sausage, bacon, pork ham, beef ham, stewed beef, and braised chicken) were obtained from a local supermarket (Beijing, China). The method of NO_2^- extraction in meat samples was implemented on the basis of the People's Republic of China National Food Safety Standard (GB 5009.33–2016). 5.0 g of crushed sample was weighed and placed in a 250 mL glass conical flask with a stopper, followed by 12.5 mL of saturated borax solution (50 g/L) and approximately 150 mL of distilled water at 70 °C. After that, the conical flask was heated in a boiling water bath for 15 mins before being cooled to room temperature. To transfer the extracted liquid into a 200 mL volumetric flask, put in 5 mL of potassium ferrocyanide (106 g/L), 5 mL of zinc acetate (220 g/L) and distilled water in order, then shake well. The homogenate was placed for 30 mins then filtered using filter paper to remove unsolvable and useless substances. Finally, 30 mL of initial filtrate was discarded, and the final filtrate obtained was preserved in the refrigerator at 4 °C for later use.

3.2.7. Statistical analysis

The nitrite detection results are expressed as the mean values \pm standard deviations by using Statistix 8.1 software package (Analytical Software, St Paul, MN, USA). In addition, all graphs were constructed using Origin 2021.

3.3. Results and Discussion

3.3.1. Basic characterizations of Rh6G@MOF-5

The morphological and structural characterization of Rh6G@MOF-5 was determined by the following tests. Firstly, the PXRD was performed to verify the

successful preparation of the Rh6G@MOF-5 composite. As shown in **Figure 3-2A**, the prepared MOF-5 and Rh6G@MOF-5 exhibited similar diffraction peaks to the simulation one, indicating that the prepared MOFs presented an intact structure and showed high crystallinity. The encapsulated Rh6G had a negligible effect on the MOF-5 lattice. In addition, analogous XRD sharp diffraction peaks of MOF-5 and Rh6G@MOF-5 demonstrated that Rh6G dyes were encapsulated into the cavity instead of physically aggregated and adsorbed on the surface of the MOF-5 crystal. A similar phenomenon was also documented by Ye et al. (2019), who showed that the encapsulating of 5-aminofluorescein through the “ship in a bottle” approach only gave rise to color change without morphology change in parent MOF-801.

The FT-IR spectra of MOF-5 and Rh6G@MOF-5 composites were also characterized to determine the molecular structure (**Figure 3-2B**). According to the literature, the observed peaks at 530 cm^{-1} and 750 cm^{-1} resulted from the stretching vibration of Zn—O and C—H in the tetrahedral Zn_4O crystal cluster of MOF-5, respectively (Petit & Bandoz, 2009). The characteristic absorption peaks of MOF-5 nanocrystals situated at 1395 cm^{-1} and 1600 cm^{-1} were in line with the symmetrical and asymmetric stretching vibrations of the carboxyl group, which is one of the principal functional groups of H_2BDC ligands (Hu et al., 2021). The results were in agreement with the MOF-5’s structure. Furthermore, no visible difference could be found in the FT-IR spectra between MOF-5 and Rh6G@MOF-5, and no blue or red shift after Rh6G encapsulation, illustrating that the Rh6G had successfully enclosed into the pores of MOF-5 and the organic dye in nanocrystals did not affect the building of MOF-5. Besides, the characteristic peaks of Rh6G were not observed in Rh6G@MOF-5, further indicating that Rh6G fluorescein was localized inside the pores of MOF-5. This is consistent with PXRD analysis results.

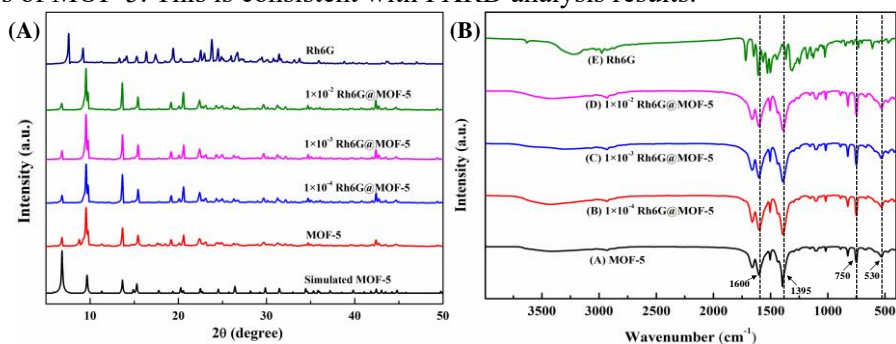


Figure 3-2 (A) PXRD patterns of simulated MOF-5, synthesized MOF-5, 10^{-4} Rh6G@MOF-5, 10^{-3} Rh6G@MOF-5, 10^{-2} Rh6G@MOF-5 and Rh6G. (B) FT-IR spectra of MOF-5, 10^{-4} Rh6G@MOF-5, 10^{-3} Rh6G@MOF-5, 10^{-2} Rh6G@MOF-5 and Rh6G.

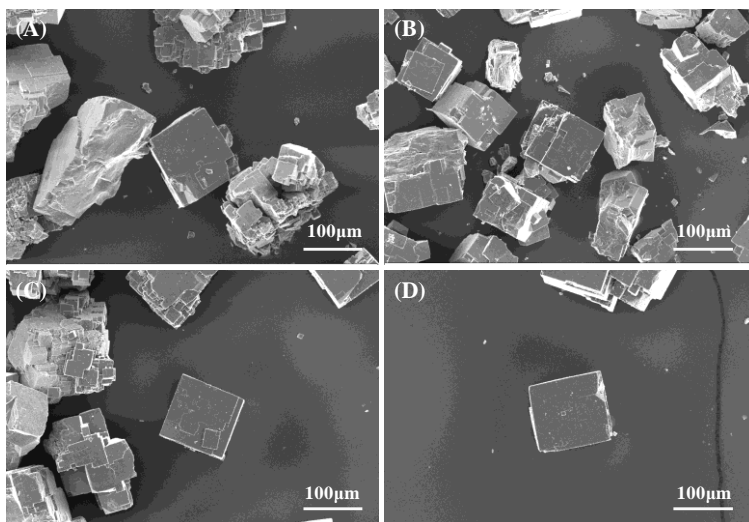


Figure 3-3 SEM images of MOF-5 (A), 10^{-4} Rh6G@MOF-5 (B), 10^{-3} Rh6G@MOF-5 (C) and 10^{-2} Rh6G@MOF-5 (D) under magnification $500\times$.

As revealed by SEM images (**Figure 3-3**), the shape of the obtained MOF-5 and Rh6G@MOF-5 presented the “cube sugar-like” morphology, similar results have also been reported by Guo et al. (2019b). As we can see, they all presented good dispersibility, uniform size, and no significant morphological differences. And the Rh6G@MOF-5 was a regular crystal combined with some nanoscale sub-crystals. The morphology of all Rh6G@MOF-5 composites matched well with the pure MOF-5, further proving that the crystal structure of MOF was not affected by the Rh6G-loading process regardless of the concentrations of Rh6G dye molecules. This appearance allows us to dominate the grain size of the proposed Rh6G@MOF-5 so long as the morphology of the original MOF-5 can be effectively mediated in an appropriate way (Ye et al., 2019). All these above results illustrate that Rh6G dye molecules have been successfully incorporated into parental MOF-5 and the skeleton structure of MOF-5 is maintained.

3.3.2. Photoluminescence studies of Rh6G@MOF-5

According to above characterization of synthesized Rh6G@MOF-5, Rh6G dye molecules have been successfully incorporated into the cavities of MOF-5 with well interspersing because of the uniform pore confinement effect. The digital photographs of Rh6G, Rh6G mixed with MOF-5, MOF-5 and Rh6G@MOF-5 with different Rh6G concentrations under visual light and 365 nm UV light were taken for observation with the naked eye (**Figure 3-4A**).

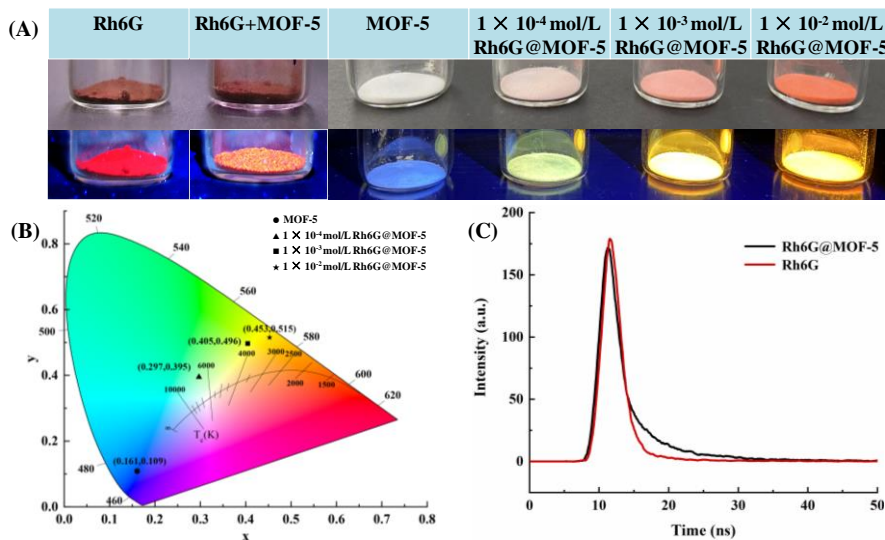


Figure 3-4 (A) Photographs of Rh6G, Rh6G+MOF-5, MOF-5, and Rh6G@MOF-5 with different Rh6G concentrations under visual light and 365 nm UV light. (B) CIE chromaticity coordinates for Rh6G@MOF-5 with different Rh6G concentrations. (C) Time-resolved fluorescence decay curves of Rh6G and Rh6G@MOF-5.

In addition, fluorescence spectra were recorded in order to optimize the loading amount of fluorescent dye in MOF-5. It should be emphasized that no fluorescence emission was obtained in the solid-state Rh6G molecules for the ACQ effect, which usually exists in aggregated dye molecules due to nonradiative energy transfer (**Figure 3-5A**). Furthermore, the mechanically ground mixture of Rh6G and MOF-5 had no significant improvement effect as well (**Figure 3-5B**). As shown in **Figure 3-4A**, with the rise of the Rh6G additions (range from 0 to 1×10^{-2} mol/L), the color of Rh6G@MOF-5 changed from white to faint pink to pink to orange, and the corresponding fluorescence color of Rh6G@MOF-5 represented blue, green, strong yellow, and weaker yellow color, respectively, matching well with the fact that an increasing number of Rh6G dye molecules were loaded into the original MOF-5. Furthermore, seen from the calculated Commission Internationale de L'Eclairage (CIE) chromaticity coordinates diagram, they are (0.161, 0.109), (0.297, 0.395), (0.405, 0.496) and (0.453, 0.515) for the series of Rh6G@MOF-5 composites (0 to 1×10^{-2} mol/L Rh6G levels) (**Figure 3-4B**). The CIE coordinates moved from the blue region to the orange region with the increase of embedded Rh6G molecules, which was consistent with the emission color of Rh6G@MOF-5 under UV light. All the above results further demonstrated that Rh6G molecules are uniformly linked to the channels of MOF-5 through covalent bonding as a modulator, since almost no significant color change was shown after several washes, thus the formation of aggregates in the solid state was inhibited.

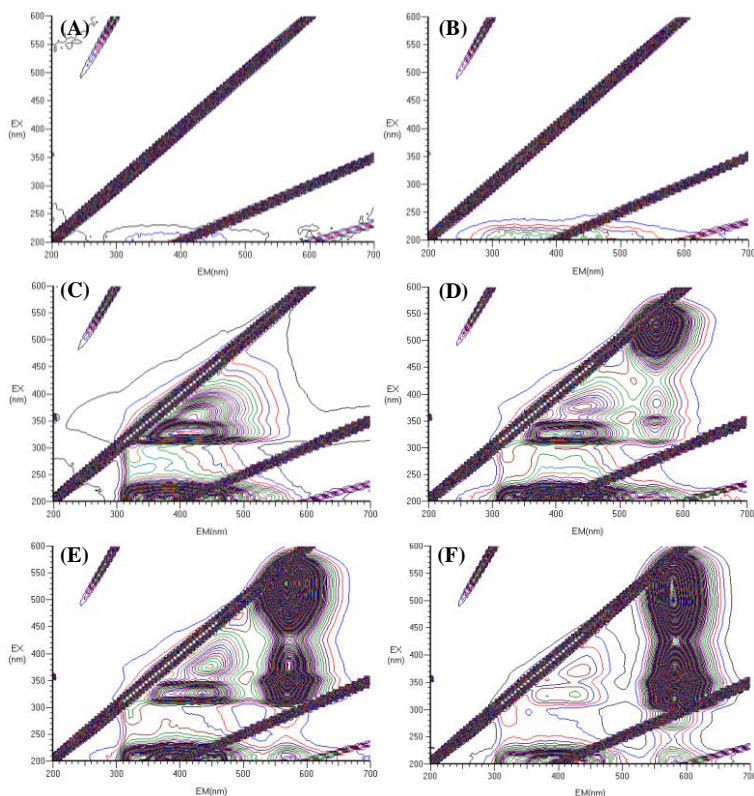


Figure 3-5 The 3D-fluorescence spectra of Rh6G (A), Rh6G+MOF-5 (B) MOF-5 (C), 10^{-4} Rh6G@MOF-5 (D), 10^{-3} Rh6G@MOF-5 (E) and 10^{-2} Rh6G@MOF-5 (F) solid powders.

Three fluorescence peaks were identified from the 3-D front-face fluorescence spectra of Rh6G@MOF-5. Excitation/Emission (Ex/Em) peak located at 330 nm/430 nm was attributed to MOF-5, Ex/Em peaks located at 350 nm/570 nm and 530 nm/570 nm were attributed to Rh6G (**Figure 3-5C to F**). It is found that fluorescence intensities of 350 nm/570 nm Rh6G peak was positively correlated with the amount of fluorescein. However, once the addition of Rh6G reached 1×10^{-2} mol/L, obvious fluorescence quenching located at 530 nm/570 nm was noticed, which was in accordance with the ACQ phenomenon of the free dye molecules (**Figure 3-6**). Based on that, the optimal amount of Rh6G was set at 1×10^{-3} mol/L to provide sufficient active sites and simultaneously protect Rh6G against a potential ACQ phenomenon for further experiments.

In order to further explore the interaction of Rh6G fluorescein and MOF-5 in this nanocomposite, the fluorescence decay curves of both Rh6G and the Rh6G@MOF-5 composite were measured. As **Figure 3-4C** displayed, after embedding Rh6G

molecules into the cavities of MOF-5, the fluorescence lifetime of Rh6G increased from 1.82 to 5.20 ns. The decrease in aggregation and deprotonation of Rh6G molecules after encapsulation into the MOF-5 framework was considered to increase the lifetime of Rh6G@MOF-5. The lifetime-prolonging Rh6G@MOF-5 hybrid showed significant advantages for practical applications of this LMOF in sensing (Guo et al., 2019a).

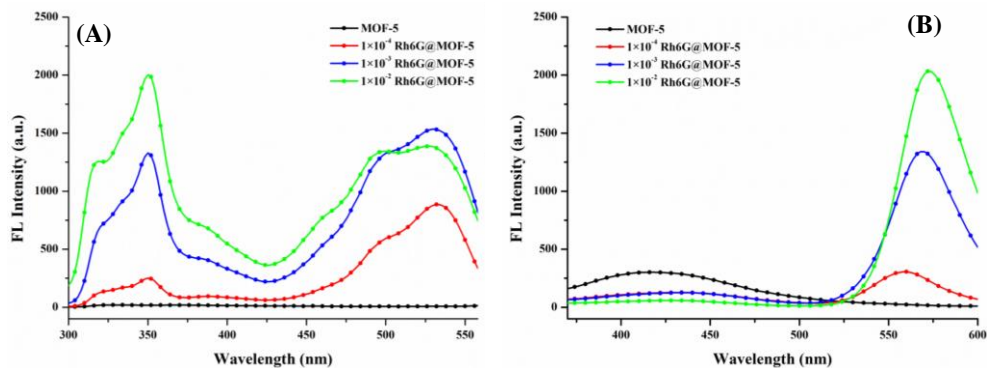


Figure 3-6 (A) Excitation spectrum for MOF-5, 10^{-4} Rh6G@MOF-5, 10^{-3} Rh6G@MOF-5 and 10^{-2} Rh6G@MOF-5 under EM=570nm. (B) Emission spectrum for MOF-5, 10^{-4} Rh6G@MOF-5, 10^{-3} Rh6G@MOF-5 and 10^{-2} Rh6G@MOF-5 under EX=350nm.

3.3.3. Optimization of detection condition

Generally, the rhodamine derivative displays a non-fluorescence spirolactam structure in neutral or alkaline conditions, yet it shows a strong fluorescence xanthenes structure in acidic conditions. This xanthenes structure may react with NO_2^- , thus displaying a sensing signal via quenching its emission (Wu & Nie, 2015). Moreover, nitrite sensing is frequently performed in an acidic solution so that sensing molecules are able to react with NO_2^- fully. As a consequence, a suitable acidic medium (HCl concentration) is necessary to be considered for ensuring this sensing process. Emission quenching (F_0-F) of Rh6G@MOF-5 suspension under various HCl concentrations was shown in **Figure 3-7A**. Notably, fluorescence quenching values increase obviously with increasing HCl concentrations from 0 mol/L to 0.4 mol/L, which may be attributed to the fact that protons accelerated the reaction between NO_2^- and Rh6G@MOF-5. Then, F_0-F values become smooth and non-fluctuating with increasing HCl concentrations from 0.4 mol/L to 1.0 mol/L. Hence, the optimal acid condition was chosen as 0.4 mol/L HCl concentration in this work since its fluorescence quenching achieved both maximum probe quenching and stable signal.

In addition, reaction time is another optimized factor to completely react and quench between nitrite ions and the Rh6G@MOF-5 sensing probe. To display the response time of Rh6G@MOF-5 toward nitrite, their fluorescence intensity variation

was summarized in **Figure 3-7B**. After the addition of the nitrite solution to the Rh6G@MOF-5 suspension, in its initial 20 min, the fluorescence intensities of the probe decreased rapidly, then this fluorescence quenching became smooth, and the sensing process finally achieved equilibrium after 20 min. Therefore, 20 minutes was chosen as the optimal reaction time, indicating that maximum quenching can be achieved within 20 min. This fluorescence response time was slightly shorter than previous reports since the uniform and porous structure of synthesized MOF-5 could improve analyte diffusion and promote the interaction of nitrite with the fluorescent recognition site (Hu et al., 2014; Huang et al., 2019).

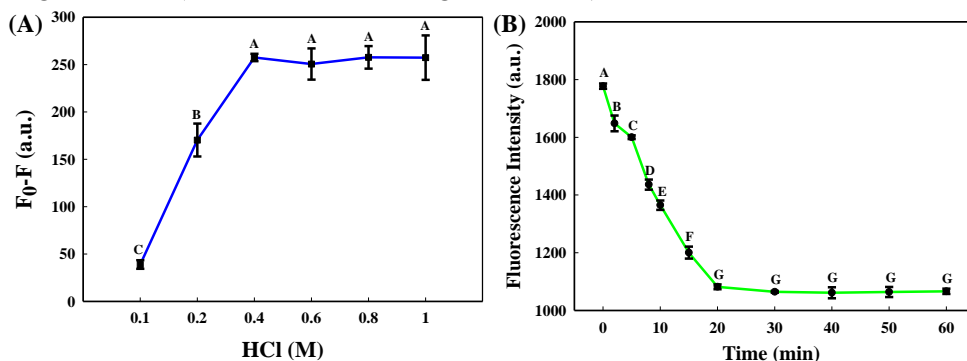


Figure 3-7 (A) Effect of HCl concentration on the Rh6G@MOF-5-based sensor for nitrite (10 μ M). F_0 means initial emission intensity without nitrite ion and F means emission intensity after adding nitrite ion. (B) Fluorescence intensity of Rh6G@MOF-5 suspension after reaction with nitrite (10 μ M) for different times.

3.3.4. Fluorescence detection for nitrite based on Rh6G@MOF-5 sensor

The fluorescence intensity of the chemo-synthesized Rh6G@MOF-5 system in the presence of various NO_2^- concentrations ranging from 0 mmol/L to 300 mmol/L was recorded using the above suitable conditions (**Figure 3-8A**). It was clear that the fluorescence emission peaking at 545 nm is quenched gradually as the nitrite ion concentration increases. As shown in **Figure 3-8C**, a well linear relationship ($F = 1744.77 - 65.40 C$, $R^2 = 0.9975$) was obtained between fluorescence intensity and NO_2^- concentration ranging from 1 μ mol/L to 10 μ mol/L. Furthermore, the limitation of detection (LOD) was defined as $3\sigma/s$, where σ is the standard deviation of blank measurements and s is the slope of the linear calibration plot, respectively (Guo et al., 2019b). The LOD of nitrite ion obtained by the method reported herein was calculated to be 0.2 μ mol/L, it is far below the ceiling concentration of NO_2^- in meat products (Zhang et al., 2016). The above results suggest that this sensitive Rh6G@MOF-5 fluorescence probe can be applied for efficient detection of nitrite ions in meat samples. **Figure 3-8D** also showed a strong and positive correlation between NO_2^-

concentration and fluorescence intensity in the range of 20 – 200 $\mu\text{mol/L}$ ($R^2 > 0.990$).

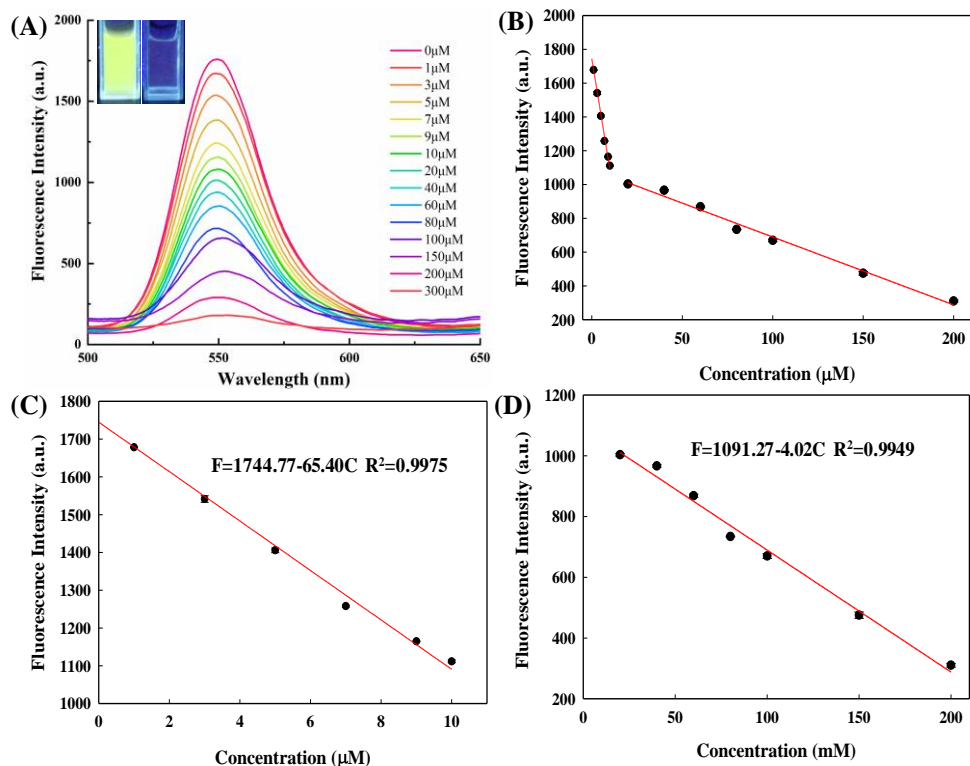


Figure 3-8 (A) Evolvement of the fluorescence emission spectra of the Rh6G@MOF-5 suspension under various concentrations of nitrite (0-300 μM). Inset shows the corresponding photos of Rh6G@MOF-5 in the absence (left) and presence (right) of 1 mmol/L nitrite ion under 365 nm UV light. (B), (C) and (D) Standard curve for the determination of nitrite concentration.

3.3.5. Anti-interference performance of Rh6G@MOF-5

Apart from sensitivity, the anti-interference is deemed another vital factor in evaluating the luminescent probe when detecting nitrite ions in a complex meat product system. Hence, the selectivity of the Rh6G@MOF-5 nanosensor platform toward NO_2^- was investigated. The possibly competitive interferences in meat samples, such as NO_3^- , SO_4^{2-} , CO_3^{2-} , Cl^- , K^+ , Na^+ , Ca^{2+} , Mg^{2+} , Pb^{2+} , Zn^{2+} , Cu^{2+} , Mn^{2+} , Fe^{2+} , Fe^{3+} , Al^{3+} , H_2PO_4^- and HPO_4^{2-} , were added to test the selective performance of Rh6G@MOF-5 under the same conditions (**Figure 3-9**). Even though the added concentration of seventeen different interference ions (1×10^{-4} mol/L) was 10 times that of NO_2^- in the detection system, only NO_2^- treatment (1×10^{-5} mol/L) displays an

obvious enhancement on the $(F_0-F)/F_0$ of the Rh6G@MOF-5 suspension, indicating that Rh6G@MOF-5 nanosensor has a great anti-interference capability and was not disturbed by other competitive ions. Due to the low LOD, wide detection range, high sensitivity, and great specificity toward NO_2^- , this LMOF could serve as an efficient NO_2^- detection platform with high accuracy in meat product system.

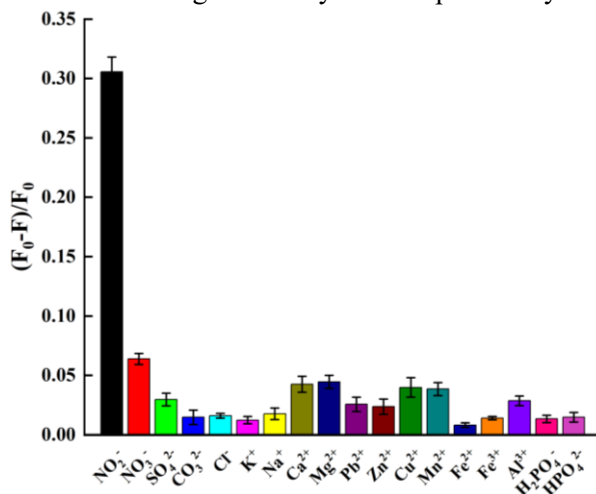


Figure 3-9 Fluorescence quenching efficiency $(F_0-F)/F_0$ of the Rh6G@MOF-5 system containing different potential interferences (NO_3^- , SO_4^{2-} , CO_3^{2-} , Cl^- , K^+ , Na^+ , Ca^{2+} , Mg^{2+} , Pb^{2+} , Zn^{2+} , Cu^{2+} , Mn^{2+} , Fe^{2+} , Fe^{3+} , Al^{3+} , H_2PO_4^- and HPO_4^{2-}). The concentration of NO_2^- is 10 μM . The concentration of all other interferences is 100 μM .

3.3.6. Application in meat products

To assess the potential feasibility of the synthesized LMOF fluorescent sensor in complex meat products, six kinds of meat samples, including sausage, bacon, ham, and spiced meat products, were tested for NO_2^- determination. In the light of the procedure of the standardization method (GB 5009.33–2016), the NO_2^- was extracted from the above samples, different concentrations of NO_2^- standard solution were added, and the same method was used to estimate the recovery. As shown in **Table 3-1**, the obtained results did not demonstrate a significant difference with standard addition concentrations. The nitrite contents of sausage, bacon, pork ham, beef ham, spiced beef, and spiced chicken were 7.83 mg/kg, 6.45 mg/kg, 9.03 mg/kg, 7.45 mg/kg, 7.66 mg/kg and 3.81 mg/kg, respectively. The calculated quantitative recoveries of nitrite ranged from 96.1% to 103.20% with RSDs of less than 4%, indicating the designed probe's high analytical accuracy, precision, and reliability for the real-time detection of NO_2^- in meat products. Therefore, the Rh6G@MOF-5 could be an efficient and potential novel nanosensor platform for the NO_2^- recognition assay in actual application.

Table 3-1 Nitrite Determination in meat product samples by Rh6G@MOF-5 sensor system.

Samples	Added (mg/kg)	Found (mg/kg)	RSD (% , n=3)	Recovery (% , n=3)
Sausages	0.00	7.83	3.29	–
	6.40	14.47	2.87	96.1
	13.80	21.79	0.49	101.1
Bacon	0.00	6.45	3.88	–
	6.40	13.45	0.81	101.5
	13.80	20.18	1.74	99.4
Pork ham	0.00	9.03	2.70	–
	6.40	16.15	1.29	103.2
	13.80	22.46	2.46	97.3
Beef ham	0.00	7.45	1.63	–
	6.40	14.54	2.39	102.8
	13.80	21.46	0.58	101.5
Spiced beef	0.00	7.66	3.21	–
	6.40	14.62	1.21	100.9
	13.80	21.03	0.59	96.9
Spiced chicken	0.00	3.81	3.29	–
	6.40	10.72	1.69	100.2
	13.80	17.27	2.06	97.6

3.4. Conclusion

In summary, a novel LMOF-based nanocomposite (Rh6G@MOF-5) has been successfully synthesized by encapsulating Rh6G within the porous crystalline structure of Zn(II)-MOF-5 using a straightforward solvothermal method. This probe can be conveniently prepared and works effectively under acidic conditions, showing rapid fluorescence responses toward NO_2^- . Importantly, the probe displayed outstanding sensitivity and selectivity towards NO_2^- over other substances. Additionally, Rh6G@MOF-5 was successfully used for the determination of NO_2^- in six types of meat samples with satisfactory results. Therefore, we believe that these unique properties of the Rh6G@MOF-5 nanoprobe will make it a superior tool for NO_2^- detection in a range of food monitoring applications.

4

**Chapter IV. Synchronous fluorescence
detection of nitrite in meat products based
on dual-emitting Rh6G@UiO-66-NH₂ and
its portable hydrogel test kit**

Short overview

Chapter 4 aimed to fabricate a ratiometric LMOF-based nanosensor (Rh6G@UIO-66-NH₂) by combining Zr-MOF (UIO-66-NH₂) with luminescent rhodamine 6G (Rh6G), distinguishing it from the single-emission nanosensor described in Chapter 3. We utilized synchronous fluorescence spectroscopy to establish a linear relationship between the fluorescence intensity ratio of the sensor ($I_{\text{Rh6G}}/I_{\text{MOF}}$) and various nitrite concentrations, thereby enabling application in analyzing real meat sample. Then, to expand the applications of solid-state Rh6G@UIO-66-NH₂ powders, we developed a portable LMOF-based gelatin hydrogel test kit. This kit was employed for the dual-mode detection of nitrite (colorimetric and fluorescent sensing). We achieved this by transferring the photo information of the hydrogel test kit into digital toner parameters.

The work from the present chapter was published on *Journal of Hazardous Materials*, as can be retrieved by:

Siyang Deng, Junmei Liu, Dong Han, Xinting Yang, Huan Liu, Chunhui Zhang, Christophe Blecker. (2024). Synchronous fluorescence detection of nitrite in meat products based on dual-emitting dye@MOF and its portable hydrogel test kit. *Journal of Hazardous Materials*, 463, 132898. <https://doi.org/10.1016/j.jhazmat.2023.132898>.

Abstract: A novel ratiometric fluorescent nanoprobe (Rh6G@UO-66-NH₂) was fabricated for efficient nitrite (NO₂⁻) detection in the present study. When NO₂⁻ was introduced, it interacted with the amino groups on the surface of Rh6G@UO-66-NH₂, forming diazonium salts that led to the quenching of blue fluorescence. With this strategy, a good linear relationship between NO₂⁻ concentration and the fluorescent intensity ratio of the nanoprobe in the range of 1–100 μM was established, with a detection limit of 0.021 μM. This dual-readout nanosensor was applied to analyze the concentration of NO₂⁻ in real meat samples, achieving satisfactory recovery rates of 94.72% to 104.52%, highlighting the practical potential of this method. Furthermore, a portable Gel/Rh6G@UO-66-NH₂ hydrogel test kit was constructed for on-spot dual-mode detection of NO₂⁻. This kit allows for convenient colorimetric analysis and fluorometric detection when used in conjunction with a smartphone. All the photos taken with the portable kit was converted into digital information using ImageJ software. It provides colorimetric and fluorescent visual detection of NO₂⁻ over a range of 0.1–1.5 mM, achieving a direct quantitative tool for NO₂⁻ identification. This methodology presents a promising strategy for NO₂⁻ detection and expands the application prospects for on-spot monitoring of food safety assessment.

Keywords: NO₂⁻, Rh6G@UO-66-NH₂, luminescent metal organic framework, dual-mode detection, on-spot visualization

4.1. Introduction

Nitrite (NO_2^-) has been used as an essential additive in processed meat products during the curing stage for centuries. It's valued for its ability to provide excellent color protection, act as an antioxidant, enhance flavor, and served as an antiseptic agent (Hou et al., 2020; Lee et al., 2017). Serving as a color retention agent, NO_2^- plays a pivotal role in producing rose-colored nitrosyl myoglobin by reacting with myoglobin, thereby enhancing the visual appeal of meat products (Yang et al., 2021). Additionally, due to its antiseptic and antioxidation properties, NO_2^- is used to extend the shelf life of meat products and inhibit the growth of pathogenic and putrefying bacteria (particularly *Clostridium botulinum*), thereby enhancing the safety of meat products (Hospital et al., 2016; Berardo et al., 2016; Skibsted, 2011). Nevertheless, it is worth noting that excessive consumption of NO_2^- can cause several adverse health effects, including methemoglobinemia, esophageal and gastric cancers, and so on (Waga et al., 2017; Rong et al., 2021; Berardi et al., 2021). While NO_2^- itself is not a carcinogen, it can degrade to nitric oxide inside the meat system, which can react with secondary amines to form carcinogenic and mutagenic N-nitrosamines in the stomach (Deng et al., 2021; Iammarino et al., 2020). It is worth noting that NO_2^- has been classified as a carcinogen listed by the World Health Organization (WHO) and is subject to restrictions by worldwide authorities (Yu et al., 2022). Therefore, it is of vital significance to accurately detect NO_2^- content in food systems.

Several classic NO_2^- detection techniques, such as electrochemistry, chromatography, and spectrophotometry, have been published to date (Li et al., 2016; Mako et al., 2020; Wang et al., 2017). However, these traditional analysis methods have their limitations, including the need for sophisticated and costly equipment, the requirement for professional and trained operators, and high testing costs. In contrast, fluorescence detection methods relying on metal organic frameworks (MOFs) are preferred for NO_2^- assays due to their simplicity, sensitivity, accuracy, and cost-effectiveness. MOFs are well-known for their representative and adjustable three-dimensional (3-D) network structure, appropriate specific areas, and highly uniform nanoscale cavities, which effectively enhance targets concentration and promote recognition and sensitivity of guest targets (Wu & Yan, 2018). As a subcategory of MOFs, dye@MOF, which consists of fluorescent dye molecules and fundamental MOF architecture, has gained prominence as a candidate for fluorescent sensing applications (Zhang et al., 2019). Dye@MOF can provide different responses and amplify emission ranges for targets based on the dual-emitting or multi-emitting fluorescence intensities of luminescent guest species and MOF (Zhang et al., 2020). Up until now, most reported MOFs-based nanoprobes have focused on single-emission sensors for NO_2^- detection. However, single-emission sensors may be susceptible to non-detection factors or environmental interference during the detection process (Hao et al., 2020; Huang et al., 2019; Wu & Yan, 2018). Hence, it is of significance to propose an efficient dye@MOF sensing platform to enhance accuracy and anti-interference based on ratiometric fluorescence.

As far as we know, synchronous fluorescence spectroscopy (SFS) can simultaneously scan excitation and emission wavelengths, and the corresponding SFS spectrum is obtained on the condition of maintaining a certain wavelength difference ($\Delta\lambda = \lambda_{em} - \lambda_{ex}$). Given that distinct fluorophores possess intrinsic λ_{ex} and λ_{em} , the collection of SFS provides a direct means of performing multicomponent analysis on complex systems by scanning multiple wavelengths. Therefore, it has proven to be a highly effective method for revealing the comprehensive chemical properties of samples (Genis et al., 2019; Samokhvalov, 2020). The outstanding advantages of SFS are that it can simplify spectra, reduce scattering light interferences and spectral overlap, and enhance selectivity to a large extent, compared to standard fluorescence spectroscopic methods (Włodarska et al., 2018; Dankowska & Kowalewski, 2019a). Therefore, the SFS spectrum holds great potential for simultaneously providing information about MOF and luminescent dye molecules when applied to the analysis of NO₂⁻ in a food matrix.

It is well known that the 3-D framework structure of numerous MOFs is vulnerable to collapse when exposed to hydrophilic media for a long period of time. However, previous studies have proved that the remarkable stability of UiO-66-NH₂ in an aqueous solution, including acidic solutions, as well as at high temperatures. This stability makes it particularly suitable for applications as sensors with the state of tiny particles or powders in sensing systems (Lu et al., 2016; Ma et al., 2019). To enhance practicality and convenience in applications, one of the ideal strategies is the creation of a cast and straightforward MOF thin film containing the as-synthesized dye@UiO-66-NH₂ powder and hydrogel. This approach can facilitate the efficient development of MOF-based composites. Hydrogel is currently recognized as a highly hydrophilic polymer chain with 3-D solid networks, facilitating the dispersion of MOF powders within it (Badsha et al., 2021; Javanbakht et al., 2020). In addition, this waterproof dye@MOF with high activity can also tune the properties of hydrogel as a reinforcing additive (Wang et al., 2019). Hydrogel is useful for detecting various targets in a variety of sensing applications, particularly in the development of visual detection platforms due to its minimal fluorescence emission and background color (Hou et al., 2019).

In response to the above-mentioned circumstance, this study establishes a novel fluorescent sensing nanoprobe based on fluorescein (Rh6G) and Zr-based MOF (UiO-66-NH₂), donated as Rh6G@UiO-66-NH₂. This was achieved by in situ encapsulating Rh6G molecules into the Zr-MOF architecture through solvothermal conditions (**Figure 4-1**). As expected, the synthesized Rh6G@UiO-66-NH₂ nanocomposite displays the dual emission characteristics due to energy transfer from Zr-based MOF to organic dye. Therefore, the SFS technique, coupled with the dye@MOF, was applied for the rapid detection of NO₂⁻ residues in meat product. As a self-calibrating fluorescence sensor, Rh6G@UiO-66-NH₂ can accurately, sensitively, and selectively detect NO₂⁻ by using the ratio of the fluorescence intensity I_{Rh6G}/I_{MOF} , which shows a clearly linear relationship with different concentrations of NO₂⁻. More significantly,

an available sensing platform was fabricated through immobilizing Rh6G@UiO-66-NH₂ on a gelatin hydrogel matrix, through which semi-quantitative detection of NO₂⁻ can be achieved by the naked eye based on fluorescent color under ultraviolet (UV) light. Accordingly, this study offered significant MOF nanocomposite and immobilized hydrogels for the quantification and visualization of NO₂⁻ residues in meat products.

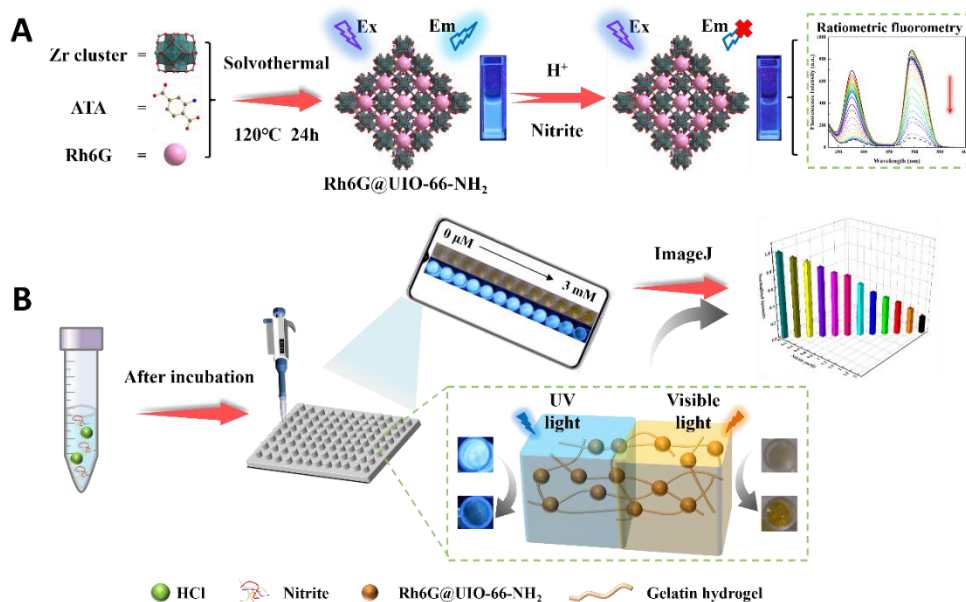


Figure 4-1 (A) Schematic illustration of the synthetic procedure for LMOF Rh6G@UiO-66-NH₂ nanoprobe and their sensing mechanism toward analytes of NO₂⁻. (B) Reaction process of the Gel/ Rh6G@UiO-66-NH₂ hydrogel test kit for NO₂⁻ assay.

4.2. Materials and Methods

4.2.1. Chemicals and Materials

Chemicals were procured from commercial sources. Zirconium chloride (ZrCl₄), 2-amino-terephthalic acid (ATA), N, N-dimethylformamide (DMF), acetic acid (AA), hydrochloric acid (HCl), potassium ferrocyanide, zinc acetate, and rhodamine 6G (Rh6G) were obtained from Aladdin reagent company (Shanghai, China). NO₂⁻ and aqueous solutions containing interference ions (NO₃⁻, SO₄²⁻, CO₃²⁻, Cl⁻, K⁺, Na⁺, Ca²⁺, Mg²⁺, Pb²⁺, Zn²⁺, Cu²⁺, Mn²⁺, Fe²⁺, Fe³⁺, Al³⁺, H₂PO₄⁻ and HPO₄²⁻) were sourced from Macklin Biochemical Co., Ltd. (Shanghai, China). All reagents and solvents were commercially available and used as received, without undergoing purification procedure.

4.2.2. Synthesis of UiO-66-NH₂

UiO-66-NH₂ was synthesized using a solvothermal method based on a previously reported approach with minor modifications (Katz et al., 2013). In summary, ZrCl₄ (0.5 mmol/L) and ATA (0.5 mmol/L) were dissolved in DMF (50 mL) at room temperature, and the resulting mixture underwent ultrasonic treatment for 20 min. Subsequently, 5 mL of acetic acid was added to the obtained solution, followed by an additional 10 min of sonication. The resulting mixture was then transferred to a 100 mL Teflon reactor and maintained at 120 °C for 24 h. After cooling to room temperature, the faint yellow powder obtained was centrifuged, washed with DMF and methanol (each wash repeated at least three times) to remove any remaining unreacted ligands and metals, and finally dried under vacuum at 120 °C for 12 h.

4.2.3. Synthesis of Rh6G@UiO-66-NH₂

According to the reported literature (Shi et al., 2021), UiO-66-NH₂ (100 mg) was dispersed in ethanol (20 mL) containing varying Rh6G concentrations (0, 0.5, 1.0, 1.5, and 2.0 mmol/L). Afterward, the mixture was transferred into a Teflon reactor (100 mL) after being ultrasonically treated for 5 min and heated at 120 °C for 24 h. Then, the resulting precipitates were centrifuged and washed multiple times with ethanol and ultrapure water until the supernatant became colorless, effectively removing excess Rh6G dye. The Rh6G@UiO-66-NH₂ powders were collected and dried in a vacuum at 120 °C for 12 h.

4.2.4. General procedure of nitrite determination using Rh6G@UiO-66-NH₂ sensor

To investigate the sensing system's response to NO₂⁻, a series of aqueous solutions with different NO₂⁻ concentrations (ranging from 0 to 3 mM) were prepared and tested them in an acidic environment at room temperature. To generate an initial Rh6G@UiO-66-NH₂ suspension, 5.0 mg of synthesized Rh6G@UiO-66-NH₂ powder was added to 20 mL of deionized water and stirred the mixture magnetically for 20 min. The resulting Rh6G@UiO-66-NH₂ stock suspension was stored in a refrigerator at 4 °C for further use. Next, 100 μL of Rh6G@UiO-66-NH₂ stock solution was mixed with 800 μL of HCl solution (0.05 M), and 100 μL different concentrations of a freshly prepared NO₂⁻ aqueous solution was incrementally added to the above mixture. The resulting mixed solution was thoroughly incubated at room temperature for 15 min, the reacted solution was transferred into a fluorescent cuvette before recording the synchronous fluorescence spectra with $\Delta\lambda = 60$ nm. In addition, each peak was measured more than three times, with the average values utilized to calculate the intensity ratio.

4.2.5 Selectivity and anti-interference test using Rh6G@UiO-66-NH₂ sensor

To examine the selectivity and anti-interference capability of the Rh6G@UiO-66-

NH₂ probe for NO₂⁻, the fluorescent spectra of the mixture of the Rh6G@UIO-66-NH₂ and the interfering ions were investigated in the absence and presence of NO₂⁻. Various anions and cations that coexist with NO₂⁻ in meat products (such as NO₃⁻, SO₄²⁻, CO₃²⁻, Cl⁻, K⁺, Na⁺, Ca²⁺, Mg²⁺, Pb²⁺, Zn²⁺, Cu²⁺, Mn²⁺, Fe²⁺, Fe³⁺, Al³⁺, H₂PO₄⁻, and HPO₄²⁻) were introduced into the detection system as interference, replacing or coexisting with the NO₂⁻ standard solution. Briefly, the procedure involved mixing 100 μL of the selected ion (1 mM) with 100 μL of the Rh6G@UIO-66-NH₂ suspension (0.25 mg/mL) in a test tube. The mixture was then combined with 800 μL of a 0.05 M HCl solution and allowed to react at room temperature for 15 min. Simultaneously, an identical solution described above was prepared, followed by the sequential addition of 100 μL of NO₂⁻ (100 μM) into the test tube, again allowing it to react for 15 min at room temperature. Subsequently, all prepared solutions were transferred to a quartz cuvette for recording fluorescence spectra. And the fluorescence intensity was recorded three times to ensure the stability and reliability of the experimental results.

4.2.6 Analysis of real samples using Rh6G@UIO-66-NH₂ sensor

Five representative categories of commercial meat products, including pork, beef, and chicken, were purchased from a local supermarket (Beijing, China). All meat samples were collected to verify the feasibility of the self-calibration fluorescence sensor. It is worth mentioning that the NO₂⁻ was processed and extracted from meat product samples in accordance with the China national standard (GB 5009.33–2016). And the detailed extraction procedure was referred to our previous report (Deng et al., 2022). In brief, 5.0 g of each of the following: sausage, bacon, ham, stewed beef, and braised chicken, were weighed and placed into separate 250 mL glass conical flask with stoppers. To each flask, 12.5 mL of saturated borax solution (50 g/L) and approximately 150 mL of distilled water at 70 °C were added. The conical flasks were then heated in a boiling water bath for 15 min before being cooled to room temperature. To transfer the extracted liquid, 5 mL of potassium ferrocyanide (106 g/L), 5 mL of zinc acetate (220 g/L), and distilled water were added sequentially, followed by thorough shaking. The resulting homogenate was left to stand for 30 min and then filtered using filter paper to remove insoluble and unwanted substances. Finally, 30 mL of the initial filtrate was discarded, and the remaining filtrate was preserved in a refrigerator at 4 °C for future use. The real meat product samples were used to measure NO₂⁻ by the fluorescence sensor Rh6G@UIO-66-NH₂, the same procedures and conditions were followed as 3.2.4. However, the pure NO₂⁻ solution was replaced by an equal volume of meat product extraction spiked with different concentrations of NO₂⁻.

4.2.7 Preparation of portable test kit using Rh6G@UiO-66-NH₂ immobilized gelatin hydrogels

Generally, 1.0 g of gelatin powder was dissolved in 9 mL of deionized water at

60 °C, and then 10 mL of Rh6G@UiO-66-NH₂ suspension (0.5 mg/mL) was added to the above solution. The mixture was subsequently cooled to 40 °C and stirred thoroughly to ensure uniformity. Then, 150 µL of the prepared solution was carefully transferred into a 96-well microplate to form the gelatin hydrogel. The hydrogel was then stored at room temperature (25 °C) for future use.

4.2.8 Nitrite determination using Gel/Rh6G@UiO-66-NH₂ hydrogel test kit

For detecting NO₂⁻, 800 µL of HCl solution (0.05 mol/L) and 100 µL of different concentrations of NO₂⁻ solution were mixed together, and then 150 µL of the above reaction solution was introduced to the gelatin hydrogel kit for incubation for 30 min. Then, the color change of the gelatin hydrogel was captured using a smartphone camera. To ensure the stability of the light source during image capture, white light bulbs were incorporated to simulate visible light, along with a 365 nm UV lamp for simulating UV light in the darkroom. And a fixed angle and position was selected for image capture to maximize image quality and minimize background interference. Under the predetermined illumination of visible and ultraviolet lights, the color of the Gel/Rh6G@UiO-66-NH₂ test kit was captured using a smartphone, and then the images were analyzed by ImageJ software. All measurements were conducted in triplicate.

4.2.9 Selectivity and anti-interference using Gel/Rh6G@UiO-66-NH₂ hydrogel test kit

The selectivity and anti-interference capability of the Gel/Rh6G@UiO-66-NH₂ test kit for NO₂⁻ were investigated by introducing the same interfering ions that has been discussed in section 4.2.5. These ions were introduced both in the absence and presence of NO₂⁻ into the Gel/Rh6G@UiO-66-NH₂ test kit. To carry out the experiment, a mixture of 800 µL of HCl solution (0.05 mol/L) and 100 µL of the selected ion (1 mM) solution were prepared. Simultaneously, an identical solution described above was prepared, and then 100 µL of NO₂⁻ (100 µM) was sequentially added into the test tube. Then, 150 µL of the resulting reaction solution was introduced to the Gel/Rh6G@UiO-66-NH₂ hydrogel test kit and incubated for 30 min at room temperature. All test kit images were captured under visible and ultraviolet light irradiation, and the color information in these images was analyzed using a smartphone. All measurements were performed in triplicate.

4.2.10 Apparatus

Both 3-D fluorescence spectra and synchronous fluorescence spectra were collected using a Hitachi F-7000 fluorescence spectrophotometer (Tokyo, Japan). The acquisition parameters for 3-D fluorescence spectroscopy were as follows: The excitation wavelength range was changed from 200 nm to 600 nm, and emission wavelength was changed from 200 nm to 700 nm in steps of 5 nm, respectively. The

slit width of excitation and emission was set to 5 nm. The scanning rate and detector voltage were 30000 nm/min and 500 V, respectively. For synchronous fluorescence spectra, excitation and emission were collected simultaneously, with the photoexcitation wavelength (λ_{Ex}) ranging from 200 nm to 600 nm in 1 nm increments. The wavelength offsets ($\Delta\lambda = \lambda_{Em} - \lambda_{Ex}$) was set at 60 nm. Slit widths for both excitation and emission were maintained at 5 nm. The scan speed was set at 1200 nm/min, and the PMT detector voltage (V) was adjusted to medium (700 V). To ensure accuracy and minimize measurement errors, fluorescence measurements were conducted in triplicate for each sample, and subsequent analysis used the average of these three measurements. UV-vis spectra were recorded by a UV 3600i Plus spectrophotometer (Shimadzu, Japan). For powder X-ray diffraction (PXRD) patterns, measurements were conducted using the Panalytical X-ray Diffractometer Smartlab-9kW (Tokyo, Japan) with Cu K α radiation ($\lambda = 1.5406 \text{ \AA}$, 40kV, 250mA). Fourier transform infrared (FTIR) spectra were obtained within the 4000–400 cm^{-1} region using a Thermo Scientific Nicolet IS5 FTIR spectrophotometer. Scanning electron microscopy (SEM) images were captured using the FEI Inspect F50 scanning electron microscope. Physical adsorption property measurement was carried out using a porosity analyzer Autosorb-iQ2-MP (Quantachrome, USA) with N₂ adsorption analysis.

4.3. Results and Discussion

4.3.1 Characterizations of Rh6G@UiO-66-NH₂

The crystal structures of both the as-prepared UiO-66-NH₂ and Rh6G@UiO-66-NH₂ were characterized based on the PXRD patterns (**Figure 4-2A**). The characteristic peaks of the synthesized UiO-66-NH₂ at 2θ angles of 7.30 °, 8.42 °, and 25.62 ° closely matched well with the simulated ones, confirming the successful synthesis and high crystallinity of the desired sample (Aghili et al., 2020). Upon adsorption of different concentrations of fluorescein Rh6G, these analogous PXRD patterns showed little change in the crystalline framework (**Figure 4-2B**). Simultaneously, no characteristic diffraction peaks of Rh6G were observed in Rh6G@UiO-66-NH₂, demonstrating that the absorption of Rh6G presumably had a negligible effect on the UiO-66-NH₂ lattice. Rh6G appeared to be encapsulated or embedded into the cavity rather than physically aggregating on the surface of the UiO-66-NH₂ crystal due to the favorable dispersion of Rh6G and the unique porous framework of the MOF (Shi et al., 2021).

Afterward, FTIR spectra of UiO-66-NH₂ and Rh6G@UiO-66-NH₂ were recorded to characterize their molecular structure, as shown in **Figure 4-2C** and **4-2D**. In the UiO-66-NH₂ spectra (**Figure 4-2C**), two characteristic peaks at 483 cm^{-1} and 665 cm^{-1} were assigned to the O–H and C–H vibrations of UiO-66-NH₂, and a peak at 770 cm^{-1} corresponded to the stretching vibration of Zr–O bonds. Additionally, peaks at

1387 cm⁻¹, 1571 cm⁻¹ and 1655 cm⁻¹ were assigned to the C=O stretching vibration of the carboxyl group, and the peaks at 3365 and 3431 cm⁻¹ corresponded to the symmetric and asymmetric N-H vibrations of the amino group from the organic ligand ATA (Aghili et al., 2021; Cao et al., 2022). Similar results were observed in the Rh6G@UiO-66-NH₂ spectra, except for the appearance of the C=O stretching vibration peak at 1655 cm⁻¹, which was attributed to anchored Rh6G molecules on UiO-66-NH₂. Moreover, no distinctive peaks corresponding to Rh6G were detected in the Rh6G@UiO-66-NH₂ nanomaterial, indicating that the majority of Rh6G molecules were encapsulated within the pores of UiO-66-NH₂, with their vibrations of Rh6G impeded by the 3-D structure of UiO-66-NH₂ (Gao et al., 2018). There was no visible difference in FT-IR spectra among Rh6G@UiO-66-NH₂ samples with different concentrations, further indicating the minimal influence of the organic dye on the crystal structure of UiO-66-NH₂.

The morphological and structural characterizations of UiO-66-NH₂ and Rh6G@UiO-66-NH₂ were illustrated through SEM images. In **Figure 4-2E** and **4-2F**, both UiO-66-NH₂ and Rh6G@UiO-66-NH₂ nanomaterials exhibited irregular octahedral particles, each approximately 75 nm in size, with no apparent differences in morphology observed before and after Rh6G encapsulation.

Comparing the porosity of UiO-66-NH₂ before and after encapsulating fluorescein Rh6G can help verify their permanent porosities and functionalization. The nitrogen (N₂) adsorption-desorption isotherms of UiO-66-NH₂ and synthesized Rh6G@UiO-66-NH₂ were recorded at 77 K, and the results of porosity analysis and surface area are presented in **Figure 4-2G**. The adsorption isotherms clearly exhibited a sharp increase in N₂ adsorption at very low relative pressures, followed by a gradual rise up to high relative pressures, while a small hysteresis observed at relatively high pressures. Consequently, it can be deduced that both UiO-66-NH₂ and Rh6G@UiO-66-NH₂ displayed analogous type I isotherms, indicating the existence of abundant micropores and mesopores (Jiao et al., 2023; Shi et al., 2021). Moreover, the calculated BET surface area of Rh6G@UiO-66-NH₂ was 292.752 m²/g, which is considerably smaller than that of pristine UiO-66-NH₂ (461.064 m²/g). This further confirms the successful synthesis, which is consistent with previous literatures (Jiao et al., 2023; Li et al., 2023). The above results indicated that the microporous channels of the UiO-66-NH₂ support were loaded with Rh6G dyes and may be partly unblocked after encapsulation. These measurements collectively confirm the successful incorporation of Rh6G fluorescein into UiO-66-NH₂ while preserving the skeleton structure and crystalline of UiO-66-NH₂.

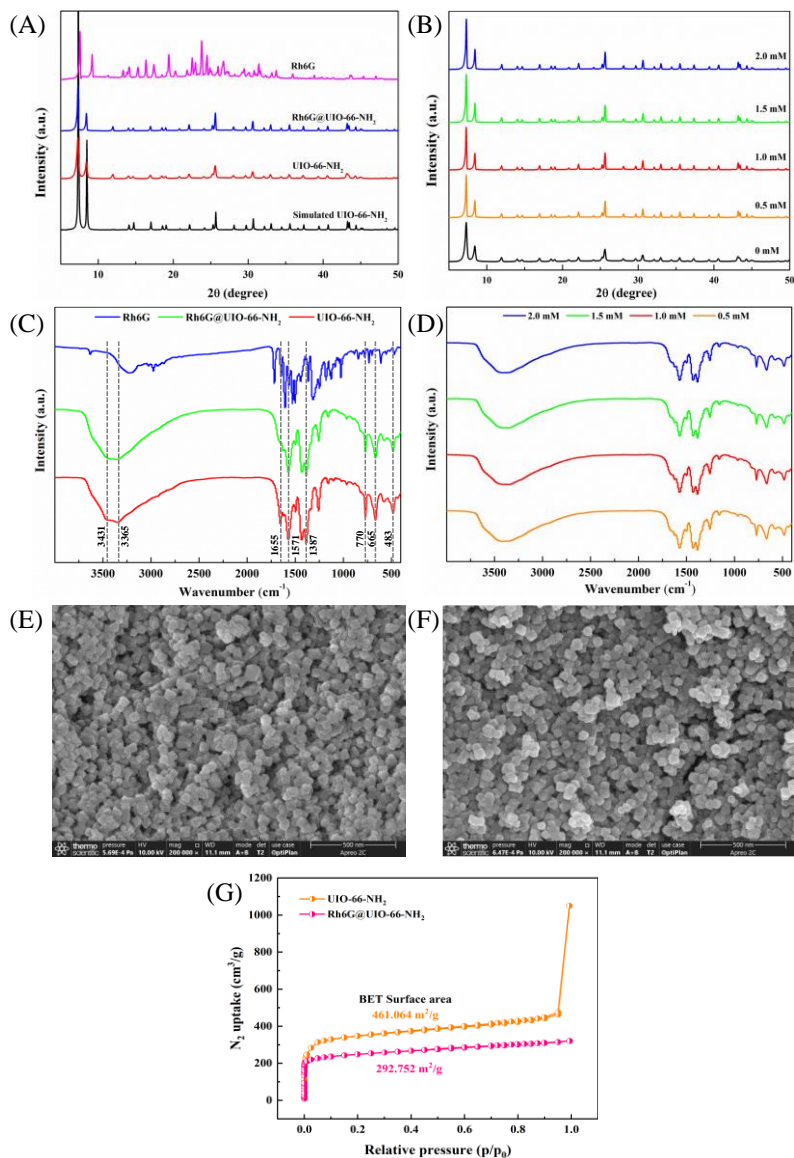


Figure 4-2 (A) The PXRD patterns for the simulated UIO-66-NH₂ (black curve), UIO-66-NH₂ (red curve), Rh6G@UIO-66-NH₂ (blue curve), and Rh6G (pink curve). (B) The PXRD patterns of Rh6G@UIO-66-NH₂ nanoparticles with different Rh6G concentrations. (C) The FT-IR patterns of UIO-66-NH₂ (red curve), Rh6G@UIO-66-NH₂ (green curve), and Rh6G (blue curve). (D) The FT-IR patterns of Rh6G@UIO-66-NH₂ nanoparticles with different Rh6G concentrations. SEM images of synthesized (E) UIO-66-NH₂ and (F) Rh6G@UIO-66-NH₂. (G) Nitrogen (N₂) adsorption-desorption isotherms from UIO-66-NH₂ and Rh6G@UIO-66-NH₂.

4.3.2 Photophysical properties of Rh6G@UiO-66-NH₂

In order to investigate the influence of Rh6G dye on the optical properties of Rh6G@UiO-66-NH₂ nanocomposites, the 3D front-face fluorescence spectra of UiO-66-NH₂ (Figure 4-3A) and Rh6G@UiO-66-NH₂ (Figure 4-3B to 4-3E) were determined. As shown in Figure 4-3, UiO-66-NH₂ exhibited a single Excitation/Emission (Ex/Em) peak located at around 370 nm/455 nm, representing the blue emission band attributed to the π - π^* transition of the ATA ligand. However, in the fluorescent contour map of Rh6G@UiO-66-NH₂, apart from the MOF peak, another Ex/Em peak at 520 nm/545 nm corresponding to the characteristic fluorescence of Rh6G was also evident. This is noteworthy because in the solid state of Rh6G dye, fluorescence emission is typically absent due to the aggregation-caused quenching (ACQ) phenomenon (Figure 4-4). This superior structure of Rh6G@UiO-66-NH₂ inhibits nonradiative energy transfer commonly observed in aggregated dye molecules, thereby preventing quenching of the dye emission (Guo et al., 2019a). These results further indicate that Rh6G dye molecules were successfully encapsulated without sacrificing their native luminescent properties (Yoo et al., 2019). Moreover, the synthesized UiO-66-NH₂ powder exhibited a faint yellow color. Visually, the color of Rh6G@UiO-66-NH₂ transitioned from light pink to pink by the naked eye with increasing amount of Rh6G molecules (ranging from 0.5 mM to 2.0 mM). This color change corresponded well with the loading of a greater number of Rh6G dye molecules into the initial UiO-66-NH₂ structure.

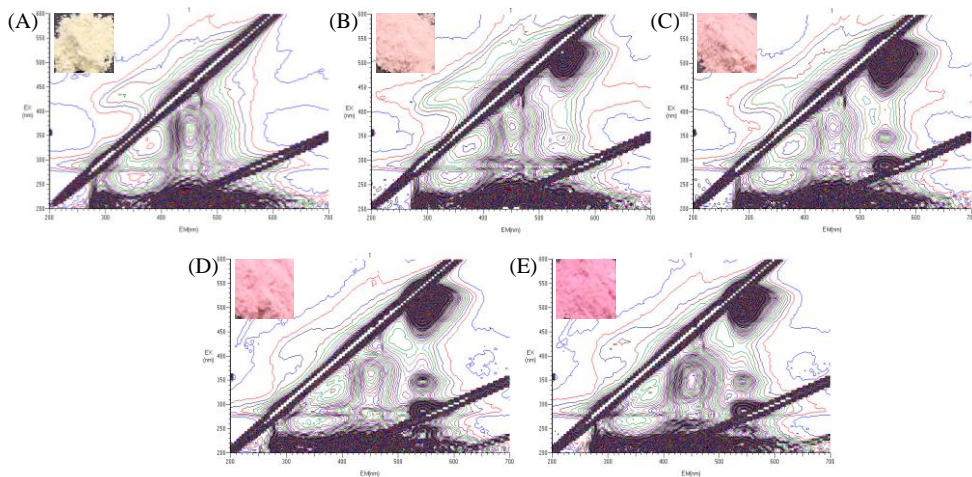


Figure 4-3 The 3D-fluorescence spectra of Rh6G@UiO-66-NH₂ solid powders with (A) 0 mM Rh6G, (B) 0.5 mM Rh6G, (C) 1.0 mM Rh6G, (D) 1.5 mM Rh6G, and (E) 2.0 mM Rh6G in aqueous solution. Inset shows a photo of the corresponding UiO-66-NH₂ and Rh6G@UiO-66-NH₂ solid powders.

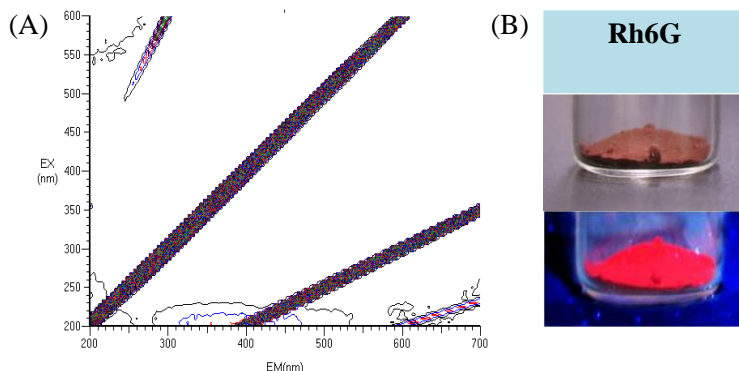


Figure 4-4 (A) The 3D-fluorescence spectra of Rh6G solid powder. (B) photographs of Rh6G solid powder under visual light and 365 nm UV light.

According to the 3-D fluorescence spectra of nanocomposites (shown in **Figure 4-3**), drawing a straight line (defined as: $X_{em} = Y_{ex} + \Delta\lambda$, where $\Delta\lambda = \lambda_{em} - \lambda_{ex}$) on the 3-D fluorescence spectrum can simulate the result of synchronous fluorescence scanning. The $\Delta\lambda$ value of synchronous fluorescence can theoretically be predicted from the 3-D fluorescence spectra. In this study, the optimal $\Delta\lambda$ condition was set at 60 nm and employed in the following analysis. Both 3-D and synchronous fluorescence spectroscopy can obtain the information on multiple fluorescent substances in the nanocomposites simultaneously. Synchronous fluorescence spectroscopy can simplify spectral analysis by reducing the influence of light scattering and saved detection time, taking only a few seconds for each scan, however 3-D fluorescence spectroscopy needs nearly 5 minutes for each scanning. As displayed in **Figure 4-5A**, synchronous fluorescence spectra of Rh6G@UiO-66-NH₂ samples with different Rh6G concentrations simultaneously provide information on organic dyes and MOF as well. The Rh6G@UiO-66-NH₂ nanocomposite with 1.0 mM Rh6G exhibited the highest peak intensity at an excitation wavelength near 495 nm among the tested treatments (**Figure 4-5B**). This observation suggests that the appropriate amounts of dye molecules can be accommodated, and Rh6G molecules are gradually isolated within the cages of UiO-66-NH₂, maintaining a monodisperse state. Consequently, concentration-dependent fluorescence enhancement is observed. However, this status was disrupted when the amount of Rh6G dyes exceeded 1.0 mM. Obviously, luminescence quenching occurs, possibly due to non-radiative pathways resulting from the short-range interactions among organic dye molecules. This leads to the occurrence of the ACQ effect within the MOF cages once again (Ye et al., 2019). Consequently, a concentration of 1.0 mM Rh6G@UiO-66-NH₂ was chosen to investigate its sensing performance for optimal ratiometric detection of NO₂⁻. This concentration was selected because it provides an abundance of active sites while

simultaneously safeguarding Rh6G against potential ACQ, making it suitable for subsequent experiments.

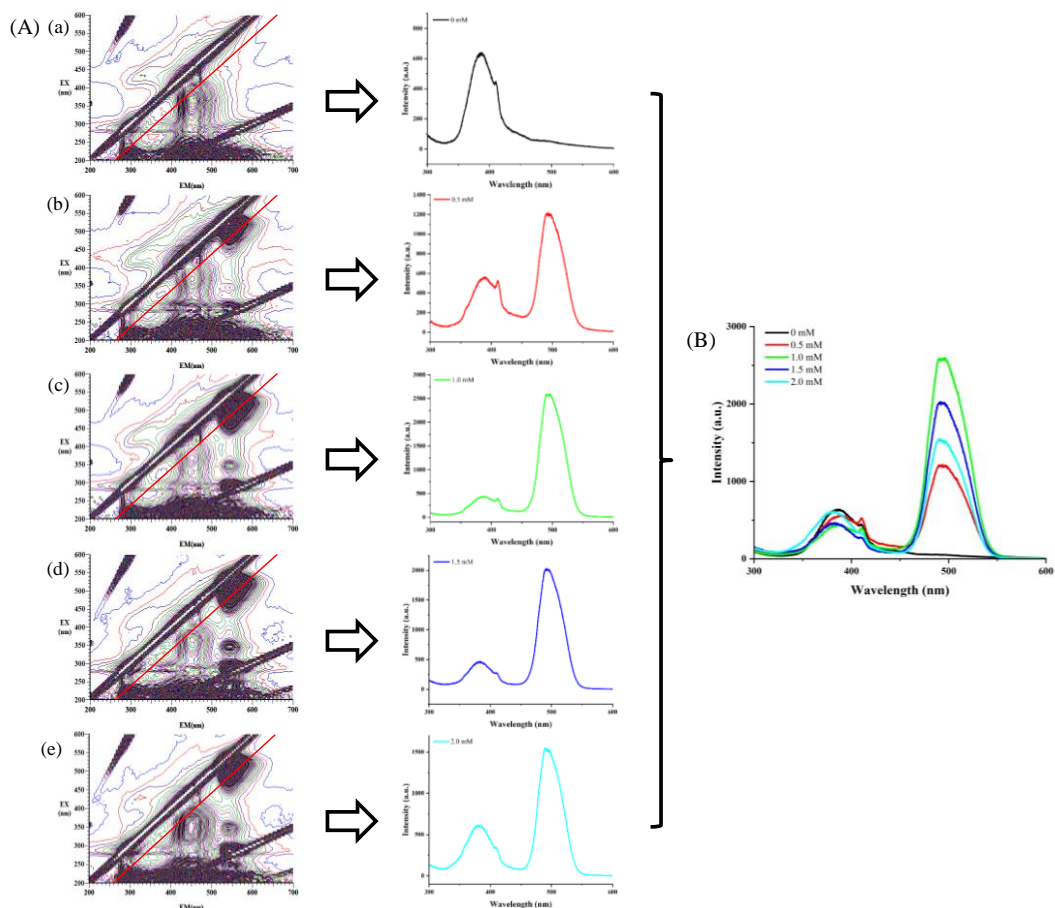


Figure 4-5 (A) The 3-D fluorescence spectra and (B) synchronous fluorescence spectroscopy of Rh6G@UiO-66-NH₂ sample ($\Delta\lambda = 60$ nm).

As depicted in **Figure 4-6**, the UV-vis diffuse reflectance spectrum of the Rh6G@UiO-66-NH₂ solid exhibited two distinctive absorption peaks. On the one hand, there was a prominent absorption band ranging from 300 nm to 455 nm, with an absorption peak at 378 nm, attributed to UiO-66-NH₂. This was confirmed by the UV-vis spectrum indicated by the black line, which is associated with the $\pi \rightarrow \pi^*$ electronic transition of the aromatic ring. On the other hand, a characteristic absorption peak of Rh6G appeared at 534 nm, within the range of 458–583 nm after adsorption. This demonstrated a noticeable red shift compared to the absorption peak

of the Rh6G solution, indicating the confinement effect of the MOF framework. Taken together, the above results confirmed the successful absorption of fluorescein Rh6G onto the as-prepared UiO-66-NH₂ powder.

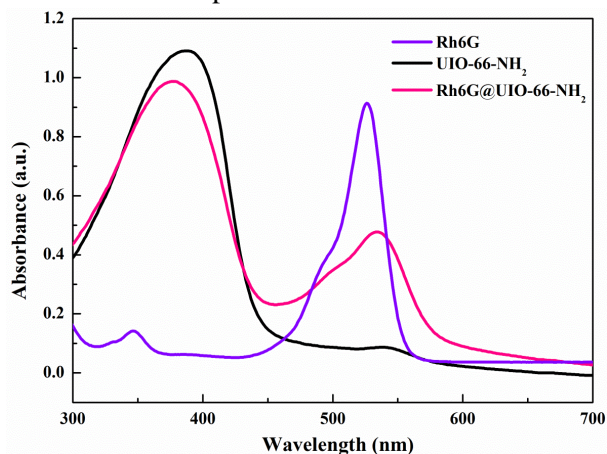


Figure 4-6 UV-vis absorption spectra of Rh6G, UiO-66-NH₂, and Rh6G@UiO-66-NH₂.

4.3.3 Optimization of detection condition

Moreover, key experimental parameters, containing acidity and reaction time, were optimized for the Rh6G@UiO-66-NH₂ sensing system to achieve the optimal signal response. It can be seen in **Figure 4-7A** that the concentration of HCl in the nanoprobe suspension was varied from 0.01 M to 1.0 M. The fluorescence intensities of both peak MOF (Ex wavelength at 378 nm) and Rh6G (Ex wavelength at 495 nm) reached their maximum values when the HCl concentration was set at 0.05 M. This phenomenon can be attributed to the fact that the rhodamine derivative exhibits a xanthen structure with strong fluorescence emission in such an appropriate acid medium (Zhang, et al., 2016a). However, when the HCl concentration exceeded 0.05 M, the fluorescence intensity of peak UiO-66-NH₂ gradually decreased with increasing acidity. The decline may be attributed to the neutralization of the amino groups of MOFs by hydrogen ions in strong acid media, which play a key role in this sensing system. Therefore, for the sake of experimental convenience, 0.05 M of HCl was chosen as the optimal acid condition for the subsequent studies.

Accordingly, to enhance the efficiency of Rh6G@UiO-66-NH₂ in responding to NO₂⁻, the influence of reaction time was also investigated. The relationship between the fluorescence intensity ratio of Rh6G@UiO-66-NH₂ ($I_{\text{Rh6G}}/I_{\text{MOF}}$) and response time after adding NO₂⁻ (100 μM) is displayed in **Figure 4-7B**. The results show that the response value $I_{\text{Rh6G}}/I_{\text{MOF}}$ initially increased as time passed. The change in $I_{\text{Rh6G}}/I_{\text{MOF}}$ of the sensing system tended to stabilize after a response time of 15 min, indicating that the reaction efficiently and rapidly reached completion. Thus, 15 min was chosen as the optimal reaction time between Rh6G@UiO-66-NH₂ and NO₂⁻ for further

research.

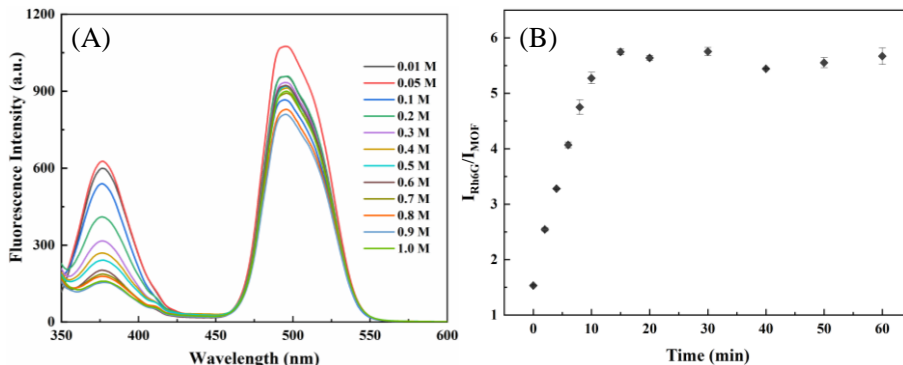


Figure 4-7 (A) Effect of HCl concentration (H^+) on fluorescent intensity of Rh6G@UiO-66-NH₂-based sensor. (B) Fluorescence intensity of Rh6G@UiO-66-NH₂ suspension after reaction with nitrite for different times.

4.3.4 Establishment of Rh6G@UiO-66-NH₂-based sensor for nitrite

Normally, conventional single-signal fluorescence sensing is easily affected by external conditions and inefficient in detecting NO_2^- in complex samples or aqueous solutions (Yoo et al., 2019). To address this limitation, a self-calibrated fluorescence sensing platform based on the dual independent fluorescence emission peaks of dye@MOF for ratiometric detection was employed. This approach reduces interference from the external environment and amplifies signal readouts, enabling more sensitive detection. Under optimized conditions, the dual fluorescence response of the Rh6G@UiO-66-NH₂ sensing system was used to detect a range of NO_2^- concentrations (0–1000 μ M) (**Figure 4-8**). As the NO_2^- concentration increased, the fluorescence signal of UiO-66-NH₂ (Ex wavelength at 378 nm) was noticeably quenched, along with a decreasing trend in Rh6G fluorescence at 495 nm (**Figure 4-8A**). Besides, the characteristic emission of UiO-66-NH₂ was more significantly quenched than that of Rh6G when low amounts of NO_2^- were added (0–100 μ M).

Figure 4-8B demonstrated a strong linear relationship between the fluorescence intensity ratio of the sensor (I_{Rh6G}/I_{MOF}) and low concentrations of NO_2^- , ranging from 1 μ M to 100 μ M, described by the first-order linear equation $I_{Rh6G}/I_{MOF} = 1.21 + 4.68 \times 10^{-2} C_1$ (with a correlation coefficient $R^2 = 0.983$). The limit of detection (LOD) for NO_2^- using Rh6G@UiO-66-NH₂ was calculated to be 0.021 μ M, following the formula $3\sigma/s$ (where σ represents the standard deviation of blank measurements, and s is the slope of the linear calibration plot). This LOD is significantly lower than the maximum allowable concentration of NO_2^- in meat products (Zhang et al., 2016). Significantly, as depicted in the insert of **Figure 4-8A**, a distinct change in fluorescence color is observable following the quenching process, enabling the visual

detection of NO_2^- .

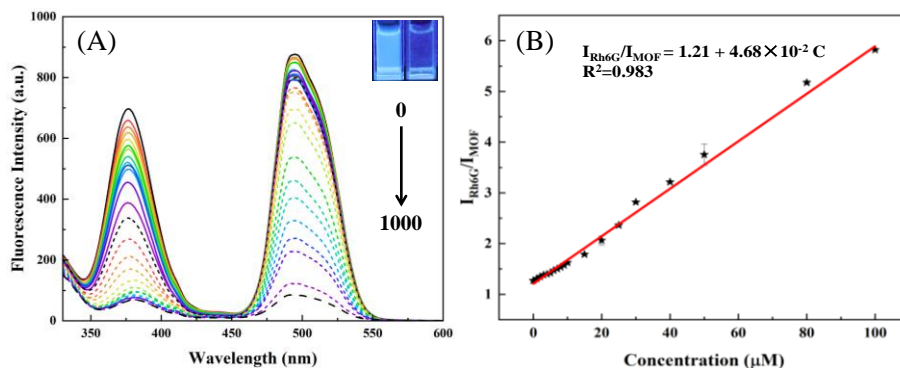


Figure 4-8 (A) Synchronous fluorescence spectra of Rh6G@UIO-66-NH₂ suspension toward different concentration of NO_2^- (0-1000 μM). Inset images shows the corresponding photos of Rh6G@UIO-66-NH₂ in the absence (left) and presence (right) of NO_2^- ion under 365 nm UV light. (B) The trends of fluorescent intensity ratio $I_{264\text{nm}}/I_{440\text{nm}}$ with different concentration of nitrite.

4.3.5. Selectivity and Anti-interference performance of Rh6G@UIO-66-NH₂ toward nitrite

To assess the selectivity and anti-interference performance of the Rh6G@UIO-66-NH₂ sensing system toward NO_2^- , the impact of various interfering substances on its fluorescence responses was explored. Then, Rh6G@UIO-66-NH₂ was mixed separately with solutions containing NO_2^- and other interfering ions, with NO_2^- at a concentration of 100 μM while other interfering substances were fixed at 1 mM. The fluorescent intensity ratio of the nanosensor is displayed in **Figure 4-9**. In the presence of NO_2^- under 0.05 M HCl, the fluorescence intensity ratio ($I_{\text{Rh6G}}/I_{\text{MOF}}$) of Rh6G@UIO-66-NH₂ significantly increased to 5.60. However, treatment with other co-existing interfering ions, including NO_3^- , SO_4^{2-} , CO_3^{2-} , Cl^- , Cr^- , K^+ , Na^+ , Ca^{2+} , Mg^{2+} , Pb^{2+} , Zn^{2+} , Cu^{2+} , Mn^{2+} , Fe^{2+} , Fe^{3+} , Al^{3+} , H_2PO_4^- , and HPO_4^{2-} , had no notable impact on this dual emission nanosensor. This lack of interference is attributed to the specific interaction between the amino group from Rh6G@UIO-66-NH₂ and NO_2^- . Furthermore, the sensor's resistance to interference is investigated, which is another key criterion for evaluating its performance in practical applications. To evaluate the anti-interference performance, the above-mentioned interfering ions were added to the Rh6G@UIO-66-NH₂ sensing systems designed for NO_2^- detection, thereby conducting a competition experiment. As shown in **Figure 4-9B**, all groups exhibited a distinct enhancement in the fluorescence intensity ratio. This indicates that the influence of these interferents on the NO_2^- detection using the Rh6G@UIO-66-NH₂ detecting platform can be considered negligible. In summary, the above consequences demonstrate that the fabricated nanocomposite meets the sensitivity and selectivity

requirements for monitoring NO₂⁻ in meat products. Furthermore, the facile and efficient preparation procedure introduces innovative concepts for developing new nanosensors.

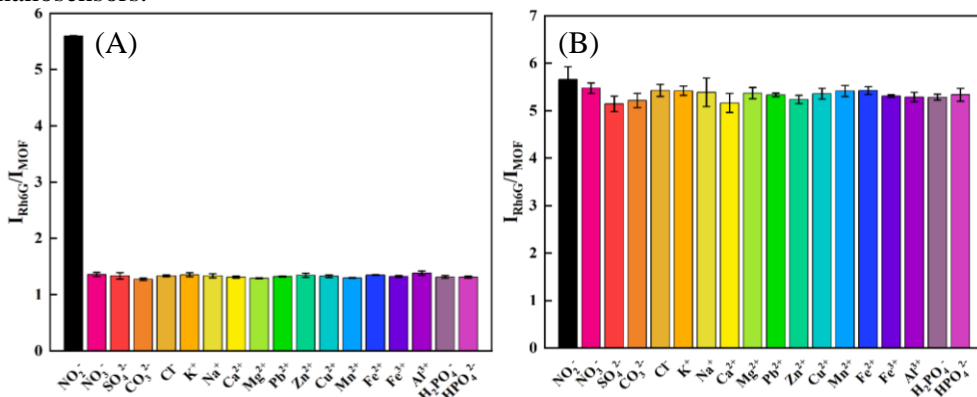


Figure 4-9 (A) The selectivity and (B) specificity of proposed sensing platform. The concentration of NO₂⁻ is 100 μM and the concentration of all other interfering substances are ten times higher than NO₂⁻.

4.3.6. Application in real samples

To further verify the practicability and feasibility of the ratiometric fluorescence nanoprobe for the real sample detection, the proposed method based on the Rh6G@UiO-66-NH₂ was applied to determine NO₂⁻ contents in five commercially available meat samples. The recovery rate was calculated by the standard addition method, and the results are listed in **Table 4-1**. The detected NO₂⁻ concentration in sausage, bacon, ham, stewed beef, and braised chicken were found to be 2.86 mg/kg, 2.43 mg/kg, 3.43 mg/kg, 4.53 mg/kg, and 3.25 mg/kg, respectively. Subsequently, the NO₂⁻ standard solution was introduced to the samples and analyzed them. The recovery tests yielded results in the range of 94.72%–104.52%, with relative standard deviations (RSDs) of less than 4%. These outcomes demonstrate the excellent analytical accuracy, precision, and reliability of the designed probe for detecting NO₂⁻ in meat products. Therefore, the proposed Rh6G@UiO-66-NH₂ nanoprobe holds significant potential as a valuable and efficient novel tool for rapid NO₂⁻ detection in practical applications and food safety assessment.

Table 4-1 Nitrite determination in meat product samples by Rh6G@UIO-66-NH₂ sensor system.

Samples	Added (mg/kg)	Found (mg/kg)	RSD (% , n=3)	Recovery (% , n=3)
Sausages	0.00	2.86	1.32	–
	2.10	4.81	0.42	96.97
	4.20	7.17	2.61	101.56
Bacon	0.00	2.43	2.83	–
	2.10	4.30	1.61	94.92
	4.20	6.68	2.31	100.75
Ham	0.00	3.43	1.54	–
	2.10	5.34	2.11	96.56
	4.20	7.46	2.60	97.77
Stewed beef	0.00	4.53	1.63	–
	2.10	6.93	0.22	104.52
	4.20	8.67	3.26	99.31
Braised chicken	0.00	3.25	0.35	–
	2.10	5.42	2.31	101.31
	4.20	7.39	1.99	99.19

4.3.7. Precise sensing of nitrite by a portable test kit.

To broaden the practical application of Rh6G@UIO-66-NH₂ powders, it is convenient to develop a portable hydrogel test kit that can be used for on-site screening of NO₂⁻ to ensure food security and monitor environmental pollution. Gelatin (Gel), derived from the partial hydrolysis of collagen in animal bones and leathers, is an amphoteric biopolymer known for its admirable properties, including good biocompatibility, biodegradability, and nontoxicity (Abou-Zeid et al., 2019). Gelatin itself possesses abundant hydroxyl, amino, and carboxyl functional groups, which make gelation and functionalization easy, facilitating direct chemical reactions between Gel and dye@MOF without the need for additional polymers to form a stable hydrogel compound (Njaramba et al., 2023; Yang et al., 2021). Hence, Gelatin is selected as a suitable carrier for fabricating a stimuli-responsive hydrogel test kit in this work. The Gel/Rh6G@UIO-66-NH₂ hydrogel compounds were constructed by immobilizing Rh6G@UIO-66-NH₂ into Gel hydrogel, and a commercial microplate was manufactured to create Gel/Rh6G@UIO-66-NH₂ hydrogel arrays, which could serve as a sensing platform for the visualized and fluorometric detection of NO₂⁻. Subsequently, to meet the need of on-site analysis, a visual NO₂⁻ detection method was developed by integrating the Gel/Rh6G@UIO-66-NH₂ hydrogel test kit with a smartphone. This was made possible by leveraging the powerful capabilities of the smartphone's digital camera program and its computational capabilities.

For precise sensing of NO₂⁻, the essential 0.05 M HCl was first introduced to

various concentrations of NO₂⁻, then dropped above cocktail solution of HCl and NO₂⁻ onto the Gel/Rh6G@UiO-66-NH₂ hydrogel test kit (the detailed experimental procedure is depicted in **Figure 4-1B**). As revealed in **Figure 4-10A**, the colors of the as-prepared hydrogel matrices varied depending on the NO₂⁻ ion concentrations. Their visible colors changed from pale yellow to golden yellow, and their fluorescence colors changed from bright to dark in a distinct gradient as the NO₂⁻ concentration increased. Such color-gradient changes are consistent with the results obtained from the Rh6G@UiO-66-NH₂ suspension in the presence of NO₂⁻ at different concentration, reflecting that gelatin hydrogel does not affect the reaction of NO₂⁻ with amino group of the Rh6G@UiO-66-NH₂ nanoprobe. After the colorimetric reaction, images of the kit were captured using the built-in cameras of smartphones to identify the visualized and fluorescence color response of Gel/Rh6G@UiO-66-NH₂ hydrogels (**Figure 4-10B**). Through an image processing program, optical image information was directly translated into tonal parameters to realize quantitative NO₂⁻ detection. As displayed in **Figure 4-10B**, the normalized hue intensity of the kit gradually decreased with increasing NO₂⁻ concentration (the working concentration of the NO₂⁻ ions was between 0.1–3 mM). A good linear relationship between normalized hue intensity and the concentration of NO₂⁻ was observed in the range from 0.1 mM to 1.5 mM for the Gel/Rh6G@UiO-66-NH₂ hydrogel test kit under sunlight. The regression equation can be expressed as $y = -0.39C + 0.98$ ($R^2 = 0.979$), and the detection limit is calculated to be 0.09 mM (**Figure 4-10C**). Similar results were also obtained in **Figure 4-10D** and **4-10E**, demonstrating that the normalized hue intensity of the fluorescence color of the test kit exhibited a good linear response ($R^2 = 0.972$) to the NO₂⁻ concentration in the range of 0.1–1.5 mM.

In addition, selective identification and anti-interference performance are meaningful indices to estimate the practicality of the hydrogel test kit toward the target. Therefore, the afore-mentioned interfering substances were introduced into the hydrogel test kit to simulate practical conditions. **Figure 4-11A** depicts the color change upon adding NO₂⁻ or common interfering substances into the Gel/Rh6G@UiO-66-NH₂ hydrogels test kit. Only NO₂⁻ group caused a remarkable response, leading to a noticeable deepening in visible color and a reduction in fluorescence color. The interferences had little effect on the color change of the constructed system, indicating the adequate specificity of the proposed hydrogel kit for NO₂⁻. Following, distinct color variations were observed with the naked eye when incubating NO₂⁻ and co-existing interfering substances together (**Figure 4-11B**). By analyzing the color information (**Figure 4-11C** and **4-11D**), the normalized intensity histogram further demonstrated that the intensity of the Gel/Rh6G@UiO-66-NH₂ hydrogel test kit was barely affected by interfering substances, whether under sunlight or UV light. Meanwhile, the kit's response to NO₂⁻ remained constant in the presence of common interferences, revealing excellent specificity and a strong anti-interference capacity. Apart from the excellent specific identification capability of Rh6G@UiO-66-NH₂ toward NO₂⁻, another factor contributing to this specificity might be the

ability of the Gel hydrogel to act as a barrier, preventing the infiltration of biomacromolecules and small molecules through its porous structure (Wang et al., 2022). In summary, the Gel hydrogel, pretreated with Rh6G@UIO-66-NH₂, can be used for on-site monitoring and semi-quantitative analysis of NO₂⁻ with the naked eye.

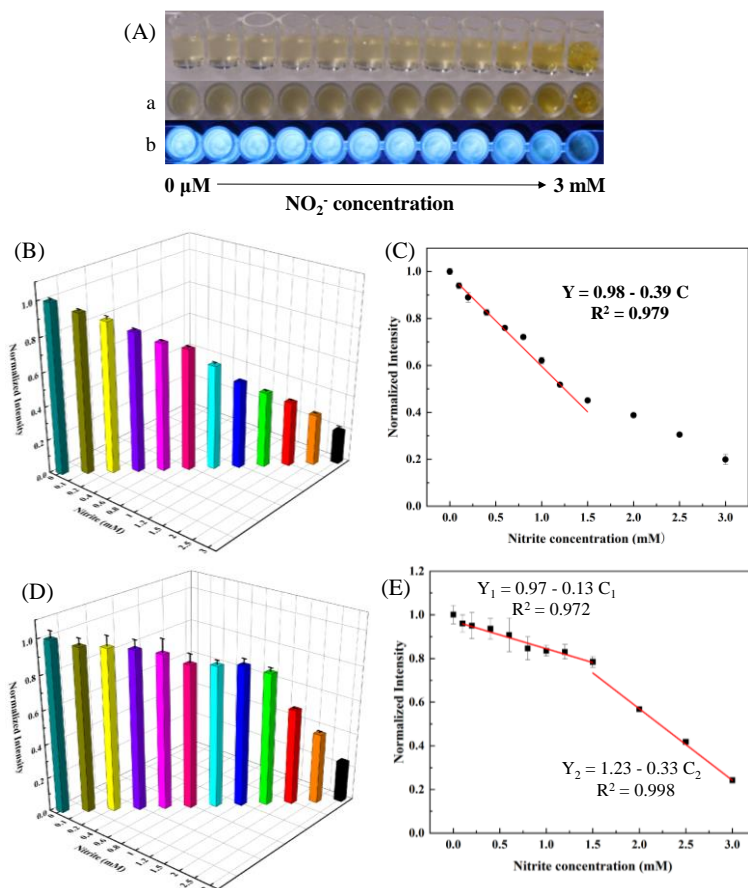


Figure 4-10 (A) The photograph of kit with different concentrations of NO₂⁻ under sunlight (a) and UV light (b). (B) The normalized hue intensity of kit digitized by ImageJ software (under sunlight). (C) Corresponding relationship between the concentration of NO₂⁻ and hue intensity (under sunlight). (D) The normalized hue intensity of kit digitized by ImageJ software (under UV light). (E) Corresponding relationship between the concentration of NO₂⁻ and hue intensity (under UV light).

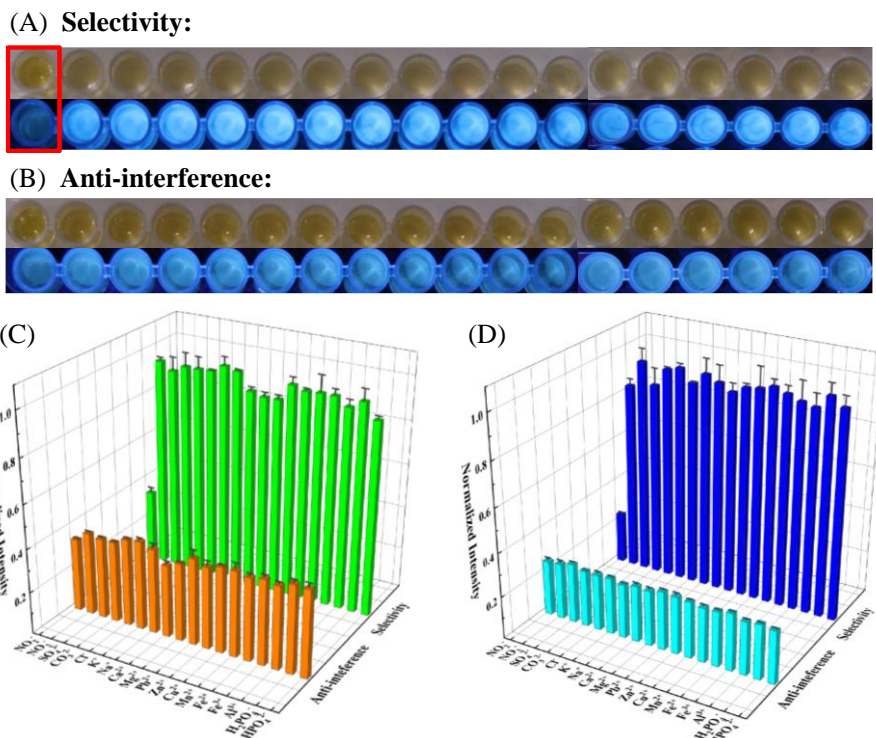


Figure 4-11 The photographs of kit in the presence of interfering ions, (A): selectivity; (B): anti-interfering. The corresponding normalized hue intensity of selectivity and interference effect in the kit under sunlight (C) and UV light (D).

4.4. Conclusion

In general, a novel probe has been successfully developed by combining the MOF of UiO-66-NH₂ with Rh6G via a one-pot approach for quantitative monitoring of NO₂⁻ contamination via ratiometric fluorescent signal recognition. Accordingly, a portable hydrogel test kit named Gel/Rh6G@UiO-66-NH₂ was fabricated. The special diazo-reaction between the amino group of UiO-66-NH₂ and NO₂⁻ quenches the blue fluorescence of Rh6G@UiO-66-NH₂, whereas the initial Rh6G dyes served as a reference, leading to an obviously distinguished color change from blue to colorless. Both signal outputs of ratiometric fluorescence of Rh6G@UiO-66-NH₂ and hue intensity value of Gel/Rh6G@UiO-66-NH₂ show high sensitivity and selectivity with as low as LODs of 0.021 μM and 0.09 mM. Overall, the functionalized LMOF sensor and its hydrogel test kit present advantages of rapid and quantitative analysis NO₂⁻ with both ratiometric fluorescence and color recognition in complex food samples, demonstrating the potential for fast and accurate detection for food safety.

5

Chapter V. Application ratio fluorescent nanoprobe 5-AF@UIO-66 and its hydrogel test kit for on-site and visual detection of nitrite in meat products

Short overview

Although the brilliant LMOF-based hydrogel test kit was successfully established in Chapter 4, it has not been applied to detect nitrite in real meat samples. Therefore, Chapter 5 aimed to synthesize a self-calibrated LMOF-based nanosensor (5-AF@UIO-66), designed using Zr-MOF (UIO-66) and another type of dye molecule, 5-Aminofluorescein (5-AF). Based on this, agarose was selected as a matrix, and we finally obtained another portable hydrogel test kit (Agarose/5-AF@UIO-66). The photos of the Agarose/5-AF@UIO-66 after reacting with nitrite can be recorded by the novel image capture system, named the Chemiluminescence Imaging System, and transferred into normalized hue intensity relative to various nitrite concentrations. Most importantly, we achieved nitrite detection in actual meat products using the Agarose/5-AF@UIO-66 test kit.

Abstract: A novel ratiometric fluorescent nanosensor based on luminescent metal organic framework (LMOF, denoted as 5-AF@UIO-66) for efficient nitrite (NO_2^-) ion detection was constructed in this work. The nanocomposite exhibited enhanced fluorescence capabilities for the recognition of NO_2^- , inducing the bright yellow fluorescence quenching of 5-AF. The UIO-66 served as an internal reference, the fluorescent intensity ratio ($I_{264\text{nm}}/I_{440\text{nm}}$) of 5-AF@UIO-66 increased linearly along with the concentration range of 1–12 μM for NO_2^- ($R^2 = 0.970$) and with the limit of detection (LOD) of 0.14 μM . In addition, we further fabricated a stimuli-responsive LMOF-based hydrogel test kit for precisely quantified NO_2^- content by combining it with a chemiluminescence imaging system. Interestingly, the photo image of the Aga/5-AF@UIO-66 hydrogel test kit could be converted into digital data, creating a direct quantitative and visual method for the identification of NO_2^- . The user-friendly design of the on-site hydrogel kit not only reduced the sample-to-answer response time to 10 min but also provided excellent analysis sensitivity (LOD of 0.43 μM), accuracy, and stability. As a result, the kit proved successful in analyzing real food samples, offering a novel approach for on-site monitoring and demonstrating substantial potential for widespread application in ensuring food safety.

Keywords: NaNO_2^- , luminescent metal organic framework, agarose hydrogel test kit, synchronous fluorescence, chemiluminescence imaging, visualization detection

5.1. Introduction

Nitrite (NO_2^-) stands as the predominant nitrogen-containing compound found in the human environment, and it is commonly used as an essential antioxidant, color-retention agent, and antimicrobial agent in food, particularly processed meat products (Ma et al., 2020; Sepahvand et al., 2021). However, it is worth noting that NO_2^- has been included in the World Health Organization's (WHO) roster of carcinogens (Wang et al., 2021). Because excessive ingestion of NO_2^- can cause several negative and harmful diseases in human health, for instance, blue blood disease, esophageal and gastric cancers, and so on (Flores & Toldrá, 2021; Rong et al., 2021; Yu et al., 2022), owing to high consumption and/or high residual content of NO_2^- inside meat. Some authorities around the world have promulgated relevant regulations to limit the existence of NO_2^- in processed meat. The current Chinese National Standard (GB 2760-2014) has restricted the maximum amount of sodium nitrite (NaNO_2) added to processed meat to 0.15 g/kg. Moreover, the concentration of residual NaNO_2 in the great mass of processed meat that assures the meat product's innocuousness and safety for consumers has been set to range from 30 to 70 mg/kg. Whereas the European Union has reported that the maximum permitted concentration and residual content of NaNO_2 are up to 100 or 150 mg/kg (EU, 2008) and 60 mg/kg (EU Regulation No 1333, 2008) for many types of meat products, respectively (Ledezma-Zamora et al., 2021). Accordingly, it is of vital significance to establish a precise and fast on-site monitoring sensor for NO_2^- for food safety regulation and public health.

Comparing several conventional techniques for NO_2^- determination, including chromatography, spectrophotometry, the electrochemical method, and capillary electrophoresis, efficient spectrofluorimetry based on a fluorescent nanoprobe is more popular than those analytical methods because of its simplicity, accuracy, sensitivity, portability, and high reproducibility at a low cost. To date, plenty of fluorescent nanoprobe with a single emissive peak, like small organic molecules, organic-inorganic hybrid materials, MOFs, etc., have been developed for NO_2^- determination in foods (Deng et al., 2022; Ren et al., 2018; Tan et al., 2023). Nevertheless, nanoprobe possessing single emissions are normally limited by some shortages caused by biological backgrounds, unstable equipment efficiency, environmental influences, and inhomogeneous spatial concentration (Wan et al., 2022). However, as a novel and burgeoning analytical approach, the ratiometric fluorescence method with a built-in self-calibration can efficiently avoid the above interferences by monitoring the ratios of emission peak intensities at two different wavelengths (Liu et al., 2019). The ratiometric fluorescent nanoprobe has higher sensitivity and accuracy than the single-emission sensors. Furthermore, among the several commonly used scan modes of fluorescence spectroscopy, synchronous fluorescence spectroscopy (SFS) can simultaneously scan excitation and emission wavelengths, and the corresponding SFS spectrum is obtained on the condition of maintaining a certain wavelength difference ($\Delta\lambda = \lambda_{em} - \lambda_{ex}$), which has been demonstrated to be a highly effective technique,

reliably furnishing comprehensive chemical information about samples (Samokhvalov, 2020; Xue et al., 2021). To the best of our knowledge, there has been no investigation into combining the advantages of a ratiometric fluorescent nanoprobe with synchronous scan mode so that it can be more powerfully used in NO_2^- detection.

Metal organic frameworks (MOFs), synthesized through the self-assembly of metal centers and organic ligands, can serve as a charming platform for sensing a variety of chemical compounds owing to their tunable compositions, high porosity, and modifiable structures (Chen et al., 2017; Li et al., 2020). As an essential subunit of MOF nanomaterials, some LMOFs that are composed by incorporating luminescent dye molecular into MOFs have gained much interest, as they can be used for self-calibrating systems owing to the dual or multiple emitting peaks with which the MOFs and luminescent dye molecular can be referenced with each other (Gutiérrez et al., 2022; Sánchez et al., 2022). Furthermore, the distinct structure of MOFs is beneficial to preconcentrate the target so that selectivity and specificity are improved, and it combines with the luminescence unit to form a novel LMOF nanomaterial to encounter the complicated and rigorous environment of food safety evaluation. In recent years, some dye-loaded LMOF self-calibrating sensors have been employed in various scientific fields like fluorescent bioimaging, volatile organic molecules, light-emitting devices, temperature sensing, and chemical sensing through an intensity-varying signal with a single emission peak (Gao et al., 2018; Li et al., 2019; Sánchez et al., 2022; Yang et al., 2021). In addition, even though several researchers have reported results about the detection of NO_2^- using ratiometric fluorescent quantum dots like carbon nanodots (Das et al., 2022; Liu et al., 2019; Wang et al., 2022). As far as we know, there are still few studies on dual-emissive LMOF with visual fluorescence for the detection of NO_2^- at a trace level, particularly in food products, which deserve further exploration.

Hydrogels are established by cross-linked hydrophilic polymer networks with three-dimensional macromolecular structures that are capable of retaining large amounts of water (Badsha et al., 2021; Guo et al., 2020; Zhang et al., 2021). The desired physical properties of hydrogels include high porosity, large loading capacities, good biocompatibility, and so on. The three-dimensional networks can enhance the dispersion of MOFs within hydrogel matrices. Conversely, MOFs can engage with other components or modulate the properties of hydrogel matrices. Therefore, hydrogels are able to serve as an ideal material platform for such accommodating nanomaterials as MOFs, so that MOF-based hydrogels combine the advantageous properties of hydrogels and MOFs and show potentialities in the field of chemical and biological sensing. On the other hand, hydrogels have negligible fluorescence emissions and background colors, so they are suitable for visual detection in fluorescent sensing applications (Gao et al., 2018; Kim et al., 2017).

Hence, we utilized dye molecular (5-AF) and Zr-based MOF (UIO-66) as raw materials to synthesize LMOF nanocomposite (named 5-AF@UIO-66) through in-situ encapsulation of 5-AF into the structure of UIO-66 by stirring and adsorption

methods (a schematic diagram of the whole process is shown in **Figure 5-1A**. The 5-AF@UIO-66 nanosensor can accurately quantify NO_2^- and display a linear relationship between the ratio of the fluorescence intensity $I_{\text{MOF}}/I_{\text{dye}}$ and increasing concentrations of NO_2^- . At the same time, the fluorescent color of the ratiometric nanoprobe, which transforms from yellow-green to colorless, can be evaluated by naked eye observation under UV light. In order to facilitate a wider practical application of the aforementioned nanoprobe, we herein developed a portable kit by preloading 5-AF@UIO-66 in an agarose hydrogel matrix for NO_2^- detection with the naked eye. For accurate quantification, the fluorescent color change of 5-AF@UIO-66 could be recorded and converted into digital data, revealing a linear correlation with the NO_2^- concentration. Thereby, it's a convenient and efficient strategy to visualize and quantify NO_2^- onsite and has broad application prospects in meat products for guaranteeing food safety.

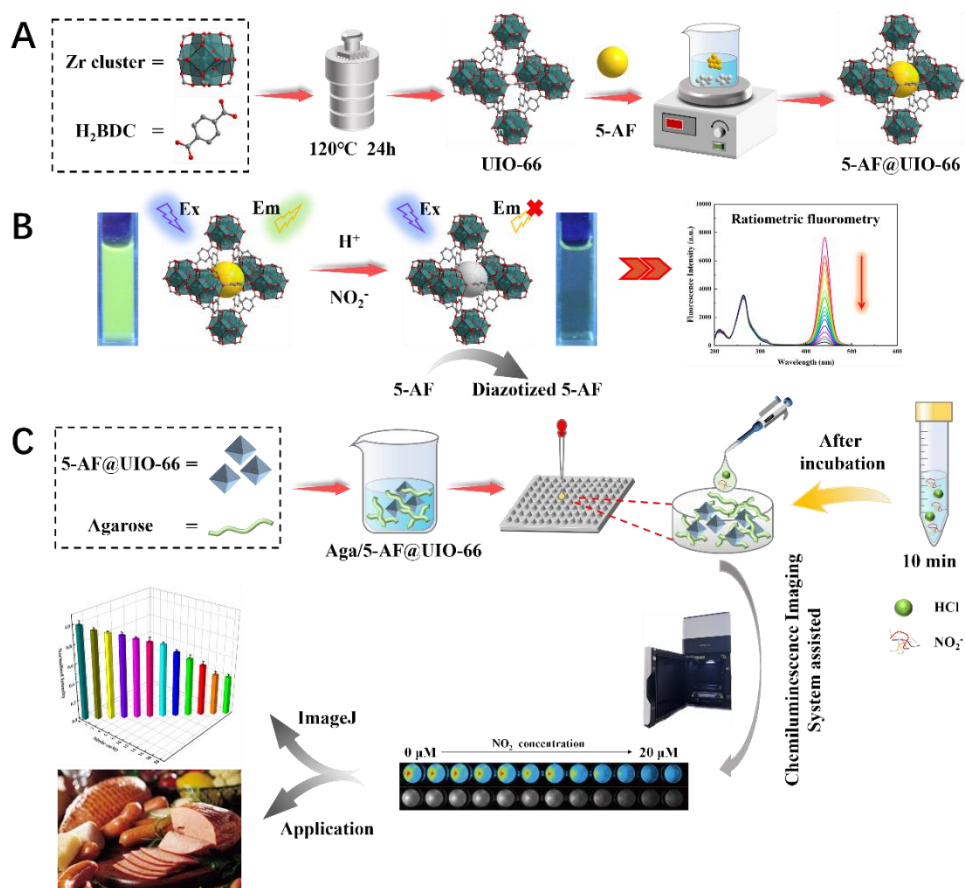


Figure 5-1 (A) Schematic diagram for the preparation of 5-AF@UIO-66 nanosensor; (B)

Illustration of the bimodal ratiometric fluorometric detection of NO_2^- based on 5-AF@UIO-66 nanosensor; (C) Schematic illustration for Aga/5-AF@UIO-66 hydrogel kit preparation and the fluorescence response to NO_2^- .

5.2. Materials and Methods

5.2.1. Chemicals and Instruments

Zirconium chloride (ZrCl_4), 1,4-terephthalic acid (H_2BDC), N, N-dimethylformamide (DMF), acetic acid (AA), ethanol, and 5-aminofluorescein (5-AF) were procured from Aladdin Reagent Company (Shanghai, China). Agarose powder, NO_2^- , and aqueous solutions of interference ions (NO_3^- , SO_4^{2-} , CO_3^{2-} , Cl^- , K^+ , Na^+ , Ca^{2+} , Mg^{2+} , Pb^{2+} , Zn^{2+} , Cu^{2+} , Mn^{2+} , Fe^{2+} , Fe^{3+} , Al^{3+} , H_2PO_4^- and HPO_4^{2-}) were obtained from Macklin Biochemical Co., Ltd. (Shanghai, China). All reagents and solvents were commercially available and used as received, without purification. The meat samples, including ham and stewed beef, were acquired from a local supermarket located in Beijing, China.

For powder X-ray diffraction (PXRD) patterns, measurements were acquired using the Panalytical X-ray Diffractometer Smartlab-9kW (Tokyo, Japan) equipped with Cu $\text{K}\alpha$ radiation ($\lambda = 1.5406 \text{ \AA}$, 40kV, 250mA). Fourier transform infrared (FT-IR) spectra were recorded employing a Thermo Scientific Nicolet IS5 FT-IR spectrophotometer covering the range of 4000–400 cm^{-1} . Scanning electron microscopy (SEM) images were captured by the FEI Inspect F50 scanning electron microscope. X-ray photoelectron spectroscopy (XPS) characterization was performed utilizing an X-ray photoelectron spectrometer of the ESCALAB XI+ model (Thermo Fisher, USA). The 3D fluorescence spectra and synchronous fluorescence spectra were both collected using a Hitachi F-7000 fluorescence spectra photometer (Tokyo, Japan). The acquisition parameters for 3D fluorescence spectroscopy were as follows: The excitation wavelength range was changed from 200 nm to 600 nm, while the emission wavelength was changed from 200 nm to 700 nm in steps of 5 nm. For synchronous fluorescence spectra, excitation and emission were collected simultaneously, and the photoexcitation wavelength λ_{Ex} ranged from 200 nm to 600 nm in 1 nm increments with wavelength offsets of ($\Delta\lambda = \lambda_{\text{Em}} - \lambda_{\text{Ex}}$) 70 nm. The DR-6000 UV-visible spectrophotometer (Hach Company, China) was used to obtain the ultraviolet-visible (UV-vis) absorption spectra. A Chemiluminescence Imaging System-Fusion Fx (Vilber Company, France), with an excitation wavelength set at 440 nm, was used to capture fluorescence images of the 5-AF@UIO-66 agarose kit.

5.2.2. Synthesis of 5-AF@UiO-66

UiO-66 was synthesized using the solvothermal method as previously reported in the literature, with a slight modification (Chang et al., 2022). Briefly, ZrCl_4 (5 mmol) and H_2BDC (5 mmol) were dissolved in DMF (40 mL) at room temperature, and the resulting solution was ultrasonically treated for 20 min to achieve a clear and

transparent mixture. Subsequently, 10 mL of acetic acid was added to the as-obtained solution and further sonicated for 10 min. The mixture was then transferred to a Teflon-lined autoclave and kept at 120 °C for 24 h for crystallization under static conditions. After cooling down to room temperature, the resulting white powder was subjected to centrifugation and washed with DMF and methanol for at least three cycles each, followed by vacuum drying at 120 °C for 12 h.

A certain concentration of 5-AF (0, 0.1, 0.5, 1.0, and 5.0 mmol/L) and UiO-66 (200 mg) were dispersed in 40 mL of ethanol and stirred at room temperature for 24 h in a dark environment. The resulting orange precipitates were designed as 5-AF@UiO-66, which were subjected to centrifugation and washed repeatedly with ethanol and deionized water. Afterward, the collected precipitates were dried under vacuum at 40 °C. The 5-AF@UiO-66 powder was composed by stirring with room temperature treatment rather than the solvothermal treatment described in our previous study (Deng et al., 2022), owing to the fact that 5-AF is sensitive to light and high temperatures.

5.2.3. Preparation of a nitrite detection kit using 5-AF@UiO-66 immobilized agarose hydrogels

Generally, 0.2 g of agarose powder is added to 10 mL of deionized water. The mixture is then heated in a water bath until complete dissolution is achieved, followed by cooling the solution to 40 °C. After that, 10 mL of the 0.5 mg/mL 5-AF@UiO-66 suspension was poured into the above solution and stirred evenly. Then, 150 μ L of the above solution was transferred into a 96-well microplate. And the Aga/5-AF@UiO-66 hydrogel kit could be formed and stored at room temperature (25 °C) for further use.

5.2.4. General procedure of nitrite determination

To investigate the response of the system to NO_2^- , a range of NO_2^- aqueous solutions with varying concentrations (0-20 μM) were prepared. The detection of NO_2^- was carried out in an acidic environment at room temperature. To generate an initial 5-AF@UiO-66 suspension, 5.0 mg of synthesized 5-AF@UiO-66 powder was introduced into 20 mL of deionized water and subjected to magnetic stirring for a duration of 20 min. The 5-AF@UiO-66 stock suspension, thus obtained, was stored at 4 °C in a refrigerator for subsequent use. Subsequently, 300 μ L of 5-AF@UiO-66 stock solution was combined with 400 μ L of a 0.3 mol/L HCl solution, and 300 μ L of a freshly prepared NO_2^- aqueous solution was added to the samples incrementally. Before recording the synchronous fluorescence spectra with a wavelength difference ($\Delta\lambda$) of 70 nm, the resulting suspension was thoroughly mixed. In addition, the following peaks were measured more than three times, and the average values were employed for the determination of the intensity ratio.

To examine the selectivity of the 5-AF@UiO-66 probe for NO_2^- , different anions and cations that coexist with NO_2^- in meat products (including NO_3^- , SO_4^{2-} , CO_3^{2-} ,

Cl⁻, Cr⁻, K⁺, Na⁺, Ca²⁺, Mg²⁺, Pb²⁺, Zn²⁺, Cu²⁺, Mn²⁺, Fe²⁺, Fe³⁺, Al³⁺, H₂PO₄⁻, and HPO₄²⁻) were introduced into the detection system as interference agents to replace the NO₂⁻ standard solution. And the fluorescent intensity was recorded three times to ensure the consistency and dependability of the experimental outcomes.

5.2.5. On-site detection of nitrite by hydrogel test kit

For the on-site detection of NO₂⁻, HCl solution (0.05 mol/L) and various concentrations of NO₂⁻ solution were mixed. Then, a volume of 150 μL of the above reaction solution was dropped into the Aga/5-AF@UiO-66 hydrogel test kit to allow NO₂⁻ ion diffusion into the hydrogel to adequately react with 5-AF@UiO-66. The equilibration time was set at 10 min at room temperature. After that, the fluorescence images of the Aga/5-AF@UiO-66 hydrogel were recorded by the Chemiluminescence Imaging System and analyzed by ImageJ software. The same procedural steps and conditions were employed for the determination of NO₂⁻ in meat product samples. However, the pure NO₂⁻ solution was substituted with an equal volume of meat product extraction spiked with various concentrations of NO₂⁻. It is worth mentioning that the NO₂⁻ was processed and extracted from meat product samples in accordance with the China national standard (GB 5009.33–2016). The detailed extraction procedure was referred to our prior report (Deng et al., 2022).

5.3. Results and Discussion

5.3.1. Chemical, structural, and morphological composition of 5-AF@UiO-66 nanoprobe

The surface functional groups of synthesized UiO-66 and 5-AF@UiO-66 samples are analyzed by the FT-IR spectroscopy technique, and the corresponding spectra are presented in **Figure 5-2A**. The characteristic absorption peaks of UiO-66 and 5-AF@UiO-66 were observed near 3386, 1658, 1583, 1398, 748, 665, and 549 cm⁻¹, respectively. The observed broad band near 3386 cm⁻¹ can be attributed to the strong stretching vibrations of —OH in the monomer unit present in the sample (Chen et al., 2022; Virmani et al., 2018). The peak around 1658 cm⁻¹ was assigned to C—O stretching, and both MOFs show two intense absorption peaks around 1582 cm⁻¹ and 1398 cm⁻¹ which correspond to the symmetric and asymmetric vibrational stretching in the backbone carboxylate groups of the organic ligand terephthalic acid (Wang et al., 2023). Additionally, the peaks around 748 cm⁻¹ and 665 cm⁻¹ are related to the C—H stretching vibration in the benzene ring of terephthalic acid (Chang et al., 2022). Moving to the low frequency region, the vibration peak at 549 cm⁻¹ is related to the asymmetric vibrational stretching of the Zr-(OC) bond, which forms between the Zr metal center and the ligand. The above observations well reveal that the functional groups of certain ligands are present in the MOFs and are consistent with the typical structure of various UiO-66 MOFs reported in the literature (Abid et al., 2012;

Gayathri et al., 2022). In addition, there was no visible difference measured in FT-IR spectra among UiO-66 and 5-AF@UiO-66, which revealed that both Zr-MOFs were prepared successfully in our work. The 5-AF molecules were enclosed in the pore of UiO-66 so that no characteristic vibrations of 5-AF were observed from the 5-AF@UiO-66 spectrum.

The PXRD patterns of the as-synthesized UiO-66 and 5-AF@UiO-66 samples are displayed in **Figure 5-2B**. The characteristic diffraction peaks of UiO-66 nanomaterial at 2θ angles were located at 7.32° , 8.46° , and 25.64° , which are basically consistent with the typical pattern of simulated UiO-66 in previous literature reports (Thi Dang et al., 2020; Wang et al., 2023). In addition, we sought to introduce 5-AF molecules inside the porous 5-AF@UiO-66 channels by the conventional absorption procedure. However, there was no visible difference in the pattern between UiO-66 and 5-AF@UiO-66 in the diffraction peak position, height, or width. The detailed peak location of the 5-AF molecule was not found in 5-AF@UiO-66's crystal data owing to its low occupancy, implying that the dye-loaded MOF retained its structural integrity and that the dye molecules were embedded into the cavity of the MOF's crystal (Let et al., 2020). The diffraction peak shapes of UiO-66 and 5-AF@UiO-66 were both sharp and possessed a high degree of crystallinity. The successful formation of UiO-66 and 5-AF@UiO-66 in our work was further confirmed by comparing the PXRD profile with that of the simulated one.

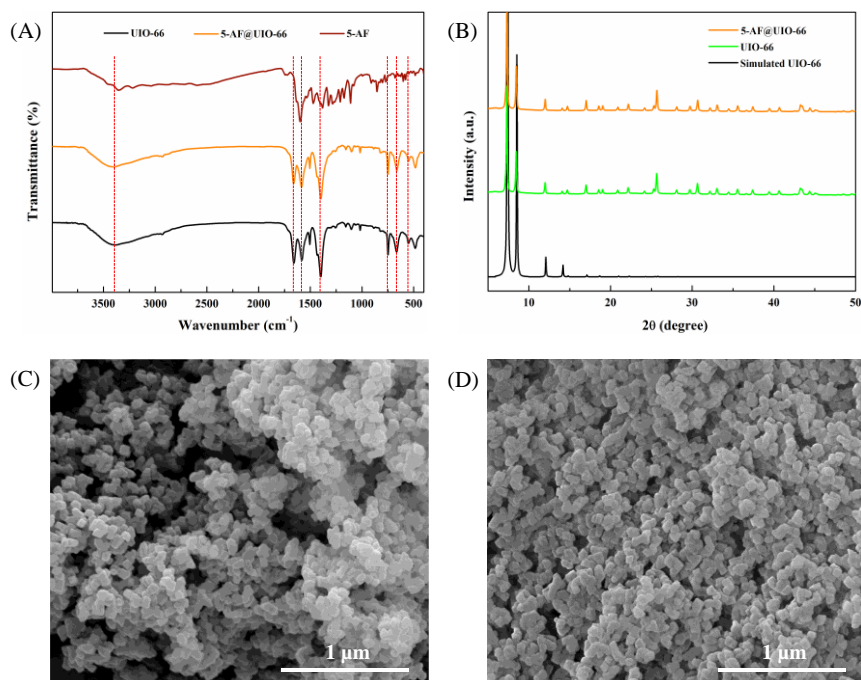


Figure 5-2 (A) FT-IR spectra of UiO-66 and 5-AF@UiO-66; (B) PXRD patterns of

simulated UIO-66, synthesized UIO-66 and 5-AF@UIO-66; SEM images of UIO-66 (C) and 5-AF@UIO-66 (D).

The surface morphology of UiO-66 and 5-AF@UiO-66 synthesized in this work was measured by means of SEM technology, and its images are shown in **Figure 5-2C** and **Figure 5-2D**. It could be seen that the overall morphology of this synthesized UiO-66 showed an irregular shape instead of a symmetrical regular octahedron appearance, maybe owing to the too small crystal size (the average particle size is approximately 99 nm), in agreement with typical UiO-66 type MOFs that have been reported in the literature (Chang et al., 2022). After loading with dye molecules, the observed SEM image of 5-AF@UiO-66 showed almost similar crystals to the UIO-66 MOF. The shape of the octahedron and smooth surface were still maintained, and the size had not changed significantly. The results corroborate that the parent UIO-66 structure is not dismantled by the inclusion of dye molecules, the 5-AF-dyes just encapsulate in the framework or adhere on the surface of MOF, which is in agreement with the indicators explained above (Let et al., 2020; Sánchez et al., 2022).

The XPS spectra were used to figure out the chemical states and elemental composition of prepared UIO-66 before and after absorbing 5-AF dye molecules. As displayed in **Figure 5-3A**, the obtained UiO-66 contained obviously elemental peaks of O1s orbital, C1s orbital, and Zr3d orbital, where these peaks were observed at binding energies of 531.8 eV, 284.8 eV, and 182.9 eV, respectively (Ma et al., 2021; Wang et al., 2023). Besides, in the magnified survey-scan spectra of 5-AF@UiO-66, N1s orbitals were also observed at 400.6 eV due to the existence of amino ligands, confirming the successful absorption of 5-AF inside the UIO-66 architecture (**Figure 5-3B**). The high-resolution XPS spectra further verified the above conclusion, and these characterization indicators proved the successful construction of UIO-66 and 5-AF@UIO-66.

The nitrogen (N₂) adsorption/desorption isotherms of UiO-66 and 5-AF@UiO-66 were used to examine the synthesized materials' specific surface area and pore diameter (**Figure 5-3C** and **5-3D**). As can be seen from **Figure 5-3C**, the N₂ sorption studies on the synthesized UiO-66 and 5-AF@UiO-66 at 77 K both revealed a reversible type I isotherm characteristics, and the pattern of the isotherms indicate that there are tremendous micropores in these nanoparticles. The shapes of N₂ adsorption/desorption isotherms of UiO-66 particles are similar to those reported previously (Chang et al., 2022; Gayathri et al., 2022), in which N₂ adsorption and desorption curves were almost identical without hysteresis loop, and the micropores in the porous particle's structure explained the adsorption at low relative pressures. Moreover, the calculated Brunauer Emmett Teller (BET) surface area of 5-AF@UiO-66 was 658.711 m²/g, which is considerably smaller than that of pristine UIO-66 (1386.540 m²/g). This further confirms the effective absorption of 5-AF by UIO-66 and successful synthesis of 5-AF@UiO-66, which is consistent with recent literatures (Deng et al., 2024). Moreover, as can be obtained from **Figure 5-3D**, the average pore

diameters distribution profile of UiO-66 and 5-AF@UiO-66 showed sharp peak at around 1.426 nm and 1.423 nm, respectively. The results indicates that a small number of 5-AF were loaded into UiO-66, most of 5-AF bind to UiO-66 through adsorption. In spite of that, 5-AF@UiO-66 still shows a large surface area, which assures effective target (NO_2^-) identification.

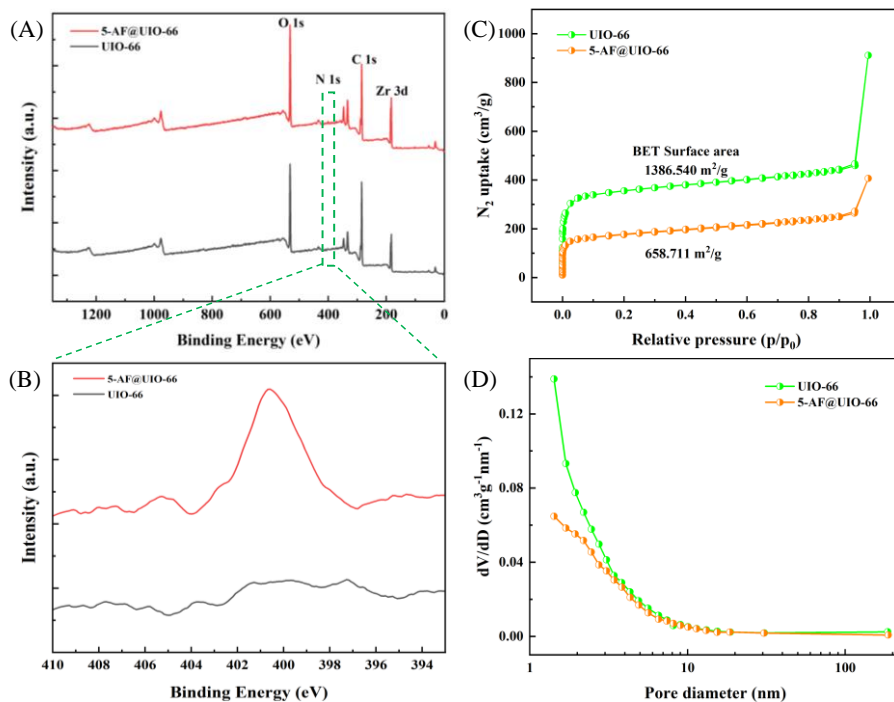


Figure 5-3 (A) The XPS spectra of UiO-66 and 5-AF@UiO-66; (B) The high-resolution XPS spectra of N 1s of UiO-66 and 5-AF@UiO-66. (C) Nitrogen (N_2) adsorption-desorption isotherms from UiO-66 and 5-AF@UiO-66. (D) The pore diameter distribution curve of UiO-66 and 5-AF@UiO-66.

5.3.2. Photoluminescence behavior of 5-AF@UiO-66 nanoprobe

In order to introduce the fluorescent dye molecule, the Zr-based UiO-66 crystals were soaked in an ethanol solution of 5-AF for stirring 24 h at ambient temperature. As a result, an immediate color change of dye@MOF was noticed after absorption processing, and crystals of 5-AF@UiO-66 were obtained. To gain insight into the charge-transfer, fluorescent behavior, and potential of UiO-66 as a luminescent material, the 3D front-face fluorescence spectra of UiO-66 and its composite nanomaterial were conducted at room temperature, and the corresponding results are displayed in **Figure 5-4**. The fluorescent property of UiO-66 exhibited its two characteristic Excitation/Emission (Ex/Em) peaks positioned at 270 nm / 330 nm and

320 nm / 360 nm, respectively. These findings indicate that the emission wavelength of UiO-66 exhibited an independent excitation feature and that its strong emission could be due to the ligand-based charge transfer (**Figure 5-4A**). However, the fluorescence spectra of dye-encapsulated nanocomposite 5-AF@UiO-66 demonstrated simultaneous emission corresponding to both UiO-66 and 5-AF. Its well-resolved emission peak emerging at 535 nm with the excitation wavelength around 315 nm, 360 nm, and 500 nm were ascribed to the characteristic fluorescence of 5-AF, while only a single Ex/Em peak located at 265 nm / 330 nm corresponded to UiO-66 (**Figure 5-4B to 5-4E**). The phenomenon of the peak positions changing may arise from the spectral overlap between the emission spectrum of UiO-66 and the absorption spectra of 5-AF dye molecules, leading to an efficient fluorescence resonance energy transfer (FRET) from UiO-66 to 5-AF dyes in this novel nanocomposite (Gao et al., 2018). These results further confirmed that 5-AF was successfully encapsulated without sacrificing its native luminescent properties.

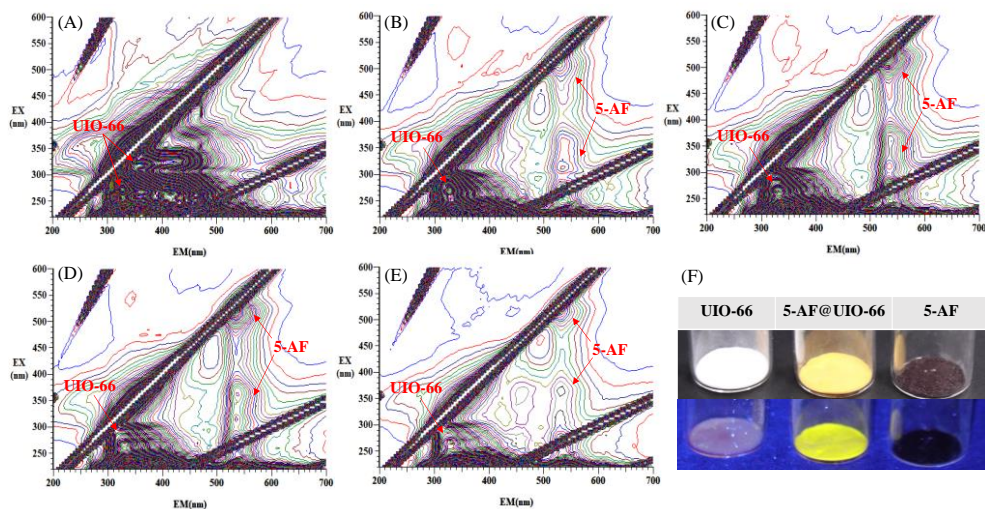


Figure 5-4 The 3D-fluorescence spectra of UiO-66 solid powder (A), and 5-AF@UiO-66 solid powders with (B) 0.1 mM 5-AF, (C) 0.5 mM 5-AF, (D) 1.0 mM 5-AF and (E) 5.0 mM 5-AF, respectively. (F) The photo of corresponding UiO-66 and 5-AF@UiO-66 solid powders under visual light and 365 nm UV light.

Additionally, fluorescent spectra were further used to fine-tune the quantity of the fluorescent dye within UiO-66. As shown in **Figure 5-4C**, with the increasing concentration of the adsorbed dye, the 5-AF@UiO-66 nanocomposite with 0.5 mM 5-AF represented the highest relative peak intensity at the emission wavelength near 535 nm of the treatments tested. The loading of 5-AF in UiO-66 was further validated by observing the increase in the fluorescent intensity of the resulting supernatant dye

solution. **Figure 5-5A** reveals that the 5-AF adsorption supernatant solution (within 0.5 mM) did not demonstrate any emission intensity, while the emission intensity of the residual adsorbent gradually enhanced along with the increasing dye concentration. The above phenomena imply that 5-AF are isolated by the cages of UiO-66 and maintain a monodisperse state under accommodating appropriate amounts of dye. However, this perfect status was broken by the aggregation-caused quenching (ACQ) effect owing to excessive aggregation of dye (over 1.0 mM of 5-AF) in the cage of MOFs again (Deng et al., 2022). Taken together, the optimal amount of 5-AF was set at 0.5 mM and its synthesized LMOF is suitable to research the sensing performance for NO_2^- detection and use for further experiments. Moreover, the color of the crystals changed from white to orange under daylight, and the corresponding fluorescent color displayed a bright yellow color under ultraviolet light (**Figure 5-4F**), which matched well with its calculated Commission Internationale de L'Eclairage (CIE) chromaticity coordinates diagram. The CIE coordinates moved from the bluish violet region to the yellow region, they are (0.237, 0.180) and (0.344, 0.430) for the UIO-66 and 5-AF@UIO-66 composites, respectively (**Figure 5-5B**).

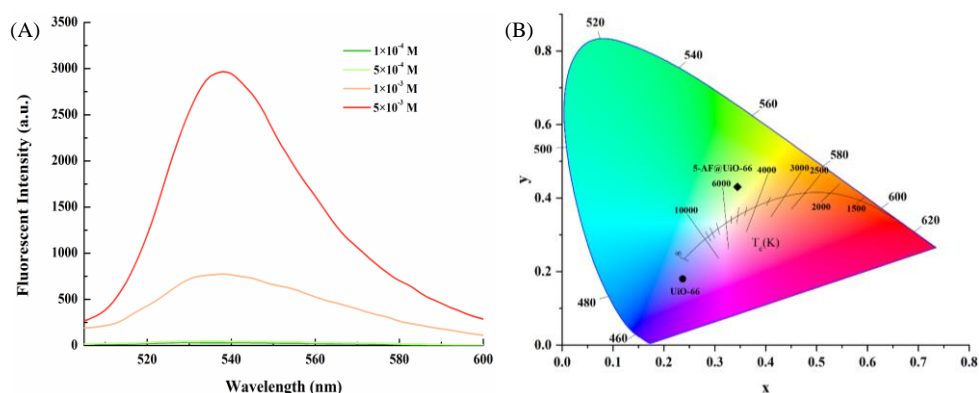


Figure 5-5 (A) The fluorescent intensity of residual 5-AF dye solution after UIO-66 absorbing. (B) CIE chromaticity coordinates for UIO-66 and 5-AF@UIO-66.

5.3.3. Optimization of detection condition

Due to the synchronous scan mode of fluorescence spectroscopy, it can not only simplify spectra, eliminate scattering light interferences, reduce spectral overlap, and improve selectivity, but also simultaneously monitor the Ex and Em throughout the main MOF and dye peak (Dankowska & Kowalewski, 2019b). Therefore, we chose $\Delta\lambda = 70$ nm so that the spectra can sensitively capture changes in MOF and dye peaks. In addition, pH and reaction time are vital experimental parameters to optimize for obtaining the optimal detection response of the sensing system.

The acidity, which exerts a pivotal influence on the fluorescence properties of the 5-AF@UIO-66 probe, holds substantial way over the reaction rate and reaction

process. Therefore, the fluorescence signals for the probe before and after adding NO_2^- under different H^+ concentrations (from 0.1 to 1.0 M) were recorded, as illustrated in **Figure 5-6A**. Notably, the peak fluorescence intensity of the 5-AF (Ex = 440 nm) reached its maximum when the concentration of HCl was 0.3 M without adding NO_2^- . While the HCl concentration exceeded 0.3 M, its fluorescent intensity significantly decreased with the increase in acidity owing to the protonation of the amine group in 5-AF. On the other hand, we also analyze the sensing attributes of the intensity ratio $I_{264 \text{ nm}}/I_{440 \text{ nm}}$, that aimed to eliminate the impact of operating error and other potential factors (**Figure 5-6B**). The fluorescent intensity ratio of 5-AF@UIO-66 after the reaction with NO_2^- appeared to have an obvious undulation. Under the HCl concentration of 0.3M, not only the maximum fluorescent intensity of 5-AF was excited, but also the difference in the fluorescent intensity ratio before and after adding NO_2^- was relatively good and stable. Thus, for ease of experimentation, 0.3 M of HCl was chosen as the optimal acid condition for the subsequent research.

In addition, the influence of reaction time on the performance of fluorescence analysis was also investigated. And **Figure 5-6C** displayed the variation in fluorescent intensity ratio of the 5-AF@UIO-66 nanoprobe with time after reacting with NO_2^- . Initially, the reaction between the 5-AF@UIO-66 nanoprobe and NO_2^- happened immediately, and the fluorescent intensity ratio of the sensing system rapidly increased. As time changed, the changes in fluorescent intensity ratio tended to be stable after 6 min and kept unchanged for further reactions. This response time is much shorter than some other nanosensors reported in previous literature, indicating that 5-AF@UIO-66 reacted with NO_2^- quickly and efficiently (Deng et al., 2022; Zhang et al., 2016). Thus, 6 min was set as the optimal reaction time between the 5-AF@UIO-66 nanoprobe and NO_2^- in this study.

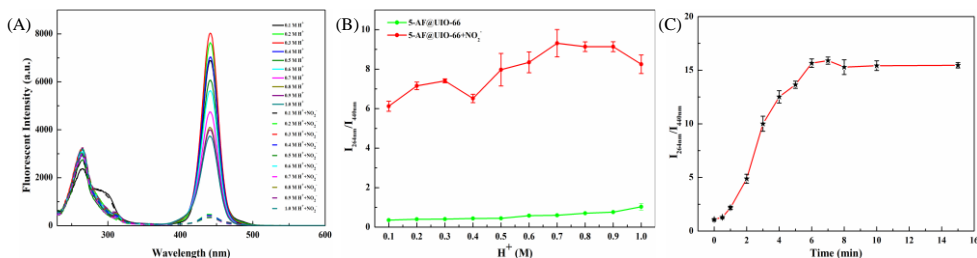


Figure 5-6 (A) Fluorescent intensities of 5-AF@UIO-66 in response to different concentrations of HCl with and without nitrite. (B) The Effect of HCl concentration on the 5-AF@UIO-66-based sensor with and without nitrite. (C) Time-dependent fluorescence intensity changes of 5-AF@UIO-66 in the presence of nitrite in HCl (0.3 M).

5.3.4. Ratiometric sensing measurement toward nitrite

In the sensing system, UIO-66 acts as an internal reference fluorescence center, imparting the LMOF nanoprobe with the ability to self-calibrate to mitigate the impact

of environmental interference, owing to its superior structure with a relatively large cavity size, a narrow pore window, and good chemical stabilities. Whereas 5-AF was found to react with target NO_2^- sensitively and selectively and quench the corresponding fluorescence, owing to the formation of diazonium salts under an optimal acid environment. Thereby, the targeted 5-AF dye molecule is combined with UIO-66 to construct a dual-emitting nanocomposite for effective detection of NO_2^- .

Based on the above optimum conditions, we sought to examine the fluorescence responses of the 5-AF@UIO-66 sensing system to NO_2^- solutions with different concentrations. As expected, the 5-AF@UIO-66 presented a dual-emitting luminescent property, which respectively showed the UIO-66 and 5-AF fluorescent peak at excitation wavelengths centered at 264 nm 440 nm when $\Delta\lambda$ set at 70 nm (**Figure 5-7A**). The prepared nanocomposite was tested against 0–20 μM aqueous solution of NO_2^- ions. The fluorescence intensity of 5-AF@UIO-66 at 440 nm was sensitive to NO_2^- and decreased gradually with the incremental addition of NO_2^- , more than 96.8% fluorescence quenching of the 5-AF fluorescent peak was found after adding 300 μl of 20 μM NO_2^- ions, while no obvious fluorescence quenching of the UIO-66 fluorescent peak was observed. The rapid and significant quenching observed can be attributed to the extensive interaction between the target NO_2^- ions and the amino group, resulting in the formation of diazotized compounds. Besides, the inset image showed the obvious evolution of the corresponding fluorescent color, the robust green luminescence exhibited by the nanoprobe in an aqueous medium was promptly extinguished upon the introduction of NO_2^- ions under 365 nm UV light.

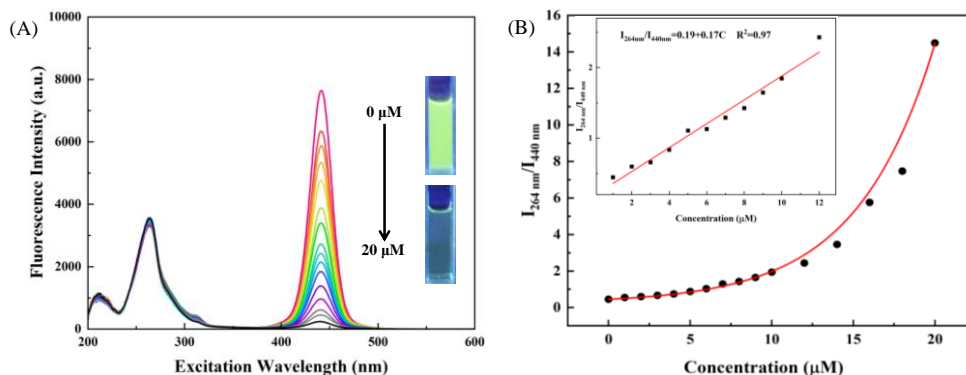


Figure 5-7 (A) Fluorescent intensity of 5-AF@UIO-66 suspension toward different concentration of NO_2^- . (B) The trends of fluorescent intensity ratio $I_{264\text{nm}}/I_{440\text{nm}}$ with different concentration of nitrite.

Furthermore, the high sensitivity of the sensing nanoprobe was further confirmed through the quantification of the quenching effect. As displayed in **Figure 5-7B** inset, there is a positively linear correlation ($I_{264\text{ nm}}/I_{440\text{ nm}} = 0.19 + 0.17 C$, $R^2 = 0.970$) between the fluorescent intensity ratio ($I_{264\text{ nm}}/I_{440\text{ nm}}$) and NO_2^- concentration in the

range of 0–12 μM . Here, the LOD was defined as $3\sigma/s$, with σ representing the standard deviation of blank measurements and s denoting the slope of the calibration curve, respectively (Deng et al., 2022; Yu et al., 2022). The calculated LOD for the NO_2^- ion in this study is calculated to be 0.14 μM , significantly below the maximum permissible concentration of NO_2^- in meat products. The large surface area of MOF material, which can accommodate more probe molecules and boost local NO_2^- ion concentrations, is primarily responsible for the low detection limit. According to the above results, the 5-AF@UIO-66 was suitable for detecting NO_2^- as a fluorescent colorimetric probe.

5.3.5. Selectivity and anti-interference performance

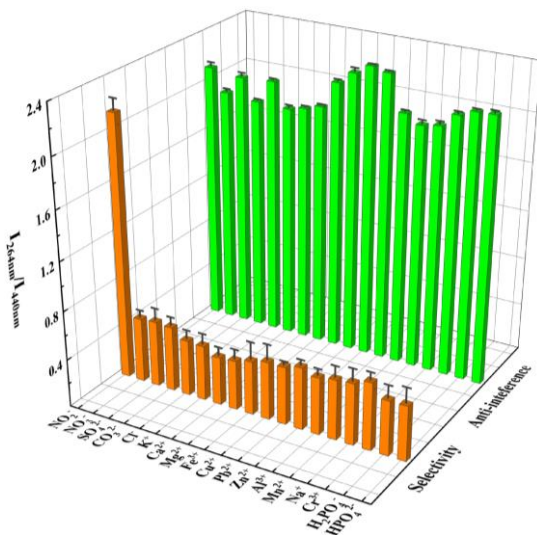


Figure 5-8 The selectivity and interference effect of proposed sensing platform. The concentration of NO_2^- is 100 μM and the concentration of all other interfering substances are ten times higher than NO_2^- .

To verify the proposed nanoprobe was exclusive for detecting NO_2^- in a real sample, the selectivity and anti-interference performance of the sensing system were further explored as crucial indicators. The fluorescent intensity ratio of 5-AF@UIO-66 in the presence of some familiar and co-existing interferences was recorded, those various anions and cations include NO_3^- , SO_4^{2-} , CO_3^{2-} , Cl^- , Cr , K^+ , Na^+ , Ca^{2+} , Mg^{2+} , Pb^{2+} , Zn^{2+} , Cu^{2+} , Mn^{2+} , Fe^{2+} , Fe^{3+} , Al^{3+} , H_2PO_4^- , and HPO_4^{2-} . The analytical results are shown in **Figure 5-8**, only NO_2^- treatment triggered the nitrosation reaction and showed a remarkable enhancing influence on the $I_{264\text{ nm}}/I_{440\text{ nm}}$ of the sensing system. However, the other interferents caused minimal or insignificant fluorescent intensity ratio changes, even as their concentrations reached 10-fold that of NO_2^- . Moreover, when 10 μM NO_2^- was introduced to the 5-AF@UIO-66 nanocomposite suspension with

the above interferents (100 μM), all groups displayed a distinct enhancing change in the fluorescent intensity ratio. The above results indicated that the effect of interferents present in meat products on the detection of NO_2^- based on 5-AF@UIO-66 can be ignored, the nanoprobe exhibited good selectivity and specificity for NO_2^- detection and could be applied NO_2^- detection in actual meat samples.

5.3.6. Precise sensing of nitrite by agarose hydrogel test kit

Based on the aforementioned strategy, we proceeded to fabricate a portable testing kit by immobilizing the well-dispersed 5-AF@UIO-66 within agarose hydrogels to obtain a solid sensing platform to realize fast, low-cost, and on-site detection of NO_2^- . The agarose (Aga) hydrogel was chosen as the supporting matrix owing to its negligible fluorescent background, controllable shape, and large loading capacity (Hou et al., 2021; Zhan et al., 2019). Furthermore, the porous structure of agarose would also enhance the diffusion mechanism of the analyte within the gel matrix (Gao et al., 2018). This portable testing kit broadened the practicability of the 5-AF@UIO-66 nanoprobe, and the process of NO_2^- detection using the test kit was demonstrated by **Figure 5-1C**. In order to detect NO_2^- distinctly and conveniently with the naked eye, we combined the Aga/5-AF@UIO-66 hydrogel portable test kit with the chemiluminescence imaging system (Fusion Fx equipped with the DarQ-9 camera). The excitation wavelength of the chemiluminescence imaging system is set to 440 nm, which is in line with the optimal fluorescence characteristics of 5-AF@UIO-66, and the most obvious color change can be observed when reacting with nitrite. On-site quantitative analysis of NO_2^- can be accomplished by capturing fluorescence images using the imaging system and evaluating their hue intensities with ImageJ software, which allows quantitative detection of targets.

To assess the analytical capabilities of the Aga/5-AF@UIO-66 agarose hydrogels for NO_2^- detection, the hydrogels were immersed in solutions containing varying concentrations of NO_2^- . As revealed in **Figure 5-9A**, the red intensity in the image color of the hydrogels test kit vanished accordingly and turned blue, and corresponding black and white images changed from bright to dark, which enables convenient visual distinction of the NO_2^- concentration based on the observed multicolor variations by the naked eye. Consequently, it holds significant promise for semiquantitative NO_2^- analysis owing to its fast detection efficiency for on-spot detection. Utilizing an image-processing method, the hue histogram can be viewed as digital data that is used to depict color-change detection (**Figure 5-9B**). Upon the increase of NO_2^- ion concentration (0–20 μM), the normalized hue intensity of the fluorescent color of Aga/5-AF@UIO-66 hydrogel test kit decreased gradually from 1.00 to 0.41. A good linear relationship between normalized hue intensity and the concentration of NO_2^- in the range of 1–20 μM was obtained from the Aga/5-AF@UIO-66 hydrogel test kit. The regression equation can be expressed as $y = -0.027x - 0.987$ ($R^2 = 0.979$), and the detection limit toward NO_2^- was calculated to be 0.43 mM (**Figure 5-9C**).

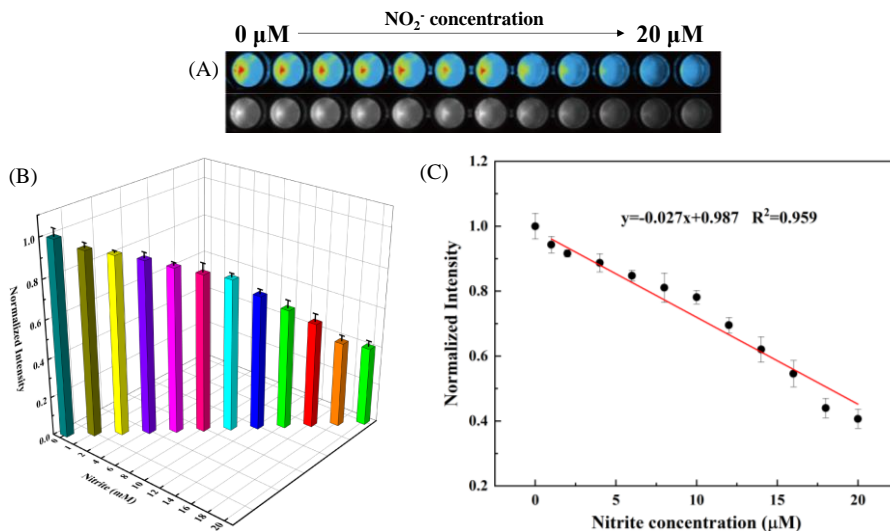


Figure 5-9 (A) The photograph of kit with different concentrations of NO_2^- . (B) The normalized hue intensity of kit digitized by ImageJ software. (C) Corresponding relationship between the concentration of NO_2^- and hue intensity.

The selectivity and anti-interference of NO_2^- are essential features to evaluate the practicality of the hydrogel test kit, especially when applied to NO_2^- -containing solutions or food matrices. Hence, the 18 common interferences were introduced on the Aga/5-AF@UIO-66 hydrogel test kit, and the fluorescence images of the hydrogel test kit in response to NO_2^- and these interferences were investigated to explore their selectivity and specificity. As depicted in **Figure 5-10A**, no significant color change of the test kit was observed by the potential interferences, only the first treatment, which added NO_2^- , exhibited noticeable fluorescent quenching. The normalized intensity histogram depicted in **Figure 5-10C** provides additional illustration that the interference substances lack the capability to initiate the diazo reaction and produce diazotized substances, whereas only NO_2^- caused a remarkable response, even though the concentration of common interferences was ten times that of NO_2^- . Additionally, simultaneous incubation NO_2^- and co-existing interferences was used to assess the anti-interference capacity of the Aga/5-AF@UIO-66 hydrogel test kit (**Figure 5-10B**). Despite the presence of other interferences at high concentrations, the Aga/5-AF@UIO-66 hydrogels all exhibited blue color variations with the naked eye. The findings were in agreement with **Figure 5-10C**, which showed the fluorescent quenching had occurred, indicating that the response of the Aga/5-AF@UIO-66 hydrogel test kit toward NO_2^- remained consistent even in the presence of interfering substances. Accordingly, the strong selectivity and anti-interference ability of the Aga/5-AF@UIO-66 hydrogel test kit are sufficient to eliminate the interference of meat components and identify NO_2^- in meat products. The integration of 5-AF@UIO-

66 with an agarose hydrogel test kit has great potential for precise monitoring of NO_2^- in real samples.

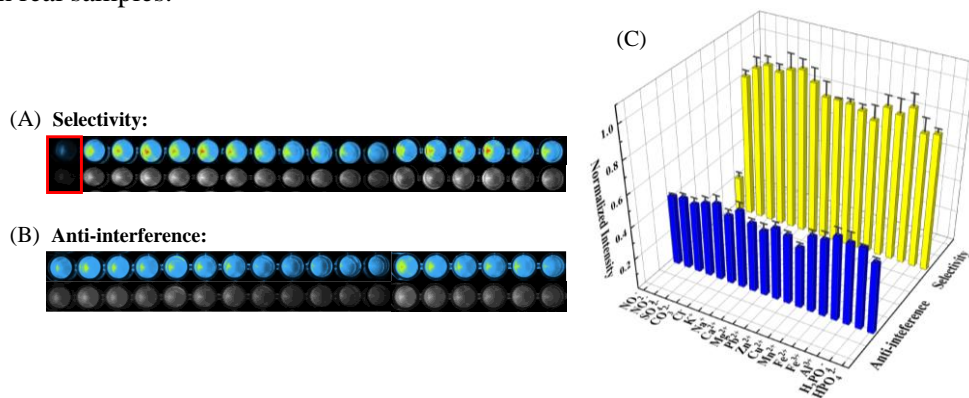









Figure 5-10 (A) Selectivity: the photographs of kit in the presence of NO_2^- or interfering ions. (B) Anti-interference: the photographs of kit in the presence of both NO_2^- and interfering ions. (C) The corresponding normalized hue intensity of selectivity and interference effect in the kit.

5.3.7. Application in actual meat samples

The colorimetric/fluorescent 5-AF@UIO-66-immobilized agarose hydrogel test kit was utilized to test NO_2^- in real meat samples (ham and stew beef) to validate its feasibility and practicality. The precision and accuracy of the test kit in NO_2^- assessment were investigated employing the standard addition approach, and the recovery rates of NO_2^- were determined based on the image of the hydrogel test kit. Both above samples were spiked with NO_2^- standard solution at three different levels: 0.28, 2.8, and 5.6 mg/kg, followed by detection. Notably, the hydrogel test kits exhibited distinct color changes before and after incubation in meat samples containing NO_2^- addition. As displayed in **Table 5-1**, the outcomes revealed that the recoveries of NO_2^- fluctuated from 95.2 to 107.1% with relative standard deviations (RSDs) less than 4%, which satisfied the monitoring requirements. Evidently, the robust and portable 5-AF@UIO-66-based agarose hydrogel possessed high analytical accuracy and reliability for monitoring NO_2^- in meat products, which offers a facile and outstanding way to ensure food safety.

Table 5-1 Nitrite Determination in meat product samples by Aga/5-AF@UIO-66 hydrogel test kit.

Samples	Added (mg/kg)	Found (mg/kg)	RSD (% , n=3)	Recovery (% , n=3)	
Control	0.00		–	–	
	0.28		3.69	2.27	107.1
Ham	2.80		6.14	2.76	98.6
	5.60		8.72	3.01	95.2
	0.28		4.40	0.82	96.4
Stewed beef	2.80		7.09	2.54	105.7
	5.60		9.67	1.46	98.9

5.3.8. Evaluation of the proposed fluorescence sensors

Compared with other previously reported methods for nitrite detection, the detectors based on these five fluorescent nanosensor platforms all demonstrated improved selectivity, detection range, and LOD. The LOD, detecting range, and response time of the Rh6G@MOF-5 nanoprobe, Rh6G@UiO-66-NH₂ nanoprobe, Gel/Rh6G@UIO-66-NH₂ hydrogel test kit, 5-AF@UIO-66 nanoprobe, and Aga/5-AF@UIO-66 portable hydrogel test kit are either outperforming or closely comparable to the most reported sensors. This is attributed to the large specific surface area of porous material, which not only accommodates more identified probes but also enhances the local concentration of nitrite ion recognition sites (Xie et al., 2020; Zhang et al., 2016) (**Table 5-2**). Furthermore, it has been confirmed that the proposed nanoprobe and its hydrogel test kit demonstrate excellent sensitivity and reliability for the detection of NO₂⁻ in the sensing system. Comparing with conventional methods (like chromatography, electrochemistry, griess assay, and capillary analysis as shown in **Table 5-2**), spectrofluorimetric method offers several advantages over conventional methods for nitrite detection, including higher sensitivity, selectivity, rapid detection, and versatility. These advantages make spectrofluorimetry (especially fluorescent nanoprobe serves as sensor) an attractive option for nitrite detection in various fields, ranging from food safety and environmental monitoring to biomedical research.

5.4. Conclusion

In conclusion, we created a platform for on-site nitrite detection based on ratiometric nanosensor 5-AF@UIO-66. With high sensitivity and rapid response, this fluorescent probe exhibited excellent nitrite detection performance. Under acidic conditions, the interaction of nitrosyl cation (NO^+) with 5-AF to generate diazotized substances enabled 5-AF@UIO-66 to accurately and stably recognize nitrite. In addition, we demonstrated the applicability of high-strength and high-load Aga/5-AF@UIO-66 hydrogels test kit in most detection scenarios, thereby supporting the viability of the suggested monitoring strategy for trace nitrite particles. The Chemiluminescence Imaging System-based detection platform could use analyte color information to semi-quantitatively estimate the nitrite content on-site, with the advantages of safety and simplicity, making it suitable for rapid trace nitrite detection. We believe that this strategy could serve as an alternative to on-site identification and the real-time monitoring of hazardous substances.

Table 5-2 Performance comparison of three novel sensor in this study compared with other reported nitrite detection methods.

Sensor Material	Year	Detecting range	Detection limit	Response time	Applications	Ref.
Tb ³⁺ @In-MOF	2018	0–70 μ M	–	–	Water samples	(Wu & Yan, 2018)
Rh110@MOF-801	2019	2–7 μ M	0.2 μ M	40 min	Tap water	(Huang et al., 2019)
UiO-66-NH ₂	2020	0–10 mM	77 μ M	120 s	Food (bream and Sausage)	(Hao et al., 2020)
UiO-66-NH ₂ -Cit	2020	0–800 μ M	–	10 min	–	(Zhu et al., 2020b)
Tb-MOF	2020	0–15.6 μ M	28.25 nM	–	Tap water	(Min et al., 2020)
Tb-MOF	2021	4–200 μ M	1.25 μ M	2 min	Water samples	(Yang et al., 2021)
Eu ³⁺ @UiO-66-(COOH) ₂	2021	0–60 μ M	0.69 μ M	–	–	(Li et al., 2021)
r-CDs	2022	0–40 μ M	0.149 μ M	15 min	Food (ham and bacon)	(Yu et al., 2022)
Chromatography (HPIEC-SCD)	2019	5–250 μ g/g	0.2 μ g/g	–	Food (fish and shrimp)	(Chiesa et al., 2019)
Electrochemistry (Cu/MWCNT/rGO)	2019	0.1–75.0 μ M	30 nM	–	Food (salami, sausage)	(Bagheri et al., 2017)
Griess assay (CQDs)	2020	2.5–100 μ M	2.5 μ M	30 min	Food (bacon, ham)	(Wu et al., 2020)
Capillary analysis (CA/EDA-CDs)	2019	20–500 μ g/L	6.5 μ g/L	20 min	Food and water	(Li et al., 2019)
Rh6G@MOF-5	This work	0–200 μ M	0.2 μ M	20 min	Food (meat products)	Chapter III
Rh6G@UIO-66-NH ₂	This work	0–100 μ M	0.021 μ M	15 min	Food (meat products)	Chapter IV
Gel/Rh6G@UIO-66-NH ₂	This work	0.1–1.5 mM	0.09 mM	15 min	–	Chapter IV
5-AF@UIO-66	This work	0–20 μ M	0.14 μ M	6 min	–	Chapter V

Study on Rapid Detection of Nitrite in Meat Products Based on Luminescent Metal-Organic Framework (LMOF) Nanocomposite

Aga/5-AF@UIO-66	This work	0–20 μM	0.43 μM	10 min	Food (meat products)	Chapter V
-----------------	-----------	--------------------	--------------------	--------	----------------------	-----------

“–”, no mentioned.

6

Chapter VI. General discussion, conclusion, and perspective

6.1. General discussion

In the realm of luminescence-based sensors, the careful selection of sensor materials is paramount to achieving effective detection of the target analyte. Typically, the luminescent performance of MOFs can be realized through two primary strategies. One approach involves synthesizing MOFs using luminescent metal ions (e.g., lanthanide ions such as Eu^{3+} , Ln^{3+} , Tb^{3+} , and Dy^{3+}) as the coordination center or employing organic ligands with aromatic or conjugated moieties as the linker. Alternatively, another strategy entails encapsulating luminescent guest molecules or nanoparticles within non-luminescent MOFs, resulting in induced luminescence (L. Xu et al., 2019). This study adopts the latter synthesis method for developing LMOF-based sensors, offering novel perspectives and expanded possibilities for nitrite detection. The three porous luminescent MOF-based materials proposed, namely Rh6G@MOF-5 , Rh6G@UIO-66-NH_2 , and 5-AF@UIO-66 , integrate both luminescence response and adsorption capabilities. This dual functionality proves advantageous for achieving superior detection performance and heightened sensitivity.

The operational mechanism of MOF-based stimuli-responsive luminescent materials predominantly relies on fluorescence quenching. Various mechanisms contribute to the fluorescence quenching observed in MOF-based sensors, with common factors including Förster resonance energy transfer (FRET), photoinduced electron transfer (PET), inner filter effect (IFE), and competition for excitation light between the MOF and analyte. FRET occurs due to the overlap between the emission spectrum of the MOF-based material and the absorption spectrum of the target analyte. The PET mechanism is activated when there exists a disparity in the energy levels of the lowest unoccupied molecular orbital (LUMO) between the luminescent MOF and the analyte. If the LUMO energy level of the analyte is lower than that of the LMOF, the excited electrons of the MOF transfer to the analyte, resulting in fluorescence quenching. IFE manifests when the excitation and/or emission light is attenuated by an absorber within the detection system. Additionally, the competition for excitation between the luminescent MOF and the analyte can lead to energy degradation, consequently causing fluorescence quenching in the MOF (Cheng et al., 2021; B. Wang et al., 2020).

6.1.1. Possible mechanism of Rh6G@MOF-5 nanoprobe to nitrite

Therefore, in chapter III, in view of better understanding the origin of the excellent NO_2^- -sensing ability of Rh6G@MOF-5 , the possible synthesis approach and fluorescence quenching mechanism of the Rh6G@MOF-5 sensing platform were investigated and expressed in **Figure 3-1**. Therefore, the optical properties of NO_2^- and the Rh6G@MOF-5 sensor were first compared. The UV-Vis absorption of NO_2^- and the fluorescence Ex and Em spectrum of Rh6G@MOF-5 were displayed in **Figure 6-1**. It is clear that NO_2^- had a characteristic UV-Vis absorption spectrum with a wide range from 320 to 500 nm. The absorption peak overlapped with the Ex peak (350 nm) of Rh6G@MOF-5 , however, no significant overlap was observed between

the Em spectrum of Rh6G@MOF-5 and the absorption spectrum of NO_2^- , suggesting that the quenched fluorescence of Rh6G@MOF-5 by NO_2^- might result from IFE rather than Förster resonance energy transfer (FRET) (Cheng et al., 2021). Previous literatures have displayed that the emission quenching between nitrite and Rh6G-based nanosensor could be ascribed to a static quenching mechanism, which is consistent with our conclusion since IFE belonged to a static quenching process (Dhanya et al., 2012; Zhang et al., 2016). The interaction of NO_2^- with Rh6G entrapped MOF-5 structure, on the other hand, depended on electron-withdrawing effect, namely, nitrosyl cation (NO^+) formed from NO_2^- in acid medium and the attack of electron deficient NO^+ with secondary amine group of Rh6G, resulting in the formation of nitroso group derivative, which quenched the representative fluorescence of rhodamine to some extent (**Figure 3-1B**) (Viboonratanasri et al., 2018; Wang et al., 2012; Zhang et al., 2016a).

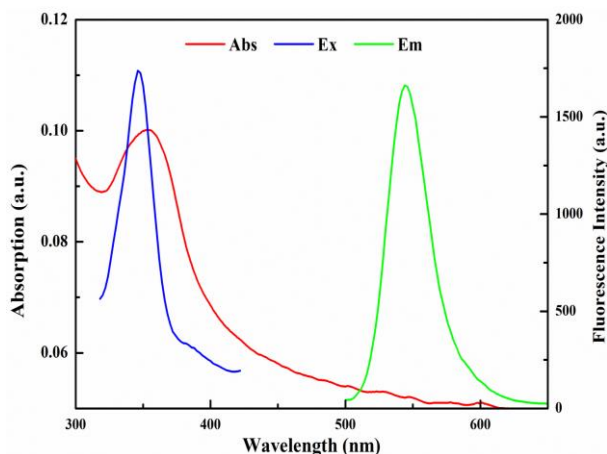


Figure 6-1 The mechanism of the Rh6G@MOF-5 sensing nanoprobe toward NO_2^- . UV-vis absorption of NO_2^- , fluorescence excitation and emission of Rh6G@MOF-5.

6.1.2. Possible mechanism of Rh6G@UiO-66-NH₂ nanoprobe to nitrite

Distinguishing from the fluorescence quenching mechanism discussed earlier, the synchronous fluorescence spectroscopy was introduced and combined it with the Rh6G@UiO-66-NH₂ nanoprobe to simultaneously gather information on both organic dyes and MOF. In this chapter, Rh6G served as a reference during the initial sensing stage. The fluorescent quenching mechanism of Rh6G@UiO-66-NH₂ may be attributed to the amino groups of UiO-66-NH₂ exposed on the nanocomposite's surface, which are more readily involved in deamination reactions with NO_2^- in the sensing system at the outset. As a result, UiO-66-NH₂, with strong fluorescence, transforms into non-fluorescent UiO-66 in a dispersed water medium due to the

changes in electron density. This result is consistent with previous reports reported by Hao et al. (2020), where UIO-66-NH₂ was successfully utilized as a fluorescence turn-off probe for the detection of NO₂⁻ through diazotization and reduction. Subsequently, with higher additions of NO₂⁻ (over 100 μM), the fluorescence intensity of Rh6G decreased significantly. In acidic conditions, an electron-deficient nitrosyl cation (NO⁺), derived from NO₂⁻, interacts with the organic dye Rh6G embedded in the MOF framework, forming a nitroso group derivative. The fluorescence of Rh6G gradually quenches due to the weak electron-donating ability of the nitroso group derivative (Viboonratanasri et al., 2018; Zhang et al., 2016).

6.1.3. Possible mechanism of 5-AF@UIO-66 nanoprobe to nitrite

To investigate the highly sensitive detection of 5-AF@UIO-66 for NO₂⁻, the spectroscopic properties of 5-AF@UIO-66 after adding different reactants were further explored. As shown in **Figure 6-2A**, there was just one fluorescent peak at excitation wavelengths near 288 nm for 5-AF@UIO-66 nanocomposite, which is based on pristine UIO-66 (line a). While there was no obvious fluorescent peak located at 440 nm in the presence of 5-AF@UIO-66 suspension. The tendency of line b is similar to that of line a, which indicated that there is no interaction between NO₂⁻ and the 5-AF@UIO-66 probe. It should be noted that a weakly acidic condition (0.3 M of HCl) could greatly induce fluorescence excitation of 5-AF, a characteristic peak at 440 nm appeared with bright green fluorescence emission (line c) because of the diazotization from protonation of the amino group of the 5-AF dye under suitable acid conditions. According to line d, the fluorescence intensity of 5-AF@UIO-66 at 440 nm was significantly quenched upon the introduction of NO₂⁻, while the fluorescent peak originating from UIO-66 at 288 nm had a minor enhancement. Additionally, the alteration in fluorescence color of 5-AF@UIO-66 under UV light changed from light green to colorless. It is speculated that the reason for this phenomenon may be caused by the interaction of nitrosyl cation (NO⁺) with 5-AF to generate diazotized substances, which reduces the original resonance energy transfer from Zr-MOF to 5-AF.

Furthermore, the proposed mechanism of NO₂⁻ on the luminescence of this LMOF sensing platform is also verified by the changes in UV-vis absorption spectra, as shown in **Figure 6-2B**. The results clearly show that the 5-AF@UIO-66 nanoprobe has a pronounced absorption peak at 481 nm. Following the interaction of 5-AF@UIO-66 with HCl, a novel absorption peak emerged approximately at 439 nm. This observation suggests that new compounds had been formed arising from the interaction of H⁺ with the surface groups on 5-AF (this reflected the formation of diazo groups) (M. Yu et al., 2022). While the absorption peak of 5-AF@UIO-66 at 439 nm gradually weakened upon NO₂⁻ addition, which confirmed the diazonium reaction between 5-AF@UIO-66 and NO₂⁻ under optimal HCl conditions and produced diazonium salt. Based on this observation, we deduce that the fluorescent response of 5-AF@UIO-66 to NO₂⁻ primarily stems from the involvement of amino groups participating in the reaction, leading to their transformation into other functional

groups upon interaction with NO_2^- ions. A part of the energy for the emission of 5-AF@UIO-66 is transferred to NO_2^- ion, hence decreasing the emission intensity, and this interaction disrupts the $n-\pi^*$ transition process of 5-AF@UIO-66 (Zhan et al., 2019; Zhang et al., 2018).

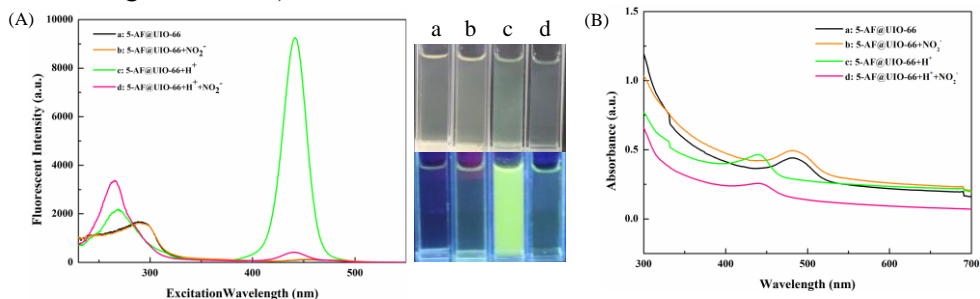


Figure 6-2 (A) Fluorescent and (B) absorbance intensity of reaction solution: 5-AF@UIO-66 (a), 5-AF@UIO-66 + NO_2^- (b), 5-AF@UIO-66 + H^+ (c), and 5-AF@UIO-66 + H^+ + NO_2^- (d).

In addition, all three fabricated LMOF fluorescence nanosensors can also serve as colorimetric sensors. Colorimetric sensors are characterized by their ability to alter optical properties upon interaction with the target analyte. These sensors offer advantages such as rapid response times, simplicity, and cost-effectiveness. In recent years, the emergence of universal digital imaging has opened new and exciting possibilities for colorimetric sensors (M. Chen et al., 2017; Huang et al., 2018). Typically, the color change in colorimetric sensors is initiated by the chromogenic reaction of optical dyes, and the quantification of target analytes can be achieved by measuring the resulting color change (Fang et al., 2018). Fluorescent chromophores, such as Rh6G or 5-AF, transition from “on” to “off” mode upon the addition of nitrite, leading to the quenching of the fluorescent emission of dyes. Therefore, as illustrated in **Figure 3-8A**, **Figure 4-8A**, and **Figure 5-7A**, the color of Rh6G@MOF-5, Rh6G@UiO-66-NH₂, and 5-AF@UIO-66 suspension respectively changed from fluorescent green, light blue, and robust green to colorless after reacting with nitrite solutions.

Previously, colorimetric sensing products, such as aptode and strips, have been developed for the quick determination of various analytes due to their practicality, simplicity, and visual quantification advantages (Reddy et al., 2017; X. Yan et al., 2017). Inspired by these studies, there is potential to create other colorimetric sensing products to expand the application scope of above powdered LMOF-based nanomaterials. The portable hydrogel test kit emerges as the primary choice, given that the sensing mechanisms of these colorimetric hydrogel sensors align with the previously mentioned colorimetric sensing principles, rendering them simpler yet advanced colorimetric sensors. In addition, some instruments or devices, including

computers, mobile phones, microscopes, and others, have been employed to enhance the sensitivity and facilitate high-throughput data analysis of colorimetric sensing products (Q. Chen et al., 2016; J. Hou et al., 2015; Kangas et al., 2017; Q. Li & Wei, 2018). In Chapter IV, a mobile phone was utilized for imaging the Gel/Rh6G@UIO-66-NH₂ hydrogel test kit sensor in dual-mode sensing under ambient lighting and UV 365 nm conditions. This resulted in a quick and convincing determination of nitrite, demonstrating potential for nitrite detection in food systems. Furthermore, a novel chemiluminescence imaging system was introduced in Chapter V as an imaging tool. Nitrite solutions were dropped on the Aga/5-AF@UIO-66 hydrogel test kit, resulting in significant color change of the agarose hydrogel under suitable acidic conditions. Finally, the chemiluminescence imaging system, assisting with the Aga/5-AF@UIO-66 hydrogel test kit, could also be used as a tool for nitrite detection in real meat products. Regardless of whether it was Gel/Rh6G@UIO-66-NH₂ or Aga/5-AF@UIO-66 hydrogel test kit, both exhibited high sensitivity and specificity. Therefore, this kind of hydrogel sensing system reveals great potential for real-time, quick, and high-throughput screening of nitrite in food safety.

6.2. Conclusions

To summarize, a hybrid and functionalized LMOF composite (Rh6G@MOF-5) was synthesized by encapsulating organic dye Rh6G into the porous crystalline Zn (II)-MOF-5 by a facile solvothermal approach. This “Turn-off” mode nanoprobe exhibited better sensing performance, such as excellent selectivity, a low detection limit (0.2 μmol/L), and a short response time (20 min) toward nitrite. Furthermore, Rh6G@MOF-5 not only served as a regulator for nitrite determination but also prolonged the fluorescence lifetime of Rh6G. It is worth noting that this nanocomposite presents high reliability, sensitivity, and convenience for nitrite detection for meat product testing. Therefore, it may be a promising candidate for the detection of nitrite ions in complex food systems or supply effective guidance to design dye-loading LMOF materials for trace substance detection.

Besides, a ratiometric fluorescence sensing probe (Rh6G@UIO-66-NH₂) for NO₂⁻ detection in meat products was successfully developed. After combining Rh6G and UIO-66-NH₂, the resulting Rh6G@UIO-66-NH₂ showed significantly improved NO₂⁻ capture efficiency, along with fast response kinetics, high sensitivity, excellent selectivity, and a low detection limit. The proposed method was successfully applied to detect NO₂⁻ in five different meat products with a high level of accuracy, indicating its potential for practical applications. Furthermore, a dual-mode portable test kit (Gel/Rh6G@UIO-66-NH₂ hydrogel kit) was further constructed using gelatin hydrogel as a matrix, which was employed for on-site detection of NO₂⁻ via combining with a smartphone based on fluorescent and visible nanocolorimetry. Owing to its excellent portability, cost-effectiveness, simplicity of operation, rapid response features, and vibrant color display, the Gel/Rh6G@UIO-66-NH₂ hydrogels

kit holds great promise and potential for convenient on-site visual detection and precise monitoring of NO_2^- in food samples.

In addition, the Zr-based MOF UIO-66 as an internal reference we opted, successfully synthesizing a facile, time-saving, and cost-effective nanocomposite (5-AF@UIO-66) that functions as a sensitive and selective sensor for NO_2^- ions. In the presence of NO_2^- ions, this ratiometric fluorescent nanocomposite both undergoes colorimetric color (transition from green to colorless) and fluorescence changes, which has improved sensing performance with a short response time (6 min) and a low detection limit (0.14 μM) for NO_2^- ions. In light of the above strategy, we further chose agarose hydrogel as a solid-phase scaffold to synthesize an Aga/5-AF@UIO-66 fluorescence test kit. This portable test kit combined with chemiluminescence imaging system-based nanocolorimetry, with the help of translating its photofluorescent images into digital information, was employed for on-site and in situ monitoring of NO_2^- in a low-cost and highly efficient manner. The results demonstrated that the vivid colors of the test kit could be used for visual semiquantitative NO_2^- detection with the naked eye within 10 min, and the Aga/5-AF@UIO-66-based hydrogel test kit validated the potential application with satisfactory recoveries in meat samples. Hence, the proposed hydrogel test kit, which possesses great advantages and convenience, offers a prospective method for the on-site reliable detection of NO_2^- in food safety management.

In addition, it is worth noting that this spectrofluorimetric method offers higher sensitivity compared to conventional methods. Fluorescent probes can exhibit strong and specific responses to nitrite ions, allowing for the detection of nitrite at lower concentrations. In addition, these proposed LMOF-based fluorescent probes can be designed to exhibit high selectivity for nitrite ions over other interfering substances. By carefully selecting the probe molecule and tuning its properties, fluorescence spectroscopy can achieve excellent selectivity, reducing the likelihood of false-positive or false-negative results. This enhanced selectivity is crucial in complex sample matrices. Moreover, the fluorescence signal generated by the interaction between the fluorescent probe and nitrite ions can be measured quickly and accurately, allowing for rapid analysis of samples. This rapid detection capability is advantageous in applications where timely results are essential, such as on-site testing or continuous monitoring. Thus, this versatility makes spectrofluorimetry combining LMOF nanosensor a valuable tool for nitrite detection in diverse applications.

6.3. Perspectives

In this study, three novel LMOF-based fluorescence nanosensors have been developed and successfully applied to detect nitrite in real meat samples. They all represented excellent selectivity and sensitivity to nitrite in fluorescent sensing process, achieving satisfactory recoveries in real sample applications. Therefore, developing novel MOFs materials with good stability and applying them in the food

industry is one of the worthwhile directions for future intensive study. Based on the foundation laid by previous studies and the scope of this work, some prospects for future research directions are proposed as follows:

(1) Three novel LMOF nanoprobe established in this study are categorized as “turn-off” type fluorescent sensors, with the luminescent guests belonging to the category of fluorescent dyes. However, fluorescent-based nanosensors involve both fluorescence enhancement (turn-on) and fluorescence quenching (turn-off) of the fluorophore. Turn-on type nanosensors are emerging as a powerful alternative due to their sensitivity, simplicity, rapidity, good specificity, ease of mass fabrication, and suitability for field use. In further research, we can design novel “turn-on” type LMOF composite materials based on fluorogens with Aggregation-induced emission characteristics (AIEgens) for nitrite detection. This approach paves the way for enabling “turn-on” type luminescent sensors for practical applications in nitrite detection.

(2) The phenomenon of aggregation-induced emission (AIE) is characterized by weak or negligible emissions in dilute solutions but strong emissions in aggregated or solid-state states, attributed to the restriction of intramolecular rotation (RIR). This presents a promising strategy for constructing crystalline MOFs with high fluorescent emissions, particularly for optical sensing applications. With an in-depth analysis of the latest applications, this emerging and powerful AIE sensing platform exhibits the outstanding advantages of rapidity, high sensitivity, and good accuracy in analytes detection, as well as predestined capabilities in constructing portable solid-state sensors. Due to these characteristics in combination with other unique benefits, including structural diversity and excellent photophysical properties, the free phenyl rings of the tetraphenylethylene (TPE)-based linker can function as dynamic AIE molecular rotors in a MOF structure to form the novel sensor AIE@MOF, AIE@MOF sensing platforms offer new methods and technologies for monitoring food quality and safety.

(3) In addition to detecting nitrite in meat products, our future research direction can shift towards monitoring the shelf life of meat products or the freshness of raw meat cooperating with MOF-based sensing tools. The use of high food safety-rated natural pigments as colorants for intelligent food packaging is a future development direction. Therefore, our future research can be based on different types of natural pigments (such as anthocyanins) and MOF composite nanomaterials to prepare chromatic intelligent packaging indicator films for real-time monitoring of changes in the quality of meat products. This type of intelligent food packaging indicator film primarily detects changes in the internal environment of the packaging or the meat products within using indicator labels and obtains information on the quality and safety of the food during storage and transportation through color changes in the indicator film. This can provide consumers with food safety information.

References

- Abid, H. R., Ang, H. M., & Wang, S. (2012). Effects of ammonium hydroxide on the structure and gas adsorption of nanosized Zr-MOFs (UiO-66). *Nanoscale*, 4(10), 3089–3094. <https://doi.org/10.1039/C2NR30244F>
- Abou-Zeid, R. E., Awwad, N. S., Nabil, S., Salama, A., & Youssef, M. A. (2019). Oxidized alginate/gelatin decorated silver nanoparticles as new nanocomposite for dye adsorption. *International Journal of Biological Macromolecules*, 141, 1280–1286. <https://doi.org/10.1016/j.ijbiomac.2019.09.076>
- Aghili, F., Ghoreyshi, A. A., Rahimpour, A., & Van der Bruggen, B. (2020). New Chemistry for Mixed Matrix Membranes: Growth of Continuous Multilayer UiO-66-NH₂ on UiO-66-NH₂-Based Polyacrylonitrile for Highly Efficient Separations. *Industrial & Engineering Chemistry Research*, 59(16), 7825–7838. <https://doi.org/10.1021/acs.iecr.9b07063>
- Aghili, F., Ghoreyshi, A. A., Van der Bruggen, B., & Rahimpour, A. (2021). Introducing gel-based UiO-66-NH₂ into polyamide matrix for preparation of new super hydrophilic membrane with superior performance in dyeing wastewater treatment. *Journal of Environmental Chemical Engineering*, 9(4), 105484. <https://doi.org/10.1016/j.jece.2021.105484>
- Ahmad, S., Ahmad, M., Manzoor, K., Purwar, R., & Ikram, S. (2019). A review on latest innovations in natural gums based hydrogels: Preparations & applications. *International Journal of Biological Macromolecules*, 136, 870–890. <https://doi.org/10.1016/j.ijbiomac.2019.06.113>
- Almeida, L. E. F., Kamimura, S., de Souza Batista, C. M., Spornick, N., Nettleton, M. Y., Walek, E., Smith, M. L., Finkel, J. C., Darbari, D. S., Wakim, P., & Quezado, Z. M. N. (2020). Sick cell disease subjects and mouse models have elevated nitrite and cGMP levels in blood compartments. *Nitric Oxide*, 94, 79–91. <https://doi.org/10.1016/j.niox.2019.10.011>
- Altunay, N., & Elik, A. (2020). A green and efficient vortex-assisted liquid-phase microextraction based on supramolecular solvent for UV–VIS determination of nitrite in processed meat and chicken products. *Food Chemistry*, 332, 127395. <https://doi.org/10.1016/j.foodchem.2020.127395>
- Alvarado, C., & McKee, S. (2007). Marination to Improve Functional Properties and Safety of Poultry Meat. *Journal of Applied Poultry Research*, 16(1), 113–120. <https://doi.org/10.1093/japr/16.1.113>
- Aminzare, M., Hashemi, M., Ansarian, E., Bimkar, M., Azar, H. H., Mehrasbi, M. R., Daneshamooz, S., Raeisi, M., Jannat, B., & Afshari, A. (2019). Using Natural Antioxidants in Meat and Meat Products as Preservatives: A Review. *Advances in Animal and Veterinary Sciences*, 7(5). <https://doi.org/10.17582/journal.aavs/2019/7.5.417.426>
- Ananthoji, R., Eubank, J. F., Nouar, F., Mouttaki, H., Eddaoudi, M., & Harmon, J. P. (2011). Symbiosis of zeolite-like metal–organic frameworks (rho-ZMOF) and hydrogels: Composites for controlled drug release. *Journal of Materials Chemistry*, 21(26), 9587–9594. <https://doi.org/10.1039/C1JM11075F>

- Axelrod, H. D., & Engel, N. A. (1975). Fluorometric determination of subnanogram levels of nitrite using 5-aminofluorescein. *Analytical Chemistry*, 47(6), 922–924. <https://doi.org/10.1021/ac60356a054>
- Badea, M., Amine, A., Benzine, M., Curulli, A., Moscone, D., Lupu, A., Volpe, G., & Palleschi, G. (2004). Rapid and Selective Electrochemical Determination of Nitrite in Cured Meat in the Presence of Ascorbic Acid. *Microchimica Acta*, 147(1–2). <https://doi.org/10.1007/s00604-004-0220-8>
- Badsha, M. A. H., Khan, M., Wu, B., Kumar, A., & Lo, I. M. C. (2021). Role of surface functional groups of hydrogels in metal adsorption: From performance to mechanism. *Journal of Hazardous Materials*, 408, 124463. <https://doi.org/10.1016/j.jhazmat.2020.124463>
- Bae, Y. J., Cho, E. S., Qiu, F., Sun, D. T., Williams, T. E., Urban, J. J., & Queen, W. L. (2016). Transparent Metal–Organic Framework/Polymer Mixed Matrix Membranes as Water Vapor Barriers. *ACS Applied Materials & Interfaces*, 8(16), 10098–10103. <https://doi.org/10.1021/acsami.6b01299>
- Bagheri, H., Hajian, A., Rezaei, M., & Shirzadmehr, A. (2017). Composite of Cu metal nanoparticles-multiwall carbon nanotubes-reduced graphene oxide as a novel and high performance platform of the electrochemical sensor for simultaneous determination of nitrite and nitrate. *Journal of Hazardous Materials*, 324, 762–772. <https://doi.org/10.1016/j.jhazmat.2016.11.055>
- Bedale, W., Sindelar, J. J., & Milkowski, A. L. (2016). Dietary nitrate and nitrite: Benefits, risks, and evolving perceptions. *Meat Science*, 120, 85–92. <https://doi.org/10.1016/j.meatsci.2016.03.009>
- Benkerroum, N. (2016). Biogenic Amines in Dairy Products: Origin, Incidence, and Control Means. *Comprehensive Reviews in Food Science and Food Safety*, 15(4), 801–826. <https://doi.org/10.1111/1541-4337.12212>
- Berardi, G., Albenzio, M., Marino, R., D’Amore, T., Di Taranto, A., Vita, V., & Iammarino, M. (2021). Different use of nitrite and nitrate in meats: A survey on typical and commercial Italian products as a contribution to risk assessment. *LWT*, 150, 112004. <https://doi.org/10.1016/j.lwt.2021.112004>
- Berardo, A., De Maere, H., Stavropoulou, D. A., Rysman, T., Leroy, F., & De Smet, S. (2016). Effect of sodium ascorbate and sodium nitrite on protein and lipid oxidation in dry fermented sausages. *Meat Science*, 121, 359–364. <https://doi.org/10.1016/j.meatsci.2016.07.003>
- Bergamaschi, G., Musicò, A., Frigerio, R., Strada, A., Pizzi, A., Talone, B., Ghezzi, J., Gautieri, A., Chiari, M., Metrangolo, P., Vanna, R., Baldelli Bombelli, F., Cretich, M., & Gori, A. (2022). Composite Peptide–Agarose Hydrogels for Robust and High-Sensitivity 3D Immunoassays. *ACS Applied Materials & Interfaces*, 14(4), 4811–4822. <https://doi.org/10.1021/acsami.1c18466>
- Bhardwaj, N., Bhardwaj, S., Mehta, J., Kim, K.-H., & Deep, A. (2016). Highly sensitive detection of dipicolinic acid with a water-dispersible terbium-metal organic framework. *Biosensors and Bioelectronics*, 86, 799–804. <https://doi.org/10.1016/j.bios.2016.07.063>
- Bhat, R., Rai, R. V., & Karim, A. A. (2010). Mycotoxins in Food and Feed: Present Status

- and Future Concerns. *Comprehensive Reviews in Food Science and Food Safety*, 9(1), 57–81. <https://doi.org/10.1111/j.1541-4337.2009.00094.x>
- Biswas, S., Chowdhury, B., & Ray, B. C. (2004). A novel spectrofluorimetric method for the ultra trace analysis of nitrite and nitrate in aqueous medium and its application to air, water, soil and forensic samples. *Talanta*, 64(2), 308–312. <https://doi.org/10.1016/j.talanta.2004.02.018>
- Brender, J., Olive, J., Felkner, M., Suarez, L., Hendricks, K., & Marckwardt, W. (2004). INTAKE OF NITRATES AND NITRITES AND BIRTH DEFECTS IN OFFSPRING. *Epidemiology*, 15(4), S184.
- Brockgreitens, J., & Abbas, A. (2016). Responsive Food Packaging: Recent Progress and Technological Prospects. *Comprehensive Reviews in Food Science and Food Safety*, 15(1), 3–15. <https://doi.org/10.1111/1541-4337.12174>
- Canbay, E., Şahin, B., Kiran, M., & Akyilmaz, E. (2015). MWCNT–cysteamine–Nafion modified gold electrode based on myoglobin for determination of hydrogen peroxide and nitrite. *Bioelectrochemistry*, 101, 126–131. <https://doi.org/10.1016/j.bioelechem.2014.09.001>
- Cao, M., Xiao, F., Yang, Z., Chen, Y., & Lin, L. (2022). Purification of oil-containing emulsified wastewater via PAN nanofiber membrane loading PVP–UiO-66–NH₂. *Separation and Purification Technology*, 297, 121514. <https://doi.org/10.1016/j.seppur.2022.121514>
- Chakraborty, A., Sutar, P., Yadav, P., Eswaramoorthy, M., & Maji, T. K. (2018). Charge-Assisted Self-Assembly of ZIF-8 and Laponite Clay toward a Functional Hydrogel Nanocomposite. *Inorganic Chemistry*, 57(23), 14480–14483. <https://doi.org/10.1021/acs.inorgchem.8b02545>
- Chang, C., & Zhang, L. (2011). Cellulose-based hydrogels: Present status and application prospects. *Carbohydrate Polymers*, 84(1), 40–53. <https://doi.org/10.1016/j.carbpol.2010.12.023>
- Chang, R.-M., Zhang, Y.-Y., Zhang, G.-B., Zhang, X.-X., Chen, A.-J., Zhang, W., & Li, Y. (2022). Application of thermal alkaline hydrolysis technology to improve the loading and in-vitro release of gallic acid in UiO-66. *Food Chemistry*, 391, 133238. <https://doi.org/10.1016/j.foodchem.2022.133238>
- Chang, Z., Yang, D.-H., Xu, J., Hu, T.-L., & Bu, X.-H. (2015). Flexible Metal–Organic Frameworks: Recent Advances and Potential Applications. *Advanced Materials*, 27(36), 5432–5441. <https://doi.org/10.1002/adma.201501523>
- Chen, D.-M., Zhang, N.-N., Liu, C.-S., & Du, M. (2017). Dual-Emitting Dye@MOF Composite as a Self-Calibrating Sensor for 2,4,6-Trinitrophenol. *ACS Applied Materials & Interfaces*, 9(29), 24671–24677. <https://doi.org/10.1021/acsami.7b07901>
- Chen, F., Wang, Y.-M., Guo, W., & Yin, X.-B. (2019). Color-tunable lanthanide metal–organic framework gels. *Chemical Science*, 10(6), 1644–1650. <https://doi.org/10.1039/C8SC04732D>
- Chen, H., Qiu, C., Jiang, Y., Liao, X., Wu, D., Shen, M., & Ding, T. (2022). Silver nanoparticles on UiO-66 (Zr) metal-organic frameworks for water disinfection application. *Food Science and Human Wellness*, 11(2), 269–276.

- <https://doi.org/10.1016/j.fshw.2021.11.017>
- Chen, M., Gan, N., Zhou, Y., Li, T., Xu, Q., Cao, Y., & Chen, Y. (2017). A novel aptamer-metal ions- nanoscale MOF based electrochemical biocodes for multiple antibiotics detection and signal amplification. *Sensors and Actuators B: Chemical*, 242, 1201–1209. <https://doi.org/10.1016/j.snb.2016.08.185>
- Chen, Q., Hu, W., Su, J., Li, H., Ouyang, Q., & Zhao, J. (2016). Nondestructively sensing of total viable count (TVC) in chicken using an artificial olfaction system based colorimetric sensor array. *Journal of Food Engineering*, 168, 259–266. <https://doi.org/10.1016/j.jfoodeng.2015.08.003>
- Chen, T., Tong, A., & Zhou, Y. (2007). 2-Amino-5,7-dimethyl-1,8-naphthyridine as a fluorescent reagent for the determination of nitrite. *Spectrochimica Acta Part A: Molecular and Biomolecular Spectroscopy*, 66(3), 586–589. <https://doi.org/10.1016/j.saa.2006.03.036>
- Chen, W.-H., Liao, W.-C., Sohn, Y. S., Fadeev, M., Cecconello, A., Nechushtai, R., & Willner, I. (2018). Stimuli-Responsive Nucleic Acid-Based Polyacrylamide Hydrogel-Coated Metal–Organic Framework Nanoparticles for Controlled Drug Release. *Advanced Functional Materials*, 28(8), 1705137. <https://doi.org/10.1002/adfm.201705137>
- Chen, W.-M., Meng, X.-L., Zhuang, G.-L., Wang, Z., Kurmoo, M., Zhao, Q.-Q., Wang, X.-P., Shan, B., Tung, C.-H., & Sun, D. (2017). A superior fluorescent sensor for Al³⁺ and UO₂²⁺ based on a Co(II) metal–organic framework with exposed pyrimidyl Lewis base sites. *Journal of Materials Chemistry A*, 5(25), 13079–13085. <https://doi.org/10.1039/C7TA01546A>
- Chen, Z., Jiang, H., Li, M., O’Keeffe, M., & Eddaoudi, M. (2020). Reticular Chemistry 3.2: Typical Minimal Edge-Transitive Derived and Related Nets for the Design and Synthesis of Metal–Organic Frameworks. *Chemical Reviews*, 120(16), 8039–8065. <https://doi.org/10.1021/acs.chemrev.9b00648>
- Cheng, W., Tang, X., Zhang, Y., Wu, D., & Yang, W. (2021). Applications of metal-organic framework (MOF)-based sensors for food safety: Enhancing mechanisms and recent advances. *Trends in Food Science & Technology*, 112, 268–282. <https://doi.org/10.1016/j.tifs.2021.04.004>
- Chiesa, L., Arioli, F., Pavlovic, R., Villa, R., & Panseri, S. (2019). Detection of nitrate and nitrite in different seafood. *Food Chemistry*, 288, 361–367. <https://doi.org/10.1016/j.foodchem.2019.02.125>
- Chopra, S., Dhumal, S., Abeli, P., Beaudry, R., & Almenar, E. (2017). Metal-organic frameworks have utility in adsorption and release of ethylene and 1-methylcyclopropene in fresh produce packaging. *Postharvest Biology and Technology*, 130, 48–55. <https://doi.org/10.1016/j.postharvbio.2017.04.001>
- Cross, A. J., Ferrucci, L. M., Risch, A., Graubard, B. I., Ward, M. H., Park, Y., Hollenbeck, A. R., Schatzkin, A., & Sinha, R. (2010). A Large Prospective Study of Meat Consumption and Colorectal Cancer Risk: An Investigation of Potential Mechanisms Underlying this Association. *Cancer Research*, 70(6), 2406–2414. <https://doi.org/10.1158/0008-5472.CAN-09-3929>
- da Luz, L. L., Milani, R., Felix, J. F., Ribeiro, I. R. B., Talhavini, M., Neto, B. A. D.,

- Chojnacki, J., Rodrigues, M. O., & Júnior, S. A. (2015). Inkjet Printing of Lanthanide–Organic Frameworks for Anti-Counterfeiting Applications. *ACS Applied Materials & Interfaces*, 7(49), 27115–27123. <https://doi.org/10.1021/acsami.5b06301>
- Dankowska, A., & Kowalewski, W. (2019a). Comparison of different classification methods for analyzing fluorescence spectra to characterize type and freshness of olive oils. *European Food Research and Technology*, 245(3), 745–752. <https://doi.org/10.1007/s00217-018-3196-z>
- Dankowska, A., & Kowalewski, W. (2019b). Tea types classification with data fusion of UV–Vis, synchronous fluorescence and NIR spectroscopies and chemometric analysis. *Spectrochimica Acta Part A: Molecular and Biomolecular Spectroscopy*, 211, 195–202. <https://doi.org/10.1016/j.saa.2018.11.063>
- Das, P., Biswas, S., Bhattacharya, S. S., & Nath, P. (2022). Carbon Nanodot–Neutral Red–Based Photometric and Fluorescence Sensing for Trace Detection of Nitrite in Water and Soil Using Smartphone. *ACS Applied Nano Materials*, 5(3), 3265–3274. <https://doi.org/10.1021/acsanm.1c03702>
- Davis, T. A., Volesky, B., & Mucci, A. (2003). A review of the biochemistry of heavy metal biosorption by brown algae. *Water Research*, 37(18), 4311–4330. [https://doi.org/10.1016/S0043-1354\(03\)00293-8](https://doi.org/10.1016/S0043-1354(03)00293-8)
- de Lima, H. H. C., da Silva, C. T. P., Kupfer, Vicente. L., de C. Rinaldi, J., Kioshima, E. S., Mandelli, D., Guilherme, M. R., & Rinaldi, A. W. (2021). Synthesis of resilient hybrid hydrogels using UiO-66 MOFs and alginate (hydroMOFs) and their effect on mechanical and matter transport properties. *Carbohydrate Polymers*, 251, 116977. <https://doi.org/10.1016/j.carbpol.2020.116977>
- Della Rocca, J., Liu, D., & Lin, W. (2011). Nanoscale Metal–Organic Frameworks for Biomedical Imaging and Drug Delivery. *Accounts of Chemical Research*, 44(10), 957–968. <https://doi.org/10.1021/ar200028a>
- Deng, S., Bai, X., Li, Y., Wang, B., Kong, B., Liu, Q., & Xia, X. (2021). Changes in moisture, colour, residual nitrites and N-nitrosamine accumulation of bacon induced by nitrite levels and dry-frying temperatures. *Meat Science*, 181, 108604. <https://doi.org/10.1016/j.meatsci.2021.108604>
- Deng, S., Liu, H., Zhang, C., Yang, X., & Blecker, C. (2022). LMOF serve as food preservative nanosensor for sensitive detection of nitrite in meat products. *LWT*, 169, 114030. <https://doi.org/10.1016/j.lwt.2022.114030>
- Deng, S., Liu, J., Han, D., Yang, X., Liu, H., Zhang, C., & Blecker, C. (2024). Synchronous fluorescence detection of nitrite in meat products based on dual-emitting dye@MOF and its portable hydrogel test kit. *Journal of Hazardous Materials*, 463, 132898. <https://doi.org/10.1016/j.jhazmat.2023.132898>
- Deng, Y., Qian, J., Zhou, Y., & Niu, Y. (2021). Preparation of N/S doped carbon dots and their application in nitrite detection. *RSC Advances*, 11(18), 10922–10928. <https://doi.org/10.1039/D0RA10766B>
- Dhanya, S., Joy, J., & Rao, T. P. (2012). Fabrication and characterization of rhodamine 6G entrapped sol–gel film test strip for virtually specific and sensitive sensing of nitrite. *Sensors and Actuators B: Chemical*, 173, 510–516.

- <https://doi.org/10.1016/j.snb.2012.07.050>
- Ebrahim, F. M., Nguyen, T. N., Shyshkanov, S., Gładysiak, A., Favre, P., Zacharia, A., Itskos, G., Dyson, P. J., & Stylianou, K. C. (2019). Selective, Fast-Response, and Regenerable Metal–Organic Framework for Sampling Excess Fluoride Levels in Drinking Water. *Journal of the American Chemical Society*, *141*(7), 3052–3058. <https://doi.org/10.1021/jacs.8b11907>
- Fang, X., Zong, B., & Mao, S. (2018). Metal–Organic Framework-Based Sensors for Environmental Contaminant Sensing. *Nano-Micro Letters*, *10*(4), 64. <https://doi.org/10.1007/s40820-018-0218-0>
- Ferysiuk, K., & Wójciak, K. M. (2020). Reduction of Nitrite in Meat Products through the Application of Various Plant-Based Ingredients. *Antioxidants*, *9*(8), Article 8. <https://doi.org/10.3390/antiox9080711>
- Filgueiras, M. F., de Jesus, P. C., & Borges, E. M. (2021). Quantification of Nitrite in Food and Water Samples Using the Griess Assay and Digital Images Acquired Using a Desktop Scanner. *Journal of Chemical Education*, *98*(10), 3303–3311. <https://doi.org/10.1021/acs.jchemed.0c01392>
- Flores, M., & Toldrá, F. (2021). Chemistry, safety, and regulatory considerations in the use of nitrite and nitrate from natural origin in meat products—Invited review. *Meat Science*, *171*, 108272. <https://doi.org/10.1016/j.meatsci.2020.108272>
- Fraihat, S. M. (2017). Green methods for the determination of nitrite in water samples based on a novel diazo coupling reaction. *Green Processing and Synthesis*, *6*(2), 245–248. <https://doi.org/10.1515/gps-2016-0005>
- Furukawa, H., Cordova, K. E., O’Keeffe, M., & Yaghi, O. M. (2013). The Chemistry and Applications of Metal-Organic Frameworks. *Science*, *341*(6149), 1230444. <https://doi.org/10.1126/science.1230444>
- Gao, D.-Y., Liu, Z., & Cheng, Z.-L. (2022). Superhydrophilic and underwater superoleophobic in-situ derived 2D Ni-Fe MOF/HNTs composite-enhanced polyvinyl alcohol (PVA) hydrogel membrane for gravity-driven oil/water separation. *Journal of Environmental Chemical Engineering*, *10*(3), 107904. <https://doi.org/10.1016/j.jece.2022.107904>
- Gao, F., Zhang, L., Wang, L., She, S., & Zhu, C. (2005). Ultrasensitive and selective determination of trace amounts of nitrite ion with a novel fluorescence probe mono[6-N(2-carboxy-phenyl)]-β-cyclodextrin. *Analytica Chimica Acta*, *533*(1), 25–29. <https://doi.org/10.1016/j.aca.2004.10.082>
- Gao, N., Huang, J., Wang, L., Feng, J., Huang, P., & Wu, F. (2018). Ratiometric fluorescence detection of phosphate in human serum with a metal-organic frameworks-based nanocomposite and its immobilized agarose hydrogels. *Applied Surface Science*, *459*, 686–692. <https://doi.org/10.1016/j.apsusc.2018.08.092>
- Gao, X., Wang, Y., Ji, G., Cui, R., & Liu, Z. (2018). One-pot synthesis of hierarchical-pore metal–organic frameworks for drug delivery and fluorescent imaging. *CrystEngComm*, *20*(8), 1087–1093. <https://doi.org/10.1039/C7CE02053H>
- Garai, A., Shepherd, W., Huo, J., & Bradshaw, D. (2013). Biomineral-inspired growth of metal–organic frameworks in gelatin hydrogel matrices. *Journal of Materials*

- Chemistry B*, 1(30), 3678–3684. <https://doi.org/10.1039/C3TB20814A>
- Gayathri, K., Vinothkumar, K., Teja, Y. N., Al-Shehri, B. M., Selvaraj, M., Sakar, M., & Balakrishna, R. G. (2022). Ligand-mediated band structure engineering and physiochemical properties of UiO-66 (Zr) metal-organic frameworks (MOFs) for solar-driven degradation of dye molecules. *Colloids and Surfaces A: Physicochemical and Engineering Aspects*, 653, 129992. <https://doi.org/10.1016/j.colsurfa.2022.129992>
- Geng, Y., Wang, Z., Zhou, J., Zhu, M., Liu, J., & James, T. D. (2023). Recent progress in the development of fluorescent probes for imaging pathological oxidative stress. *Chemical Society Reviews*, 52(11), 3873–3926. <https://doi.org/10.1039/D2CS00172A>
- Genis, D. O., Bilge, G., Sezer, B., Durna, S., & Boyaci, I. H. (2019). Identification of cow, buffalo, goat and ewe milk species in fermented dairy products using synchronous fluorescence spectroscopy. *Food Chemistry*, 284, 60–66. <https://doi.org/10.1016/j.foodchem.2019.01.093>
- Georgescu-State, R., van Staden, J. (Koos) F., & Popescu-Mandoc, L.-R. (2018). Fluorimetric determination of nitrite in water using a novel fluorescent dye. *Microchemical Journal*, 137, 418–421. <https://doi.org/10.1016/j.microc.2017.11.021>
- Gong, J., Venkateswaran, S., Tanner, M. G., Stone, J. M., & Bradley, M. (2019). Polymer Microarrays for the Discovery and Optimization of Robust Optical-Fiber-Based pH Sensors. *ACS Combinatorial Science*, 21(5), 417–424. <https://doi.org/10.1021/acscmbosci.9b00031>
- Greer, F. R., Shannon, M., the Committee on Nutrition, & and the Committee on Environmental Health. (2005). Infant Methemoglobinemia: The Role of Dietary Nitrate in Food and Water. *Pediatrics*, 116(3), 784–786. <https://doi.org/10.1542/peds.2005-1497>
- Griesche, C., & Baeumner, A. J. (2020). Biosensors to support sustainable agriculture and food safety. *TrAC Trends in Analytical Chemistry*, 128, 115906. <https://doi.org/10.1016/j.trac.2020.115906>
- Griffiths, E., Dooley, D., Graham, M., Van Domselaar, G., Brinkman, F. S. L., & Hsiao, W. W. L. (2017). Context Is Everything: Harmonization of Critical Food Microbiology Descriptors and Metadata for Improved Food Safety and Surveillance. *Frontiers in Microbiology*, 8. <https://www.frontiersin.org/articles/10.3389/fmicb.2017.01068>
- Guo, L., Liu, Y., Kong, R., Chen, G., Liu, Z., Qu, F., Xia, L., & Tan, W. (2019). A Metal–Organic Framework as Selectivity Regulator for Fe³⁺ and Ascorbic Acid Detection. *Analytical Chemistry*, 91(19), 12453–12460. <https://doi.org/10.1021/acs.analchem.9b03143>
- Guo, L., Liu, Y., Kong, R., Chen, G., Wang, H., Wang, X., Xia, L., & Qu, F. (2019). Turn-on fluorescence detection of β -glucuronidase using RhB@MOF-5 as an ultrasensitive nanoprobe. *Sensors and Actuators B: Chemical*, 295, 1–6. <https://doi.org/10.1016/j.snb.2019.05.064>
- Guo, X., Wang, Y., Qin, Y., Shen, P., & Peng, Q. (2020). Structures, properties and

- application of alginic acid: A review. *International Journal of Biological Macromolecules*, *162*, 618–628. <https://doi.org/10.1016/j.ijbiomac.2020.06.180>
- Guo, X., Zhu, N., Lou, Y., Ren, S., Pang, S., He, Y., Chen, X.-B., Shi, Z., & Feng, S. (2020). A stable nanoscaled Zr-MOF for the detection of toxic mycotoxin through a pH-modulated ratiometric luminescent switch. *Chemical Communications*, *56*(40), 5389–5392. <https://doi.org/10.1039/D0CC01006E>
- Guo, Y., Bae, J., Fang, Z., Li, P., Zhao, F., & Yu, G. (2020). Hydrogels and Hydrogel-Derived Materials for Energy and Water Sustainability. *Chemical Reviews*, *120*(15), 7642–7707. <https://doi.org/10.1021/acs.chemrev.0c00345>
- Guo, Y., Wang, R., Wei, C., Li, Y., Fang, T., & Tao, T. (2023). Carbon quantum dots for fluorescent detection of nitrite: A review. *Food Chemistry*, *415*, 135749. <https://doi.org/10.1016/j.foodchem.2023.135749>
- Gutiérrez, M., Zhang, Y., & Tan, J.-C. (2022). Confinement of Luminescent Guests in Metal–Organic Frameworks: Understanding Pathways from Synthesis and Multimodal Characterization to Potential Applications of LG@MOF Systems. *Chemical Reviews*, *122*(11), 10438–10483. <https://doi.org/10.1021/acs.chemrev.1c00980>
- Han, M.-L., Wen, G.-X., Dong, W.-W., Zhou, Z.-H., Wu, Y.-P., Zhao, J., Li, D.-S., Ma, L.-F., & Bu, X. (2017). A heterometallic sodium–europium-cluster-based metal–organic framework as a versatile and water-stable chemosensor for antibiotics and explosives. *Journal of Materials Chemistry C*, *5*(33), 8469–8474. <https://doi.org/10.1039/C7TC02885G>
- Hao, X., Liang, Y., Zhen, H., Sun, X., Liu, X., Li, M., Shen, A., & Yang, Y. (2020). Fast and sensitive fluorescent detection of nitrite based on an amino-functionalized MOFs of UiO-66-NH₂. *Journal of Solid State Chemistry*, *287*, 121323. <https://doi.org/10.1016/j.jssc.2020.121323>
- Hasegawa, Y., & Kitagawa, Y. (2022). Luminescent lanthanide coordination polymers with transformative energy transfer processes for physical and chemical sensing applications. *Journal of Photochemistry and Photobiology C: Photochemistry Reviews*, *51*, 100485. <https://doi.org/10.1016/j.jphotochemrev.2022.100485>
- He, K., Li, Z., Wang, L., Fu, Y., Quan, H., Li, Y., Wang, X., Gunasekaran, S., & Xu, X. (2019). A Water-Stable Luminescent Metal–Organic Framework for Rapid and Visible Sensing of Organophosphorus Pesticides. *ACS Applied Materials & Interfaces*, *11*(29), 26250–26260. <https://doi.org/10.1021/acsami.9b06151>
- Hezari, S., Olad, A., & Dilmaghani, A. (2022). Modified gelatin/iron- based metal-organic framework nanocomposite hydrogel as wound dressing: Synthesis, antibacterial activity, and *Camellia sinensis* release. *International Journal of Biological Macromolecules*, *218*, 488–505. <https://doi.org/10.1016/j.ijbiomac.2022.07.150>
- Honikel, K.-O. (2008). The use and control of nitrate and nitrite for the processing of meat products. *Meat Science*, *78*(1), 68–76. <https://doi.org/10.1016/j.meatsci.2007.05.030>
- Hoque, Md. S., Benjakul, S., & Prodpran, T. (2011). Properties of film from cuttlefish (*Sepia pharaonis*) skin gelatin incorporated with cinnamon, clove and star anise extracts. *Food Hydrocolloids*, *25*(5), 1085–1097.

- <https://doi.org/10.1016/j.foodhyd.2010.10.005>
- Hospital, X. F., Hierro, E., Stringer, S., & Fernández, M. (2016). A study on the toxigenesis by *Clostridium botulinum* in nitrate and nitrite-reduced dry fermented sausages. *International Journal of Food Microbiology*, 218, 66–70. <https://doi.org/10.1016/j.ijfoodmicro.2015.11.009>
- Hou, C.-Y., Fu, L.-M., Ju, W.-J., & Wu, P.-Y. (2020). Microfluidic colorimetric system for nitrite detection in foods. *Chemical Engineering Journal*, 398, 125573. <https://doi.org/10.1016/j.cej.2020.125573>
- Hou, D., You, Y., Wu, X., Li, C., Wu, S., Zhang, C., & Xian, Y. (2021). A nanosized metal–organic framework for visual detection of fluoride ions with smartphone via colorimetric test kit. *Sensors and Actuators B: Chemical*, 332, 129508. <https://doi.org/10.1016/j.snb.2021.129508>
- Hou, J., Zhang, H., Yang, Q., Li, M., Jiang, L., & Song, Y. (2015). Hydrophilic–Hydrophobic Patterned Molecularly Imprinted Photonic Crystal Sensors for High-Sensitive Colorimetric Detection of Tetracycline. *Small*, 11(23), 2738–2742. <https://doi.org/10.1002/smll.201403640>
- Hou, L., Qin, Y., Li, J., Qin, S., Huang, Y., Lin, T., Guo, L., Ye, F., & Zhao, S. (2019). A ratiometric multicolor fluorescence biosensor for visual detection of alkaline phosphatase activity via a smartphone. *Biosensors and Bioelectronics*, 143, 111605. <https://doi.org/10.1016/j.bios.2019.111605>
- Hromadka, J., Tokay, B., Correia, R., Morgan, S. P., & Korposh, S. (2018). Carbon dioxide measurements using long period grating optical fibre sensor coated with metal organic framework HKUST-1. *Sensors and Actuators B: Chemical*, 255, 2483–2494. <https://doi.org/10.1016/j.snb.2017.09.041>
- Hu, S., Ouyang, W., Guo, L., Lin, Z., Jiang, X., Qiu, B., & Chen, G. (2017). Facile synthesis of Fe₃O₄/g-C₃N₄/HKUST-1 composites as a novel biosensor platform for ochratoxin A. *Biosensors and Bioelectronics*, 92, 718–723. <https://doi.org/10.1016/j.bios.2016.10.006>
- Hu, X., Shi, J., Shi, Y., Zou, X., Arslan, M., Zhang, W., Huang, X., Li, Z., & Xu, Y. (2019). Use of a smartphone for visual detection of melamine in milk based on Au@Carbon quantum dots nanocomposites. *Food Chemistry*, 272, 58–65. <https://doi.org/10.1016/j.foodchem.2018.08.021>
- Hu, Y., Yang, H., Wang, R., & Duan, M. (2021). Fabricating Ag@MOF-5 nanoplates by the template of MOF-5 and evaluating its antibacterial activity. *Colloids and Surfaces A: Physicochemical and Engineering Aspects*, 626, 127093. <https://doi.org/10.1016/j.colsurfa.2021.127093>
- Hu, Z., Deibert, B. J., & Li, J. (2014). Luminescent metal–organic frameworks for chemical sensing and explosive detection. *Chemical Society Reviews*, 43(16), 5815–5840. <https://doi.org/10.1039/C4CS00010B>
- Hu, Z., Lustig, W. P., Zhang, J., Zheng, C., Wang, H., Teat, S. J., Gong, Q., Rudd, N. D., & Li, J. (2015). Effective Detection of Mycotoxins by a Highly Luminescent Metal–Organic Framework. *Journal of the American Chemical Society*, 137(51), 16209–16215. <https://doi.org/10.1021/jacs.5b10308>
- Huang, C., Ye, Y., Zhao, L., Li, Y., & Gu, J. (2019). One-Pot Trapping Luminescent

- Rhodamine 110 into the Cage of MOF-801 for Nitrite Detection in Aqueous Solution. *Journal of Inorganic and Organometallic Polymers and Materials*, 29(5), 1476–1484. <https://doi.org/10.1007/s10904-019-01111-5>
- Huang, K.-J., Wang, H., Guo, Y.-H., Fan, R.-L., & Zhang, H.-S. (2006). Spectrofluorimetric determination of trace nitrite in food products with a new fluorescent probe 1,3,5,7-tetramethyl-2,6-dicarbethoxy-8-(3',4'-diaminophenyl)-difluoroboradiaza-s-indacene. *Talanta*, 69(1), 73–78. <https://doi.org/10.1016/j.talanta.2005.08.062>
- Huang, K.-J., Xie, W.-Z., Zhang, H.-S., & Wang, H. (2008). Ultra-trace level determination of nitrite in human saliva by spectrofluorimetry using 1,3,5,7-tetramethyl-8-(3,4-diaminophenyl)-difluoroboradiaza-s-indacene. *Microchimica Acta*, 161(1), 201–207. <https://doi.org/10.1007/s00604-007-0784-1>
- Huang, X., Yin, Z., Wu, S., Qi, X., He, Q., Zhang, Q., Yan, Q., Boey, F., & Zhang, H. (2011). Graphene-Based Materials: Synthesis, Characterization, Properties, and Applications. *Small*, 7(14), 1876–1902. <https://doi.org/10.1002/sml.201002009>
- Huang, Z., Korenaga, T., & Helaleh, M. I. H. (2000). Kinetic Spectrofluorimetric Determination of Nitrite in Water Samples and Nitrogen Dioxide in the Atmosphere Sampled by the Liquid Droplet Method. *Microchimica Acta*, 134(3), 179–183. <https://doi.org/10.1007/s006040050064>
- Iammarino, M., Mangiacotti, M., & Chiaravalle, A. E. (2020). Anion exchange polymeric sorbent coupled to high-performance liquid chromatography with UV diode array detection for the determination of ten N-nitrosamines in meat products: A validated approach. *International Journal of Food Science & Technology*, 55(3), 1097–1109. <https://doi.org/10.1111/ijfs.14410>
- Javanbakht, S., Hemmati, A., Namazi, H., & Heydari, A. (2020). Carboxymethylcellulose-coated 5-fluorouracil@MOF-5 nano-hybrid as a bio-nanocomposite carrier for the anticancer oral delivery. *International Journal of Biological Macromolecules*, 155, 876–882. <https://doi.org/10.1016/j.ijbiomac.2019.12.007>
- Javanbakht, S., Nabi, M., Shadi, M., Amini, M. M., & Shaabani, A. (2021). Carboxymethyl cellulose/tetracycline@UiO-66 nanocomposite hydrogel films as a potential antibacterial wound dressing. *International Journal of Biological Macromolecules*, 188, 811–819. <https://doi.org/10.1016/j.ijbiomac.2021.08.061>
- Ji, G., Liu, J., Gao, X., Sun, W., Wang, J., Zhao, S., & Liu, Z. (2017). A luminescent lanthanide MOF for selectively and ultra-high sensitively detecting Pb²⁺ ions in aqueous solution. *Journal of Materials Chemistry A*, 5(21), 10200–10205. <https://doi.org/10.1039/C7TA02439H>
- Jia, J., Lu, W., Li, L., Gao, Y., Jiao, Y., Han, H., Dong, C., & Shuang, S. (2020). Orange-emitting N-doped carbon dots as fluorescent and colorimetric dual-mode probes for nitrite detection and cellular imaging. *Journal of Materials Chemistry B*, 8(10), 2123–2127. <https://doi.org/10.1039/C9TB02934F>
- Jiao, C., Hu, M., Hu, T., & Zhang, J. (2023). Enhanced proton conductivity and overall water splitting efficiency of dye@MOF by post-modification of MOF. *Journal of Solid State Chemistry*, 322, 123978. <https://doi.org/10.1016/j.jssc.2023.123978>
- Jie, N., Yang, D., Jiang, Q., Zhang, Q., & Wei, L. (1999). A Fluorescence Quenching

- Method for the Determination of Nitrite with Indole. *Microchemical Journal*, 62(3), 371–376. <https://doi.org/10.1006/mchj.1999.1746>
- Kangas, M. J., Burks, R. M., Atwater, J., Lukowicz, R. M., Williams, P., & Holmes, A. E. (2017). Colorimetric Sensor Arrays for the Detection and Identification of Chemical Weapons and Explosives. *Critical Reviews in Analytical Chemistry*, 47(2), 138–153. <https://doi.org/10.1080/10408347.2016.1233805>
- Kanikireddy, V., Varaprasad, K., Jayaramudu, T., Karthikeyan, C., & Sadiku, R. (2020). Carboxymethyl cellulose-based materials for infection control and wound healing: A review. *International Journal of Biological Macromolecules*, 164, 963–975. <https://doi.org/10.1016/j.ijbiomac.2020.07.160>
- Katz, M. J., Brown, Z. J., Colón, Y. J., Siu, P. W., Scheidt, K. A., Snurr, R. Q., Hupp, J. T., & Farha, O. K. (2013). A facile synthesis of UiO-66, UiO-67 and their derivatives. *Chemical Communications*, 49(82), 9449. <https://doi.org/10.1039/c3cc46105j>
- Ke, F., Peng, C., Zhang, T., Zhang, M., Zhou, C., Cai, H., Zhu, J., & Wan, X. (2018). Fumarate-based metal-organic frameworks as a new platform for highly selective removal of fluoride from brick tea. *Scientific Reports*, 8(1), Article 1. <https://doi.org/10.1038/s41598-018-19277-2>
- Kilfoy, B. A., Zhang, Y., Park, Y., Holford, T. R., Schatzkin, A., Hollenbeck, A., & Ward, M. H. (2011). Dietary nitrate and nitrite and the risk of thyroid cancer in the NIH-AARP Diet and Health Study. *International Journal of Cancer*, 129(1), 160–172. <https://doi.org/10.1002/ijc.25650>
- Kim, D. H., Hur, J., Park, H. G., & Il Kim, M. (2017). Reagentless colorimetric biosensing platform based on nanoceria within an agarose gel matrix. *Biosensors and Bioelectronics*, 93, 226–233. <https://doi.org/10.1016/j.bios.2016.08.113>
- Kohsari, I., Shariatinia, Z., & Pourmortazavi, S. M. (2016). Antibacterial electrospun chitosan-polyethylene oxide nanocomposite mats containing ZIF-8 nanoparticles. *International Journal of Biological Macromolecules*, 91, 778–788. <https://doi.org/10.1016/j.ijbiomac.2016.06.039>
- Kojima, H., Urano, Y., Kikuchi, K., Higuchi, T., Hirata, Y., & Nagano, T. (1999). Fluorescent Indicators for Imaging Nitric Oxide Production. *Angewandte Chemie International Edition*, 38(21), 3209–3212. [https://doi.org/10.1002/\(SICI\)1521-3773\(19991102\)38:21<3209::AID-ANIE3209>3.0.CO;2-6](https://doi.org/10.1002/(SICI)1521-3773(19991102)38:21<3209::AID-ANIE3209>3.0.CO;2-6)
- Lapat, A., Székelyhidi, L., & Hornyák, I. (1997). Spectrofluorimetric Determination of 1,3,5-Trinitro-1,3,5-triazacyclohexane (Hexogen, RDX) as a Nitramine Type Explosive. *Biomedical Chromatography*, 11(2), 102–104. [https://doi.org/10.1002/\(SICI\)1099-0801\(199703\)11:2<102::AID-BMC660>3.0.CO;2-0](https://doi.org/10.1002/(SICI)1099-0801(199703)11:2<102::AID-BMC660>3.0.CO;2-0)
- Ledezma-Zamora, K., Sánchez-Gutiérrez, R., Ramírez-Leiva, A., & Mena-Rivera, L. (2021a). Residual nitrite in processed meat products in Costa Rica: Method validation, long-term survey and intake estimations. *Food Chemistry*, 361, 130082. <https://doi.org/10.1016/j.foodchem.2021.130082>
- Ledezma-Zamora, K., Sánchez-Gutiérrez, R., Ramírez-Leiva, A., & Mena-Rivera, L. (2021b). Residual nitrite in processed meat products in Costa Rica: Method validation, long-term survey and intake estimations. *Food Chemistry*, 361,

130082. <https://doi.org/10.1016/j.foodchem.2021.130082>
- Lee, J. H., Alford, L., Kannan, G., & Kouakou, B. (2017). Curing properties of sodium nitrite in restructured goat meat (chevon) jerky. *International Journal of Food Properties*, 20(3), 526–537. <https://doi.org/10.1080/10942912.2016.1168833>
- Lee, K.-S., Shiddiky, M. J. A., Park, S.-H., Park, D.-S., & Shim, Y.-B. (2008). Electrophoretic analysis of food dyes using a miniaturized microfluidic system. *ELECTROPHORESIS*, 29(9), 1910–1917. <https://doi.org/10.1002/elps.200700556>
- Let, S., Samanta, P., Dutta, S., & Ghosh, S. K. (2020). A Dye@MOF composite as luminescent sensory material for selective and sensitive recognition of Fe(III) ions in water. *Inorganica Chimica Acta*, 500, 119205. <https://doi.org/10.1016/j.ica.2019.119205>
- Li, B.-L., Li, Y.-S., & Gao, X.-F. (2019). Fluorescence quenching capillary analysis for determining trace-level nitrite in food based on the citric acid/ethylenediamine nanodots/nitrite reaction. *Food Chemistry*, 274, 162–169. <https://doi.org/10.1016/j.foodchem.2018.08.112>
- Li, C., Zhu, L., Yang, W., He, X., Zhao, S., Zhang, X., Tang, W., Wang, J., Yue, T., & Li, Z. (2019). Amino-Functionalized Al-MOF for Fluorescent Detection of Tetracyclines in Milk. *Journal of Agricultural and Food Chemistry*, 67(4), 1277–1283. <https://doi.org/10.1021/acs.jafc.8b06253>
- Li, D., Ma, Y., Duan, H., Deng, W., & Li, D. (2018). Griess reaction-based paper strip for colorimetric/fluorescent/SERS triple sensing of nitrite. *Biosensors and Bioelectronics*, 99, 389–398. <https://doi.org/10.1016/j.bios.2017.08.008>
- Li, H., Meininger, C. J., & Wu, G. (2000). Rapid determination of nitrite by reversed-phase high-performance liquid chromatography with fluorescence detection. *Journal of Chromatography B: Biomedical Sciences and Applications*, 746(2), 199–207. [https://doi.org/10.1016/S0378-4347\(00\)00328-5](https://doi.org/10.1016/S0378-4347(00)00328-5)
- Li, H., Wang, K., Sun, Y., Lollar, C. T., Li, J., & Zhou, H.-C. (2018). Recent advances in gas storage and separation using metal-organic frameworks. *Materials Today*, 21(2), 108–121. <https://doi.org/10.1016/j.mattod.2017.07.006>
- Li, H., Zhou, X., Luo, L., Ding, Q., & Tang, S. (2022). Bio-orthogonally crosslinked catechol-chitosan hydrogel for effective hemostasis and wound healing. *Carbohydrate Polymers*, 281, 119039. <https://doi.org/10.1016/j.carbpol.2021.119039>
- Li, H.-Y., Zhao, S.-N., Zang, S.-Q., & Li, J. (2020). Functional metal-organic frameworks as effective sensors of gases and volatile compounds. *Chemical Society Reviews*, 49(17), 6364–6401. <https://doi.org/10.1039/C9CS00778D>
- Li, J. (2003). Spectrofluorimetric determination of total amount of nitrite and nitrate in biological sample with a new fluorescent probe 1,3,5,7-tetramethyl-8-(3',4'-diaminophenyl)-difluoroboradiaza-s-indacene. *Talanta*, 61(6), 797–802. [https://doi.org/10.1016/S0039-9140\(03\)00380-1](https://doi.org/10.1016/S0039-9140(03)00380-1)
- Li, L., Shen, S., Ai, W., Song, S., Bai, Y., & Liu, H. (2018). Facilely synthesized Eu³⁺ post-functionalized UiO-66-type metal-organic framework for rapid and highly selective detection of Fe³⁺ in aqueous solution. *Sensors and Actuators B:*

- Chemical*, 267, 542–548. <https://doi.org/10.1016/j.snb.2018.04.064>
- Li, M., Wang, H., Zhang, X., & Zhang, H. (2004). Development of a new fluorescent probe: 1,3,5,7-tetramethyl-8-(4'-aminophenyl)-4,4-difluoro-4-bora-3a,4a-diazas-indacence for the determination of trace nitrite. *Spectrochimica Acta Part A: Molecular and Biomolecular Spectroscopy*, 60(4), 987–993. [https://doi.org/10.1016/S1386-1425\(03\)00329-9](https://doi.org/10.1016/S1386-1425(03)00329-9)
- Li, Q., & Wei, G. (2018). Label-free determination of adenosine and mercury ions according to force mapping-based force-to-color variety. *Analyst*, 143(18), 4400–4407. <https://doi.org/10.1039/C8AN01043A>
- Li, R., Yu, J. C., Jiang, Z.-T., Zhou, R.-H., & Liu, H.-Y. (2020). A solid-phase fluorescent, quenching method for the determination of trace amounts of nitrite in foods with neutral red. *Journal of Food and Drug Analysis*, 11(3). <https://doi.org/10.38212/2224-6614.2700>
- Li, S., Qu, J., Wang, Y., Qu, J., & Wang, H. (2016). A novel electrochemical sensor based on carbon nanoparticle composite films for the determination of nitrite and hydrogen peroxide. *Analytical Methods*, 8(21), 4204–4210. <https://doi.org/10.1039/C6AY00030D>
- Li, W., Liu, Z., Wang, L., Gao, G., Xu, H., Huang, W., Yan, N., Wang, H., & Qu, Z. (2023). FeSx@MOF-808 composite for efficient As(III) removal from wastewater: Behavior and mechanism. *Journal of Hazardous Materials*, 446, 130681. <https://doi.org/10.1016/j.jhazmat.2022.130681>
- Li, X., Yang, X., Cui, M., Liu, Y., Wang, J., Zhang, L., & Zhan, G. (2022). A novel electrochemical sensor based on nitrite-oxidizing bacteria for highly specific and sensitive detection of nitrites. *Science of The Total Environment*, 826, 154178. <https://doi.org/10.1016/j.scitotenv.2022.154178>
- Li, Y., Wei, Z., Zhang, Y., Guo, Z., Chen, D., Jia, P., Chen, P., & Xing, H. (2019). Dual-Emitting EY@Zr-MOF Composite as Self-Calibrating Luminescent Sensor for Selective Detection of Inorganic Ions and Nitroaromatics. *ACS Sustainable Chemistry & Engineering*, 7(6), 6196–6203. <https://doi.org/10.1021/acssuschemeng.8b06500>
- Li, Y., Zhao, Y., Zhang, W., Shao, K., & Zhou, H. (2021). A Fluorescent Probe of Nitrite Based on Eu³⁺ Functionalized Metal-Organic Frameworks. *Zeitschrift Für Anorganische Und Allgemeine Chemie*, 647(10), 1091–1095. <https://doi.org/10.1002/zaac.202100040>
- Li, Y.-W., Li, J.-R., Wang, L.-F., Zhou, B.-Y., Chen, Q., & Bu, X.-H. (2012). Microporous metal–organic frameworks with open metal sites as sorbents for selective gas adsorption and fluorescence sensors for metal ions. *Journal of Materials Chemistry A*, 1(3), 495–499. <https://doi.org/10.1039/C2TA00635A>
- Li, Z., Ren, J., Bu, J., Wang, L., Shi, W., Pan, D., & Wu, M. (2020). Carbonated MOF-based graphene hydrogel for hierarchical all-carbon supercapacitors with ultra-high areal and volumetric energy density. *Journal of Electroanalytical Chemistry*, 876, 114489. <https://doi.org/10.1016/j.jelechem.2020.114489>
- Li, Z., Xu, X., Fu, Y., Guo, Y., Zhang, Q., Zhang, Q., Yang, H., & Li, Y. (2019). A water-stable luminescent metal–organic framework for effective detection of aflatoxin

- B1 in walnut and almond beverages. *RSC Advances*, 9(2), 620–625. <https://doi.org/10.1039/C8RA07804A>
- Lian, X., Fang, Y., Joseph, E., Wang, Q., Li, J., Banerjee, S., Lollar, C., Wang, X., & Zhou, H.-C. (2017). Enzyme–MOF (metal–organic framework) composites. *Chemical Society Reviews*, 46(11), 3386–3401. <https://doi.org/10.1039/C7CS00058H>
- Lin, X., Gao, G., Zheng, L., Chi, Y., & Chen, G. (2014). Encapsulation of Strongly Fluorescent Carbon Quantum Dots in Metal–Organic Frameworks for Enhancing Chemical Sensing. *Analytical Chemistry*, 86(2), 1223–1228. <https://doi.org/10.1021/ac403536a>
- Liu, D., Gu, W., Zhou, L., Wang, L., Zhang, J., Liu, Y., & Lei, J. (2022). Recent advances in MOF-derived carbon-based nanomaterials for environmental applications in adsorption and catalytic degradation. *Chemical Engineering Journal*, 427, 131503. <https://doi.org/10.1016/j.cej.2021.131503>
- Liu, H., Guo, K., Lv, J., Gao, Y., Duan, C., Deng, L., & Zhu, Z. (2017). A novel nitrite biosensor based on the direct electrochemistry of horseradish peroxidase immobilized on porous Co₃O₄ nanosheets and reduced graphene oxide composite modified electrode. *Sensors and Actuators B: Chemical*, 238, 249–256. <https://doi.org/10.1016/j.snb.2016.07.073>
- Liu, H., Peng, H., Xin, Y., & Zhang, J. (2019). Metal–organic frameworks: A universal strategy towards super-elastic hydrogels. *Polymer Chemistry*, 10(18), 2263–2272. <https://doi.org/10.1039/C9PY00085B>
- Liu, J., Chen, Y., Wang, L., Na, M., Chen, H., & Chen, X. (2019). Modification-Free Fabricating Ratiometric Nanoprobe Based on Dual-Emissive Carbon Dots for Nitrite Determination in Food Samples. *Journal of Agricultural and Food Chemistry*, 67(13), 3826–3836. <https://doi.org/10.1021/acs.jafc.9b00024>
- Liu, L., Yao, Z., Ye, Y., Liu, C., Lin, Q., Chen, S., Xiang, S., & Zhang, Z. (2019). Enhancement of Intrinsic Proton Conductivity and Aniline Sensitivity by Introducing Dye Molecules into the MOF Channel. *ACS Applied Materials & Interfaces*, 11(18), 16490–16495. <https://doi.org/10.1021/acsami.8b22327>
- Liu, Q.-H., Yan, X.-L., Guo, J.-C., Wang, D.-H., Li, L., Yan, F.-Y., & Chen, L.-G. (2009). Spectrofluorimetric determination of trace nitrite with a novel fluorescent probe. *Spectrochimica Acta Part A: Molecular and Biomolecular Spectroscopy*, 73(5), 789–793. <https://doi.org/10.1016/j.saa.2009.03.018>
- Lu, L., Chen, C., Zhao, D., Yang, F., & Yang, X. (2015). A simple and sensitive assay for the determination of nitrite using folic acid as the fluorescent probe. *Analytical Methods*, 7(4), 1543–1548. <https://doi.org/10.1039/C4AY02721C>
- Lu, Z., Wu, M., Wu, S., Yang, S., Li, Y., Liu, X., Zheng, L., Cao, Q., & Ding, Z. (2016). Modulating the optical properties of the AIE fluorophore confined within UiO-66's nanochannels for chemical sensing. *Nanoscale*, 8(40), 17489–17495. <https://doi.org/10.1039/C6NR05600H>
- Lv, R., Wang, J., Zhang, Y., Li, H., Yang, L., Liao, S., Gu, W., & Liu, X. (2016). An amino-decorated dual-functional metal–organic framework for highly selective sensing of Cr(III) and Cr(VI) ions and detection of nitroaromatic explosives. *Journal of Materials Chemistry A*, 4(40), 15494–15500.

- <https://doi.org/10.1039/C6TA05965A>
- Ma, J., Xiong, Y., Dai, X., & Yu, F. (2020). Coadsorption behavior and mechanism of ciprofloxacin and Cu(II) on graphene hydrogel wetted surface. *Chemical Engineering Journal*, 380, 122387. <https://doi.org/10.1016/j.cej.2019.122387>
- Ma, X., Chai, Y., Li, P., & Wang, B. (2019). Metal–Organic Framework Films and Their Potential Applications in Environmental Pollution Control. *Accounts of Chemical Research*, 52(5), 1461–1470. <https://doi.org/10.1021/acs.accounts.9b00113>
- Ma, Y., Han, X., Xu, S., Wang, Z., Li, W., da Silva, I., Chansai, S., Lee, D., Zou, Y., Nikiel, M., Manuel, P., Sheveleva, A. M., Tuna, F., McInnes, E. J. L., Cheng, Y., Rudić, S., Ramirez-Cuesta, A. J., Haigh, S. J., Hardacre, C., ... Yang, S. (2021). Atomically Dispersed Copper Sites in a Metal–Organic Framework for Reduction of Nitrogen Dioxide. *Journal of the American Chemical Society*, 143(29), 10977–10985. <https://doi.org/10.1021/jacs.1c03036>
- Ma, Z., Li, J., Hu, X., Cai, Z., & Dou, X. (2020). Ultrasensitive, Specific, and Rapid Fluorescence Turn-On Nitrite Sensor Enabled by Precisely Modulated Fluorophore Binding. *Advanced Science*, 7(24), 2002991. <https://doi.org/10.1002/advs.202002991>
- Maia, L. B., & Moura, J. J. G. (2014). How Biology Handles Nitrite. *Chemical Reviews*, 114(10), 5273–5357. <https://doi.org/10.1021/cr400518y>
- Mako, T. L., Levenson, A. M., & Levine, M. (2020). Ultrasensitive Detection of Nitrite through Implementation of N-(1-Naphthyl)ethylenediamine-Grafted Cellulose into a Paper-Based Device. *ACS Sensors*, 5(4), 1207–1215. <https://doi.org/10.1021/acssensors.0c00291>
- Martínez-Tomé, M. J., Esquembre, R., Mallavia, R., & Mateo, C. R. (2009). Immobilization and Characterization of 2,3-diaminonaphthalene/cyclodextrin Complexes in a Sol–Gel Matrix: A New Fluorimetric Sensor for Nitrite. *Journal of Fluorescence*, 19(1), 119–125. <https://doi.org/10.1007/s10895-008-0393-3>
- Merusi, C., Corradini, C., Cavazza, A., Borromei, C., & Salvadeo, P. (2010). Determination of nitrates, nitrites and oxalates in food products by capillary electrophoresis with pH-dependent electroosmotic flow reversal. *Food Chemistry*, 120(2), 615–620. <https://doi.org/10.1016/j.foodchem.2009.10.035>
- Mihindukulasuriya, S. D. F., & Lim, L.-T. (2014). Nanotechnology development in food packaging: A review. *Trends in Food Science & Technology*, 40(2), 149–167. <https://doi.org/10.1016/j.tifs.2014.09.009>
- Min, H., Han, Z., Wang, M., Li, Y., Zhou, T., Shi, W., & Cheng, P. (2020). A water-stable terbium metal–organic framework as a highly sensitive fluorescent sensor for nitrite. *Inorganic Chemistry Frontiers*, 7(18), 3379–3385. <https://doi.org/10.1039/D0QI00780C>
- Nakamura, M. (1980). Resorcinol as Fluorimetric Reagent for the Determination of Nitrate. *Analytical Letters*, 13(9), 771–779. <https://doi.org/10.1080/00032718008077998>
- Nam, J., Jung, I.-B., Kim, B., Lee, S.-M., Kim, S.-E., Lee, K.-N., & Shin, D.-S. (2018). A colorimetric hydrogel biosensor for rapid detection of nitrite ions. *Sensors and Actuators B: Chemical*, 270, 112–118. <https://doi.org/10.1016/j.snb.2018.04.171>

- Njaramba, L. K., Kim, M., Yea, Y., Yoon, Y., & Park, C. M. (2023). Efficient adsorption of naproxen and ibuprofen by gelatin/zirconium-based metal-organic framework/sepiolite aerogels via synergistic mechanisms. *Chemical Engineering Journal*, *452*, 139426. <https://doi.org/10.1016/j.cej.2022.139426>
- Ohta, Takafumi., Arai, Youichi., & Takitani, Shoji. (1986). Fluorometric determination of nitrite with 4-hydroxycoumarin. *Analytical Chemistry*, *58*(14), 3132–3135. <https://doi.org/10.1021/ac00127a047>
- Parani, S., Pandian, K., & Oluwafemi, O. S. (2018). Gelatin stabilization of quantum dots for improved stability and biocompatibility. *International Journal of Biological Macromolecules*, *107*, 635–641. <https://doi.org/10.1016/j.ijbiomac.2017.09.039>
- Park, S. H., Kim, K., Lim, J. H., & Lee, S. J. (2019). Selective lithium and magnesium adsorption by phosphonate metal-organic framework-incorporated alginate hydrogel inspired from lithium adsorption characteristics of brown algae. *Separation and Purification Technology*, *212*, 611–618. <https://doi.org/10.1016/j.seppur.2018.11.067>
- Pascanu, V., González Miera, G., Inge, A. K., & Martín-Matute, B. (2019). Metal-Organic Frameworks as Catalysts for Organic Synthesis: A Critical Perspective. *Journal of the American Chemical Society*, *141*(18), 7223–7234. <https://doi.org/10.1021/jacs.9b00733>
- Peers, S., Montembault, A., & Ladavière, C. (2022). Chitosan hydrogels incorporating colloids for sustained drug delivery. *Carbohydrate Polymers*, *275*, 118689. <https://doi.org/10.1016/j.carbpol.2021.118689>
- Pérez-López, M., De la Casa-Resino, I., Hernández-Moreno, D., Galeano, J., Míguez-Santiyán, M. P., de Castro-Lorenzo, A., Otero-Filgueiras, M., Rivas-López, O., & Soler, F. (2016). Concentrations of Metals, Metalloids, and Chlorinated Pollutants in Blood and Plasma of White Stork (*Ciconia ciconia*) Nestlings From Spain. *Archives of Environmental Contamination and Toxicology*, *71*(3), 313–321. <https://doi.org/10.1007/s00244-016-0302-8>
- Petit, C., & Badosz, T. J. (2009). MOF-graphite oxide nanocomposites: Surface characterization and evaluation as adsorbents of ammonia. *Journal of Materials Chemistry*, *19*(36), 6521–6528. <https://doi.org/10.1039/B908862H>
- Raja Lakshmi, P., Nanjan, P., Kannan, S., & Shanmugaraju, S. (2021). Recent advances in luminescent metal-organic frameworks (LMOFs) based fluorescent sensors for antibiotics. *Coordination Chemistry Reviews*, *435*, 213793. <https://doi.org/10.1016/j.ccr.2021.213793>
- Rasheed, T., & Rizwan, K. (2022). Metal-organic frameworks based hybrid nanocomposites as state-of-the-art analytical tools for electrochemical sensing applications. *Biosensors and Bioelectronics*, *199*, 113867. <https://doi.org/10.1016/j.bios.2021.113867>
- Reddy, P. M., Hsieh, S.-R., Chang, C.-J., & Kang, J.-Y. (2017). Detection of cyanide ions in aqueous solutions using cost effective colorimetric sensor. *Journal of Hazardous Materials*, *334*, 93–103. <https://doi.org/10.1016/j.jhazmat.2017.04.001>
- Ren, H.-H., Fan, Y., Wang, B., & Yu, L.-P. (2018). Polyethylenimine-Capped CdS

- Quantum Dots for Sensitive and Selective Detection of Nitrite in Vegetables and Water. *Journal of Agricultural and Food Chemistry*, 66(33), 8851–8858. <https://doi.org/10.1021/acs.jafc.8b01951>
- Ren, S., Li, C., Tan, Z., Hou, Y., Jia, S., & Cui, J. (2019). Carbonic Anhydrase@ZIF-8 Hydrogel Composite Membrane with Improved Recycling and Stability for Efficient CO₂ Capture. *Journal of Agricultural and Food Chemistry*, 67(12), 3372–3379. <https://doi.org/10.1021/acs.jafc.8b06182>
- Ribeiro, S. C., de Lima, H. H. C., Vicente L. Kupfer, da Silva, C. T. P., Veregue, F. R., Radovanovic, E., Guilherme, M. R., & Rinaldi, A. W. (2019). Synthesis of a superabsorbent hybrid hydrogel with excellent mechanical properties: Water transport and methylene blue absorption profiles. *Journal of Molecular Liquids*, 294, 111553. <https://doi.org/10.1016/j.molliq.2019.111553>
- Rieter, W. J., Taylor, K. M. L., & Lin, W. (2007). Surface Modification and Functionalization of Nanoscale Metal-Organic Frameworks for Controlled Release and Luminescence Sensing. *Journal of the American Chemical Society*, 129(32), 9852–9853. <https://doi.org/10.1021/ja073506r>
- Rivera-Hernández, G., Antunes-Ricardo, M., Martínez-Morales, P., & Sánchez, M. L. (2021). Polyvinyl alcohol based-drug delivery systems for cancer treatment. *International Journal of Pharmaceutics*, 600, 120478. <https://doi.org/10.1016/j.ijpharm.2021.120478>
- Rojas, S., Arenas-Vivo, A., & Horcajada, P. (2019). Metal-organic frameworks: A novel platform for combined advanced therapies. *Coordination Chemistry Reviews*, 388, 202–226. <https://doi.org/10.1016/j.ccr.2019.02.032>
- Rojas, S., Rodríguez-Diéguez, A., & Horcajada, P. (2022). Metal–Organic Frameworks in Agriculture. *ACS Applied Materials & Interfaces*, 14(15), 16983–17007. <https://doi.org/10.1021/acsami.2c00615>
- Rong, M., Wang, D., Li, Y., Zhang, Y., Huang, H., Liu, R., & Deng, X. (2021). Green-Emitting Carbon Dots as Fluorescent Probe for Nitrite Detection. *Journal of Analysis and Testing*, 5(1), 51–59. <https://doi.org/10.1007/s41664-021-00161-4>
- Sahiner, N., Demirci, S., & Yildiz, M. (2017). Synthesis and Characterization of Terephthalic Acid Based Cr³⁺, Sb³⁺, In³⁺ and V³⁺ Metal-Organic Frameworks. *Journal of Inorganic and Organometallic Polymers and Materials*, 27(5), 1333–1341. <https://doi.org/10.1007/s10904-017-0587-8>
- Salahuddin, B., Wang, S., Sangian, D., Aziz, S., & Gu, Q. (2021). Hybrid Gelatin Hydrogels in Nanomedicine Applications. *ACS Applied Bio Materials*, 4(4), 2886–2906. <https://doi.org/10.1021/acsabm.0c01630>
- Samanta, P., Desai, A. V., Sharma, S., Chandra, P., & Ghosh, S. K. (2018). Selective Recognition of Hg²⁺ ion in Water by a Functionalized Metal–Organic Framework (MOF) Based Chemodosimeter. *Inorganic Chemistry*, 57(5), 2360–2364. <https://doi.org/10.1021/acs.inorgchem.7b02426>
- Samokhvalov, A. (2020). Analysis of various solid samples by synchronous fluorescence spectroscopy and related methods: A review. *Talanta*, 216, 120944. <https://doi.org/10.1016/j.talanta.2020.120944>
- Sánchez, F., Gutiérrez, M., & Douhal, A. (2022). Novel Approach for Detecting Vapors of

- Acids and Bases with Proton-Transfer Luminescent Dyes Encapsulated within Metal–Organic Frameworks. *ACS Applied Materials & Interfaces*, 14(37), 42656–42670. <https://doi.org/10.1021/acsami.2c10573>
- Santarelli, R. L., Vendeuvre, J.-L., Naud, N., Taché, S., Guéraud, F., Viau, M., Genot, C., Corpet, D. E., & Pierre, F. H. F. (2010). Meat Processing and Colon Carcinogenesis: Cooked, Nitrite-Treated, and Oxidized High-Heme Cured Meat Promotes Mucin-Depleted Foci in Rats. *Cancer Prevention Research*, 3(7), 852–864. <https://doi.org/10.1158/1940-6207.CAPR-09-0160>
- Sepahvand, M., Ghasemi, F., & Seyed Hosseini, H. M. (2021). Plasmonic nanoparticles for colorimetric detection of nitrite and nitrate. *Food and Chemical Toxicology*, 149, 112025. <https://doi.org/10.1016/j.fct.2021.112025>
- Shakil, M. H., Trisha, A. T., Rahman, M., Talukdar, S., Kobun, R., Huda, N., & Zzaman, W. (2022). Nitrites in Cured Meats, Health Risk Issues, Alternatives to Nitrites: A Review. *Foods*, 11(21), Article 21. <https://doi.org/10.3390/foods11213355>
- Shi, J., Chen, F., Hou, L., Li, G., Li, Y., Guan, X., Liu, H., & Guo, L. (2021). Eosin Y bidentately bridged on UiO-66-NH₂ by solvothermal treatment towards enhanced visible-light-driven photocatalytic H₂ production. *Applied Catalysis B: Environmental*, 280, 119385. <https://doi.org/10.1016/j.apcatb.2020.119385>
- Singha, D. K., Majee, P., Mandal, S., Mondal, S. K., & Mahata, P. (2018). Detection of Pesticides in Aqueous Medium and in Fruit Extracts Using a Three-Dimensional Metal–Organic Framework: Experimental and Computational Study. *Inorganic Chemistry*, 57(19), 12155–12165. <https://doi.org/10.1021/acs.inorgchem.8b01767>
- Skibsted, L. H. (2011). Nitric oxide and quality and safety of muscle based foods. *Nitric Oxide*, 24(4), 176–183. <https://doi.org/10.1016/j.niox.2011.03.307>
- Song, J., Liu, S., Zhao, N., & Zhao, L. (2023). A new fluorescent probe based on metallic deep eutectic solvent for visual detection of nitrite and pH in food and water environment. *Food Chemistry*, 398, 133935. <https://doi.org/10.1016/j.foodchem.2022.133935>
- Specht, J. (2019). *Red Meat Republic: A Hoof-to-Table History of How Beef Changed America*. Princeton University Press.
- Sun, W., Zhao, X., Webb, E., Xu, G., Zhang, W., & Wang, Y. (2023). Advances in metal–organic framework-based hydrogel materials: Preparation, properties and applications. *Journal of Materials Chemistry A*, 11(5), 2092–2127. <https://doi.org/10.1039/D2TA08841J>
- Tan, L., Xie, C., Yang, Q., Luo, K., & Zhou, L. (2023). Rational construction of a robust nanoprobe for highly selective and sensitive nitrite and formaldehyde detection and imaging in real foods. *Food Chemistry*, 405, 134949. <https://doi.org/10.1016/j.foodchem.2022.134949>
- Thi Dang, Y., Hoang, H. T., Dong, H. C., Bui, K.-B. T., Nguyen, L. H. T., Phan, T. B., Kawazoe, Y., & Doan, T. L. H. (2020). Microwave-assisted synthesis of nano Hf- and Zr-based metal-organic frameworks for enhancement of curcumin adsorption. *Microporous and Mesoporous Materials*, 298, 110064. <https://doi.org/10.1016/j.micromeso.2020.110064>

- Tian, D., Liu, X.-J., Feng, R., Xu, J.-L., Xu, J., Chen, R.-Y., Huang, L., & Bu, X.-H. (2018). Microporous Luminescent Metal–Organic Framework for a Sensitive and Selective Fluorescence Sensing of Toxic Mycotoxin in Moldy Sugarcane. *ACS Applied Materials & Interfaces*, *10*(6), 5618–5625. <https://doi.org/10.1021/acsami.7b15764>
- Velásquez-Hernández, M. de J., Linares-Moreau, M., Astria, E., Carraro, F., Alyami, M. Z., Khashab, N. M., Sumby, C. J., Doonan, C. J., & Falcaro, P. (2021). Towards applications of bioentities@MOFs in biomedicine. *Coordination Chemistry Reviews*, *429*, 213651. <https://doi.org/10.1016/j.ccr.2020.213651>
- Viboonratanasri, D., Pabchanda, S., & Prompinit, P. (2018). Rapid and simple preparation of rhodamine 6G loaded HY zeolite for highly selective nitrite detection. *Applied Surface Science*, *440*, 1261–1268. <https://doi.org/10.1016/j.apsusc.2018.01.156>
- Virmani, E., Rotter, J. M., Mähringer, A., von Zons, T., Godt, A., Bein, T., Wuttke, S., & Medina, D. D. (2018). On-Surface Synthesis of Highly Oriented Thin Metal–Organic Framework Films through Vapor-Assisted Conversion. *Journal of the American Chemical Society*, *140*(14), 4812–4819. <https://doi.org/10.1021/jacs.7b08174>
- Waga, M., Takeda, S., & Sakata, R. (2017). Effect of nitrate on residual nitrite decomposition rate in cooked cured pork. *Meat Science*, *129*, 135–139. <https://doi.org/10.1016/j.meatsci.2017.03.002>
- Wan, C.-Q., Pang, Y.-H., Feng, Y.-W., & Shen, X.-F. (2022). A ratio fluorescence sensor based on rhodamine B embedded metal-organic framework for glyphosate detection in agri-food products. *Food Chemistry*, *394*, 133446. <https://doi.org/10.1016/j.foodchem.2022.133446>
- Wan, Y., Zheng, Y. F., Wan, H. T., Yin, H. Y., & Song, X. C. (2017). A novel electrochemical sensor based on Ag nanoparticles decorated multi-walled carbon nanotubes for applied determination of nitrite. *Food Control*, *73*, 1507–1513. <https://doi.org/10.1016/j.foodcont.2016.11.014>
- Wang, B., Liu, J.-H., Yu, J., Lv, J., Dong, C., & Li, J.-R. (2020). Broad spectrum detection of veterinary drugs with a highly stable metal-organic framework. *Journal of Hazardous Materials*, *382*, 121018. <https://doi.org/10.1016/j.jhazmat.2019.121018>
- Wang, B., Lv, X.-L., Feng, D., Xie, L.-H., Zhang, J., Li, M., Xie, Y., Li, J.-R., & Zhou, H.-C. (2016). Highly Stable Zr(IV)-Based Metal–Organic Frameworks for the Detection and Removal of Antibiotics and Organic Explosives in Water. *Journal of the American Chemical Society*, *138*(19), 6204–6216. <https://doi.org/10.1021/jacs.6b01663>
- Wang, B.-H., & Yan, B. (2019). A dye@MOF crystalline probe serving as a platform for ratiometric sensing of trichloroacetic acid (TCA), a carcinogen metabolite in human urine. *CrystEngComm*, *21*(31), 4637–4643. <https://doi.org/10.1039/C9CE00924H>
- Wang, C., Liu, D., & Lin, W. (2013). Metal–Organic Frameworks as A Tunable Platform for Designing Functional Molecular Materials. *Journal of the American Chemical Society*, *135*(36), 13222–13234. <https://doi.org/10.1021/ja308229p>

- Wang, F., Wang, C., Yu, Z., Xu, K., Li, X., & Fu, Y. (2016). Two multifunctional Mn(II) metal-organic frameworks: Synthesis, structures and applications as photocatalysis and luminescent sensor. *Polyhedron*, *105*, 49–55. <https://doi.org/10.1016/j.poly.2015.11.043>
- Wang, H., Wan, N., Ma, L., Wang, Z., Cui, B., Han, W., & Chen, Y. (2018). A novel and simple spectrophotometric method for detection of nitrite in water. *Analyst*, *143*(19), 4555–4558. <https://doi.org/10.1039/C8AN01063C>
- Wang, H., Yang, W., Liang, S.-C., Zhang, Z.-M., & Zhang, H.-S. (2000). Spectrofluorimetric determination of nitrite with 5,6-diamino-1,3-naphthalene disulfonic acid. *Analytica Chimica Acta*, *419*(2), 169–173. [https://doi.org/10.1016/S0003-2670\(00\)01000-X](https://doi.org/10.1016/S0003-2670(00)01000-X)
- Wang, J., & Ni, Y. (2020). Ammonium molybdate-assisted shape-controlled synthesis of fluorescent Co(II)-based MOFs nanoflakes as highly-sensitive probes for selective detection of vanillin in milk powders. *Materials Research Bulletin*, *123*, 110721. <https://doi.org/10.1016/j.materresbull.2019.110721>
- Wang, L., Li, B., Zhang, L., Zhang, L., & Zhao, H. (2012). Fabrication and characterization of a fluorescent sensor based on Rh 6G-functionized silica nanoparticles for nitrite ion detection. *Sensors and Actuators B: Chemical*, *171–172*, 946–953. <https://doi.org/10.1016/j.snb.2012.06.008>
- Wang, L., Xu, H., Gao, J., Yao, J., & Zhang, Q. (2019a). Recent progress in metal-organic frameworks-based hydrogels and aerogels and their applications. *Coordination Chemistry Reviews*, *398*, 213016. <https://doi.org/10.1016/j.ccr.2019.213016>
- Wang, L., Xu, H., Gao, J., Yao, J., & Zhang, Q. (2019b). Recent progress in metal-organic frameworks-based hydrogels and aerogels and their applications. *Coordination Chemistry Reviews*, *398*, 213016. <https://doi.org/10.1016/j.ccr.2019.213016>
- Wang, M., Zhu, H., Liu, B., Hu, P., Pan, J., & Niu, X. (2022). Bifunctional Mn-Doped N-Rich Carbon Dots with Tunable Photoluminescence and Oxidase-Mimetic Activity Enabling Bimodal Ratiometric Colorimetric/Fluorometric Detection of Nitrite. *ACS Applied Materials & Interfaces*, *14*(39), 44762–44771. <https://doi.org/10.1021/acsami.2c14045>
- Wang, P.-L., Xie, L.-H., Joseph, E. A., Li, J.-R., Su, X.-O., & Zhou, H.-C. (2019). Metal-Organic Frameworks for Food Safety. *Chemical Reviews*, *119*(18), 10638–10690. <https://doi.org/10.1021/acs.chemrev.9b00257>
- Wang, Q., Ma, S., Huang, H., Cao, A., Li, M., & He, L. (2016). Highly sensitive and selective spectrofluorimetric determination of nitrite in food products with a novel fluorogenic probe. *Food Control*, *63*, 117–121. <https://doi.org/10.1016/j.foodcont.2015.11.023>
- Wang, Q.-H., Yu, L.-J., Liu, Y., Lin, L., Lu, R., Zhu, J., He, L., & Lu, Z.-L. (2017). Methods for the detection and determination of nitrite and nitrate: A review. *Talanta*, *165*, 709–720. <https://doi.org/10.1016/j.talanta.2016.12.044>
- Wang, R., Ruan, G., Sun, Y., Zhao, D., Yu, H., Zhang, C.-W., Li, L., & Liu, J. (2021). A full-wavelength coverage colorimetric sensor depending on polymer-carbon nanodots from blue to red for visual detection of nitrite via smartphone. *Dyes and Pigments*, *191*, 109383. <https://doi.org/10.1016/j.dyepig.2021.109383>

- Wang, S., McGuirk, C. M., d'Aquino, A., Mason, J. A., & Mirkin, C. A. (2018). Metal–Organic Framework Nanoparticles. *Advanced Materials*, *30*(37), 1800202. <https://doi.org/10.1002/adma.201800202>
- Wang, S., Zhang, L., Yang, H., Li, C., Wang, Z., Xiong, J., Xv, Y., Wang, Z., Shen, J., & Jiang, H. (2023). The effects of UiO-66 ultrafine particles on the rapid detection of sulfonamides in milk: Adsorption performance and mechanism. *Food Chemistry*, *417*, 135878. <https://doi.org/10.1016/j.foodchem.2023.135878>
- Wang, T., Zhang, L., & Xin, H. (2022). A Portable Fluorescent Hydrogel-Based Device for On-Site Quantitation of Organophosphorus Pesticides as Low as the Sub-ppb Level. *Frontiers in Chemistry*, *10*. <https://www.frontiersin.org/articles/10.3389/fchem.2022.855281>
- Wang, X., Fan, J., Ren, R., Jin, Q., & Wang, J. (2016). Rapid determination of nitrite in foods in acidic conditions by high-performance liquid chromatography with fluorescence detection. *Journal of Separation Science*, *39*(12), 2263–2269. <https://doi.org/10.1002/jssc.201600093>
- Wang, Y., Peng, H., Wang, H., Zhang, M., Zhao, W., & Zhang, Y. (2022). In-situ synthesis of MOF nanoparticles in double-network hydrogels for stretchable adsorption device. *Chemical Engineering Journal*, *450*, 138216. <https://doi.org/10.1016/j.cej.2022.138216>
- Wang, Y.-M., Tian, X.-T., Zhang, H., Yang, Z.-R., & Yin, X.-B. (2018). Anticounterfeiting Quick Response Code with Emission Color of Invisible Metal–Organic Frameworks as Encoding Information. *ACS Applied Materials & Interfaces*, *10*(26), 22445–22452. <https://doi.org/10.1021/acsami.8b06901>
- Włodarska, K., Khmelinskii, I., & Sikorska, E. (2018). Authentication of apple juice categories based on multivariate analysis of the synchronous fluorescence spectra. *Food Control*, *86*, 42–49. <https://doi.org/10.1016/j.foodcont.2017.11.004>
- Wolff, I. A., & Wasserman, A. E. (1972). Nitrates, Nitrites, and Nitrosamines. *Science*, *177*(4043), 15–19. <https://doi.org/10.1126/science.177.4043.15>
- Wu, D., Xu, J., Chen, Y., Yi, M., & Wang, Q. (2018). Gum Arabic: A promising candidate for the construction of physical hydrogels exhibiting highly stretchable, self-healing and tensility reinforcing performances. *Carbohydrate Polymers*, *181*, 167–174. <https://doi.org/10.1016/j.carbpol.2017.10.076>
- Wu, H., Shen, X., Huo, D., Ma, Y., Bian, M., Shen, C., & Hou, C. (2020). Fluorescent and colorimetric dual-readout sensor based on Griess assay for nitrite detection. *Spectrochimica Acta Part A: Molecular and Biomolecular Spectroscopy*, *225*, 117470. <https://doi.org/10.1016/j.saa.2019.117470>
- Wu, H., & Tong, C. (2020). Dual-Emission Fluorescent Probe for the Simultaneous Detection of Nitrite and Mercury(II) in Environmental Water Samples Based on the Tb³⁺-Modified Carbon Quantum Dot/3-Aminophenylboronic Acid Hybrid. *Analytical Chemistry*, *92*(13), 8859–8866. <https://doi.org/10.1021/acs.analchem.0c00455>
- Wu, J., Jiang, L., Verwilst, P., An, J., Zeng, H., Zeng, L., Niu, G., & Kim, J. S. (2019). A colorimetric and fluorescent lighting-up sensor based on ICT coupled with PET for rapid, specific and sensitive detection of nitrite in food. *Chemical*

- Communications*, 55(67), 9947–9950. <https://doi.org/10.1039/C9CC05048E>
- Wu, J.-X., & Yan, B. (2018). Luminescent Hybrid Tb³⁺ Functionalized Metal–Organic Frameworks Act as Food Preservative Sensor and Water Scavenger for NO₂⁻. *Industrial & Engineering Chemistry Research*, 57(21), 7105–7111. <https://doi.org/10.1021/acs.iecr.8b00762>
- Wu, Y.-C., & Nie, F. (2015). A core–shell structured nanocomposite modified with rhodamine derivative for nitrite ion sensing. *Sensors and Actuators B: Chemical*, 212, 120–126. <https://doi.org/10.1016/j.snb.2015.02.007>
- Xiang, G., Wang, Y., Zhang, H., Fan, H., Fan, L., He, L., Jiang, X., & Zhao, W. (2018). Carbon dots based dual-emission silica nanoparticles as ratiometric fluorescent probe for nitrite determination in food samples. *Food Chemistry*, 260, 13–18. <https://doi.org/10.1016/j.foodchem.2018.03.150>
- Xiao, J., Chen, S., Yi, J., Zhang, H. F., & Ameer, G. A. (2017). A Cooperative Copper Metal–Organic Framework-Hydrogel System Improves Wound Healing in Diabetes. *Advanced Functional Materials*, 27(1), 1604872. <https://doi.org/10.1002/adfm.201604872>
- Xiao-wei, H., Xiao-bo, Z., Ji-yong, S., Zhi-hua, L., & Jie-wen, Z. (2018). Colorimetric sensor arrays based on chemo-responsive dyes for food odor visualization. *Trends in Food Science & Technology*, 81, 90–107. <https://doi.org/10.1016/j.tifs.2018.09.001>
- Xie, X., Huang, X., Lin, W., Chen, Y., Lang, X., Wang, Y., Gao, L., Zhu, H., & Chen, J. (2020). Selective Adsorption of Cationic Dyes for Stable Metal–Organic Framework ZJU-48. *ACS Omega*, 5(23), 13595–13600. <https://doi.org/10.1021/acsomega.0c00385>
- Xu, H., Cui, L., An, Y., & Jin, X. (2021). Sodium Carboxymethylcellulose as Versatile Biotemplates of Zeolitic Imidazolate Frameworks for Reduced Graphene Oxide-/N-Doped Porous Carbon Hydrogel Electrodes for Supercapacitors. *Energy & Fuels*, 35(24), 20320–20329. <https://doi.org/10.1021/acs.energyfuels.1c02979>
- Xu, L., Pan, M., Fang, G., & Wang, S. (2019). Carbon dots embedded metal-organic framework@molecularly imprinted nanoparticles for highly sensitive and selective detection of quercetin. *Sensors and Actuators B: Chemical*, 286, 321–327. <https://doi.org/10.1016/j.snb.2019.01.156>
- Xu, X.-Y., Lian, X., Hao, J.-N., Zhang, C., & Yan, B. (2017). A Double-Stimuli-Responsive Fluorescent Center for Monitoring of Food Spoilage based on Dye Covalently Modified EuMOFs: From Sensory Hydrogels to Logic Devices. *Advanced Materials*, 29(37), 1702298. <https://doi.org/10.1002/adma.201702298>
- Xue, S.-S., Tan, J., Xie, J.-Y., & Li, M.-F. (2021). Rapid, simultaneous and non-destructive determination of maize flour and soybean flour adulterated in quinoa flour by front-face synchronous fluorescence spectroscopy. *Food Control*, 130, 108329. <https://doi.org/10.1016/j.foodcont.2021.108329>
- Yan, B. (2021). Luminescence response mode and chemical sensing mechanism for lanthanide-functionalized metal–organic framework hybrids. *Inorganic Chemistry Frontiers*, 8(1), 201–233. <https://doi.org/10.1039/D0QI01153C>
- Yan, C., Jin, J., Wang, J., Zhang, F., Tian, Y., Liu, C., Zhang, F., Cao, L., Zhou, Y., & Han,

- Q. (2022). Metal–organic frameworks (MOFs) for the efficient removal of contaminants from water: Underlying mechanisms, recent advances, challenges, and future prospects. *Coordination Chemistry Reviews*, 468, 214595. <https://doi.org/10.1016/j.ccr.2022.214595>
- Yan, X., Li, H., Hu, T., & Su, X. (2017). A novel fluorimetric sensing platform for highly sensitive detection of organophosphorus pesticides by using egg white-encapsulated gold nanoclusters. *Biosensors and Bioelectronics*, 91, 232–237. <https://doi.org/10.1016/j.bios.2016.11.058>
- Yang, G.-L., Jiang, X.-L., Xu, H., & Zhao, B. (2021). Applications of MOFs as Luminescent Sensors for Environmental Pollutants. *Small*, 17(22), 2005327. <https://doi.org/10.1002/sml.202005327>
- Yang, L., Wang, F., Zhao, J., Kong, X., Lu, K., Yang, M., Zhang, J., Sun, Z., & You, J. (2021). A facile dual-function fluorescent probe for detection of phosgene and nitrite and its applications in portable chemosensor analysis and food analysis. *Talanta*, 221, 121477. <https://doi.org/10.1016/j.talanta.2020.121477>
- Yang, W., Wang, J., Han, Y., Luo, X., Tang, W., Yue, T., & Li, Z. (2021). Robust MOF film of self-rearranged UiO-66-NO₂ anchored on gelatin hydrogel via simple thermal-treatment for efficient Pb(II) removal in water and apple juice. *Food Control*, 130, 108409. <https://doi.org/10.1016/j.foodcont.2021.108409>
- Yang, X., Zhang, M., Xu, J., Wen, S., Zhang, Y., & Zhang, J. (2021). Synthesis of fluorescent terbium-based metal-organic framework for quantitative detection of nitrite and ferric ions in water samples. *Spectrochimica Acta Part A: Molecular and Biomolecular Spectroscopy*, 253, 119553. <https://doi.org/10.1016/j.saa.2021.119553>
- Yang, X., Zhang, Q., Zhang, S., Lai, M., Ji, X., Ye, Y., Li, H., & Zhao, M. (2023). Molecule fluorescent probes for sensing and imaging analytes in plants: Developments and challenges. *Coordination Chemistry Reviews*, 487, 215154. <https://doi.org/10.1016/j.ccr.2023.215154>
- Yang, X., Zhang, S., Lai, M., Ji, X., Ye, Y., Tang, J., Liu, X., & Zhao, M. (2023). Fluorescent probes for lighting up ferroptotic cell death: A review. *Talanta*, 260, 124628. <https://doi.org/10.1016/j.talanta.2023.124628>
- Ye, Y., Zhao, L., Hu, S., Liang, A., Li, Y., Zhuang, Q., Tao, G., & Gu, J. (2019). Specific detection of hypochlorite based on the size-selective effect of luminophore integrated MOF-801 synthesized by a one-pot strategy. *Dalton Transactions*, 48(8), 2617–2625. <https://doi.org/10.1039/C8DT04692A>
- Yildiz, G., Oztekin, N., Orbay, A., & Senkal, F. (2014). Voltammetric determination of nitrite in meat products using polyvinylimidazole modified carbon paste electrode. *Food Chemistry*, 152, 245–250. <https://doi.org/10.1016/j.foodchem.2013.11.123>
- Yin, B., Liang, R., Liang, X., Fu, D., Wang, L., & Sun, G. (2021). Construction of Stable Wide-Temperature-Range Proton Exchange Membranes by Incorporating a Carbonized Metal–Organic Frame into Polybenzimidazoles and Polyacrylamide Hydrogels. *Small*, 17(43), 2103214. <https://doi.org/10.1002/sml.202103214>
- Yoo, J., Ryu, U., Kwon, W., & Choi, K. M. (2019). A multi-dye containing MOF for the

- rationometric detection and simultaneous removal of Cr2O7²⁻ in the presence of interfering ions. *Sensors and Actuators B: Chemical*, 283, 426–433. <https://doi.org/10.1016/j.snb.2018.12.031>
- Yu, F., Bai, X., Liang, M., & Ma, J. (2021). Recent progress on metal-organic framework-derived porous carbon and its composite for pollutant adsorption from liquid phase. *Chemical Engineering Journal*, 405, 126960. <https://doi.org/10.1016/j.cej.2020.126960>
- Yu, K.-K., Pan, S.-L., Li, K., Shi, L., Liu, Y.-H., Chen, S.-Y., & Yu, X.-Q. (2021). A novel near-infrared fluorescent sensor for zero background nitrite detection via the “covalent-assembly” principle. *Food Chemistry*, 341, 128254. <https://doi.org/10.1016/j.foodchem.2020.128254>
- Yu, M., Zhang, H., Liu, Y., Zhang, Y., Shang, M., Wang, L., Zhuang, Y., & Lv, X. (2022). A colorimetric and fluorescent dual-readout probe based on red emission carbon dots for nitrite detection in meat products. *Food Chemistry*, 374, 131768. <https://doi.org/10.1016/j.foodchem.2021.131768>
- Yumin, A., Ligu, D., Yi, Y., & Yongna, J. (2022). Mechanical properties of an interpenetrating network poly(vinyl alcohol)/alginate hydrogel with hierarchical fibrous structures. *RSC Advances*, 12(19), 11632–11639. <https://doi.org/10.1039/D1RA07368K>
- Zainal, S. H., Mohd, N. H., Suhaili, N., Anuar, F. H., Lazim, A. M., & Othaman, R. (2021). Preparation of cellulose-based hydrogel: A review. *Journal of Materials Research and Technology*, 10, 935–952. <https://doi.org/10.1016/j.jmrt.2020.12.012>
- Zhan, Y., Zeng, Y., Li, L., Luo, F., Qiu, B., Lin, Z., & Guo, L. (2019). Ratiometric Fluorescent Hydrogel Test Kit for On-Spot Visual Detection of Nitrite. *ACS Sensors*, 4(5), 1252–1260. <https://doi.org/10.1021/acssensors.9b00125>
- Zhang, F., Yao, H., Chu, T., Zhang, G., Wang, Y., & Yang, Y. (2017). A Lanthanide MOF Thin-Film Fixed with Co3O4 Nano-Anchors as a Highly Efficient Luminescent Sensor for Nitrofurantoin Antibiotics. *Chemistry – A European Journal*, 23(43), 10293–10300. <https://doi.org/10.1002/chem.201701852>
- Zhang, F., Yao, H., Zhao, Y., Li, X., Zhang, G., & Yang, Y. (2017). Mixed matrix membranes incorporated with Ln-MOF for selective and sensitive detection of nitrofurantoin antibiotics based on inner filter effect. *Talanta*, 174, 660–666. <https://doi.org/10.1016/j.talanta.2017.07.007>
- Zhang, F., Zhu, X., Jiao, Z., Liu, X., & Zhang, H. (2018). Sensitive naked eye detection and quantification assay for nitrite by a fluorescence probe in various water resources. *Spectrochimica Acta Part A: Molecular and Biomolecular Spectroscopy*, 200, 275–280. <https://doi.org/10.1016/j.saa.2018.04.025>
- Zhang, J., He, X., Kong, Y.-R., Luo, H.-B., Liu, M., Liu, Y., & Ren, X.-M. (2021). Efficiently Boosting Moisture Retention Capacity of Porous Superprotonic Conducting MOF-802 at Ambient Humidity via Forming a Hydrogel Composite Strategy. *ACS Applied Materials & Interfaces*, 13(31), 37231–37238. <https://doi.org/10.1021/acsami.1c11054>
- Zhang, J., Yue, C., Ke, Y., Qu, H., & Zeng, L. (2023). Fluorescent probes for the detection of biogenic amines, nitrite and sulfite in food: Progress, challenges and

- perspective. *Advanced Agrochem*, 2(2), 127–141. <https://doi.org/10.1016/j.aac.2023.03.001>
- Zhang, K., Luo, X., Yang, L., Chang, Z., & Luo, S. (2021). Progress toward Hydrogels in Removing Heavy Metals from Water: Problems and Solutions—A Review. *ACS ES&T Water*, 1(5), 1098–1116. <https://doi.org/10.1021/acsestwater.1c00001>
- Zhang, N., Zhang, D., Zhao, J., & Xia, Z. (2019). Fabrication of a dual-emitting dye-encapsulated metal–organic framework as a stable fluorescent sensor for metal ion detection. *Dalton Transactions*, 48(20), 6794–6799. <https://doi.org/10.1039/C9DT01125K>
- Zhang, S.-B., Zhai, H.-C., Huang, S.-X., & Cai, J.-P. (2014). A site-directed CO₂ detection method for monitoring the spoilage of stored grains by insects and fungi in Chinese horizontal warehouses. *Journal of Stored Products Research*, 59, 146–151. <https://doi.org/10.1016/j.jspr.2014.07.002>
- Zhang, W., Banerjee, D., Liu, J., Schaefer, H. T., Crum, J. V., Fernandez, C. A., Kukkadapu, R. K., Nie, Z., Nune, S. K., Motkuri, R. K., Chapman, K. W., Engelhard, M. H., Hayes, J. C., Silvers, K. L., Krishna, R., McGrail, B. P., Liu, J., & Thallapally, P. K. (2016). Redox-Active Metal–Organic Composites for Highly Selective Oxygen Separation Applications. *Advanced Materials*, 28(18), 3572–3577. <https://doi.org/10.1002/adma.201600259>
- Zhang, X., Tu, R., Lu, Z., Peng, J., Hou, C., & Wang, Z. (2021). Hierarchical mesoporous metal–organic frameworks encapsulated enzymes: Progress and perspective. *Coordination Chemistry Reviews*, 443, 214032. <https://doi.org/10.1016/j.ccr.2021.214032>
- Zhang, X., Wang, H., Fu, N.-N., & Zhang, H.-S. (2003). A fluorescence quenching method for the determination of nitrite with Rhodamine 110. *Spectrochimica Acta Part A: Molecular and Biomolecular Spectroscopy*, 59(8), 1667–1672. [https://doi.org/10.1016/S1386-1425\(02\)00404-3](https://doi.org/10.1016/S1386-1425(02)00404-3)
- Zhang, Y., Gutiérrez, M., Chaudhari, A. K., & Tan, J.-C. (2020). Dye-Encapsulated Zeolitic Imidazolate Framework (ZIF-71) for Fluorochromic Sensing of Pressure, Temperature, and Volatile Solvents. *ACS Applied Materials & Interfaces*, 12(33), 37477–37488. <https://doi.org/10.1021/acscami.0c10257>
- Zhang, Y., Li, B., Ma, H., Zhang, L., & Zheng, Y. (2016). Rapid and facile ratiometric detection of an anthrax biomarker by regulating energy transfer process in bio-metal-organic framework. *Biosensors and Bioelectronics*, 85, 287–293. <https://doi.org/10.1016/j.bios.2016.05.020>
- Zhang, Y., Nie, J., Wei, H., Xu, H., Wang, Q., Cong, Y., Tao, J., Zhang, Y., Chu, L., Zhou, Y., & Wu, X. (2018). Electrochemical detection of nitrite ions using Ag/Cu/MWNT nanoclusters electrodeposited on a glassy carbon electrode. *Sensors and Actuators B: Chemical*, 258, 1107–1116. <https://doi.org/10.1016/j.snb.2017.12.001>
- Zhang, Y., Su, Z., Li, B., Zhang, L., Fan, D., & Ma, H. (2016). A Recyclable Magnetic Mesoporous Nanocomposite with Improved Sensing Performance toward Nitrite. *ACS Applied Materials & Interfaces*, 8(19), 12344–12351. <https://doi.org/10.1021/acscami.6b02133>

- Zhang, Y., Zhang, Y., Jia, J., Peng, H., Qian, Q., Pan, Z., & Liu, D. (2023). Nitrite and nitrate in meat processing: Functions and alternatives. *Current Research in Food Science*, 6, 100470. <https://doi.org/10.1016/j.crfs.2023.100470>
- Zhao, H., Li, N., Ma, C., Wei, Z., Zeng, Q., Zhang, K., Zhao, N., & Tang, B. Z. (2023). An AIE probe for long-term plasma membrane imaging and membrane-targeted photodynamic therapy. *Chinese Chemical Letters*, 34(4), 107699. <https://doi.org/10.1016/j.cclet.2022.07.042>
- Zhao, L., Gan, J., Xia, T., Jiang, L., Zhang, J., Cui, Y., Qian, G., & Yang, Z. (2019). A luminescent metal–organic framework integrated hydrogel optical fibre as a photoluminescence sensing platform for fluorescence detection. *Journal of Materials Chemistry C*, 7(4), 897–904. <https://doi.org/10.1039/C8TC05154B>
- Zhao, S., Gao, M., & Li, J. (2021). Lanthanides-based luminescent hydrogels applied as luminescent inks for anti-counterfeiting. *Journal of Luminescence*, 236, 118128. <https://doi.org/10.1016/j.jlumin.2021.118128>
- Zhao, X., Chang, L., Hu, Y., Xu, S., Liang, Z., Ren, X., Mei, X., & Chen, Z. (2022). Preparation of Photocatalytic and Antibacterial MOF Nanozyme Used for Infected Diabetic Wound Healing. *ACS Applied Materials & Interfaces*, 14(16), 18194–18208. <https://doi.org/10.1021/acsami.2c03001>
- Zheng, X.-J., Liang, R.-P., Li, Z.-J., Zhang, L., & Qiu, J.-D. (2016). One-step, stabilizer-free and green synthesis of Cu nanoclusters as fluorescent probes for sensitive and selective detection of nitrite ions. *Sensors and Actuators B: Chemical*, 230, 314–319. <https://doi.org/10.1016/j.snb.2016.02.063>
- Zhou, L., Anwar, M. M., Zahid, M., Shostrom, V., & Mirvish, S. S. (2014). Urinary Excretion of N-Nitroso Compounds in Rats Fed Sodium Nitrite and/or Hot Dogs. *Chemical Research in Toxicology*, 27(10), 1669–1674. <https://doi.org/10.1021/tx5000188>
- Zhou, Q., Dong, X., Zhang, B., Zhang, X., Ou, K., Wang, Q., Liao, Y., Yang, Y., & Wang, H. (2022). Naked-eye sensing and target-guiding treatment of bacterial infection using pH-tunable multicolor luminescent lanthanide-based hydrogel. *Journal of Colloid and Interface Science*, 610, 731–740. <https://doi.org/10.1016/j.jcis.2021.11.121>
- Zhu, H., Zhang, Q., & Zhu, S. (2016). Alginate Hydrogel: A Shapeable and Versatile Platform for in Situ Preparation of Metal–Organic Framework–Polymer Composites. *ACS Applied Materials & Interfaces*, 8(27), 17395–17401. <https://doi.org/10.1021/acsami.6b04505>
- Zhu, K., Fan, R., Zheng, X., Wang, P., Chen, W., Sun, T., Gai, S., Zhou, X., & Yang, Y. (2019). Dual-emitting dye-CDs@MOFs for selective and sensitive identification of antibiotics and MnO₄⁻ in water. *Journal of Materials Chemistry C*, 7(47), 15057–15065. <https://doi.org/10.1039/C9TC04700J>
- Zhu, Q., Li, Y., Wang, W., Sun, G., Yan, K., & Wang, D. (2018). High performance HKUST-1@PVA-co-PE/PVA hybrid hydrogel with enhanced selective adsorption. *Composites Communications*, 10, 36–40. <https://doi.org/10.1016/j.coco.2018.05.005>
- Zhu, S., Zhao, L., & Yan, B. (2020). A novel spectroscopic probe for detecting food

-
- preservative NO₂⁻: Citric acid functionalized metal-organic framework and luminescence sensing. *Microchemical Journal*, 155, 104768. <https://doi.org/10.1016/j.microc.2020.104768>
- Zhuang, Y., Yu, F., Chen, H., Zheng, J., Ma, J., & Chen, J. (2016). Alginate/graphene double-network nanocomposite hydrogel beads with low-swelling, enhanced mechanical properties, and enhanced adsorption capacity. *Journal of Materials Chemistry A*, 4(28), 10885–10892. <https://doi.org/10.1039/C6TA02738E>

Appendix-publications

1. Articles

(1) **Deng, S.**, Liu, J., Han, D., Yang, X., Liu, H., Zhang, C., & Blecker, C. (2024). Synchronous fluorescence detection of nitrite in meat products based on dual-emitting dye@MOF and its portable hydrogel test kit. *Journal of Hazardous Materials*, 463, 132898. <https://doi.org/10.1016/j.jhazmat.2023.132898> (Chapter IV)

(2) **Deng, S.**, Liu, H., Zhang, C., Yang, X., & Blecker, C. (2022). LMOF serve as food preservative nanosensor for sensitive detection of nitrite in meat products. *LWT-Food Science and Technology*, 169, 114030. <https://doi.org/10.1016/j.lwt.2022.114030> (Chapter III)

(3) **Deng, S.**, Liu, Y., Huang, F., Liu, J., Han, D., Zhang, C., & Blecker, C. (2021). Evaluation of volatile flavor compounds in bacon made by different pig breeds during storage time. *Food Chemistry*, 357, 129765. <https://doi.org/10.1016/j.foodchem.2021.129765>

(4) Han, D¹., **Deng, S¹.,** Wang, H., Huang, F., Fauconnier, M.-L., Li, H., Zheng, J., Meng, L., Zhang, C., & Li, X. (2023). Lipid oxidation and flavor changes in saturated and unsaturated fat fractions from chicken fat during a thermal process. *Food & Function*, 14(14), 6554–6569. <https://doi.org/10.1039/D3FO01061A>

(5) **Deng, S.**, Han, D., Yang, X., Liu, H., Zhang, C., & Blecker, C. A facile detection method for nitrite in food products: On-site agarose hydrogel test kit based on a luminescent metal-organic framework sensor. (under review in *Food Chemistry*) (Chapter V)

2. Patents

(1) Zhang C. H., **Deng S. Y.**, Li, X., Huang, F., & Han, D. Preparation method and detection method of fluorescent nanoprobe based on Rh6G@MOF-5. CN114989446B. (Chapter III)

3. Flash presentations and posters

(1) The 10th China Food and Agricultural Products Safety Inspection Technology and Quality Control International Forum: **Poster Presentation** of own project, **1st author** (CHINA) entitled “LMOF serve as food preservative nanosensor for sensitive detection of nitrite in meat products” and **the author** was invited to present a flash presentation. 03/08/2022.